



Facoltà di Scienze Matematiche Fisiche e Naturali

**Optical and electronic properties of  
Copper and Silver: from Density  
Functional Theory  
to Many Body Effects**

*Andrea Marini*

Il supervisor

*Prof. Rodolfo Del Sole*

Il coordinatore

*Prof. Piergiorgio Picozza*

*Prof. Giovanni Onida*

Tesi presentata per il conseguimento del  
titolo di *Dottore di Ricerca in Fisica*

---

*XIV CICLO*



# Acknowledgments

I began this research three years ago without knowing anything of the physics discussed in this thesis and I must say that, although my knowledge has not improved to much, I had a wonderful time with my group. It has been a pleasure for me to have many discussions with Rodolfo, Giovanni, Maurizia, Patrizia, Gianni, Conor (unfortunately (?) only in the last year). I want to thank all of them because from each one I have learnt something about the physics and the methods discussed in this thesis. I will never thank enough Conor for having read this thesis and for correcting me “one or two” spelling errors. Thanks “Irish-man” !.

Everywhere my work will bring me I will remember the few steps that divide my office from that of Rodolfo, from whom I have always received valuable suggestions and encouragements. I have to thank Rodolfo also for the confidence he had in me at the beginning, for his curiosity and for the freedom I had during these three years.

Thanks, also, to Angel, Lucia and Valerio. In our (too short) meetings I have received from them many useful suggestions and much help.

Finally, the people that has supported me throughout these three years and before: my mother, my beautiful wife Alessia and Gianni S.. Thanks ! I should not thank my friends but I will: Walter, who when I first entered into Physics, said to me that I am not good enough for this work (and maybe he is right !?) and Paolo for all the patience in listening to my complaints during never-ending phone calls from Paris.

Thanks to all !

*Andrea*



# Contents

<b>Introduction</b>	<b>v</b>
<b>1 Single particle approach and many-body corrections to the electronic excitations of solids</b>	<b>1</b>
1.1 Optical properties and plasma effects . . . . .	2
1.1.1 Macroscopic averages and Local Field effects . . . . .	6
1.1.2 Sum rules for $\epsilon$ and $\epsilon^{-1}$ . . . . .	9
1.1.3 Energy loss of external fields and charges . . . . .	10
1.2 Density-Functional-Theory . . . . .	11
1.2.1 The Hohenberg-Kohn theorem . . . . .	12
1.2.2 Kohn-Sham equations . . . . .	14
1.2.3 Local Density Approximation . . . . .	16
1.3 Green's function approach to the many-body problem . . . . .	17
1.3.1 Conserving approximations . . . . .	17
1.3.2 Examples of conserving approximations . . . . .	23
The Hartree and Hartee-Fock approximations . . . . .	23
The T-Matrix approximation . . . . .	24
1.3.3 Hedin's equations . . . . .	26
1.3.4 $GW$ and $GW_0$ Self-energies . . . . .	30
1.3.5 From Kohn-Sham particles to many-body quasiparticles . . .	31
Bibliography . . . . .	35
<b>2 Optical properties and band structure of copper within Density-Functional-Theory</b>	<b>37</b>
2.1 Pseudopotential generation . . . . .	38
2.2 Ground state properties . . . . .	40
2.3 LDA band structure . . . . .	42

2.4	Absorption spectrum: non–local pseudopotentials and intraband transitions . . . . .	43
2.4.1	Intraband transitions . . . . .	50
2.4.2	Local field effects . . . . .	52
	Bibliography . . . . .	57
<b>3</b>	<b>Quasiparticle band structure of Copper in the <i>GW</i> approximation</b>	<b>59</b>
3.1	Copper: a case study for noble metals . . . . .	60
3.2	Theoretical framework . . . . .	62
3.2.1	Exchange self energy . . . . .	62
3.2.2	The screening function . . . . .	63
3.3	Numerical details . . . . .	65
3.3.1	Exchange self-energy: Fermi surface effects . . . . .	67
3.3.2	Matrix elements of the mass operator . . . . .	71
3.3.3	Iterative solution of quasiparticle equation . . . . .	78
3.4	Band Structure Results . . . . .	81
	Bibliography . . . . .	85
<b>4</b>	<b>Lifetimes of d–holes in Copper</b>	<b>87</b>
4.1	The <i>GW</i> equations revisited . . . . .	88
4.2	The numerical approach . . . . .	91
4.3	Results and discussion . . . . .	98
4.4	A model self–consistent calculation . . . . .	101
4.4.1	The case study of silicon . . . . .	104
	Bibliography . . . . .	109
<b>5</b>	<b>The plasmon resonance and the reflectance spectrum of Silver in the <i>GW</i> approximation</b>	<b>111</b>
5.1	DFT–LDA and <i>GW</i> band structure . . . . .	114
5.2	Electron energy loss and reflectance spectrum . . . . .	115
	Bibliography . . . . .	123
	<b>Conclusions</b>	<b>125</b>
	<b>Appendix: The Self–Energy/Local Field code</b>	<b>129</b>
A.3	The Input/Output . . . . .	130
A.4	The user prompt and the main input file . . . . .	132

A.5	Runlevel 2: general preparation run $N^0$ 1 . . . . .	134
A.6	Runlevel 3: Local Field effects . . . . .	136
A.6.1	The Jellium polarization function . . . . .	137
A.7	Runlevel 4: general preparation run $N^0$ 2 . . . . .	138
A.8	Runlevel 5: exchange–correlation and bare–exchange matrix elements . . . . .	139
A.9	Runlevel 6: Plasmon–Pole parameters . . . . .	140
A.10	Runlevel 7: the full screening function . . . . .	140
A.11	Runlevel 8: <i>GW</i> quasiparticle energies . . . . .	142
A.12	Runlevel 9: <i>GW</i> quasiparticle lifetimes . . . . .	143
	Bibliography . . . . .	147
	<b>Publications</b>	<b>149</b>





# Introduction

*“The many-body problem has attracted attention since the philosophers of old speculated over the question of how many angels could dance on the head of a pin.”*

Richard D. Mattuck

As in the “angel” problem, solid state physics has to face two problems in describing the physics of matter. First of all there are many “angels” (electrons, atoms, molecules. . .). Secondly, for to be a problem, these bodies interact one with each other. As a consequence, for example, all the electrons of a solid reacts together to an external perturbation to restore the initial equilibrium.

The importance of the many-body problem derives from the fact that almost any real physical system one can think of is composed of a set of interacting particles. Furthermore, it turns out that in the calculation of physical properties of such system – for example, the energy levels or the dielectric constant – interactions between particles play a very important role.

The subject of this thesis is to study, with the use of modern many-body techniques, the electronic and optical properties of two noble metals: copper and silver.

We are dealing with a peculiar kind of metals: those containing spatially localized  $d$ -character orbitals underlying the (broader)  $s/p$  states. Therefore attempting to apply all the fundamentals of many-body theory developed in the 1950s<sup>1</sup> to describe the homogeneous electron gas, one could inquire about the role played by these localized atomic orbitals. Neglecting this role (because of their localization that could avoid any participation in the electronic reactions) the metallic screening should prevail, leading to an interpretation of the systems as composed of nearly non-interacting electrons.

Moreover copper and silver are *noble* metals. This means that the  $d$ -shell is completely full, so that no electron-hole excitations within the  $d$ -shell are possi-

---

<sup>1</sup>D. Pines, *The Many-Body problem*, Addison Wesley 1961,1997

ble. Consequently a simple  $s/p$ -metal behavior could follow and we could expect a mean-field theory (such as Density Functional theory) to work properly, describing correctly the experimental results.

As we will see in the forthcoming chapters the assumption of  $d$ -states not participating in the electronic and optical properties of the medium is far from being true.  $d$ -orbitals will play a key role in all the calculations presented here and the aim of this thesis is to develop a theoretical framework that is able to reproduce correctly the experimental results.

In the Chapter 1 the general theoretical framework of linear response theory, Density Functional Theory and many-body approach is introduced. It does not intend to be exhaustive; merely functional for the description of the experimental quantities calculated in the forthcoming chapters.

In Chapter 2 an accurate, first-principles study of the electronic structure and absorption spectrum of bulk copper within Density Functional Theory in the Local Density Approximation is presented. The plane wave basis used to expand the Bloch wavefunction requires the use of pseudopotentials. It will be shown that norm-conserving pseudopotentials can be used to work at full convergence with a relatively small plane-wave basis. However, we will see that these pseudopotentials are strongly dependent from the angular momentum, with a steep  $d$ -component that, if not correctly included in momentum matrix elements, yields macroscopically wrong results in the absorption spectrum in that many optical transitions in the energy range  $1.8, 5.0 eV$  are strongly suppressed. We will see that the correct definition of momentum matrix elements enhance the optical transition from  $d$ -bands to  $s/p$ -bands, yielding a good agreement with experimental data. We will find, however, an overestimation (of  $\sim 20\%$ ) of the absorption spectrum. I will show that this is not due to the pseudopotential approach via a series of calculations using different pseudopotentials including also the deep core levels in the atomic valence.

The Density Functional band structure is compared with experimental photoemission, finding discrepancies that are distinctly band- and  $\mathbf{k}$ -dependent. In a recent work <sup>2</sup> very-low-energy electron diffraction (VLEED) is used to measure the band structure of copper. The authors, looking at the discrepancies found between Density Functional Theory calculations and experimental results, state that it is intriguing to find such pronounced “deviations from the band theory”, copper being “a prototype weakly correlated system”. In Chapter 3, I show that these two state-

---

<sup>2</sup>V.N. Strocov et al, Phys. Rev. Lett. **81**, 4943 (1998).

ments of the experimentalists about the *deviations* from band theory and the *weak* correlation in copper are not completely true. It is true that copper deviates from Density Functional band theory I will show, infact that Many–Body *quasiparticle* band theory turns out to be in excellent agreement with experimental results.

Moreover, copper turns out to be a far from weakly correlated system, as correlation energies of  $\sim 10\text{ eV}$  are found. Again this is due to correlations among the very localized *d*-orbitals. Only by including properly the deep *3s/3p* core levels do we obtain physical results as the bare exchange with *d*-orbitals turns out to be responsible for contributions of the order of  $10\text{ eV}$ .

The Many–Body calculation is done within the *GW* approximation for the self–energy operator that, although exact in the homogeneous electron gas for high densities, is able to correctly describe the screening effects also at the metallic regime and, more importantly, in the presence of localized, atomic like, orbitals. The strong correlation effects, however, indicate that the screening in copper is not as effective as in simple metals and, again, the role played by *d*-orbitals is crucial in reproducing the experimental results.

Density functional theory is mathematically represented by an hermitian hamiltonian, so that the corresponding single particle states have infinite lifetime. However, experimentally, holes created by means of photoemission are detected with an intrinsic energy width, which corresponds to an energy indetermination due to a finite lifetime. Following the excellent *GW* band structure obtained in Chapter 3, I have used the same theoretical method to calculate the lifetime of *d*-holes in copper.

The results found compare well with recent experimental results, improving the agreement with respect to the state–of–the–art approaches. These neglect the self–energy corrections in the band structure, as well as the transfer of weight from the quasiparticle peak to higher energy regions of the spectra. Although the good results found, the “well–done” *GW* is shown to contain decay channels involving the same renormalized and unrenormalized *d*-levels. In Chapter 4 these (apparently nonphysical) events are discussed and motivated in the spirit of non selfconsistent *GW*. Some calculations beyond the non selfconsistent approach are proposed, showing that, similarly to the band structure, at self–consistency results are expected to worsen.

The last chapter of this thesis (Chapter 5) is devoted to a well–known drawback of Density Functional Theory: the plasmon resonance of silver observed in electron energy loss spectra as a sharp peak just below the interband threshold, and in the

reflectivity as a deep minimum <sup>3</sup>. Using Density Functional Theory the plasmon peak is only poorly reproduced, with an underestimation of the position and of the intensity of the resonance.

This is more surprising if compared with copper, semiconductors or simple metals where the independent particle approximation correctly reproduces the experimental spectra. I will present the first *Ab-Initio GW* calculation of the optical properties of silver with the correct threshold behavior and, consequently, the correct plasmon resonance. Electron energy loss spectra as well as reflectivity turn out to be in excellent agreement with experiment. This result is discussed and interpreted coherently with the results obtained for copper, silicon and simple metals.

For the first time the damping mechanism of the plasmon is proved theoretically, by means of the non trivial self-energy corrections found in silver. In agreement with several experiments on silver alloys, I show that *GW* shifts optical transitions near the *L*-point to below the main absorption threshold giving the finite width to the plasmon resonance.

---

<sup>3</sup>F. Wooten, *Optical Properties of solids*, Academic Press, NY 1972

# Chapter 1

## Single particle approach and many-body corrections to the electronic excitations of solids

A physical system is constituted of a set of  $N$  electrons interacting by means of Coulomb interaction. Furthermore each electron interacts with the ionic potential and the distribution of the atomic positions characterizes the configuration of the system. In this thesis we will study bulk solids, for which the atomic distribution is assumed ordered and periodic.

But this is the system at rest. Our knowledge of its electronic structure is expressed in the theoretical reproduction of some observable measured in experiments. The aim of this first chapter is to present the observable measured in optical experiments and the theoretical general tools use to interpret the results.

The physics of an interacting electronic system perturbed by an external disturbance can be described writing the hamiltonian like

$$H_{tot} = H_{solid} + H_{ext} \quad (1.1)$$

where  $H_{tot}$  is the total hamiltonian,  $H_{solid}$  is the interacting hamiltonian of the system at rest and  $H_{ext}$  is the external perturbation (in our case the electromagnetic field).

In Section 1.1 we will introduce the observable defined within linear response theory, where all the physical quantities are expanded at the first order in  $H_{ext}$ . In Section 1.2 and 1.3 we will summarize the state-of-the-art theory used to calculate excited states of  $H_{solid}$ .

Indeed, although the system is initially at rest,  $H_{ext}$  projects its ground state

on a new set of infinite excited states. Unfortunately the calculation of these excited states by simply solving the equation of motion for  $H_{solid}$  is impossible and perturbation theory must be used.

## 1.1 Optical properties and plasma effects

In discussing the response of a solid to an external electromagnetic field some general relations between the transport coefficients and the optical and energy loss spectra of the medium can be extracted. As is well known, two constants, the index of refraction and the extinction coefficient completely describe the optical properties of a system. In the case of electron energy loss spectra, one is interested on losses amounting to tens of volts compared to the incident–electron energies lying in the kilovolt range. It should be emphasized that the two external disturbances in question correspond respectively to transverse field and longitudinal fields. The transverse field is perpendicular to the direction of propagation, whereas the longitudinal field is parallel.

The frequency and wave number dependent dielectric function  $\epsilon(\mathbf{q}, \omega)$ , and its inverse, the so called dielectric response function  $\epsilon^{-1}(\mathbf{q}, \omega)$ , represent the most natural quantities from a theoretical point of view for the description of the elementary excitations of the system produced by photons or fast electrons.

In this section, following the approach of Ehrenreich [1], we will introduce a general theoretical framework of the interaction of a fully interacting solid with an external electromagnetic field, imposing gauge–invariant to all the physical quantities. We will see that this requirement leads to important relations and useful sum–rules that can be quantitatively compared with the experiment.

As usual, one begins with the hamiltonian for an N–body system

$$H = \sum_{i=1}^N \left\{ 1/2 [\mathbf{p}_i - \mathbf{A}^{ext}(\mathbf{r}_i, t)]^2 + V(\mathbf{r}_i) + \phi^{ext}(\mathbf{r}_i, t) \right\} + H_{coul}, \quad (1.2)$$

written in atomic units. Eq.(1.2) involves the coordinates and momenta  $\mathbf{r}_i$  and  $\mathbf{p}_i$  of particle  $i$ , an external vector potential  $\mathbf{A}^{ext}(\mathbf{r}_i, t)$ , an external scalar potential  $\phi^{ext}(\mathbf{r}_i, t)$ , a single–particle periodic potential  $V(\mathbf{r}_i)$  and the residual Coulomb

interaction  $H_{coul}$ . The total hamiltonian can be written as

$$H = H_{solid} + H^{ext}(t), \quad (1.3)$$

$$H_{solid} = H_0 + H_{coul} = \sum_i (\mathbf{p}_i^2 + V(\mathbf{r}_i)) + H_{coul}, \quad (1.4)$$

$$H^{ext}(t) = -1/2 \sum_i [\mathbf{p}_i/2\mathbf{A}^{ext}(\mathbf{r}_i, t) + \mathbf{A}^{ext}(\mathbf{r}_i, t)\mathbf{p}_i + \phi^{ext}(\mathbf{r}_i, t)]. \quad (1.5)$$

The term  $A^2$  has been neglected in this linear treatment of the response to the external fields.  $H^{ext}$  can be rewritten as

$$H^{ext}(t) = - \int d\mathbf{r} \mathbf{j}(\mathbf{r}) \cdot \mathbf{A}^{ext}(\mathbf{r}, t) + \int d\mathbf{r} \rho(\mathbf{r}) \phi^{ext}(\mathbf{r}, t), \quad (1.6)$$

with

$$\mathbf{j}(\mathbf{r}) = 1/2 \sum_i [\mathbf{p}_i \delta(\mathbf{r} - \mathbf{r}_i) + \delta(\mathbf{r} - \mathbf{r}_i) \mathbf{p}_i], \quad (1.7)$$

$$\rho(\mathbf{r}) = \sum_i \delta(\mathbf{r} - \mathbf{r}_i); \quad (1.8)$$

introducing the current and charge operators. The first consequence of the presence of an external perturbation is the change in the electronic state of the solid: if  $|\Psi\rangle$  is the ground state of  $H_{solid}$  representing the status of the system at  $t = -\infty$  at first order perturbation expansion  $|\Psi\rangle$  will evolve in  $|\Psi(t)\rangle$  given by

$$|\Psi(t)\rangle \approx |\Psi\rangle + i \int_{-\infty}^t dt' H_I^{ext}(t') |\Psi\rangle, \quad (1.9)$$

and all the physical quantities are affected by this dynamics. In Eq. (1.9)  $H_I^{ext}(t)$  is represented in the interaction representation respect to  $H_{solid}$ . So the induced current, defined as

$$\begin{aligned} \mathbf{j}^{ind}(\mathbf{r}, t) &\equiv \langle \Psi(t) | \mathbf{j}(\mathbf{r}) - \rho(\mathbf{r}) \mathbf{A}^{ext}(\mathbf{r}, t) | \Psi(t) \rangle \\ &= \langle \Psi_I(t) | \mathbf{j}_I(\mathbf{r}, t) - \rho_I(\mathbf{r}, t) \mathbf{A}^{ext}(\mathbf{r}, t) | \Psi_I(t) \rangle, \end{aligned} \quad (1.10)$$

using Eq. (1.9) becomes

$$\mathbf{j}^{ind}(\mathbf{r}, t) = -n(\mathbf{r}) \mathbf{A}^{ext}(\mathbf{r}, t) - i \int_{-\infty}^t \langle [\mathbf{j}_I(\mathbf{r}, t'), H_I^{ext}(\mathbf{r}, t')] \rangle dt'; \quad (1.11)$$

where the averages are made on the ground state  $|\Psi\rangle$ ,  $n(\mathbf{r}) = \langle \Psi | \rho(\mathbf{r}) | \Psi \rangle$  and we have used the important consequence of our definition of current, Eq. (1.7)

$$\langle \Psi | \mathbf{j}(\mathbf{r}) | \Psi \rangle = 0, \quad (1.12)$$

due to the absence of any charge–current in the unperturbed ground state. In the next chapter we will see that in presence of a non–local potential Eq. (1.12) would give a non vanishing charge–current if the definition given in Eq. (1.7) is not modified.

After substituting the explicit expression for  $H^{ext}$  we obtain

$$\begin{aligned} \mathbf{j}^{ind}(\mathbf{r}, t) = & -\langle \rho \rangle \mathbf{A}^{ext}(\mathbf{r}, t) + i \int_{-\infty}^t dt' \int d\mathbf{r}' \chi_{jj}^c(\mathbf{r}\mathbf{r}', t-t') \cdot \mathbf{A}^{ext}(\mathbf{r}', t') \\ & - i \int_{-\infty}^t dt' \int d\mathbf{r}' \chi_{j\rho}^c(\mathbf{r}\mathbf{r}', t-t') \phi^{ext}(\mathbf{r}', t'), \end{aligned} \quad (1.13)$$

where the absorptive response functions are introduced

$$\chi_{jj}^c(\mathbf{r}\mathbf{r}', t-t') \equiv \frac{1}{2} \langle [\mathbf{j}_I(\mathbf{r}, t), \mathbf{j}_I(\mathbf{r}, t')] \rangle, \quad (1.14)$$

$$\chi_{j\rho}^c(\mathbf{r}\mathbf{r}', t-t') \equiv \frac{1}{2} \langle [\mathbf{j}_I(\mathbf{r}, t), \rho_I(\mathbf{r}, t')] \rangle, \quad (1.14')$$

$$\chi_{\rho\rho}^c(\mathbf{r}\mathbf{r}', t-t') \equiv \frac{1}{2} \langle [\rho_I(\mathbf{r}, t), \rho_I(\mathbf{r}, t')] \rangle. \quad (1.14'')$$

Before going on it should be noted that these expressions explicitly include the causal nature of the time evolution of the system: in Eq. (1.13) the response of the system at time  $t$  due to an external field occurs at times later than those at which the field acts.

Now we define the complex response functions that, linked to the retarded Green's functions, will be suitable for diagrammatic many–body expansion:

$$\chi_{jj}(\mathbf{r}\mathbf{r}', t) \equiv 2i\theta(t) \chi_{jj}^c(\mathbf{r}\mathbf{r}', t) \quad (1.15)$$

so that  $\mathbf{j}^{ind}(\mathbf{r}, t)$  can be rewritten as

$$\begin{aligned} \mathbf{j}^{ind}(\mathbf{r}, t) = & -n(\mathbf{r}) \mathbf{A}^{ext}(\mathbf{r}, t) + \iint_{-\infty}^{\infty} d\mathbf{r}' dt' \chi_{jj}(\mathbf{r}\mathbf{r}', t-t') \cdot \mathbf{A}^{ext}(\mathbf{r}', t') \\ & - \iint_{-\infty}^{\infty} d\mathbf{r}' dt' \chi_{j\rho}(\mathbf{r}\mathbf{r}', t-t') \phi^{ext}(\mathbf{r}', t'). \end{aligned} \quad (1.16)$$

In exactly the same way the induced charge

$$\begin{aligned} \rho^{ind}(\mathbf{r}, t) = & \iint_{-\infty}^{\infty} d\mathbf{r}' dt' \chi_{\rho j}(\mathbf{r}\mathbf{r}', t-t') \cdot \mathbf{A}^{ext}(\mathbf{r}', t') \\ & - \iint_{-\infty}^{\infty} d\mathbf{r}' dt' \chi_{\rho\rho}(\mathbf{r}\mathbf{r}', t-t') \phi^{ext}(\mathbf{r}', t'), \end{aligned} \quad (1.17)$$

can be obtained to first order. The general tensor character of the current–current commutator should be noted. The present treatment, however, will be specialized to cubic crystals (like Cu and Ag) for which this quantity is a scalar.



Eq. (1.16–1.17) are the main result of this first general part of the approach to the linear response theory. However we have introduced three correlation functions (current–current, current–charge and charge–charge), that complicate considerably the practical implementation to real systems. At this point is fundamental to introduce the requirement of gauge–invariance of the theory in order to reduce the theoretical quantities introduced. We recall that if new potentials  $\overline{\phi}^{ext}(\mathbf{r}, t)$  and  $\overline{\mathbf{A}}^{ext}(\mathbf{r}, t)$  are introduced so that

$$\overline{\phi}^{ext}(\mathbf{r}, t) = \phi^{ext}(\mathbf{r}, t) - \frac{\partial}{\partial t} \Lambda(\mathbf{r}, t), \quad (1.18)$$

$$\overline{\mathbf{A}}^{ext}(\mathbf{r}, t) = \mathbf{A}^{ext}(\mathbf{r}, t) - \frac{\partial}{\partial \mathbf{r}} \Lambda(\mathbf{r}, t), \quad (1.19)$$

where  $\Lambda(\mathbf{r}, t)$  is an arbitrary scalar function, the observable quantities such as  $\mathbf{j}^{ind}$  and  $\rho^{ind}$  must remain unchanged. This property permits the deduction of some useful relations. Since we are dealing here with linear response we can freely assume the external field to be monochromatic (moreover such a field conforms the experimental conditions in the optical case). As consequence

$$\mathbf{A}^{ext}(\mathbf{r}, t) = \mathbf{A}^{ext}(\mathbf{r}, \omega) e^{i(\mathbf{q}\cdot\mathbf{r} - \omega t)}, \quad (1.20)$$

and imposing, first, that

$$\mathbf{j}^{ind}(\mathbf{r}, t) \Big|_{\Lambda(\mathbf{r}, t)=0} = \mathbf{j}^{ind}(\mathbf{r}, t) \Big|_{\Lambda(\mathbf{r}, t) \neq 0}, \quad (1.21)$$

we get the conditions

$$\frac{\partial}{\partial \mathbf{r}'} \cdot \chi''_{jj}(\mathbf{r}\mathbf{r}', \omega) = -i\omega \chi''_{j\rho}(\mathbf{r}\mathbf{r}', \omega), \quad (1.22)$$

$$2i \chi''_{j\rho}(\mathbf{r}\mathbf{r}', t) \Big|_{t=0} = n(\mathbf{r}) \frac{\partial}{\partial \mathbf{r}'} \delta(\mathbf{r} - \mathbf{r}'); \quad (1.22')$$

where  $\chi'$  and  $\chi''$  are the real and imaginary part of  $\chi$ . Similarly, a relation between  $\chi''_{j\rho}$  and  $\chi''_{\rho\rho}$  can be established by making a gauge transformation on the expression for  $\rho^{ind}$

$$\frac{\partial}{\partial \mathbf{r}'} \cdot \chi''_{\rho\rho}(\mathbf{r}\mathbf{r}', \omega) = -i\omega \chi''_{\rho\rho}(\mathbf{r}\mathbf{r}', \omega). \quad (1.23)$$

Using these three relations two important relations can be obtained: the first is the *longitudinal sum rule*

$$n(\mathbf{r}) \frac{\partial}{\partial \mathbf{r}'} \delta(\mathbf{r} - \mathbf{r}') = \frac{1}{\pi} \frac{\partial}{\partial \mathbf{r}'} \int \frac{d\omega'}{\omega'} \chi''_{jj}(\mathbf{r}\mathbf{r}', \omega'), \quad (1.24)$$

while the second is the expansion of  $\mathbf{j}^{ind}(\mathbf{r}, \omega)$  in terms of the external electric field

$$\mathbf{j}^{ind}(\mathbf{r}, \omega) = -i\omega \int d\mathbf{r}' \tilde{\alpha}(\mathbf{r}\mathbf{r}', \omega) \mathbf{E}^{ext}(\mathbf{r}', \omega), \quad (1.25)$$

with

$$\mathbf{E}^{ext}(\mathbf{r}, \omega) \equiv \frac{\partial}{\partial \mathbf{r}} \phi^{ext}(\mathbf{r}, \omega) + i\omega \mathbf{A}^{ext}(\mathbf{r}, \omega), \quad (1.26)$$

$$\tilde{\alpha}(\mathbf{r}\mathbf{r}', \omega) \equiv \frac{1}{\omega^2} [\chi_{jj}(\mathbf{r}\mathbf{r}', \omega) - n(\mathbf{r}) \delta(\mathbf{r} - \mathbf{r}')]; \quad (1.27)$$

where  $\tilde{\alpha}(\mathbf{r}\mathbf{r}', \omega)$  is the quasi-susceptibility. It should be remembered that the true susceptibility  $\alpha(\mathbf{r}\mathbf{r}', \omega)$  involves the total field  $E^{tot}(\mathbf{r}, \omega)$ .

### 1.1.1 Macroscopic averages and Local Field effects

The kinds of longitudinal and transverse disturbances that are being dealt with are such that the external fields are slowly varying over the unit cell. More precisely the wavelength  $\lambda = 2\pi/|\mathbf{q}|$  is such that  $\lambda \ll \Omega^{1/3}$ , where  $\Omega$  is the unit cell volume of the crystal lattice.

In this regime the link between microscopic and Maxwell equations is obtained regarding the cell position  $\mathbf{R}$  as continuous coordinates. To achieve this we start writing the slowly varying external field as

$$\mathbf{E}^{ext}(\mathbf{r}, \omega) = \mathbf{E}^{ext}(\mathbf{q}, \omega) e^{i\mathbf{q}\cdot\mathbf{r}}. \quad (1.28)$$

Fourier transforming the  $\mathbf{j}^{ind}(\mathbf{r}, \omega)$  and  $\tilde{\alpha}(\mathbf{r}\mathbf{r}', \omega)$  functions

$$\mathbf{j}^{ind}(\mathbf{r}, \omega) = \sum_{\mathbf{q}} \mathbf{j}^{ind}(\mathbf{r}, \mathbf{q}, \omega) e^{i\mathbf{q}\cdot\mathbf{r}}, \quad (1.29)$$

$$\tilde{\alpha}(\mathbf{r}\mathbf{r}', \omega) = \sum_{\mathbf{q}} \tilde{\alpha}(\mathbf{r}\mathbf{r}', \mathbf{q}, \omega) e^{i\mathbf{q}\cdot(\mathbf{r}-\mathbf{r}')}, \quad (1.29')$$

where the residual dependence of  $\mathbf{j}(\mathbf{r}, \mathbf{q}, \omega)$  and  $\tilde{\alpha}(\mathbf{r}\mathbf{r}', \mathbf{q}, \omega)$  from  $(\mathbf{r}, \mathbf{r}')$  is due to the lack of continuous translation invariance of the crystal. Using Eq. (1.29') Eq. (1.25) can be rewritten as

$$\begin{aligned} \mathbf{j}^{ind}(\mathbf{r}, \omega) &= -i\omega \int d\mathbf{r}' \frac{1}{(2\pi)} \int d\mathbf{q}' \tilde{\alpha}(\mathbf{r}\mathbf{r}', \mathbf{q}'\omega) e^{i\mathbf{q}'\cdot(\mathbf{r}-\mathbf{r}')} \mathbf{E}^{ext}(\mathbf{q}', \omega) e^{i\mathbf{q}'\cdot\mathbf{r}'} \\ &= -i\omega e^{i\mathbf{q}\cdot\mathbf{r}} \int \frac{d\mathbf{q}'}{2\pi} \left[ \int d\mathbf{r}' \tilde{\alpha}(\mathbf{r}\mathbf{r}', \mathbf{q}'\omega) e^{i\mathbf{q}'\cdot(\mathbf{r}-\mathbf{r}')} \mathbf{E}^{ext}(\mathbf{q}', \omega) \right] \\ &\approx -i\omega e^{i\mathbf{q}\cdot\mathbf{r}} \int \frac{d\mathbf{q}'}{2\pi} \Omega \sum_{\mathbf{R}} e^{i\mathbf{R}\cdot(\mathbf{q}-\mathbf{q}')} \left[ \int_0^{\Omega} \frac{d\mathbf{r}'}{\Omega} \tilde{\alpha}(\mathbf{r}\mathbf{r}', \mathbf{q}'\omega) \mathbf{E}^{ext}(\mathbf{q}', \omega) \right], \quad (1.30) \end{aligned}$$

where we have used the fact that the external electric field is slowly varying in the unit cell. Finally we obtain that

$$\mathbf{j}^{ind}(\mathbf{r}, \omega) = -i\omega \langle \tilde{\alpha}(\mathbf{r}\mathbf{r}', \mathbf{q}'\omega) \rangle_0 \mathbf{E}^{ext}(\mathbf{q}', \omega), \quad (1.31)$$

$$\langle \tilde{\alpha}(\mathbf{r}\mathbf{r}', \mathbf{q}'\omega) \rangle_0 \equiv \int_0 \frac{d\mathbf{r}'}{\Omega} \tilde{\alpha}(\mathbf{r}\mathbf{r}', \mathbf{q}'\omega), \quad (1.32)$$

and only the  $\mathbf{q}$  component is seen to remain. Now, using Eq. (1.31), we can finally pass to the macroscopic coordinates. Because of the lattice periodicity

$$\langle \mathbf{j}^{ind}(\mathbf{r}, \omega) \rangle_{\mathbf{R}} \equiv \int_{\mathbf{R}} \frac{d\mathbf{r}'}{\Omega} \mathbf{j}^{ind}(\mathbf{r}, \omega) = \langle \mathbf{j}^{ind}(\mathbf{r}, \omega) \rangle_0, \quad (1.33)$$

so that

$$\langle \mathbf{j}^{ind}(\mathbf{r}, \omega) \rangle_0 = \int_{\mathbf{R}} \frac{d\mathbf{r}'}{\Omega} \sum_{\mathbf{K}} \mathbf{j}^{ind}(\mathbf{q} + \mathbf{K}, \omega) e^{i\mathbf{K}\cdot\mathbf{r}} = \mathbf{j}^{ind}(\mathbf{q} + \mathbf{0}, \omega); \quad (1.34)$$

where  $\mathbf{K}$  is a reciprocal lattice vector. Analogously

$$\begin{aligned} \langle \langle \tilde{\alpha}(\mathbf{r}\mathbf{r}', \omega) \rangle \rangle_0 &\equiv \left\langle \int_0 \frac{d\mathbf{r}'}{\Omega} \tilde{\alpha}(\mathbf{r}\mathbf{r}', \mathbf{q}'\omega) \right\rangle_{\mathbf{R}} \\ &= \iint \frac{\mathbf{r}\mathbf{r}'}{\Omega^2} \sum_{\mathbf{K}, \mathbf{K}'} \tilde{\alpha}(\mathbf{q} + \mathbf{K}, \mathbf{q} + \mathbf{K}', \omega) e^{i\mathbf{K}\cdot\mathbf{r}} e^{-i\mathbf{K}'\cdot\mathbf{r}'} = \tilde{\alpha}(\mathbf{q} + \mathbf{0}, \mathbf{q} + \mathbf{0}, \omega) \equiv \tilde{\alpha}(\mathbf{q}, \omega). \end{aligned} \quad (1.35)$$

Thus we obtain the form

$$\mathbf{j}^{ind}(\mathbf{q}, \omega) = -i\omega \tilde{\alpha}(\mathbf{q}, \omega) \mathbf{E}^{ext}(\mathbf{q}, \omega), \quad (1.36)$$

whose appearance is now the same as in the translationally invariant case. It must be emphasized that the average procedure obtained so far is not valid for the response of the system to the total electric field.

To clarify better this point we need to introduce the more conventional susceptibilities and dielectric constants, starting from the Maxwell equations:

$$\nabla \cdot \mathbf{E}^{ext} = 4\pi\rho^{ext}, \quad \nabla \times \mathbf{E}^{tot} = -\frac{\partial \mathbf{B}}{\partial t}, \quad (1.37)$$

$$\nabla \cdot \mathbf{B} = 0, \quad \nabla \times \mathbf{B}^{tot} = \frac{\partial \mathbf{E}^{tot}}{\partial t} + 4\pi\mathbf{j}^{tot}, \quad (1.37')$$

where the total charge and current are expressed in terms of the external and induced quantities

$$\mathbf{j}^{tot} = \mathbf{j}^{ext} + \mathbf{j}^{ind}, \quad \rho^{tot} = \rho^{ext} + \rho^{ind}. \quad (1.38)$$

These equations are obtained from the microscopic ones by means of averages such as introduced before, where the coordinates appearing in Eq. (1.37) are the cell positions  $\mathbf{R}$

$$\langle \mathbf{E}(\mathbf{r}, \omega) \rangle_{\mathbf{R}} = \mathbf{E}(\mathbf{R}, \omega), \quad (1.39)$$

and similar relations define the “macroscopic” derivative. We may now define the microscopic frequency dependent *longitudinal* dielectric constant  $\epsilon_L(\mathbf{r}\mathbf{r}', \omega)$

$$\nabla \cdot \int d\mathbf{r}' \epsilon_L(\mathbf{r}\mathbf{r}', \omega) \mathbf{E}^{tot}(\mathbf{r}', \omega) = 4\pi\rho^{ext}(\mathbf{r}, \omega), \quad (1.40)$$

that, together with the relationship

$$\nabla \cdot \mathbf{E}^{ext}(\mathbf{r}, \omega) = 4\pi\rho^{ext}(\mathbf{r}, \omega), \quad (1.41)$$

implies

$$\int d\mathbf{r}' \epsilon_L(\mathbf{r}\mathbf{r}', \omega) \mathbf{E}^{tot}(\mathbf{r}', \omega) = \mathbf{E}^{ext}(\mathbf{r}, \omega) + \nabla \times F(\mathbf{r}, \omega); \quad (1.42)$$

where  $F(\mathbf{r}', \omega)$  is an arbitrary vector. Since, as pointed out before, average of response functions are mostly readily obtained when they multiply the much slowly varying external fields, it is convenient to consider the inverse dielectric function  $\epsilon^{-1}(\mathbf{r}', \omega)$ , defined as

$$\mathbf{E}^{tot}(\mathbf{r}', \omega) = \int d\mathbf{r}'' \epsilon^{-1}(\mathbf{r}'\mathbf{r}'', \omega) [\mathbf{E}^{ext}(\mathbf{r}'', \omega) + \nabla \times F(\mathbf{r}'', \omega)], \quad (1.43)$$

so that, since for cubic crystals  $\langle \epsilon^{-1} \nabla \times F \rangle_0 = 0$ , we find

$$\mathbf{E}^{tot}(\mathbf{q}, \omega) = \epsilon_L^{-1}(\mathbf{q}, \omega) \mathbf{E}^{ext}(\mathbf{q}, \omega) \implies \epsilon_L(\mathbf{q}, \omega) = \langle \langle \epsilon_L^{-1}(\mathbf{r}\mathbf{r}', \omega) \rangle \rangle_0^{-1}. \quad (1.44)$$

This is an important result showing that, generally

$$\epsilon_L(\mathbf{q}, \omega) \neq \langle \langle \epsilon_L(\mathbf{r}\mathbf{r}', \omega) \rangle \rangle_0. \quad (1.45)$$

The difference between Eq. (1.44) and Eq. (1.45) is due to the so-called *Local Field Effects*, linked to the absence of the continuous translation invariance present in the homogeneous electron gas.

At this point it may be worth-while to digress briefly in order to consider the condition for plasma oscillation in the solid imposed by Eq. (1.44). Since the plasmon corresponds to a collective excitation of the electrons in the system, which, as a normal mode must persist, it is possible to have a non-vanishing induced current

and hence a total field inside the system without the presence of an external field. From Eq. (1.44) it is seen that this implies

$$\epsilon_L(\mathbf{q}, \omega_p(\mathbf{q})) = \text{Re}[\epsilon_L(\mathbf{q}, \omega_p(\mathbf{q}))] + i \text{Im}[\epsilon_L(\mathbf{q}, \omega_p(\mathbf{q}))] = 0, \quad (1.46)$$

where  $\omega_p(\mathbf{q})$  is the plasma frequency. In practice, a well-defined plasma oscillations can be observed if  $\text{Re}[\epsilon_L(\mathbf{q}, \omega_p(\mathbf{q}))] = 0$  and  $\text{Im}[\epsilon_L(\mathbf{q}, \omega_p(\mathbf{q}))] \ll 1$ . The latter condition, as we will see in the case of Ag, implies that although non vanishing, the damping of the plasmon is small.

Returning now to the main development, Maxwell equations allow to obtain the relations between  $\epsilon_L(\mathbf{q}, \omega)$ ,  $\tilde{\alpha}(\mathbf{q}, \omega)$  and the true polarizability  $\alpha(\mathbf{q}, \omega)$  defined as

$$\mathbf{j}^{ind}(\mathbf{q}, \omega) = i\omega\alpha_L(\mathbf{q}, \omega)\mathbf{E}^{tot}(\mathbf{q}, \omega). \quad (1.47)$$

These relations are:

$$\alpha_L(\mathbf{q}, \omega) = \frac{\epsilon_L(\mathbf{q}, \omega) - 1}{4\pi}, \quad (1.48)$$

$$\epsilon_L^{-1}(\mathbf{q}, \omega) = 1 - 4\pi\tilde{\alpha}(\mathbf{q}, \omega). \quad (1.49)$$

Regarding the transverse disturbance, for which  $\nabla \cdot \mathbf{E}^{tot} = 0$ , the definition of  $\epsilon_T(\mathbf{q}, \omega)$  is now linked to the relation between the total electric field and the external current (not the charge like in the longitudinal case), but the important result is that in the long-wavelength limit  $\mathbf{q} \rightarrow \mathbf{0}$

$$\epsilon_T^{-1}(\mathbf{0}, \omega) = 1 - 4\pi\tilde{\alpha}(\mathbf{0}, \omega) \implies \epsilon_L(\mathbf{0}, \omega) = \epsilon_T(\mathbf{0}, \omega), \quad (1.50)$$

that is, for cubic crystals the longitudinal and transverse dielectric constants are equal in the long-wavelength limit [1]. It is this result which implies that optical and electron energy-loss experiments, which corresponds respectively to transverse and longitudinal disturbances, yield identical information concerning the elementary excitations at  $\mathbf{q} = \mathbf{0}$ .

### 1.1.2 Sum rules for $\epsilon$ and $\epsilon^{-1}$

Having defined the longitudinal and transverse dielectric constants, it is now desirable to express the previous derived longitudinal sum rule in terms of  $\epsilon$  and  $\epsilon^{-1}$ . We shall now restrict our attention exclusively to the  $\mathbf{q} \rightarrow \mathbf{0}$  limit where

$$\epsilon^{-1}(\omega) = \epsilon_L^{-1}(\omega) = 1 - 4\pi\tilde{\alpha}(\omega). \quad (1.51)$$

The averaged form of Eq. (1.27) is

$$\tilde{\alpha}(\omega) = 1/\omega^2 [\chi_{jj}(\omega) - n_{el}], \quad (1.52)$$

while the averaged longitudinal sum rule is

$$\frac{1}{\pi} \int_{-\infty}^{\infty} \frac{d\omega'}{\omega'} \chi_{jj}''(\omega') = n_{el} \implies \int_0^{\infty} d\omega' \omega' \text{Im} [\epsilon^{-1}(\omega')] = -\frac{\pi}{2} \omega_p^2; \quad (1.53)$$

with  $\omega_p^2 = 4\pi n_{el}$  and  $n_{el} = \Omega^{-1} \int d\mathbf{r} n(\mathbf{r})$ . The corresponding result for  $\epsilon(\omega)$  follows from its analytical properties and asymptotic behavior

$$\int_0^{\infty} d\omega' \omega' \text{Im} [\epsilon(\omega')] = \frac{\pi}{2} \omega_p^2. \quad (1.54)$$

### 1.1.3 Energy loss of external fields and charges

A last step is necessary to link the optical functions defined so far to the experimental quantities. The rate at which an external field does work on a system, or the energy loss of that field, is given by

$$\frac{dW}{dt} = \frac{d}{dt} \langle \Psi(t) | H_{solid} | \Psi(t) \rangle = i \langle \Psi(t) | [H^{ext}(t), H_{solid}] | \Psi(t) \rangle, \quad (1.55)$$

that, using the equation of motion for  $|\Psi(t)\rangle$ , can be rewritten as

$$\begin{aligned} & \langle \Psi(t) | [H^{ext}(t), H_{solid}] | \Psi(t) \rangle \\ &= i \frac{d}{dt} \langle \Psi(t) | H^{ext}(t) | \Psi(t) \rangle - \langle \Psi(t) | \frac{d}{dt} H^{ext}(t) | \Psi(t) \rangle, \end{aligned} \quad (1.56)$$

so to obtain

$$\frac{dW}{dt} = \int d\mathbf{r} \left[ \mathbf{A}^{ext}(\mathbf{r}, t) \frac{d\mathbf{j}^{ind}(\mathbf{r}, t)}{dt} - \phi^{ext}(\mathbf{r}, t) \frac{d\rho^{ind}(\mathbf{r}, t)}{dt} \right]. \quad (1.57)$$

Using the expansions given by Eqs. (1.16) and Eq. (1.17) for  $\mathbf{j}^{ind}(\mathbf{r}, t)$  and  $\rho^{ind}(\mathbf{r}, t)$  we obtain

$$\frac{dW}{dt} = - \int dt' d\mathbf{r} d\mathbf{r}' \mathbf{A}^{ext}(\mathbf{r}, \omega) \frac{d}{dt} \chi_{jj}(\mathbf{r}\mathbf{r}', t-t') \mathbf{A}^{ext}(\mathbf{r}'t'), \quad (1.58)$$

in the transverse case and

$$\frac{dW}{dt} = - \int dt' d\mathbf{r} d\mathbf{r}' \phi^{ext}(\mathbf{r}, t) \frac{d}{dt} \chi_{\rho\rho}(\mathbf{r}\mathbf{r}', t-t') \phi^{ext}(\mathbf{r}'t'), \quad (1.59)$$

in the longitudinal. The average energy loss is obtained by averaging over a cycle of the external monochromatic field and taking the real part. In the transverse case we obtain

$$\overline{\frac{dW}{dt}} = 1/2 \int d\mathbf{r} d\mathbf{r}' [\mathbf{A}^{ext}(\mathbf{r}, t)]^* \omega \chi_{jj}''(\mathbf{r}\mathbf{r}', \omega) \mathbf{A}^{ext}(\mathbf{r}', \omega), \quad (1.60)$$

while a similar result involving  $\rho^{ext}$  and  $\chi''_{\rho\rho}$  is obtained for the longitudinal case. Consider, now, the absorption of light by the solid; if

$$\mathbf{A}^{ext}(\mathbf{r}, \omega) = -i/\omega \mathbf{E}^{ext}(\mathbf{q}, \omega) e^{i\mathbf{q}\cdot\mathbf{r}}, \quad (1.61)$$

we get

$$\frac{dW}{dt} = \frac{\omega}{8\pi} [-Im(\epsilon^{-1}(\omega))] |\mathbf{E}^{ext}(\mathbf{q}, \omega)|^2 = \frac{\omega}{8\pi} Im[\epsilon(\omega)] |\mathbf{E}^{tot}(\mathbf{q}, \omega)|^2. \quad (1.62)$$

In the case of energy loss of electrons, the external charge density can be assumed classical (because of the large electron energy) so that  $\rho^{ext}(\mathbf{r}, t) = \delta(\mathbf{r} - \mathbf{v}t)$  and

$$\rho^{ext}(\mathbf{q}, \omega) = 2\pi\delta(\omega - \mathbf{q}\cdot\mathbf{v}) = |\mathbf{q}|^2/4\pi\rho^{ext}(\mathbf{q}, \omega), \quad (1.63)$$

with  $\mathbf{v}$  electron velocity. Now the energy loss of the incident electron per unit path length is the quantity usually calculated. It is given by the real part of

$$\frac{dW}{dx} = \frac{dW}{|\mathbf{v}|dt} = \frac{1}{|\mathbf{v}|} \int dt' d\mathbf{r} d\mathbf{r}' \phi^{ext}(\mathbf{r}, t) \frac{d}{dt} \chi_{\rho\rho}(\mathbf{r}\mathbf{r}', t-t') \phi^{ext}(\mathbf{r}'t'), \quad (1.64)$$

but Eqs. (1.22) can be used to relate  $\chi_{\rho\rho}$  to  $\chi_{jj}$

$$\chi''_{\rho\rho}(\omega) = \left(\frac{|\mathbf{q}|}{\omega}\right)^2 \chi''_{jj}(\omega) = -\frac{|\mathbf{q}|^2}{4\pi} Im[\epsilon^{-1}(\omega)]. \quad (1.65)$$

We thus find, from Eq. (1.64), the well-known result

$$\frac{dW}{dx} = -\frac{1}{2\pi^2|\mathbf{v}|} \int d\mathbf{q} d\omega \frac{\omega}{|\mathbf{v}|^2} Im[\epsilon^{-1}(\omega)] \delta(\omega - \mathbf{q}\cdot\mathbf{v}). \quad (1.66)$$

## 1.2 Density-Functional-Theory

In the last section we have introduced a set of observables measured in optical and energy loss experiments. From Eq. (1.9) follows that, although the system is initially at rest, the evolved ground state under the action of the external disturbance acquires components over all the possible excited states of the system.

The calculation of these excited states is, however, a formidable task. Many different approaches are possible but all of them have to restore some reasonable approximations. In Section 1.3 we will introduce the Green's function concept where the excited states are easily linked to the spectral decomposition of the function. But, as we will see, both theory and implementation are rather complicate.

A completely different approach is devoted to the definition of the best single-particle potential able to reproduce the full spectra of excitations of the system.

Clearly in this case all is described in terms of Fock states, product of these “best” single-particle states. We will see, as examples, the Hartree and Hartree-Fock approximations. All these approaches define the “best” single-particle potential through a variational principle.

A similar approach is that of the Thomas-Fermi model [2], with a, non marginal, characteristic: the model does express the ground state energy in terms of the density alone. This could appear as an heuristic attempt to cut the chain of many-body correlations contained in the full interacting hamiltonian.

Moreover the notion that ground state properties of a quantum many-particle systems can be characterized solely in terms of the one-particle density is not obvious. This could appear as an indication that the Thomas-Fermi model still remains an heuristic model, and the link between ground state energy and density a lucky property.

In this framework the basic theorem of Hohenberg-Kohn has a fundamental importance. The original theorem states that an exact representation of the ground state properties of a stationary, non relativistic many-particle systems in terms of the exact ground state density is possible. This is the basis of Density-Functional-Theory (DFT).

In the following we will describe this basic theorem for a rather simple cases. A rigorous foundation of DFT has been extended to cover practically all the situations of interest [2].

### 1.2.1 The Hohenberg-Kohn theorem

The hamiltonian describing the fully interacting system at rest, Eq. (1.2), contains a Coulomb part plus a single-particle contribution. This term is completely defined if the external potential  $V(\mathbf{r})$  is given

$$\hat{H} = \hat{T} + \hat{V} + \hat{H}_{coul}. \quad (1.67)$$

In second quantised notation Eq. (1.67) reads

$$\hat{H} = \int d\mathbf{r} \psi^\dagger(\mathbf{r}) \frac{\nabla^2}{2} \psi(\mathbf{r}) + \int d\mathbf{r} \psi^\dagger(\mathbf{r}) V(\mathbf{r}) \psi(\mathbf{r}) + \hat{H}_{coul}. \quad (1.68)$$

To prove the Hohenberg-Kohn theorem [3] we define a set  $\mathcal{V}$  of local one-particle potentials with the property that the solutions of each eigenvalue problem

$$\hat{H}|\Phi\rangle = \left(\hat{T} + \hat{V} + \hat{H}_{coul}\right)|\Phi\rangle = E|\Phi\rangle \quad V \in \mathcal{V}, \quad (1.69)$$



leads to a non-degenerate ground state for the N electrons system:

$$\hat{H}|\Psi\rangle = E_{gs}|\Psi\rangle. \quad (1.70)$$

Collecting the ground states in the set  $\Psi$  we have defined, via the solution of Schrödinger Eq. (1.70), a map

$$C : \mathcal{V} \rightarrow \Psi. \quad (1.71)$$

This map is surjective by construction:  $\Psi$  contains no element which is not associated with some element of  $\mathcal{V}$ .

Next, for all ground state wavefunctions contained in  $\Psi$ , we calculate the ground state densities

$$n(\mathbf{r}) = \langle \Psi | \psi^\dagger(\mathbf{r}) \psi(\mathbf{r}) | \Psi \rangle, \quad (1.72)$$

establishing a second map:

$$D : \Psi \rightarrow \mathcal{N}. \quad (1.73)$$

This map of the ground state wavefunctions on the set of ground state densities  $\mathcal{N}$  is again surjective.

Hohenberg–Kohn theorem is, then: *the map C and D are also injective (one to one) and thus fully invertible.*

From the invertibility of maps C and D, three statements of Hohenberg–Kohn theorem follows:

(1<sup>th</sup>): having established that unique inversion of map D is possible

$$D^{-1} : n(\mathbf{r}) \rightarrow |\Psi[n]\rangle. \quad (1.74)$$

the first statement of Hohenberg–Kohn theorem can be formulated: *the Ground state expectation value of any observable is a unique functional of the exact ground state density*

$$\langle \Psi[n] | \hat{O} | \Psi[n] \rangle = O[n], \quad (1.75)$$

The inverse map

$$(CD)^{-1} : n(\mathbf{r}) \rightarrow V(\mathbf{r}), \quad (1.76)$$

tells us that the knowledge of the ground state density determines the external potential of the system and thus, as the kinetic energy and the Coulomb interaction are specified, the entire hamiltonian.

(2<sup>th</sup>): The Hohenberg–Kohn theorem establishes the variational character of the energy functional

$$E_{V_0}[n] \equiv \langle \Psi[n] | \hat{T} + \hat{V}_0 + H_{coul} | \Psi[n] \rangle, \quad (1.77)$$

where  $V_0$  is the external potential of a specific system with ground state density  $n_0(\mathbf{r})$  and ground state energy  $E_0$ . The state  $|\Psi[n]\rangle$  is generated from the elements of  $\mathbf{N}$  via  $D^{-1}$ .  $E_{V_0}[n]$  has the property

$$E_0 < E_{V_0}[n] \quad \text{for } n \neq n_0, \quad (1.78)$$

and

$$E_0 = E_{V_0}[n_0]. \quad (1.79)$$

Thus the exact ground state density can be determined by minimization of the functional  $E_{V_0}[n]$ , in short

$$E_0 = \min_{n \in \mathcal{N}} E_{V_0}[n]. \quad (1.80)$$

(3<sup>th</sup>): The map  $D^{-1}$  does not depend on the potential  $V_0$  of the particular system under consideration. Thus

$$E_{V_0}[n] = F_{HK}[n] + \int d\mathbf{r} V_0(\mathbf{r}) n(\mathbf{r}), \quad (1.81)$$

with

$$F_{HK}[n] = \langle \Psi[n] | \hat{T} + H_{coul} | \Psi[n] \rangle. \quad (1.82)$$

The functional  $F_{HK}[n]$  is *universal* in the sense that it does not depend on  $V_0$ .

The three statements of *invertibility*, *variational access* and *universality* constitute the classical formulation of the Hohenberg–Kohn theorem.

## 1.2.2 Kohn–Sham equations

The Hohenberg–Kohn theorem offers no practical guide to the explicit construction of the  $F_{HK}$  universal functional. For this purpose one still has to face the full intricacies of the many–body problem.

Although there are some energy functionals for Coulomb systems derived with the theory of the homogeneous electron gas or in other, more elaborated approaches,

the situation cannot be considered satisfactory. Only with the approach introduced by Kohn and Sham [4] has one been able to calculate (not only) ground state properties of many-particles Coulomb systems with great accuracy.

Consider an auxiliary system of  $N$  non-interacting particles described by the hamiltonian

$$\hat{H}_s = \hat{T} + \hat{V}_s, \quad (1.83)$$

According to the theorem of Hohenberg-Kohn, there exists a unique energy functional

$$E_s[n] = T_s[n] + \int d\mathbf{r} V_s(\mathbf{r}) n(\mathbf{r}), \quad (1.84)$$

for which the variational principle yields the exact ground state density  $n_s(\mathbf{r})$  corresponding to  $\hat{H}_s$ .  $T_s[n]$  denotes the universal kinetic energy functional of non-interacting particles.

The central assertion of the Kohn-Sham scheme is: *for any interacting system, there exists a local single-particle potential  $V_s(\mathbf{r})$  such that the exact ground state density  $n(\mathbf{r})$  of the interacting system equals the ground state density of the auxiliary problem,*

$$n(\mathbf{r}) = n_s(\mathbf{r}). \quad (1.85)$$

Thus the ground state density  $n(\mathbf{r})$  possesses a unique representation

$$n(\mathbf{r}) = \sum_{i=1\dots N} |\phi_i(\mathbf{r})|^2, \quad (1.86)$$

in terms of the lowest  $N$  single-particle orbitals obtained from the Schrödinger equation

$$\left[ -\frac{\nabla^2}{2} + V_s(\mathbf{r}) \right] \phi_i(\mathbf{r}) = \epsilon_i \phi_i(\mathbf{r}). \quad (1.87)$$

Now consider a particular interacting system with external potential  $V_0(\mathbf{r})$  and ground state density  $n_0(\mathbf{r})$ . To determine the auxiliary potential  $V_{s,0}(\mathbf{r})$  which generates  $n_0(\mathbf{r})$  via

$$n_0(\mathbf{r}) = \sum_{i=1\dots N} |\phi_{i,0}(\mathbf{r})|^2, \quad (1.88)$$

$$\left[ -\frac{\nabla^2}{2} + V_{s,0}(\mathbf{r}) \right] \phi_{i,0}(\mathbf{r}) = \epsilon_{i,0} \phi_{i,0}(\mathbf{r}), \quad (1.89)$$

the exchange–correlation function  $E_{xc}[n]$  is introduced as

$$E_{V_0}[n] = T_s[n] + \int d\mathbf{r} V_0(\mathbf{r}) n(\mathbf{r}) + 1/2 \int d\mathbf{r} \int d\mathbf{r}' n(\mathbf{r}) v(\mathbf{r}, \mathbf{r}') n(\mathbf{r}') + E_{xc}[n], \quad (1.90)$$

$$E_{xc}[n] = F_{HK}[n] - 1/2 \int d\mathbf{r} \int d\mathbf{r}' n(\mathbf{r}) v(\mathbf{r}, \mathbf{r}') n(\mathbf{r}') - T_s[n]; \quad (1.91)$$

with  $v(\mathbf{r}, \mathbf{r}')$  Coulomb interaction. Now the Hohenberg–Kohn variational principle ensures that  $E_{V_0}[n]$  is stationary for small variations  $\delta n(\mathbf{r})$  around the minimum density  $n_0(\mathbf{r})$ . If we define

$$V_{xc}([n_0], \mathbf{r}) = \left. \frac{\delta E_{xc}[n]}{\delta n(\mathbf{r})} \right|_{n_0}, \quad (1.92)$$

the assumption that the system is non–interacting representable (the KS ansatz) also for small deviations around the  $[n_0(\mathbf{r}) + \delta n_0(\mathbf{r})]$  allows to write, by neglecting second order terms,

$$\delta T_s = - \int d\mathbf{r} V_{s,0}(\mathbf{r}) \delta n(\mathbf{r}). \quad (1.93)$$

Thus one is left with the final expression

$$V_{s,0}(\mathbf{r}) = V_0(\mathbf{r}) + \int d\mathbf{r}' v(\mathbf{r}, \mathbf{r}') n_0(\mathbf{r}') + V_{xc}([n_0], \mathbf{r}). \quad (1.94)$$

Eqs. (1.88–1.89) and the potential defined in Eq. (1.94) represents the classical Kohn–Sham scheme.

### 1.2.3 Local Density Approximation

In principle, solution of Kohn–Sham Eqs. (1.88–1.89) with the *exact* exchange–correlation potential, would give a set of fictitious single particle eigenstates whose density of states equals that one of the fully interacting system. Unluckily the exact exchange–correlation potential is not known and one has to find reasonably approximations for  $V_{xc}$ .

One of the most widely used is the *Local Density Approximation* (LDA). Introducing the exchange–correlation energy density  $\epsilon_{xc}([n]; \mathbf{r})$  as

$$E_{xc}[n] = \int d\mathbf{r} n(\mathbf{r}) \epsilon_{xc}([n]; \mathbf{r}), \quad (1.95)$$

we assume the the system *locally* appears as an homogeneous electron gas. For the latter we split  $\epsilon_{xc}([n]; \mathbf{r})$  as composed of

$$\epsilon_{xc}^{hom}(n) = \epsilon_x^{hom}(n) + \epsilon_c^{hom}(n), \quad (1.96)$$

with  $\epsilon_x^{hom}(n)$  bare exchange and  $\epsilon_c^{hom}(n)$  correlation energy density. While  $\epsilon_x^{hom}(n)$  is an analytic function of  $n$  [5]

$$\epsilon_x^{hom}(n) = -\frac{3}{4} \left[ \frac{3n}{\pi} \right]^{1/3}, \quad (1.97)$$

the correlation part can be calculated approximately using Many-Body perturbation theory [6] or via quantum Montecarlo methods [7]. The first method gives an analytic function of  $n$  while the results from numerical Montecarlo has been parametrized by, e.g., Perdew and Zunger [8].

## 1.3 Green's function approach to the many-body problem

In the last section we have introduced a theoretical framework to describe a fully interacting system in terms of a non physical gas of free particles.

Although those Kohn-Sham (KS) particles appear as fictitious quantities in the mathematical approach, they have allowed a successful starting point in the description of experimental photoemission data, as well as optical spectra [9]. However, as we will see in the implementation of DFT-LDA on Copper and Silver, the residual discrepancies between theory and experiment are due to the approximate inclusion of correlation effects.

In this section we will introduce a presentation of the many-body Green's function technique based on the, more compact, formulation of functional derivatives. The discussion about conserving approximation follows the work of Baym and Kadanoff [10] (also the figures are taken from their work of 1961). The section about *GW* is written in the spirit of the Hedin's equations [11, 12], elegant and formally simpler than the conventional diagrammatic technique [5].

### 1.3.1 Conserving approximations

We consider the same (non relativistic)  $N$ -electrons system described by the hamiltonian give in Eq. (1.2), rewritten in the more compact form

$$H = \int d\mathbf{r} \psi^\dagger(\mathbf{r}) h(\mathbf{r}) \psi(\mathbf{r}) + 1/2 \int d\mathbf{r} d\mathbf{r}' \psi^\dagger(\mathbf{r}) \psi^\dagger(\mathbf{r}') v(\mathbf{r}, \mathbf{r}') \psi(\mathbf{r}') \psi(\mathbf{r}), \quad (1.98)$$

with, now, the external potential included in the one body term  $h(\mathbf{r})$  while the Coulomb term explicitly written. The system is assumed to interact with an external

scalar potential through the hamiltonian  $H'(t)$

$$H'(t) = \int d\mathbf{r} d\mathbf{r}' \psi^\dagger(\mathbf{r}) U(\mathbf{r}, \mathbf{r}'; t) \psi(\mathbf{r}), \quad (1.99)$$

with  $U(\mathbf{r}, \mathbf{r}'; t)$  hermitian at any time in the variables  $(\mathbf{r}, \mathbf{r}')$ . This potential is further assumed to vanish in the  $|t| \rightarrow 0$  limit.

The introduction of the interaction given by Eq. (1.99) may be considered as a purely formal tool that is vanished at the end of the calculation. Nevertheless, the general formulation we will use could be used to describe the coupling of the system to an external physical local potential as that used in Section 1.1

$$U(\mathbf{r}, \mathbf{r}'; t) = \phi^{ext}(\mathbf{r}; t) \delta(\mathbf{r}, \mathbf{r}'). \quad (1.100)$$

Indeed, using Eq. (1.100) the present formulation will reproduce the same quantities defined in Section 1.1 with the explicit treatment of many-body Coulomb interaction. In the interaction representation [13] we define

$$\psi(1) = e^{iHt_1} \psi(\mathbf{r}_1) e^{-iHt_1}, \quad (1.101)$$

$$H'_I(t) = e^{iHt} H'(t) e^{-iHt}, \quad (1.102)$$

and the generalized single and two-particle Green's function

$$G_1(1, 2) = (-i) \langle \Psi | \mathcal{T} \{ S \psi(1) \psi^\dagger(2) \} | \Psi \rangle, \quad (1.103)$$

$$G_2(1, 2; 3, 4) = (-i)^2 \langle \Psi | \mathcal{T} \{ S \psi(1) \psi(2) \psi^\dagger(4) \psi^\dagger(3) \} | \Psi \rangle, \quad (1.104)$$

with

$$S = e^{-i \int_{-\infty}^{\infty} H'_I(t) dt}. \quad (1.105)$$

Starting from Eq. (1.103) and Eq. (1.104), using the definition of T-product to act separately on the negative and positive time contribution to  $G_1$  the following time evolution equation can be obtained

$$\begin{aligned} \left[ i \frac{\partial}{\partial t_1} - h(1) \right] G_1(1, 2) - \int d3 U(1, 3) G_1(3, 2) \\ = \delta(1, 2) - i \int d3 v(1, 3) G_2(1, 3^+; 2, 3^{++}), \end{aligned} \quad (1.106)$$

where we have introduced the notation

$$v(1, 2) = v(\mathbf{r}_1, \mathbf{r}_2) \delta(t_1 - t_2), \quad (1.107)$$

$$h(1) = h(\mathbf{r}_1), \quad (1.108)$$

$$U(1, 2) = U(\mathbf{r}_1, \mathbf{r}_2; t). \quad (1.109)$$

An alternative equation can be obtained following the same procedure used to get Eq. (1.106)

$$\begin{aligned} \left[ -i \frac{\partial}{\partial t_2} - h(2) \right] G_1(1, 2) - \int d3 G_1(1, 3) U(3, 2) \\ = \delta(1, 2) - i \int d3 v(2, 3) G_2(1, 3^-; 2, 3^-). \end{aligned} \quad (1.110)$$

Now we have all the ingredients to properly define a conserving approximation for  $G_1$ . The Baym–Kadanoff [10] condition reads:

*Whenever the following conditions are satisfied:*

(A) *for a given approximate  $G_2$ ,  $G_1$  satisfies both Eq. (1.106) and Eq. (1.110).*

(B) *The  $G_2$  chosen satisfies*

$$G_2(1, 3; 1^+, 3^+) = G_2(3, 1; 3^+, 1^+)$$

*then the approximate  $G_1$  satisfies all the conservation laws.*

As an example, the number conservation law, for the approximate  $G_1$  follows from statement (A) alone. Subtracting Eq. (1.110) from Eq. (1.106) we find

$$\begin{aligned} i[\partial_{t_1} + \partial_{t_2}] G_1(1, 2) + [(\nabla_1 + \nabla_2) \cdot (\nabla_1 - \nabla_2) / 2i] i G_1(1, 2) \\ = \int d3 [U(3, 2) G_1(1, 3) - U(1, 3) G_1(3, 2)] \\ - i \int d3 [v(2, 3) G_2(1, 3^-; 2, 3^-) - v(1, 3) G_2(1, 3^+; 2, 3^{++})], \end{aligned} \quad (1.111)$$

when  $2 = 1^+$  we find

$$\begin{aligned} i\partial_{t_1} G_1(1, 1^+) + \nabla_1 \cdot [(\nabla_1 - \nabla_2) / 2i i G_1(1, 2)]_{2=1^+} = \partial_{t_1} \langle \rho(1) \rangle + \nabla_1 \cdot \langle \mathbf{j}(1) \rangle \\ = \int d3 [U(3, 1) G_1(1, 3) - U(1, 3) G_1(3, 1)]. \end{aligned} \quad (1.112)$$

Eq. (1.112) is an exact statement of the number conservation law in the presence of an external disturbance which adds and removes particles from the system. For a *local* disturbance  $U(1) \delta(1 - 2)$ , that describes the coupling of the system to the density, Eq. (1.112) becomes

$$\partial_{t_1} \langle \rho(1) \rangle + \nabla_1 \cdot \langle \mathbf{j}(1) \rangle = 0, \quad (1.113)$$

which expresses the charge conservation rule. Going back to the two conditions (A) and (B) defining a conserving approximation for  $G_1$  we note that condition (B) may

always be verified by simply examining the form of the approximation for  $G_2$ . It is convenient to cast condition (A) into a form in which it too may be verified by inspection. If we define the non-interacting Green's function  $G_0(1, 2)$  to be solution of equation

$$\left[ i \frac{\partial}{\partial t_1} - h(1) \right] G_0(1, 2) = \delta(1, 2), \quad (1.114)$$

we notice that the  $\left[ i \frac{\partial}{\partial t_1} - h(1) \right]$  operator can be always substituted with the inverse  $[G_0(1, 2)]^{-1}$ . We see that the matrix product  $G_1 [G_0^{-1} - U] G$  can be constructed from both Eq. (1.106) and Eq. (1.110). Demanding that these two evaluations be identical condition (B) results equivalent to

$$\int d\tilde{1}3 G_1(1, \tilde{1}) v(\tilde{1}, 3) G_2(\tilde{1}, 3^+; 2, 3^{++}) = \int d\tilde{1}3 G_2(1, 3; \tilde{1}, 3^+) v(3, \tilde{1}) G_1(\tilde{1}, 2). \quad (1.115)$$

This equation is equivalent to condition (A). Eq. (1.115), as condition on  $G_2$ , is easily verified by inspection for a choice of approximation. In Fig.(1.1) it is shown how this can be done diagrammatically for the Hartee-Fock case.

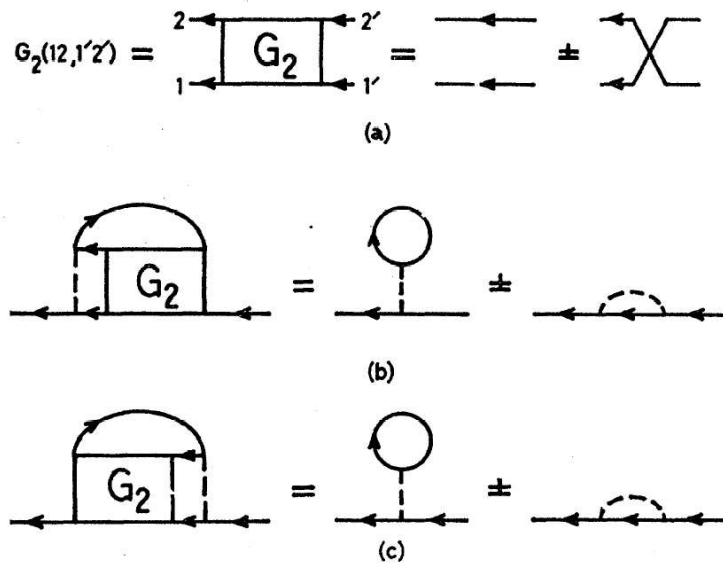


Figure 1.1: Diagrammatic statement of conditions (A) and (B) in the Hartee-Fock approximation. Diagram (a) represents the Hartee-Fock approximation for  $G_2$ . Condition (B) is simply the statement that the picture for  $G_2$  with  $1' = 1^+$  and  $2' = 2^+$  must look the same when it is turned upside downside. To see the graphical form of condition (A) in the Hartee-Fock approximation, in (b) and (c), the right and left sides, respectively, of Eq. (1.115). The dashed lines represents the bare Coulomb interaction  $v$ .

In order to rewrite Eq. (1.106) and Eq. (1.110) in a more convenient form we



define the self-energy operator  $\Sigma$

$$\Sigma(1, 2) = -i \int d34 v(1^+, 3) G_2(1, 3^+; 4, 3^{++}) G_1^{-1}(4, 2), \quad (1.116)$$

The Green's function equation is, then,

$$G^{-1}(1, 2) = G_0^{-1}(1, 2) - U(1, 2) - \Sigma(1, 2), \quad (1.117)$$

known as Dyson equation. Once we have a determination of  $G_1$ , we can find the linear response to the external disturbance by picking out the linear coefficient of  $U$  in  $G_1$ . This is

$$L(1, 2; 3, 4) \equiv \frac{\delta G_1(1, 3)}{\delta U(4, 2)}, \quad (1.118)$$

and  $L$  is the link with the linear response theory introduced and discussed in Section 1.1. Indeed, as we will show later, the T-ordered polarization function introduced in Section 1.1 is given, in the present framework, by

$$\chi(1, 2) \equiv -iL(1, 2; 1^+, 2^+). \quad (1.119)$$

In Section 1.1 we obtained the longitudinal sum rule, Eq. (1.24), imposing the gauge invariance of the induced current and charge, calculated at the first order in the external perturbation. In the present framework the same conclusion is obtained as consequence of the conservation laws for  $G_1$  (as explicitly shown in the Baym-Kadanoff work [10]).

In principle, then, we can obtain a conserving  $L$  by first solving for a conserving  $G_1$ . We can then generate  $L$  as  $\delta G_1/\delta U$ , the coefficient of  $U$  in the term in  $G_1$  that is linear in  $U$ . In practice, we can almost never solve the equation of motion for  $G_1$  in the presence of an arbitrary disturbance. Fortunately a much simpler calculation procedure is available. From the relation  $G_1^{-1}G_1 = 1$  we notice that

$$\frac{\delta G_1(1, 3)}{\delta U(4, 2)} = - \int d56 G_1(1, 5) \frac{\delta G_1^{-1}(5, 6)}{\delta U(4, 2)} G_1(6, 3). \quad (1.120)$$

Calculating  $G_1^{-1}$  from Eq. (1.117) we find

$$\frac{\delta G_1(1, 3)}{\delta U(4, 2)} = - \int d56 G_1(1, 5) \left[ \delta(4, 5) \delta(2, 6) + \frac{\delta \Sigma(5, 6)}{\delta U(4, 2)} \right] G_1(6, 3). \quad (1.121)$$

The self-energy depends on  $U$  only through its dependence on  $G_1$ . Since we know  $\Sigma$  as a functional of  $G$ , we can, then, compute  $\delta \Sigma/\delta U$  by the chain-rule for differentiation, i.e.,

$$\left. \frac{\delta \Sigma(5, 6)}{\delta U(4, 2)} \right|_{U=0} = \int d78 \left. \frac{\delta \Sigma(5, 6)}{\delta G_1(7, 8)} \right|_{U=0} \left. \frac{\delta G_1(7, 8)}{\delta U(4, 2)} \right|_{U=0}. \quad (1.122)$$

We define an effective two-particle interaction  $\Xi$ , by

$$\Xi(3, 5; 4, 6) \equiv \left. \frac{\delta \Sigma(3, 4)}{\delta G_1(6, 5)} \right|_{U=0} \quad (1.123)$$

The we combine Eq. (1.118), Eq. (1.121) and Eq. (1.122) to obtain the final integral equation for  $L$ :

$$L(1, 2; 1', 2') = G_1(1, 2') G_1(2, 1') + \int d3456 G_1(1, 3) G_1(4, 1') \Xi(3, 5; 4, 6) L(6, 2; 5, 2'), \quad (1.124)$$

known as Bethe–Salpeter equation for  $L$ .

From the definition given in Eq. (1.118) the two-particle correlation function  $L(1, 2; 1', 2')$  obeys the conservation laws for the operators constructed from the 1 and 1' variables (those coming from  $G_1$ ). It is important, however, to have  $L$  also be conserving in the 2 and 2' variables. We shall therefore demand that the approximate  $L$  satisfies

$$L(1, 2; 1', 2') = L(2, 1; 2', 1'). \quad (1.125)$$

To ensure this symmetry, we impose just one more condition on our approximation, namely:

$$\Xi(3, 5; 4, 6) = \Xi(5, 3; 6, 4). \quad (\text{Condition (C)})$$

One of the main virtues of the procedure described here is the fact that it automatically builds in the close connection between  $G$  and  $L$ .

Let us briefly review the method for constructing a conserving approximation for the two-particle correlation function  $L$ . We start by picking an approximate form for  $G_2$  as functional of  $G_1$ , which we then substitute into the equation of motion for  $G_1$ . In order that this approximation leads to a conserving  $G_1$  and  $L$ , we demand that the approximate  $G_2$  satisfies the symmetry requirements (A), (B) and (C). These three requirements can be verified by merely examining the structure of  $G_2$ . If they are met, then we can derive an approximate integral equation, whose solution is a fully conserving  $L$ , by taking the first variational derivative with respect to  $U$  of the equation of motion for  $G_1$ .

Since  $G_2 = L + G_1 G_1$ , we start from a *non conserving* approximation for  $G_2$  and end up with a *fully conserving*  $G_2$ .

### 1.3.2 Examples of conserving approximations

#### The Hartree and Hartee–Fock approximations

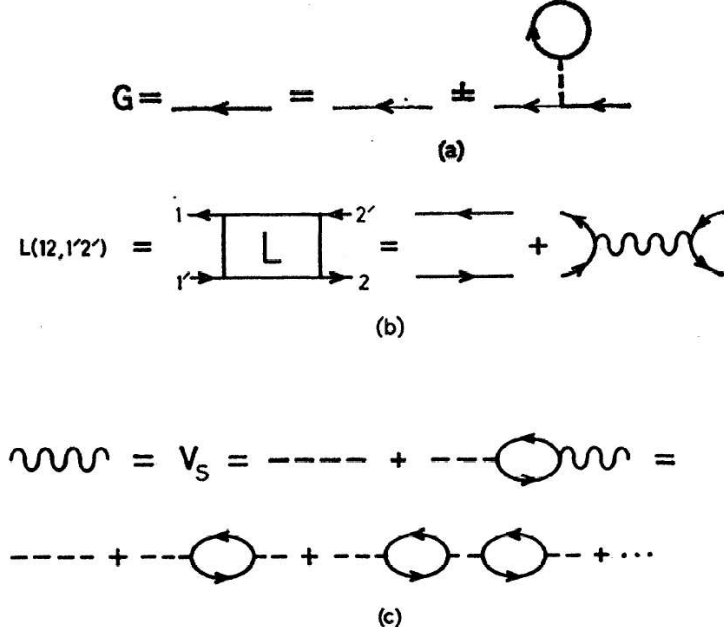


Figure 1.2: Hartree approximation. We use the light line to represent  $G_0$  and an heavy line for  $G_1$ .

The Hartree approximation, which describes the motion of the particles in the system as that of free particles in a self-consistent field, is the simplest nonperturbative (in the sense that all the  $G$ 's and  $L$ 's will include terms of arbitrarily high order in  $v$ ) approximation for  $G_1$ . We get it taking

$$G_2(1, 3^-; 2, 3^+) = G_1(1, 2) G_1(3, 3^+), \quad (1.126)$$

then following Eq. (1.116) the self-energy is defined as

$$\Sigma_H(1, 2) = i\delta(1, 2) \int d^3v v(1, 3) G_1(3, 3^+). \quad (1.127)$$

The variational derivative of Eq. (1.127) gives  $\Xi$  and, then, the following equation from  $L$

$$L(1, 2; 1, 2') = G_1(1, 2') G_1(2, 1') + i \int d^3v v(1, 3) G_1(3, 1') L(4, 2; 4, 2'). \quad (1.128)$$

Since

$$\Xi(3, 4; 3', 4') = i\delta(3, 3') \delta(4, 4') v(3, 4), \quad (1.129)$$

it is clear that conditions (A), (B) and (C) are satisfied, and  $L$  is fully conserving. Eq. (1.128) constitute the formal statement of random-phase-approximation (RPA) and it can be rewritten introducing the *dynamically screened interaction*  $W$  defined as

$$W(1, 2) = v(1, 2) + i \int d^3 4 v(1, 3) G_1(3, 4) G_1(4, 3) W(4, 2). \quad (1.130)$$

The set of equations defining the Hartree approximation are shown in Fig. (1.2).

The Hartree-Fock approximation also describes the particles as moving in an average potential field. However, this field now includes exchange effects. This is represented by the second term of the  $G_2$  Green's function of Fig. 1.1, and following the same procedure described in the Hartree case the corresponding self-energy operator and integral equation for  $L$  are shown in Fig. 1.3.

The equation for  $L$  is equivalent to the generalization of RPA to include exchange

$$\begin{aligned} L(1, 2; 1', 2') &= G_1(1, 2') G_1(2, 1') \\ &+ i \delta(1, 1') \int d^3 4 G_1(1, 3) G_1(3, 1^+) v(3, 4) L(4, 2; 4, 2') \\ &+ i \int d^3 4 G_1(1, 3) G_1(4, 1^+) v(3, 4) L(3, 2; 4, 2'). \end{aligned} \quad (1.131)$$

Like in RPA the solution of Eq. (1.131) is a sum of bubble diagrams where now each bubble is essentially composed of a hole-electron scattering matrix made of Hartree-Fock Green's functions.

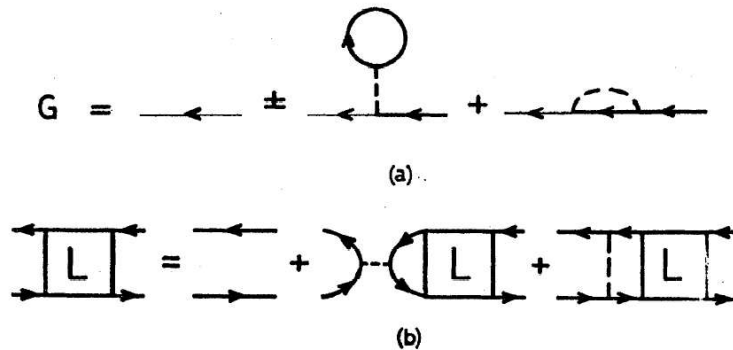


Figure 1.3: The Hartree-Fock approximation.

### The T-Matrix approximation

Both the Hartree and the Hartree-Fock approximations leave out the detailed correlations produced by interparticle collisions and they can be used to describe phenomena, like plasma oscillations, for which collisions are not important.

A conserving approximation which includes collisions effects can be constructed starting from the Bethe–Goldstone approximation for  $G_2$

$$G_2(1, 3; 1', 3') = G_1(1, 1') G_1(3, 3') + G_1(1, 3') G_1(3, 1') + i \int d45 G_2(1, 3; 4, 5) v(4, 5) G_1(4, 1') G_1(5, 3'). \quad (1.132)$$

This  $G_2$  is a sum of ladder diagrams, in which each line represents a propagator  $G_1$ . The Bethe–Goldstone approximation is conveniently described in terms of the many–particle scattering matrix  $\langle 13|T[G_1]|1'3'\rangle$  that satisfies

$$\langle 13|T[G_1]|1'3'\rangle = [\delta(1, 1') \delta(3, 3') + \delta(1, 3') \delta(3, 1')] v(1', 3') + i \int d45 \langle 13|T[G_1]|45\rangle G_1(4, 1') G_1(5, 3') v(1', 3'). \quad (1.133)$$

The relation between  $T$  and  $G_2$  is shown in Fig. 1.4. The corresponding Self–energy operator is easily written in terms of the  $T$  scattering matrix

$$\Sigma(1, 1') = i \int d34 \langle 13|T[G_1]|1'4\rangle G_1(4, 3^+), \quad (1.134)$$

and is known as *T–matrix approximation* (TMA). Constructing the corresponding  $\Xi$  operator we can derive an approximation for  $L$  that includes collisions, while maintaining all the conservation laws.

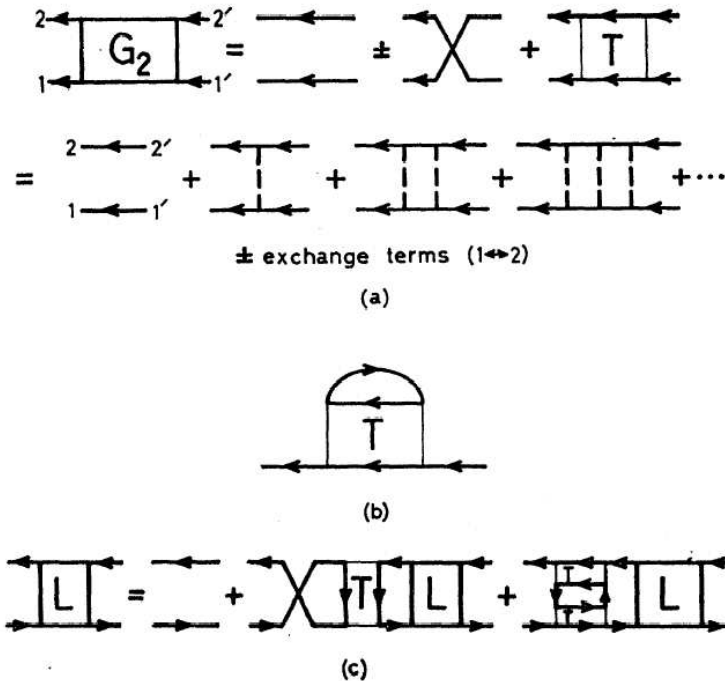


Figure 1.4: The T–Matrix approximation. (a) indicates the ladder structure of the solution of Bethe–Goldstone equation for  $G_2$ . Condition (B) is clear from this figure. (b) and (c) represents, respectively, the self–energy and the integral equation for  $L$ .

### 1.3.3 Hedin's equations

Using the Baym–Kadanoff approach we have seen that a conserving approximation can be obtained from a user defined two body Green's function  $G_2$ . Moreover the procedure used in the last section is based on a mathematical and physical link between  $G_2$ ,  $G_1$ ,  $\Sigma$  and  $L$ .

In the following we will rewrite the equation for  $G_1$  replacing  $G_2$  with the two particle effective interaction  $\Xi$ . Exploiting the deep link of the functional approach with linear response theory the self-energy problem will be rewritten as a set of nonlinear coupled integral equations suitable for systematic improvements beyond the simple basic approximation, called  $GW$  and described below.

Using a local external potential  $U(1)$ , in order to replace the two-body Green's with the functional derivative using the identity

$$G_2(1, 3; 2, 3^+) = G_1(1, 2) G_1(3, 3^+) - \frac{\delta G_1(1, 2)}{\delta U(3)}, \quad (1.135)$$

Eq. (1.106) reads

$$\begin{aligned} \left[ i \frac{\partial}{\partial t_1} - h(1) - U(1) + i \int d3 v(1, 3) G_1(3, 3^+) \right] G_1(1, 2) \\ = \delta(1, 2) - i \int d3 v(1^+, 3) \frac{\delta G_1(1, 2)}{\delta U(3)}; \end{aligned} \quad (1.136)$$

and a similar result for Eq. (1.110).

Eq. (1.136) is not yet in a form suitable for taking the  $U \rightarrow 0$  limit, since we do not know the functional dependence of  $G_1$  on  $U$ . Introducing the inverse Green's function  $G_1^{-1}(1, 2)$  defined as

$$\int d1 G_1^{-1}(1, 2) G_1(2, 3) = \int d1 G_1(1, 2) G_1^{-1}(2, 3) = \delta(1, 2), \quad (1.137)$$

the Self-energy operator becomes

$$\Sigma(1, 2) \equiv \Sigma_H(1, 2) + i \int d34 v(1^+, 3) \frac{\delta G_1(1, 4)}{\delta U(3)} G_1^{-1}(4, 2), \quad (1.138)$$

$$\bar{\Sigma}(1, 2) \equiv \Sigma_H(1, 2) + i \int d34 G_1^{-1}(1, 4) \frac{\delta G_1(4, 2)}{\delta U(3)} v(3, 2^-). \quad (1.138')$$

Here  $\Sigma_H(1, 2)$  stands for the Hartree contribution to the Self-Energy

$$\Sigma_H(1, 2) = \delta(1, 2) \left[ -i \int d3 v(1, 3) G_1(3, 3^+) \right], \quad (1.139)$$

while the rest is sometimes defined as the mass-operator  $M$  ( $\overline{M}$  when  $\overline{\Sigma}$  is considered). Finally we get

$$\left[ i \frac{\partial}{\partial t_1} - h_0(1) - U(1) \right] G_1(1, 2) - \int d3 \Sigma(1, 3) G_1(3, 2) = \delta(1, 2), \quad (1.140)$$

$$\left[ i \frac{\partial}{\partial t_2} - h_0(2) - U(2) \right] G_1(1, 2) - \int d3 G_1(1, 3) \overline{\Sigma}(3, 2) = \delta(1, 2). \quad (1.140')$$

We proceed to eliminate any explicit reference to the external potential  $U$  in the self-energy operator. To this end, we introduce the following auxiliary quantities:

(i) The *total (classical) potential*  $V$

$$V(1) = U(1) - i \int d3 v(1, 3) G_1(3, 3^+). \quad (1.141)$$

Regarding  $G_1$  as a functional of  $V$  and using the “chain rule”

$$\begin{aligned} i \int d34 v(1^+, 3) \frac{\delta G_1(1, 4)}{\delta U(3)} G_1^{-1}(4, 2) \\ = -i \int d345 v(1^+, 3) G_1(1, 4) \frac{\delta G_1^{-1}(4, 2)}{\delta V(5)} \frac{\delta V(5)}{\delta U(3)}, \end{aligned} \quad (1.142)$$

Eq. (1.138) suggests to introduce a

(ii) scalar (irreducible) vertex function  $\tilde{\Gamma}(1, 2; 3)$

$$\tilde{\Gamma}(1, 2; 3) \equiv -\frac{\delta G_1^{-1}(1, 2)}{\delta V(3)} = \delta(1, 3) \delta(2, 3) + \frac{\delta M(1, 2)}{\delta V(3)}. \quad (1.143)$$

Since the mass operator  $M$  depends on the external potential  $U$  only through its dependence on the generalized single particle Green’s function, we can again use the chain rule to obtain an integral equation for  $\tilde{\Gamma}$

$$\begin{aligned} \tilde{\Gamma}(1, 2; 3) &= \delta(1, 3) \delta(2, 3) + \int d45 \frac{\delta M(1, 2)}{\delta G_1(4, 5)} \frac{\delta G_1(4, 5)}{\delta V(3)} \\ &= \delta(1, 3) \delta(2, 3) + \int d4567 \frac{\delta M(1, 2)}{\delta G_1(4, 5)} G_1(4, 6) G_1(7, 5) \cdot \tilde{\Gamma}(6, 7; 3) \end{aligned} \quad (1.144)$$

This can be considered the equation defining  $\tilde{\Gamma}$ , whereby the limit  $U \rightarrow 0$  can explicitly be taken.

Eq. (1.144) defines the irreducible two particle effective interaction  $\tilde{\Xi}(1, 5; 4, 2)$  (we have already introduced the reducible one)

$$\tilde{\Xi}(1, 5; 4, 2) \equiv \frac{\delta M(1, 2)}{\delta G_1(4, 5)}. \quad (1.145)$$

From Eq. (1.144) we note that the unknown dependence on  $U(1)$  has been reduced, first in the vertex function and, then, by means of Eq. (1.144) in  $\tilde{\Xi}(1, 5; 4, 2)$ . In the following we will introduce other important quantities that, however, will be explicitly given in terms of  $\tilde{\Xi}$ .

- (iii) Eq. (1.138) suggests, also, to introduce an inverse (longitudinal) dielectric function  $\epsilon^{-1}$

$$\epsilon^{-1}(1, 2) = \frac{\delta V(1)}{\delta U(2)}, \quad (1.146)$$

which turns out to coincide with Eq. (1.42) obtained in Section 1.1 directly from Maxwell Equations.

Using Eq. (1.141) and the identity

$$-iG_1(1, 1^+) = \frac{\langle S\rho(1) \rangle}{\langle S \rangle}, \quad (1.147)$$

with  $\rho(1) = \psi^\dagger(1)\psi(1)$ , we can find the relation between the dielectric function and the polarizability  $\chi(1, 2)$

$$\epsilon^{-1}(1, 2) = \delta(1, 2) + \int d^3v(1, 3)\chi(3, 2), \quad (1.148)$$

where

$$\chi(1, 2) \equiv \frac{\delta\langle\rho(1)\rangle}{\delta U(2)} = \frac{\langle\mathcal{T}\{S\rho'(1)\rho'(2)\}\rangle}{\langle\mathcal{T}\{S\}\rangle}, \quad (1.149)$$

with

$$\rho'(1) \equiv \rho(1) - \langle\rho(1)\rangle; \quad (1.150)$$

is the density deviation operator. Noting that  $\langle\rho(1)\rangle = -iG_1(1, 1^+)$  we find the proof of Eq. (1.119). It is convenient to single out from  $\chi$  the part which is irreducible with respect to the bare Coulomb interaction  $v$  by regarding the average density as a functional of the total potential  $V$

$$\begin{aligned} \chi(1, 2) &= \int d^3 \frac{\delta\langle\rho(1)\rangle}{\delta V(3)} \frac{\delta V(3)}{\delta U(2)} = \int d^3 \tilde{\chi}(1, 3) \epsilon^{-1}(3, 2) \\ &= \tilde{\chi}(1, 2) + \int d^3 \tilde{\chi}(1, 3) v(3, 4) \chi(4, 2), \end{aligned} \quad (1.151)$$

where we have defined the irreducible polarizability  $\tilde{\chi}$  to be

$$\tilde{\chi}(1, 2) \equiv \frac{\delta\langle\rho(1)\rangle}{\delta V(2)}. \quad (1.152)$$



Eq. (1.151) can be regarded as an integral equation to be solved for  $\chi$  once the kernel  $\tilde{\chi}$  is specified. Knowledge of  $\tilde{\chi}$ , in turn, can be related to that of the vertex function  $\tilde{\Gamma}$

$$\tilde{\chi}(1, 2) = -i \frac{G_1(1, 1^+)}{\delta V(2)} = -i \int d^3 4 G_1(1, 3) G_1(4, 1) \tilde{\Gamma}(3, 4; 2). \quad (1.153)$$

Notice that we can explain the (longitudinal) dielectric function  $\epsilon$  in terms of  $\tilde{\chi}$  as follows:

$$\begin{aligned} \epsilon(1, 2) &\equiv \frac{\delta U(1)}{\delta V(2)} = \frac{\delta}{\delta V(2)} \left[ V(1) - \int d^3 v(1, 3) \langle \rho(3) \rangle \right] \\ &= \delta(1, 2) - \int d^3 v(1, 3) \tilde{\chi}(3, 2), \end{aligned} \quad (1.154)$$

where

$$\int d^3 \epsilon(1, 3) \epsilon^{-1}(3, 2) = \int d^3 \epsilon^{-1}(1, 3) \epsilon(3, 2) = \delta(1, 2). \quad (1.155)$$

It is convenient to use the dynamically screened interaction  $W$  defined in Eq. (1.130)

$$\begin{aligned} W(1, 2) &= \int d^3 \epsilon^{-1}(1, 3) v(3, 2) = \\ &v(1, 2) + \int d^3 4 v(1, 3) \tilde{\chi}(3, 4) W(4, 2), \end{aligned} \quad (1.156)$$

where the last line can be interpreted as an integral equation defining  $W$ .

Using the quantities introduced so far, the mass operator can be cast in its final form

$$M(1, 2) = \int d^3 4 W(1^+, 3) G_1(1, 4) \tilde{\Gamma}(4, 2; 3), \quad (1.157)$$

together with the equation for  $\overline{M}$

$$\overline{M}(1, 2) = \int d^3 4 \tilde{\Gamma}(1, 4; 3) G_1(4, 2) W(3, 2^-). \quad (1.158)$$

Notice that the limit  $U \rightarrow 0$  can be readily taken in these equations.

All the quantities considered so far are still exact. Approximations can be generated either by expressing the set of coupled equations as (infinite) series in terms of the non interacting  $G_1^0$  and  $\Gamma$ , thereby reproducing the Feynman–Dyson perturbative expansion, or by truncating the set of coupled equations by making a specific ansatz on the functional form of the mass operator  $M$  in terms of the self-consistent  $G_1$  and  $W$ .

So we have found that the many-body problem is reduced to the solution of a set of integral equations, known as Hedin equations [12]

$$M(1, 2) = \int d34 W(1^+, 3) G_1(1, 4) \tilde{\Gamma}(4, 2; 3), \quad (\text{Self - Energy})$$

$$\tilde{\Gamma}(1, 2; 3) = \delta(1, 3) \delta(2, 3) + \int d4567 \frac{\delta M(1, 2)}{\delta G_1(4, 5)} G_1(4, 6) G_1(7, 5) \tilde{\Gamma}(6, 7; 3), \quad (\text{Vertex})$$

$$W(1, 2) = v(1, 2) + \int d34 v(1, 3) \tilde{\chi}(3, 4) W(4, 2), \quad (\text{Screened Interaction})$$

$$\tilde{\chi}(1, 2) = -i \frac{G_1(1, 1^+)}{\delta V(2)} = -i \int d34 G_1(1, 3) G_1(4, 1) \tilde{\Gamma}(3, 4; 2), \quad (\text{Polarization})$$

that, together with Eq. (1.117), represent an *exact* formulation of the Many-Body problem. Moreover, although Hedin's equations are not exactly solvable, any self-consistent solution following from an approximate  $\tilde{\Xi}$  represents a conserving approach in the Baym-Kadanoff sense.

### 1.3.4 GW and $GW_0$ Self-energies

Currently one of the most successful approximation for self-energy operator is the *GW approximation* that has yielded remarkably accurate band structures for many materials [14].

*GW* approximation is obtained as first term in the expansion of Hedin equations in the expansion in the screened interaction  $W$ .

$$M(1, 2) \sim \int d34 W(1^+, 3) G_1(1, 4). \quad (1.159)$$

It is a conserving approximation, in the Baym-Kadanoff sense, as it possible to define a two-bodies Green's function that has *GW* as corresponding self-energy.

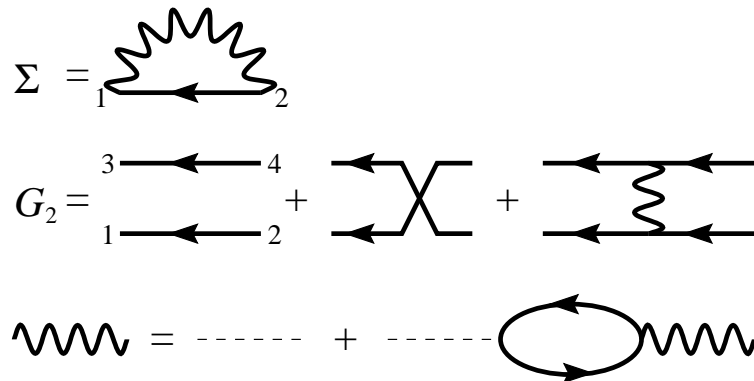


Figure 1.5: Diagrammatic representation of the self-energy  $\Sigma(1, 2)$  and the corresponding two-particle Green's function  $G_2(1, 3; 2, 4)$  in the fully self-consistent *GW* approximation. From Ref.[15].

In Fig. 1.5 the  $G_2$  for  $GW$  is shown [15]. To fulfill the Baym–Kadanoff condition, however, Dyson equation must be solved iteratively till convergence is reached. Starting from  $G_0(1, 2)$  a first approximation to  $\tilde{\chi}(1, 2)$  is constructed

$$\tilde{\chi}(1, 2) \approx \chi_0(1, 2) = -iG_0(1, 2)G_0(2, 1). \quad (1.160)$$

This is used to construct the screened interaction  $W$ , and then, the mass operator  $M$ . Using Dyson equation  $\Sigma(1, 2)$  is used to obtain  $G(1, 2)$  which will give a new form of  $\tilde{\chi}(1, 2)$  and so on. As we will see in Chapter 3 the numerical implementation of  $GW$  is rather demanding. Two possible different approaches are used: the first, neglecting self-consistency leads to a not conserving approach that we will use to calculate the band structure of copper and silver in Chapters 3–5.

An alternative approach is to update at each step of Dyson equation only the single particle Green’s function  $G_1$ , leaving the screening function  $W$  at the non-interacting level. This approach, called  $GW_0$  is not *fully* conserving but it still conserves the number of electrons in the system. This reduced fulfillment of conserving requirements has been proved numerically for the homogeneous electron gas in Ref. [16] and, more recently, analytically in the Baym–Kadanoff scheme in Ref. [15]. It will be used, in a simplified form, in Chapter 4 to study the lifetimes of d-holes in copper.

### 1.3.5 From Kohn–Sham particles to many–body quasiparticles

In the last section the many–body approach is introduced as a perturbation of the non-interacting system. However, as we will experience in Chapter 3, DFT suggests an optimal non-interacting representation of the system to start with.

This corresponds to substitute the  $h(1)$  hamiltonian of Eq. (1.98) with the Kohn–Sham one  $h_{KS}(1)$

$$h_{KS}(1)\phi_{n\mathbf{k}}(\mathbf{r}) = \left[ \frac{-\nabla^2}{2} + V_H(\mathbf{r}) + V_{xc}(\mathbf{r}) \right] \phi_{n\mathbf{k}}(\mathbf{r}) + \int d\mathbf{r}' V_{PP}(\mathbf{r}, \mathbf{r}') \phi_{n\mathbf{k}}(\mathbf{r}') = \epsilon_{n\mathbf{k}} \phi_{n\mathbf{k}}(\mathbf{r}), \quad (1.161)$$

where  $V_{PP}(\mathbf{r}, \mathbf{r}')$  is a non-local pseudopotential,  $V_{xc}(\mathbf{r})$  is the exchange and correlation potential and  $\{\phi_{n\mathbf{k}}(\mathbf{r})\}$  are the Bloch states. From Eq. (1.161) we see that  $V_H(1, 2)$  is already included in the DFT calculation. Moreover, we are using a

non-interacting Green's function  $G_0(1, 2)$  solution of equation

$$\left[ i \frac{\partial}{\partial t_1} - h_{KS}(1) \right] G_0(1, 2) = \delta(1, 2), \quad (1.162)$$

and the exchange and correlation contained in  $V_{xc}$  must be considered in the Self-energy corrections to the KS eigenstates. This can be done adding and subtracting [2]  $V_{xc}(1, 2) = V_{xc}(\mathbf{r}) \delta(1, 2)$  from Eq. (1.117)

$$G(1, 2) = G_0(1, 2) + \int d34 G_0(1, 3) [\Sigma(3, 4) - V_{xc}(3, 4)] G(4, 2). \quad (1.163)$$

As solution of Eq. (1.163) the Fourier transformed respect to  $(t_2 - t_1)$  of  $G(1, 2)$  admits the biorthonormal representation [17]

$$G(\mathbf{r}_1, \mathbf{r}_2; \omega) = \sum_{\lambda} \frac{\psi_{\lambda}(\mathbf{r}_1, \omega) \tilde{\psi}_{\lambda}^*(\mathbf{r}_2, \omega)}{\omega - E_{\lambda}(\omega)}, \quad (1.164)$$

with  $\psi_{\lambda}(\mathbf{r}_1, \omega)$ ,  $\tilde{\psi}_{\lambda}(\mathbf{r}_2, \omega)$  solution of

$$[h_0(\mathbf{r}) + V_H(\mathbf{r})] \psi_{\lambda}(\mathbf{r}, \omega) + \int d\mathbf{r}' \Sigma(\mathbf{r}, \mathbf{r}'; \omega) \psi_{\lambda}(\mathbf{r}', \omega) = E_{\lambda}(\omega) \psi_{\lambda}(\mathbf{r}, \omega), \quad (1.165)$$

$$[h_0(\mathbf{r}) + V_H(\mathbf{r})] \tilde{\psi}_{\lambda}(\mathbf{r}, \omega) + \int d\mathbf{r}' \Sigma^{\dagger}(\mathbf{r}, \mathbf{r}'; \omega) \tilde{\psi}_{\lambda}(\mathbf{r}', \omega) = E_{\lambda}^*(\omega) \tilde{\psi}_{\lambda}(\mathbf{r}, \omega), \quad (1.166)$$

where  $\Sigma^{\dagger}(\mathbf{r}, \mathbf{r}'; \omega) = [\Sigma(\mathbf{r}', \mathbf{r}; \omega)]^*$ . The quasiparticle concept comes from the assumption that it's possible to describe approximately the full energy dependence of  $G(\mathbf{r}_1, \mathbf{r}_2; \omega)$  with some well defined complex poles

$$G(\mathbf{r}_1, \mathbf{r}_2; \omega) \approx \sum_{\lambda} \frac{\psi_{\lambda}(\mathbf{r}_1, \epsilon_{\lambda}^{QP}) \tilde{\psi}_{\lambda}^*(\mathbf{r}_2, \epsilon_{\lambda}^{QP})}{\omega - \epsilon_{\lambda}^{QP}}, \quad (1.167)$$

with the *quasiparticle energies* defined by

$$\epsilon_{\lambda}^{QP} = E_{\lambda}(\epsilon_{\lambda}^{QP}). \quad (1.168)$$

Strictly speaking, this equation has, in general, no real-valued solutions; the non-local, frequency dependent potential  $\Sigma(\mathbf{r}', \mathbf{r}; \omega)$  is, in general, not hermitian; this means that the quasiparticles get a not infinite lifetime due to the presence of accessible virtual excited states where the quasiparticle can decay. Moreover  $\psi_{\lambda}(\mathbf{r}_1, \epsilon_{\lambda}^{QP})$  and  $\tilde{\psi}_{\lambda}(\mathbf{r}_1, \epsilon_{\lambda}^{QP})$  are orthonormal only when  $\Sigma(\mathbf{r}', \mathbf{r}; \omega)$  is hermitian. Mathematically in this case one has to look for solutions of Eq. (1.168) at complex frequencies through a definition of the analytic continuation of  $G(\mathbf{r}_1, \mathbf{r}_2; \omega)$  (and  $\Sigma(\mathbf{r}', \mathbf{r}; \omega)$ ).

Moreover using the quasiparticle picture one fails to describe the continuous part of the Green's function that comes from the branch cut of  $G(\mathbf{r}_1, \mathbf{r}_2; \omega)$  rather than from isolated poles [18].

The self-energy operator has the discrete translation invariance of the crystal so that the quasiparticle's wave functions can be expanded in terms Bloch functions (obtained solving the single particle hamiltonian  $h(\mathbf{r})$ ) at the same  $\mathbf{k}$ -point

$$\psi_{\lambda\mathbf{k}}(\mathbf{r}, \omega) = \sum_{n=1, N_b} \alpha_{\lambda n}^{\mathbf{k}}(\omega) \phi_{n\mathbf{k}}(\mathbf{r}), \quad (1.169)$$

$$\tilde{\psi}_{\lambda\mathbf{k}}(\mathbf{r}, \omega) = \sum_{n=1, N_b} \tilde{\alpha}_{\lambda n}^{\mathbf{k}}(\omega) \tilde{\phi}_{n\mathbf{k}}(\mathbf{r}), \quad (1.170)$$

where the sum goes over the  $N_b$  bands included in the calculation and mixed by the self energy. Eq. (1.165) and Eq. (1.166) became a  $N_b \times N_b$  linear system with  $\omega$  acting like a parameter

$$\sum_{n'} [\langle n\mathbf{k} | h_0(\mathbf{r}) + V_H(\mathbf{r}) | n'\mathbf{k} \rangle + \langle n\mathbf{k} | \Sigma(\mathbf{r}, \mathbf{r}'; \omega) | n'\mathbf{k} \rangle] \alpha_{\lambda n'}^{\mathbf{k}}(\omega) = E_{\lambda}^{\mathbf{k}}(\omega) \alpha_{\lambda n}^{\mathbf{k}}(\omega), \quad (1.171)$$

$$\sum_{n'} [\langle n\mathbf{k} | h_0(\mathbf{r}) + V_H(\mathbf{r}) | n'\mathbf{k} \rangle + \langle n\mathbf{k} | \Sigma^{\dagger}(\mathbf{r}', \mathbf{r}; \omega) | n'\mathbf{k} \rangle] \tilde{\alpha}_{\lambda n'}^{\mathbf{k}}(\omega) = [E_{\lambda}^{\mathbf{k}}(\omega)]^* \tilde{\alpha}_{\lambda n}^{\mathbf{k}}(\omega), \quad (1.172)$$

the  $N_b$  solutions of equation

$$E_n^{\mathbf{k}}(\epsilon_{n\mathbf{k}}^{QP}) = \epsilon_{n\mathbf{k}}^{QP} \quad n = 1 \dots N_b, \quad (1.173)$$

will give a set of complex poles whose real and imaginary part will be compared with experimental photoemission data.



# Bibliography

- [1] H. Ehrenreich, *The Optical Properties of Solids*, Academic, New York (1965).
- [2] R. M. Dreizler and E. K. U. Gross *Density Functional Theory*, Springer Verlag Heidelberg (1990)
- [3] P. Hohenberg and W. Khon, Phys. Rev. **136**, B864 (1964).
- [4] W. Khon and L. J. Sham, Phys. Rev. **140**, A1113 (1965).
- [5] L. Fetter and J.D. Walecka *Quantum theory of Many-Body Systems*, McGraw-Hill, New York, N.Y. 1981.
- [6] L. Hedin and B. I. Lundqvist, J. Phys. C. **4**, 2064 (1971).
- [7] D.M. Ceperley and B.I. Alder, Phys. Rev. Lett. **45**, 566 (1980).
- [8] J. P. Perdew and A. Zunger, Phys. Rev. B **23**, 5048 (1981).
- [9] R. O. Jones and I. Gunnarsson, Rev. of Modern Phys. **61**, 689 (1989).
- [10] G. Baym and L. P. Kadanoff, Phys. Rev. **124**, 287 (1961).
- [11] G. Strinati, Rivista del nuovo cimento **11**,1 (1988).
- [12] L. Hedin and S. Lundqvist: in *Solid State Physics*, edited by H. Ehrenreich, F. Seitz and D. Turnbull (Academic Press, New York, N.Y., 1969), Vol **23**, p. 1.
- [13] R. D. Mattuck, *A guide to Feynman diagrams in the Many-Body problem*, McGraw-Hill, New York (1976)
- [14] F. Aryasetiawan and O. Gunnarsson, Rep. Prog. Phys. **61**, 237-312 (1998).
- [15] A. Schindlmayr, P. García-González, and R. W. Godby, cond-mat/0110435.
- [16] U.V. Barth and B. Holm, Phys. Rev. **B 54**,8411 (1996).

- [17] P. M. Morse and H. Feshbach, *Methods of Theoretical Physics*, McGraw-Hill, New York (1953), pp 864-866
- [18] G. E. Engel, Behnam Farid, C. M. M. Nex and N. H. March, *Phys. Rev. B* **44**, 13356 (1991)



## Chapter 2

# Optical properties and band structure of copper within Density–Functional–Theory

In this second chapter, an accurate first-principles study of the electronic structure and absorption spectrum of bulk copper within Density Functional Theory in the Local Density Approximation (DFT-LDA) is presented, including the study of intraband transitions. Norm-conserving pseudopotentials (PPs) including the 3d shell (and optionally the underlying 3s and 3p shells) in the valence, requiring a relatively small plane-waves basis (60 and 140 Rydbergs cutoff, respectively) are constructed. As a consequence, these PPs are strongly non-local, yielding macroscopically wrong results in the absorption spectrum when momentum matrix elements are computed naively. The results are compared with experimental photoemission, absorption and electron energy loss data, and suggest non trivial self-energy effects, that will be discussed in the next chapter.

.....

For a long time copper has played a central role in the elucidation of the electronic structure of solids. It is a relatively inert material, very easy to handle experimentally; its energy dispersion relations (including spin-orbit interaction for some bands) have been measured with considerable precision; lifetimes of the band states as a function of the distance from Fermi level have been determined; surface states at different surfaces have been analyzed in various parts of the Brillouin zones (for a review see [1]). From the theoretical side, the study of noble metals like Copper using first-principles methods based on plane-waves and ab-initio pseudopotentials

(PPs) presents some peculiar complications in comparison with the case of simple metals or semiconductors. In fact, in addition to metallicity, which implies the use of an accurate sampling of the Brillouin zone in order to describe properly the Fermi surface, one must also keep into account the contribution of d-electrons to the bonding and to the valence bandstructure. This means that, within the PP scheme, d states cannot be frozen into the core part, but must be explicitly included into the valence, yielding a large total number of valence electrons (11 for bulk copper). Unfortunately, a Cu pseudopotential including  $3^{rd}$  shell states into the valence part is very steep. Hence, when working with a plane-wave basis, the usage of a PP of this kind may be computationally prohibitive.

On the other hand, the use of a pseudopotential without explicit treatment of 3d-electrons has been shown to be unreliable [2]. Hence, first-principles methods based on plane-waves have been used only seldom to treat Cu [2]. However, methods have been devised for the construction of softer pseudopotentials [3, 4, 5, 6], which make the inclusion of the  $3^{rd}$  shell in the valence more affordable. The price to be paid is that the construction and use of such pseudopotentials, which often display a very strong l-nonlocality, is a quite delicate matter. In particular, the choice of a reference component [7] and the transferability checks must be done with care. These difficulties are more than compensated by the simplicity and elegance of the plane-waves formalism in the subsequent calculations. In the following, two possible choices for the Cu pseudopotential are explored, i.e: a) including 3s and 3p electrons into the frozen core (a quite standard choice), and b) including the full  $3^{rd}$  shell in the valence. Fully converged Density Functional Theory – Local Density Approximation (DFT-LDA) calculations are performed at 60 and 140 Ry cutoff, respectively for case a) and b).

The chapter is organized as follows: in Section 2.1 the details of the construction of the pseudopotentials used are given; in Section 2.2 and Section 2.3 I present the ground state properties and bandstructure, respectively, obtained with the different pseudopotentials; finally, in Section 2.4, the theoretical absorption and electron energy loss spectra are compared with the experimental data, including the effects of Local Fields and intraband transitions.

## 2.1 Pseudopotential generation

The Cu atom has the ground-state electronic configuration  $[\text{Ar}]3d^{10}4s^1$ . 4s and 3d eigenvalues are separated, in DFT-LDA, by less than 0.5 eV. It is then quite obvious

that freezing all states but the 4s one into the atomic core (i.e., to neglect the polarization of the 3d electrons) cannot yield a good, transferable pseudopotential. On the other hand, inclusion of the 3d electrons into the valence (we call this a “3d” pseudopotential) yields a much slower convergence of plane-wave expansions, due to the steepness of the d-component of the PP. Unfortunately, the spatial superposition between the 3d and 3s or 3p states is quite large, despite the large ( $\simeq 70$  eV) energy separation. Hence, an even more conservative and secure choice for the PP is to include all 3s, 3p and 3d electrons into the valence: in fact, 2p and 3s states are well separated, both spatially and energetically ( $\simeq 800$  eV). This latter choice gives rise to a PP which is even harder than the “3d” one, and which will be referred to as a “3s” pseudopotential, yielding 19 valence electrons per atom.

Using the traditional pseudopotential generation scheme proposed by Bachelet, Hamann and Schlüter (BHS) [7] yields PP whose d component converges very slowly in Fourier space, requiring the use of an energy cutoff of 200 Rydbergs or more. However, PPs which converge at less than 100 Rydbergs can be constructed by using specially devised schemes as those of Refs. [3, 4, 5, 6]. In order to avoid the additional numerical complications arising from the charge-state dependence of the PP of Ref. [3], only *norm conserving* pseudopotentials are used. Moreover, the choices in generating the PP are dictated not only by the need of a fast convergence of the PP in Fourier space, but also by that of optimizing the PP accuracy and transferability, a non-trivial task when 3s and 3p states are also included into the valence. In particular, the Hamann scheme [8] (which does not try to optimize the Fourier space convergence at all) turned out to yield much more accurate and transferable norm-conserving PPs, particularly when the whole  $3^{\text{rd}}$  shell is included into the valence.

Hence, I strictly follow the Hamann procedure (described in the appendix of ref. [8]) whenever it is possible, i.e. in all cases except for the d components. For the latter, the Troullier–Martins [6] scheme is used, which allows to reduce significantly the number of plane-waves requested for convergence without losing too much in transferability. In all other cases (i.e. for the s and p components of both “3s” and “3d” pseudopotentials) the Hamann procedure is found to be more convenient, even at the cost of a slower Fourier space convergence, since the TM one yielded significantly worse results, and/or ghost states [9] when the PP were used in the Kleinman–Bylander form [10].

Another delicate point is the choice of a reference component, i.e. of a PP angular momentum component which is taken to be valid for every  $l \geq 3$ . Often, the  $l=2$

component is chosen as a reference, simply because this makes calculations easier. This choice is sometimes lacking a physical justification, and can be dangerous, as it has been shown in the case of Sn [11]. In the present case the  $l = 2$  reference had to be avoided anyway, since it yielded a much worse transferability than the  $l=0$  or  $l=1$  choices, and sometimes gave rise to ghost states in the KB form.

Several trials and tests with different cutoff radii have been done, in order to optimize the PP transferability without increasing too much the number of plane waves requested for convergence. Transferability tests included both the plot of logarithmic derivatives, and the explicit calculation of pseudoatom eigenvalues in some excited electronic configuration (both neutral and positively charged).

Finally, since 3s and 3p states in the solid preserve their atomic configuration better than 3d ones, their explicit inclusion into the valence can sometimes be avoided, by considering only the effects of the non-linearity of the exchange-correlation potential [12]. Hence, a third pseudopotential, with frozen 3s and 3p electrons but including non-linear core-corrections has also been considered, and will be referred to as the “3d+NLCC” PP. In the latter, the core charge is represented by the true one for  $r \geq 0.5$  Bohrs, and by a Gaussian model charge for  $r \leq 0.5$  Bohrs.

The resulting optimal cutoff radii and reference  $l$ -components, chosen for our “3d”, “3s”, and “3d+NLCC” pseudopotentials, are given in Table 2.1.

Pseudopotential	$r_s$ [Bohr]	$r_p$ [Bohr]	$r_d$ [Bohr]	Reference $l$ -component
“3d”	1.19 (H)	1.19 (H)	2.08 (TM)	s
“3d+NLCC”	1.10 (H)	1.19 (H)	2.08 (TM)	s
“3s”	0.49 (H)	0.60 (H)	1.19 (TM)	p

Table 2.1: Cu Pseudopotential cutoff radii and reference components. (H) and (TM) stand for Hamann (ref. [8]) and Troulliers–Martins (ref. [6]) schemes, respectively. All the pseudopotentials are norm-conserving in the sense of Bachelet, Hamann and Schlüter[7], and have been produced using a publicly available Fortran code [13].

## 2.2 Ground state properties

The first step is a self-consistent ground-state calculation, performed by minimizing the DFT–LDA energy functional with a Car–Parrinello method [15], in a standard plane-wave basis. The Ceperley–Alder [16] exchange–correlation energy and potential, as parametrized by Perdew and Zunger [17], have been used (test calculations with the Hedin–Lundqvist form [18] have also been performed: see below). All pseu-

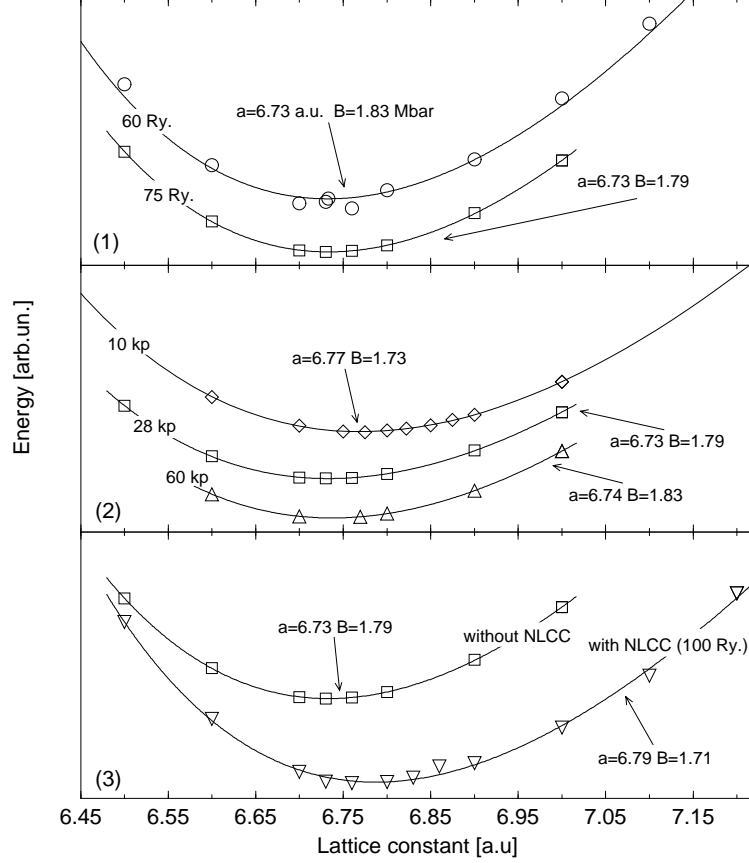


Figure 2.1: Calculated total energy vs. lattice constant for bulk Cu. Panel (1): effect of the kinetic energy cutoff at fixed number of k-points (28). Panel (2): effect of the IBZ sampling at fixed  $E_{cut}$  (75 Ry.). Panel (3): effect of nonlinear core-corrections (see text). The reported values for the equilibrium lattice constant and bulk modulus have been obtained from Murnaghan fits (continuous curves). The experimental values are  $a=6.822$  Bohrs and  $B=1.827$  MBar [20].

dopotentials are used within the fully-separable Kleinman-Bylander scheme [10], after checking that no ghost-states was present [9]. The irreducible wedge of the Brillouin zone (IBZ) was sampled with the use of Monkhorst and Pack (MP) sets [19] of  $N_k$  k-points. A very small fictitious electronic temperature (equal to  $\approx 10$  Kelvin) was used in order to accelerate the convergence of the calculated Fermi surface (for theoretical details see Ref. [14]). Convergence with respect to both the k-points sampling and the kinetic energy cutoff has been checked extensively: Fig. 2.1 and Table 2.2 show the results obtained for the “3d” pseudopotential.  $E_{cut}=60$  Ry. and  $N_k=28$  appear to give well-converged, satisfactory results, with lattice constant  $a_0$  and Bulk modulus  $B_0$  within 1.4% of the experimental values. In the calculation with NLCC, the energy cutoff had to be increased to 100 Ry, in order to describe properly the core charge. NLCC reduce the underestimation of the experimental lattice constant to 0.5 %, but they are found to be almost influential on the band-

PW cutoff (Ry)	Nk	$a_0$ [Bohr]	$B_0$ [MBar]
75	10	6.77	1.73
75	28	6.73	1.79
75	60	6.74	1.83
60	28	6.73	1.83
100+NLCC	28	6.79	1.71
Expt.	–	6.82	1.83

Table 2.2: Convergence of the calculated ground-state properties of bulk Cu.

structure, as well as on the resulting spectra (see below). Finally, calculations with the “3s” pseudopotential, much deeper than the “3d” one, required an energy cutoff of 140 Ry. Also in this case, the effect on the LDA bandstructure and spectra in the energetic region of interest are found to be very small (see below).

In summary, as long as only the LDA 4s and 3d bandstructure is concerned, the effect of the inclusion of 3s and 3p in the valence, (as well as the use of NLCC), are mainly confined to a change of the equilibrium lattice constant, which induces an indirect effect on the bandstructure energies [21].

## 2.3 LDA band structure

Fig. 2.2 summarizes the maximum relative energy differences induced by different computational details on the LDA bandstructure; the value is taken at the bottom valence in the  $\Gamma$  point ( $\Gamma_1$ ) and decreases gradually to zero at the Fermi level. By changing  $E_{cut}$  from 60 Ry to 75 Ry the band-structure remains practically identical (changes are less than 0.02 meV). At the 60 Ry cutoff, the band structure calculated with the Ceperley-Alder parametrization of the exchange-correlation potential [16, 17] is compared with that obtained using the Hedin-Lundqvist parametrization [18]; in the latter case a maximum energy shift of about 0.15 eV is found.

The inclusion of NLCC yields, instead, a maximum upward shift of about 0.21 eV with respect to the case without NLCC, mainly due to the change in the equilibrium lattice constant. To study more deeply the effects of core polarization, a band-structure calculation with the “3s” pseudopotential (see Section 2.1) was performed, where the 3s and 3p core level relaxation is fully included in the selfconsistent run. Also in this case the maximum bandshift with respect to the “3d” pseudopotential is limited to about 0.2 eV. Hence, the results obtained with the “3d” pseudopotential

at  $E_{cut}=60$  Ry. and using 28 MP k-points in the determination of the self-consistent charge density can be considered to represent the converged LDA bandstructure of bulk copper. Theoretical results are compared with the experimental photoemission data in Fig. 2.3.

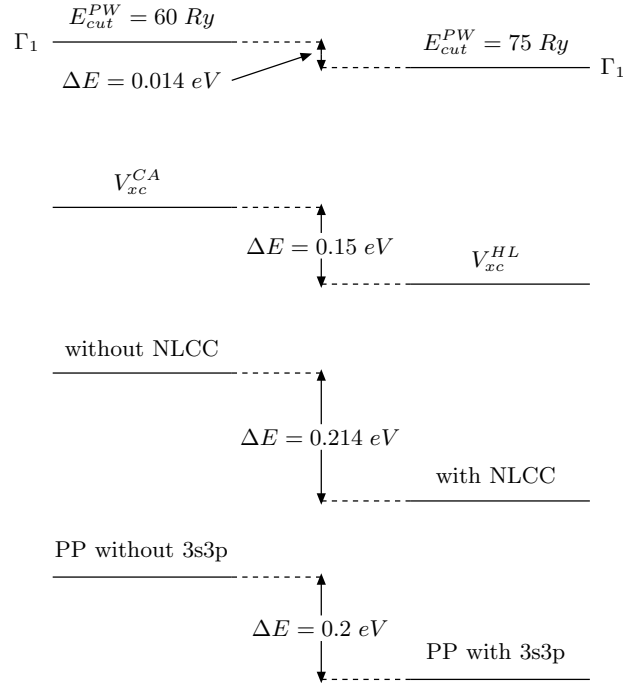


Figure 2.2: Summary of the effects of different computational details on the LDA bandstructure. The energy differences reported are the maximum ones, and correspond to the bottom valence band at the  $\Gamma$  point ( $\Gamma_1$ ). They decrease gradually to zero at the Fermi level.

At difference with the case of semiconductors, the disagreement between theory and experiment is far from being limited to a rigid shift of the Kohn-Sham occupied eigenvalues with respect to the empty ones. In fact, as also summarized in Table 2.3, the widths of the d bands are systematically overestimated, a well-known failure of LDA when applied to transition and noble metals [22].

## 2.4 Absorption spectrum: non-local pseudopotentials and intraband transitions

In Section 1.1.1 I have showed the correct procedure to follow in order to obtain the macroscopic (measured) optical properties starting from the microscopical electronic properties of the medium. Keeping the  $\mathbf{q} \rightarrow 0$  limit of Eq.(1.44) the absorption

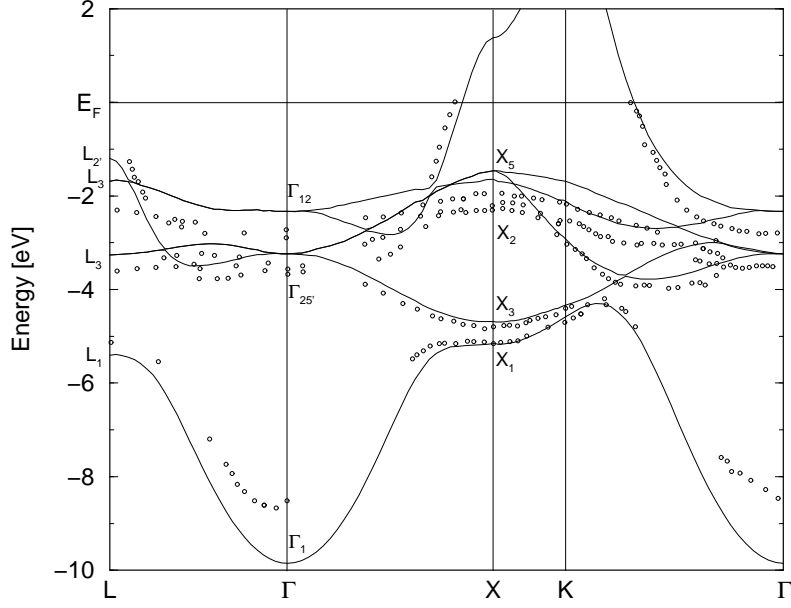


Figure 2.3: Bulk copper DFT-LDA bandstructure (full-line), compared with photoemission data (points) from Ref. [1].

		Experiment [1]	Present work
positions of d-bands	$\Gamma_{12}$	-2.78	-2.33
	$X_5$	-2.01	-1.46
	$L_3$	-2.25	-1.69
widths of d-bands	$\Gamma_{12} - \Gamma_{25'}$	0.81	0.91
	$X_5 - X_3$	2.79	3.23
	$X_5 - X_1$	3.17	3.70
	$L_3 - L_3$	1.37	1.58
	$L_3 - L_1$	2.91	3.72
positions of sp-bands	$\Gamma_1$	-8.60	-9.85
	$L_{2'}$	-0.85	-1.12
L-gap	$L_1 - L_{2'}$	4.95	4.21

Table 2.3: Comparison of Cu band widths and energy position with experimental values [1] at high-symmetry points. All energies in eV.

spectrum is given by the imaginary part of the macroscopic dielectric function

$$\epsilon_M(\omega) = \langle\langle \epsilon_L^{-1}(\mathbf{r}\mathbf{r}', \omega) \rangle\rangle_0^{-1}. \quad (2.1)$$



Now from Eq. (1.65) (using the fact that copper is a cubic material) we obtain

$$\langle\langle\epsilon_L^{-1}(\mathbf{r}\mathbf{r}',\omega)\rangle\rangle_0 = 1 + \lim_{\mathbf{q}\rightarrow 0} \frac{4\pi}{|\mathbf{q}|^2} \chi_{\rho\rho}(\mathbf{q},\omega), \quad (2.2)$$

$\chi_{\rho\rho}$  is the head ( $\mathbf{G} = \mathbf{G}' = \mathbf{0}$ ) of the Fourier components of the density–density Green’s function that we will refer to simply as  $\chi$  in the following. To calculate  $\chi$  we must solve, via some approximation, the correlation effects due to the Coulomb interaction. As observed in Section 1.3.1, the  $\chi$  introduced in Eq. (2.2) is reducible with respect to the Coulomb interaction. As long as we want to define an approximation for the interaction kernel  $\tilde{\Xi}$  we can substitute  $\chi$  with its irreducible part  $\tilde{\chi}$  Fourier by transforming Eq. (1.151)

$$\chi_{\mathbf{G}\mathbf{G}'}(\mathbf{q},\omega) = \tilde{\chi}_{\mathbf{G}\mathbf{G}'}(\mathbf{q},\omega) + \sum_{\mathbf{G}''} \tilde{\chi}_{\mathbf{G}\mathbf{G}''}(\mathbf{q},\omega) \frac{4\pi}{|\mathbf{q} + \mathbf{G}''|^2} \chi_{\mathbf{G}''\mathbf{G}'}(\mathbf{q},\omega). \quad (2.3)$$

In this thesis we will not consider many–body effects on the two–body Green’s function, so we approximate  $\tilde{\Xi} = 0$  substituting  $\tilde{\chi}$  with the RPA, non interacting polarization  $\chi^0$ . As consequence

$$\epsilon_{\mathbf{0}\mathbf{0}}^{-1}(\omega) = 1 + \lim_{\mathbf{q}\rightarrow 0} \frac{4\pi}{|\mathbf{q}|^2} \chi_{\mathbf{G}=\mathbf{0}\mathbf{G}'=\mathbf{0}}(\mathbf{q},\omega), \quad (2.4)$$

$\chi_{\mathbf{G}\mathbf{G}'}(\mathbf{q},\omega)$  solution of the equation Eq. (2.3)

$$\chi_{\mathbf{G}\mathbf{G}'}(\mathbf{q},\omega) = \chi_{\mathbf{G}\mathbf{G}'}^0(\mathbf{q},\omega) + \sum_{\mathbf{G}''} \chi_{\mathbf{G}\mathbf{G}''}^0(\mathbf{q},\omega) \frac{4\pi}{|\mathbf{q} + \mathbf{G}''|^2} \chi_{\mathbf{G}''\mathbf{G}'}(\mathbf{q},\omega). \quad (2.5)$$

Neglecting (for the moment) intraband transitions,  $\chi_{\mathbf{G}\mathbf{G}''}^0(\mathbf{q},\omega)$  is given by:

$$\chi_{\mathbf{G}\mathbf{G}'}^0(\mathbf{q},\omega) = \frac{1}{2} \int_{BZ} \frac{d^3\mathbf{k}}{(2\pi)^3} \sum_{n \neq n'} \langle n'\mathbf{k} - \mathbf{q} | e^{-i(\mathbf{q}+\mathbf{G})\cdot\mathbf{r}} | n\mathbf{k} \rangle \langle n\mathbf{k} | e^{i(\mathbf{q}+\mathbf{G}')\cdot\mathbf{r}'} | n'\mathbf{k} - \mathbf{q} \rangle \mathcal{G}_{he}^0(n, n', \mathbf{k}, \mathbf{q}, \omega), \quad (2.6)$$

with

$$\mathcal{G}_{he}^0(n, n', \mathbf{k}, \mathbf{q}, \omega) = f_{n'}(\mathbf{k} - \mathbf{q}) (2 - f_n(\mathbf{k})) \left[ \frac{1}{\omega + \epsilon_{n'}(\mathbf{k} - \mathbf{q}) - \epsilon_n(\mathbf{k}) + i\eta} - \frac{1}{\omega + \epsilon_n(\mathbf{k}) - \epsilon_{n'}(\mathbf{k} - \mathbf{q}) - i\eta} \right]. \quad (2.7)$$

with  $0 \leq f_n(\mathbf{k}) \leq 2$  representing the occupation number summed over spin components. The sums over  $k$  are transformed to integrals over the BZ, and the latter are evaluated by summing over large sets of random points contained in the whole BZ. Fully converged calculations with a small broadening require a very large number of

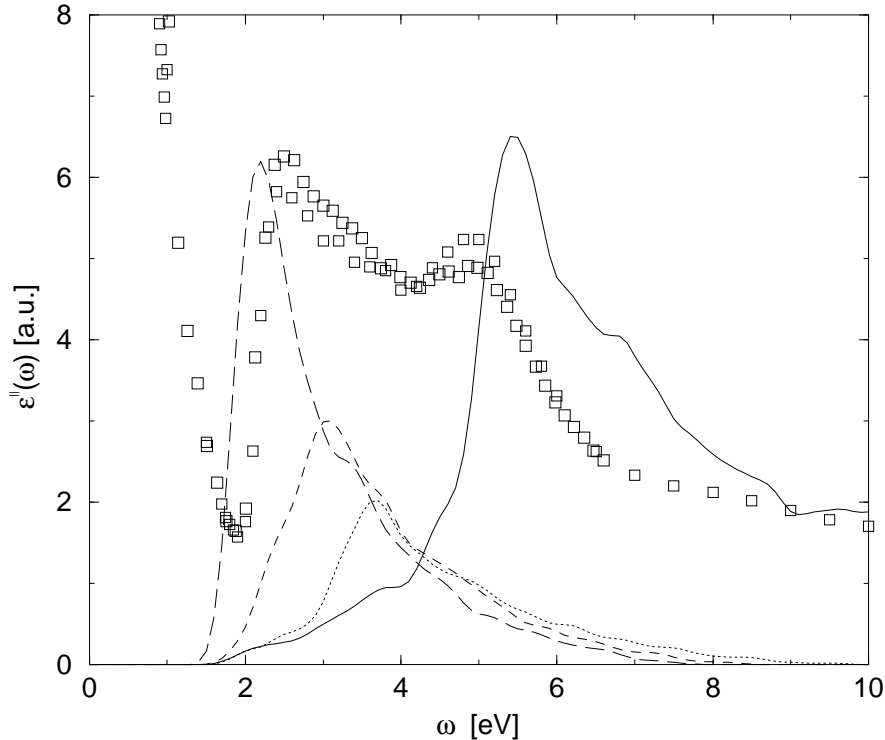


Figure 2.4: Full line: imaginary part of the macroscopic dielectric function of Cu without Local-Field effects and without including the non-local pseudopotential commutator [Eq. (2.11)], compared with experimental data (squares) from[24]. Dot, dashed and long-dashed lines correspond to the functions defined in Eq. (2.12) with  $n' = 3$ ,  $n' = 4$  and  $n' = 5$  respectively. All theoretical curves are computed with  $N_k = 15,386$ , and a Gaussian broadening of 0.15 eV (see text).

k-points [23]; the broadening used (and the corresponding number of k-points which was found to be sufficient to ensure convergence) is specified explicitly for each one of the reported spectra.

The simplest approach to the calculation of the absorption spectrum neglects the full inversion of Eq. (2.5) (i.e., neglects Local Field Effects), and assumes

$$\epsilon_M(\omega) \approx 1 - \lim_{\mathbf{q} \rightarrow \mathbf{0}} \frac{4\pi}{|\mathbf{q}|^2} \chi_{\mathbf{G}=\mathbf{0} \ \mathbf{G}'=\mathbf{0}}(\mathbf{q}, \omega). \quad (2.8)$$

The  $\mathbf{q} \rightarrow \mathbf{0}$  limit for the oscillator strengths appearing in Eq. (2.6) is calculated in the transverse gauge [25], within first order perturbation theory [26]

$$\lim_{\mathbf{q} \rightarrow \mathbf{0}} \langle n' \mathbf{k} - \mathbf{q} | e^{-i\mathbf{q} \cdot \mathbf{r}} | n \mathbf{k} \rangle = -i\mathbf{q} \cdot \frac{\langle \phi_{n' \mathbf{k} - \mathbf{q}} | \mathbf{r}, H | \phi_{n \mathbf{k}} \rangle}{\epsilon_{n'}(\mathbf{k}) - \epsilon_n(\mathbf{k})} + O(q^2), \quad (2.9)$$

where  $\phi_{n\mathbf{k}}(\mathbf{r})$  are the Bloch functions. Due to the non local character of the norm-conserving pseudopotentials, the well-known relation between  $[\mathbf{r}, H]$  and the mo-

momentum operator

$$[\mathbf{r}, H] = \mathbf{p}. \quad (2.10)$$

must be substituted by:

$$[\mathbf{r}, H] = \mathbf{p} + [\mathbf{r}, V_{NL}]. \quad (2.11)$$

The second term of the rhs of Eq. (2.11), which in simple metals and in many semiconductors is small (and often neglected in practical calculations), becomes extremely important in the case of copper due to the large nonlocality of the PP. This is demonstrated in Fig. 2.4 where the imaginary part of  $\varepsilon_M$  is calculated assuming the validity of Eq. (2.10). The experimental absorption spectrum is severely underestimated between the offset of interband transitions ( $\approx 1.74$  eV) and 5 eV. A better analysis of this behavior can be performed by plotting the quantity

$$\Im m \left[ \frac{\sum_{\mathbf{k}} \mathcal{G}_{he}^0(n, n', \mathbf{k}, \mathbf{0}, \omega)}{\omega^2} \right]. \quad (2.12)$$

with  $n = 6$  and  $n' = 3, 4, 5$  (see Fig. 2.4). This quantity is the joint density of states (JDOS) (divided by  $\omega^2$ ) for transitions between the sixth band (d-like) and the third to fifth bands (sp-like), and corresponds to assuming an oscillator strength equal to one in Eq. (2.6).

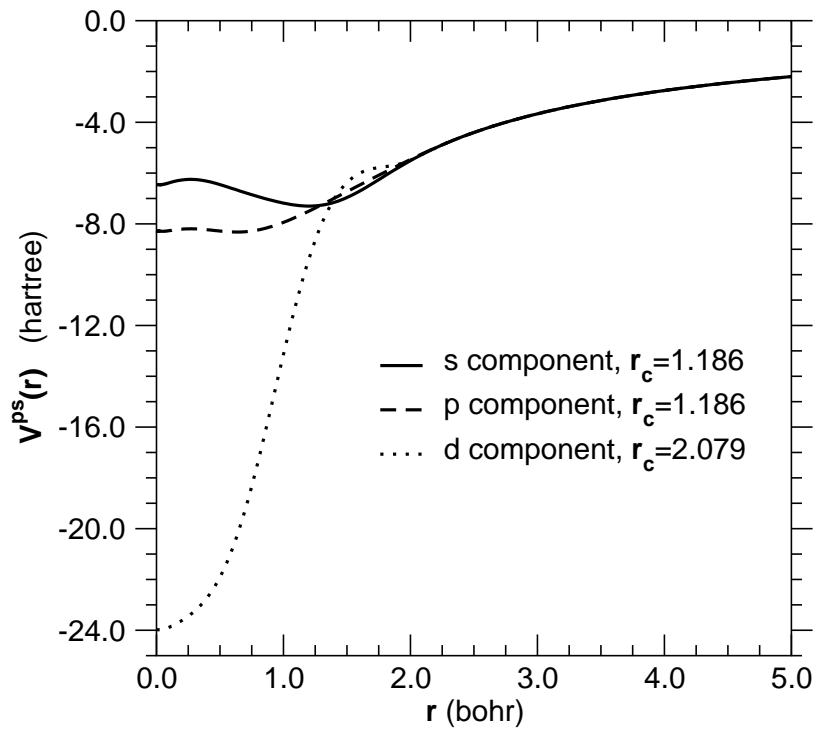


Figure 2.5:  $l$ -components of the radial part of  $V_{NL}$ .

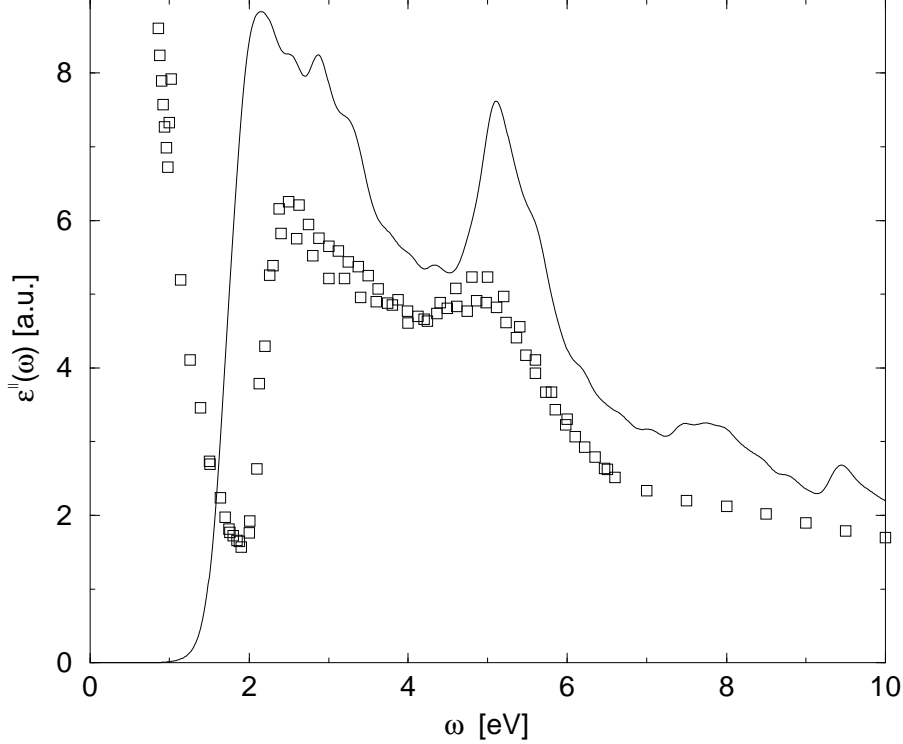


Figure 2.6: Full line: imaginary part of the macroscopic dielectric function of Cu without Local-Field effects and *including* the non-local pseudopotential commutator [Eq. (2.11)], compared with experimental data (squares)[24]. $N_k$  and broadening as in Fig. 2.4.

We see that transitions in the energy range of interest (1.8 to 5.0 eV) exist, but they are strongly suppressed due to the small values of the corresponding matrix elements of  $\mathbf{p}$ . Using both terms of Eq.(2.11), instead, the spectrum shown in Fig. 2.6 is obtained, comparing much better with experiments. The large influence of the non-local pseudopotential commutator on  $d \rightarrow s/p$  optical transitions can be understood by writing explicitly the contribution of the second term of Eq. (2.11):

$$\langle \phi_{(s/p)\mathbf{k}} | [\mathbf{r}, V_{NL}] | \phi_{(d)\mathbf{k}} \rangle = \sum_{l=s,p,d} \iint d\mathbf{r} d\mathbf{r}' \phi_{(s/p)\mathbf{k}}^*(\mathbf{r}) [\mathbf{r} V_{NL}^l(\mathbf{r}, \mathbf{r}') - V_{NL}^l(\mathbf{r}, \mathbf{r}') \mathbf{r}'] \phi_{(d)\mathbf{k}}(\mathbf{r}'), \quad (2.13)$$

where  $V_{NL}^l(\mathbf{r}, \mathbf{r}')$  is the  $l$ -orbital component of the pseudopotential, and  $\phi_{(s/p)\mathbf{k}}(\mathbf{r})$ ,  $\phi_{(d)\mathbf{k}}(\mathbf{r})$  are the  $s/p$  like and  $d$  like Bloch functions. Now approximating the sum in Eq.(2.13) with the leading terms, we obtain:

$$\langle \phi_{(s/p)\mathbf{k}} | [\mathbf{r}, V_{NL}] | \phi_{(d)\mathbf{k}} \rangle \approx \iint d\mathbf{r} d\mathbf{r}' [\phi_{(s/p)\mathbf{k}}^*(\mathbf{r}) \mathbf{r} V_{NL}^d(\mathbf{r}, \mathbf{r}') \phi_{(d)\mathbf{k}}(\mathbf{r}') - \phi_{(s/p)\mathbf{k}}^*(\mathbf{r}) (V_{NL}^s(\mathbf{r}, \mathbf{r}') + V_{NL}^p(\mathbf{r}, \mathbf{r}')) \mathbf{r}' \phi_{(d)\mathbf{k}}(\mathbf{r}')]. \quad (2.14)$$

In the case of copper the  $l$ -components of the local, radial part of  $V_{NL}$  are shown in Fig. 2.5: the  $d$  component of the pseudopotential differ from the  $p$  component near the origin by about 20 Hartrees, and this explain the strong influence on  $\epsilon_M''(\omega)$ .

Despite the strong improvement of the agreement with experiment obtained in Fig. 2.6, the theoretical curve exhibits an amplitude overestimation of about 20% with respect to the experimental absorption spectrum.

This drawback must be analyzed taking into account both the *physical approximations* involved in the theoretical approach, and the possible *residual errors* due to the PP scheme. Concerning the first, the most important point is the neglect of self-energy effects in the bandstructure calculation, and of excitonic effects in the absorption process. Concerning the PP scheme, on the other hand, a possible reason for the overestimation of the spectrum intensity could be related to the use of pseudo-wavefunctions instead of the all-electrons ones in Eq. (2.6). This effect has been studied in atoms by the authors of Ref. [27]: they found that PP calculations, even when the second term of rhs of Eq. (2.11) is correctly taken into account, can be affected by a small residual error due to the difference between all-electron wavefunctions and pseudo wavefunctions *inside the core region*. In the case of the Cu atoms,  $3d \rightarrow 4p$  transitions were found to yield a matrix element which was too large by about 10% [27].

The effect of this overestimation of the  $3d \rightarrow 4p$  intra-atomic optical matrix elements on the calculated bulk spectrum is, however, not obvious. To clarify this point, an accurate comparison of the results obtained by using the “3d” and “3s” pseudopotentials was performed, both in case of the bulk crystal and for the isolated Cu atom.

Optical transitions	<i>AE</i>	”3d“ PP	”3s“ PP
$4s \rightarrow 4p$	1.732	1.738	1.713
$3d \rightarrow 4p$	0.406	0.453	0.412

Table 2.4: Optical matrix elements for the Cu atom, calculated in the All-electrons (AE) scheme, and with the pseudopotentials. Values are in atomic units.

For the latter case, the results are summarized in Table 2.4: while the “3d” pseudopotential gives about the same results as those obtained in Ref. [27], the “3s” PP reduces the error on the intra-atomic optical matrix elements to less than 1.5 %. However in the case of the bulk crystal the amplitude of our calculated spectrum does not change appreciably when results obtained with “3d” and “3s” pseudopotentials

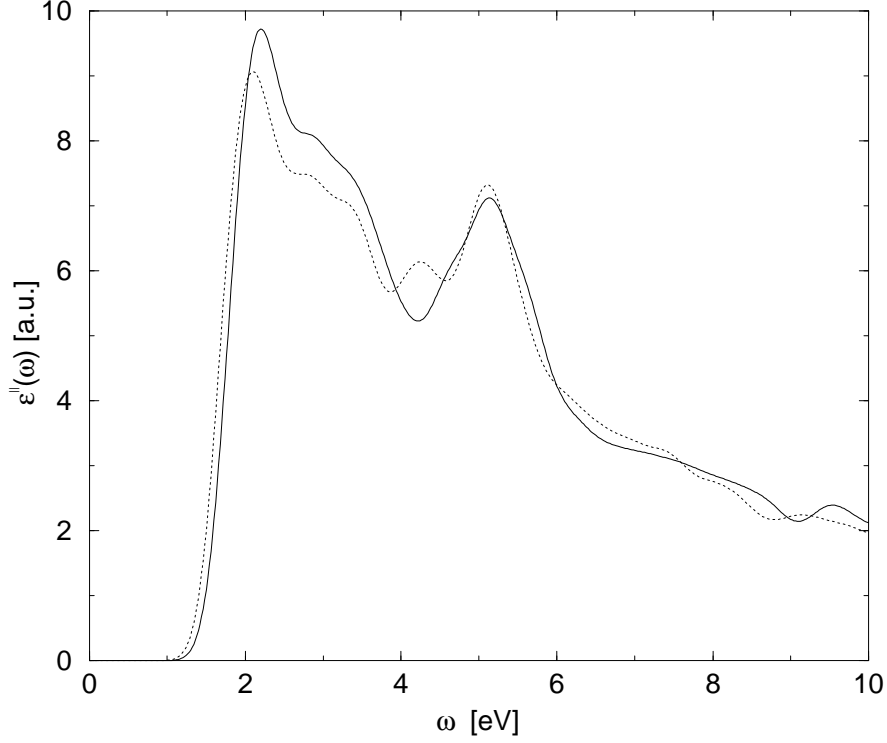


Figure 2.7: Effect of the use of a pseudopotential including the 3s and 3p shells in the valence on the calculated  $\epsilon''(\omega)$  for bulk Cu (full line : “3d” PP; dotted line: “3s” PP. See text). Due to the large number of plane-waves required by the “3s” PP, the comparison is done using a small number of k-points and a relatively large Gaussian broadening ( $N_k = 3,000$ ,  $\gamma = 0.2$  eV). Local-Field effects are neglected, and Eq. (2.11) is used.

are compared (see Fig. 2.7). This suggests that the overall intensity overestimation cannot be ascribed to the use of PP wavefunctions in Eq. (2.6).

The reason for this discrepancy between theory and experiment should hence be searched for within the physical approximations made, such as the neglect of self-energy effects, will be included in the next chapter.

### 2.4.1 Intraband transitions

A peculiar characteristic of metals is the intra-band contribution to the dielectric function, which, neglecting local field effects, is given by:

$$\epsilon'_{intra}(\omega) \equiv 1 - \lim_{\mathbf{q} \rightarrow 0} \left\{ \frac{4\pi}{|\mathbf{q}|^2} \sum_n \int_{BZ} \frac{d^3\mathbf{k}}{(2\pi)^3} [f_n(\mathbf{k}-\mathbf{q}) - f_n(\mathbf{k})] \frac{|\langle n\mathbf{k} | e^{i\mathbf{q}\cdot\mathbf{r}} | n\mathbf{k}-\mathbf{q} \rangle|^2}{\omega + \epsilon_n(\mathbf{k}-\mathbf{q}) - \epsilon_n(\mathbf{k})} \right\}, \quad (2.15)$$

with the n-sum restricted only to semi-occupied bands. In the case of copper only the sixth band contributes to Eq. (2.15). Indicating this band with  $n_F$  and using

the relation

$$f_{n_F}(\mathbf{k} - \mathbf{q}) - f_{n_F}(\mathbf{k}) = (f_{n_F}(\mathbf{k} - \mathbf{q}) - f_{n_F}(\mathbf{k})) \{\theta[f_{n_F}(\mathbf{k} - \mathbf{q}) - f_{n_F}(\mathbf{k})] - \theta[f_{n_F}(\mathbf{k}) - f_{n_F}(\mathbf{k} - \mathbf{q})]\}, \quad (2.16)$$

time-reversal symmetry allows us to rewrite Eq. (2.15) as

$$\begin{aligned} \epsilon'_{intra}(\omega) \equiv & 1 \\ & - \lim_{\mathbf{q} \rightarrow \mathbf{0}} \left\{ \frac{8\pi}{|\mathbf{q}|^2} \int_{BZ} \frac{d^3\mathbf{k}}{(2\pi)^3} (f_{n_F}(\mathbf{k} - \mathbf{q}) - f_{n_F}(\mathbf{k})) \theta[f_{n_F}(\mathbf{k} - \mathbf{q}) - f_{n_F}(\mathbf{k})] \right. \\ & \left. \frac{|\langle n\mathbf{k} | e^{i\mathbf{q}\cdot\mathbf{r}} | n\mathbf{k} - \mathbf{q} \rangle|^2 (\epsilon_{n_F}(\mathbf{k}) - \epsilon_{n_F}(\mathbf{k} - \mathbf{q}))}{\omega^2 - (\epsilon_{n_F}(\mathbf{k}) - \epsilon_{n_F}(\mathbf{k} - \mathbf{q}))^2} \right\}. \quad (2.17) \end{aligned}$$

In the small  $\mathbf{q}$  limit, Eq. (2.17) yields the well-known Drude contribution to the dielectric function

$$\epsilon'_{intra}(\omega) \equiv 1 - \frac{\omega_D^2}{\omega^2} + O(q^2), \quad (2.18)$$

with

$$\begin{aligned} \omega_D^2 = \lim_{\mathbf{q} \rightarrow \mathbf{0}} \left\{ \frac{8\pi}{|\mathbf{q}|^2} \int_{BZ} \frac{d^3\mathbf{k}}{(2\pi)^3} (f_{n_F}(\mathbf{k} - \mathbf{q}) - f_{n_F}(\mathbf{k})) \theta[f_{n_F}(\mathbf{k} - \mathbf{q}) - f_{n_F}(\mathbf{k})] \right. \\ \left. |\langle n\mathbf{k} | e^{i\mathbf{q}\cdot\mathbf{r}} | n\mathbf{k} - \mathbf{q} \rangle|^2 (\epsilon_{n_F}(\mathbf{k}) - \epsilon_{n_F}(\mathbf{k} - \mathbf{q})) \right\}. \quad (2.19) \end{aligned}$$

Since the theta function in Eq. (2.19) limits strongly the region of BZ that contributes to the integral, the  $\mathbf{k}$ -space sampling and the modulus of the chosen  $\mathbf{q}$  vector used in the numerical evaluation of Eq. (2.19) become two critical convergence parameters: for a small  $|\mathbf{q}|$  very few  $\mathbf{k}$ -points will satisfy the condition  $[f_{n_F}(\mathbf{k} - \mathbf{q}) - f_{n_F}(\mathbf{k})] \neq 0$ . In practice,  $|\mathbf{q}|$  must be small enough to reproduce the  $\mathbf{q} \rightarrow \mathbf{0}$  limit in Eq. (2.19), but large enough to allow a suitable number of  $\mathbf{k}$ -points to contribute to the sum. To obtain a well converged  $\omega_D^2$  we found it necessary to use  $\approx 16,000$  random  $\mathbf{k}$ -points in a region of the BZ such that  $\epsilon_{n_F}(\mathbf{k})$  is contained within  $\epsilon_{Fermi} \pm 0.1$  eV. The value used was  $|\mathbf{q}| = 0.005$  a.u.. A fictitious electronic temperature was introduced to smear out the Fermi surface, increasing the number of  $(\mathbf{k}, \mathbf{k} - \mathbf{q})$  pairs giving non zero contributions to Eq. (2.19). In Table 2.5 we present our results as a function of the fictitious electronic temperature. The optical mass, defined as

$$m_{opt} = \left( \frac{\omega_c}{\omega_D} \right)^2 \quad \text{with} \quad \omega_c = \sqrt{\frac{4\pi}{\Omega}} = 10.8 \text{ eV} \quad (2.20)$$

with  $\Omega$  direct lattice cell volume, converges to 1.36, a value in good agreement with the experiment [28].

$T_{el}$ [eV]	Number of intraband transitions	$\omega_D$ [ev]	$m_{opt}$
0.1	14,617	9.39	1.32
0.01	2,456	9.41	1.32
0.001	534	9.25	1.36
0.0001	310	9.28	1.36
0.00001	296	9.27	1.36

Table 2.5: Cu Drude plasma frequency and optical mass values obtained using different fictitious electronic temperatures; the experimental value for  $m_{opt}$  is 1.35[28].

## 2.4.2 Local field effects

Local-Field effects are accounted for when the macroscopic dielectric function is computed according to Eq. (2.1–2.5), i.e. by obtaining  $\chi_{\mathbf{G}\mathbf{G}'}(\mathbf{q}, \omega)$  as

$$\chi_{\mathbf{G}\mathbf{G}'}(\mathbf{q}, \omega) = \chi_{\mathbf{G}\mathbf{G}'}^0(\mathbf{q}, \omega) \left[ 1 - \frac{4\pi}{|\mathbf{q} + \mathbf{G}|^2} \chi_{\mathbf{G}\mathbf{G}'}^0(\mathbf{q}, \omega) \right]^{-1}, \quad (2.21)$$

We explicitly divide  $\chi_{\mathbf{G}\mathbf{G}'}^0(\mathbf{q}, \omega)$  into intraband and interband contributions:

$$\chi_{\mathbf{G}\mathbf{G}'}^0(\mathbf{q}, \omega) = \chi_{\mathbf{G}\mathbf{G}'}^{inter}(\mathbf{q}, \omega) + \chi_{\mathbf{G}\mathbf{G}'}^{intra}(\mathbf{q}, \omega), \quad (2.22)$$

where the interband part is given by Eq. (2.6), while for the intraband contribution we have to evaluate:

$$\chi_{\mathbf{G}\mathbf{G}'}^{intra}(\mathbf{q}, \omega) = \frac{1}{2} \int_{BZ} \frac{d^3\mathbf{k}}{(2\pi)^3} \langle n_F \mathbf{k} - \mathbf{q} | e^{-i(\mathbf{q} + \mathbf{G}) \cdot \mathbf{r}} | n_F \mathbf{k} \rangle \langle n_F \mathbf{k} | e^{i(\mathbf{q} + \mathbf{G}') \cdot \mathbf{r}'} | n_F \mathbf{k} - \mathbf{q} \rangle \mathcal{G}_{he}^0(n_F, n_F, \mathbf{k}, \mathbf{q}, \omega). \quad (2.23)$$

with  $\mathcal{G}_{he}^0(n, n', \mathbf{k}, \mathbf{q}, \omega)$  defined in Eq. (2.7). For  $\mathbf{G}, \mathbf{G}' \neq \mathbf{0}$  the oscillator strength is calculated using Fast Fourier Transforms (FFT)

$$\langle n\mathbf{k} - \mathbf{q} | e^{-i(\mathbf{q} + \mathbf{G}) \cdot \mathbf{r}} | n'\mathbf{k} \rangle = \langle u_{n\mathbf{k}} | e^{-i\mathbf{G} \cdot \mathbf{r}} | u_{n'\mathbf{k}} \rangle + O(q), \quad (2.24)$$

while for the  $\mathbf{G} = \mathbf{G}' = \mathbf{0}$  element of  $\chi^{inter}$  we use Eq. (2.9).

The method presented in Section 2.4.1 for the calculation of  $\omega_D$  could, in principle, be extended to  $\chi_{\mathbf{G}\mathbf{G}'}^{intra}(\mathbf{q}, \omega)$ . Unfortunately the explicit calculation of  $\chi^{intra}$  for all the  $(\mathbf{G}, \mathbf{G}')$  pairs is computationally prohibitive, due to the large number of  $\mathbf{k}$ -points required to reach convergence. To overcome these difficulties, we have evaluated Eq. (2.23) on a limited number of  $\mathbf{k}$ -points (a MP grid of 110 points in the irreducible wedge).  $\mathcal{G}_{he}^0(n_F, n_F, \mathbf{k}, \mathbf{q}, \omega)$  is different from zero only for  $\mathbf{k}$  very close



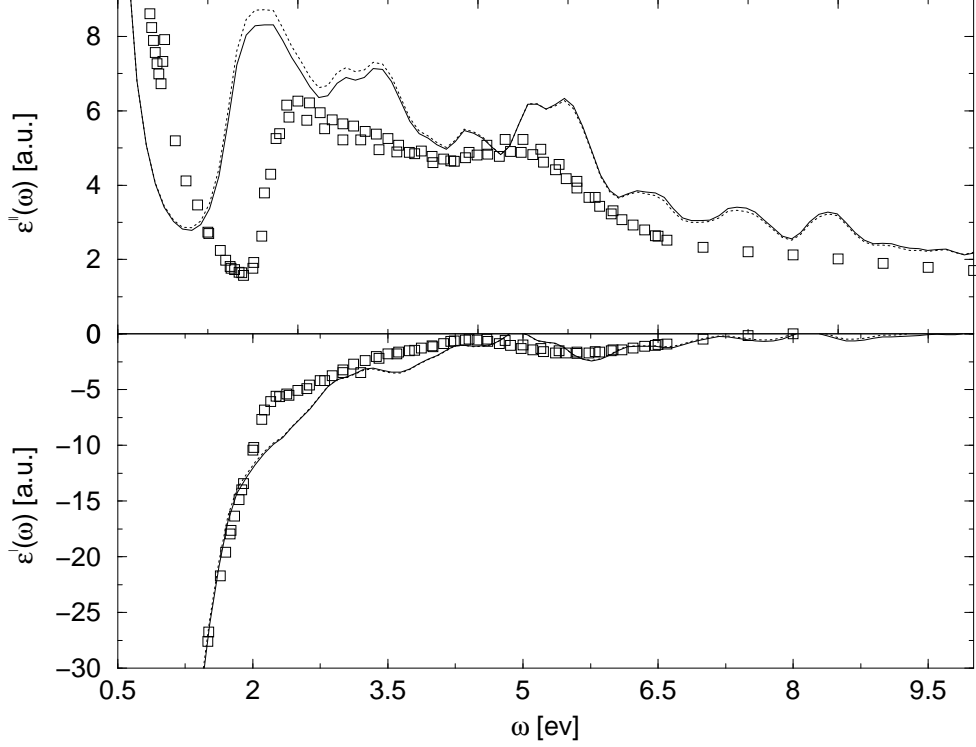


Figure 2.8: Real and imaginary part of  $\varepsilon_M(\omega)$  for bulk Cu with (full line) and without (dotted line) inclusion of Local-Field effects, compared with experimental data (squares) from Ref.[24]. Theoretical spectra are computed with  $N_k = 110$  (in the irreducible wedge of BZ), and a Lorentzian broadening of 0.4 eV (see text).

to the Fermi Surface (which, in the grid, coincides with one particular point  $\mathbf{k}_F$ ) where  $f_{n_F}(\mathbf{k} - \mathbf{q})(2 - f_{n_F}(\mathbf{k})) \neq 0$ . The oscillator strengths can be considered to be almost constant in the vicinity of the Fermi Surface. The same ansatz cannot be applied to  $\mathcal{G}_{he}^0(n_F, n_F, \mathbf{k}, \mathbf{q}, \omega)$ ; however we can use the property that near the Fermi surface the metallic band dispersion of copper is well approximated by a free-metal one, and make the following assumption for  $\chi_{\mathbf{G}\mathbf{G}'}^{intra}(\mathbf{q}, \omega)$ :

$$\chi_{\mathbf{G}\mathbf{G}'}^{intra}(\mathbf{q}, \omega) \approx \frac{1}{N_s} \left[ \sum_{\mathbf{R}} \langle n_F \mathbf{R} \mathbf{k}_F - \mathbf{q} | e^{-i(\mathbf{q} + \mathbf{G}) \cdot \mathbf{r}} | n_F \mathbf{R} \mathbf{k}_F \rangle \langle n_F \mathbf{R} \mathbf{k}_F | e^{i(\mathbf{q} + \mathbf{G}') \cdot \mathbf{r}'} | n_F \mathbf{R} \mathbf{k}_F - \mathbf{q} \rangle \right] \pi_0(\mathbf{q}, \omega), \quad (2.25)$$

where  $\mathbf{R}$  is one of the  $N_s$  symmetry operations not in the point group of  $\mathbf{k}_F$ .  $\pi_0(\mathbf{q}, \omega)$  is the non-interacting polarization calculated for a jellium model [29] with a density  $n_{el}$  yielding a classic plasma frequency  $\omega_p = \sqrt{4\pi n_{el}} = 9.27$  eV, corresponding to the value of  $\omega_D$  calculated in Section 2.4.1.

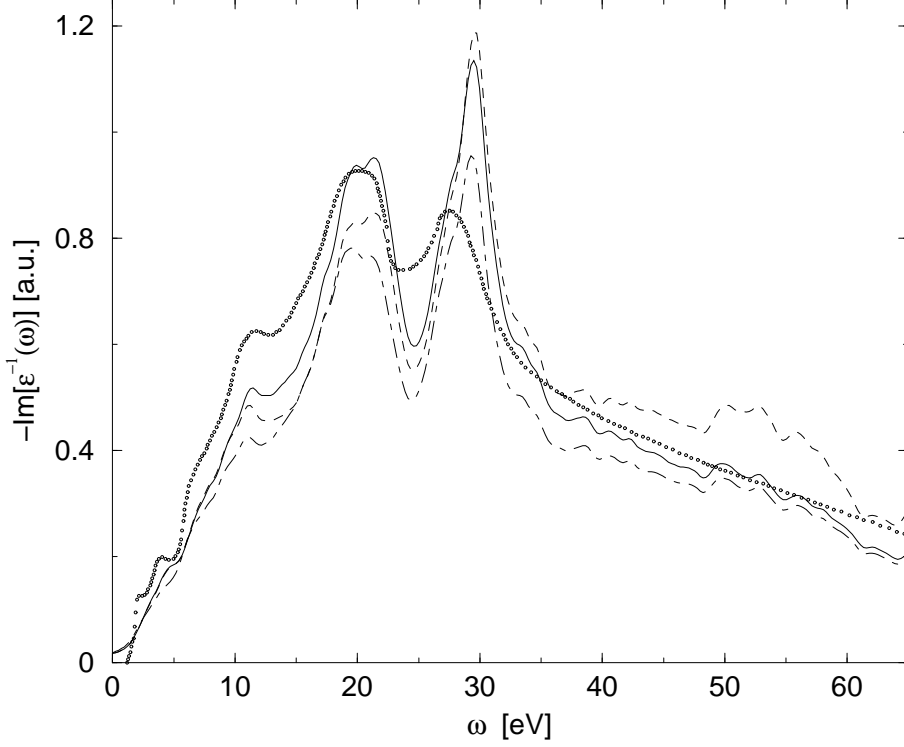


Figure 2.9: Imaginary part of the inverse macroscopic dielectric function of Cu including Local-Field effects and the Drude contribution (full line). Dashed line: results without Local-Field effects; Long-short dashes: with Local-Field effects, but without the Drude contribution. All theoretical spectra are computed with the same  $N_k$  of Fig. 2.8 but with a Lorentzian broadening of 0.9 eV. Points are the EELS data from Ref.[24].

$$\pi_0(\mathbf{q}, \omega) = -\frac{1}{2\pi^2|\mathbf{q}|} \int_0^{k_F^{jel}|\mathbf{q}|} dx x \left( \frac{1}{\omega - k_F^{jel}|\mathbf{q}| + i\eta} - \frac{1}{\omega - k_F^{jel}|\mathbf{q}| - i\eta} \right). \quad (2.26)$$

where

$$x = \frac{\omega}{k_F^{jel}|\mathbf{q}|}. \quad (2.27)$$

and

$$k_F^{jel} = (r\pi^2 n_{el})^{1/3}. \quad (2.28)$$

In Fig. 2.8 we compare our results for  $\varepsilon_M''(\omega)$  with and without Local Field Effects. The differences are small, consistent with the fact that, as expected, no large LFE are present in a metal. However Local Field effects are more important on the EELS spectrum, as shown in Fig. 2.9: in the high energy region the full inversion of  $\chi_{\mathbf{G}\mathbf{G}'}$  matrix corrects an overestimation of the intensity. The inclusion of

intraband transitions, on the other hand, turns out to be necessary not only to describe correctly the behavior of  $\varepsilon''$  at low frequencies, but also to improve the agreement of the calculated  $\varepsilon^{-1}(\omega)$  with the experimental EELS data (Fig. 2.9).



# Bibliography

- [1] R. Courths and S. Hufner, Phys. Rep. **112**, 53 (1984).
- [2] I. Campillo, A. Rubio and J.M. Pitarke, Phys. Rev. B **59**, 12188 (1999).
- [3] D. Vanderbilt, Phys. Rev. B **41**, 7892 (1990).
- [4] A. M. Rappe, K. M. Rabe, E. Kaxiras, and J.D. Joannopoulos, Phys. Rev. B **41**, 1227 (1990).
- [5] E.L. Shirley, D.C. Allan, R.M. Martin, and J. D. Joannopoulos, Phys. Rev. B **40**, 3652 (1989).
- [6] N. Troullier and J.L. Martins, Phys. Rev. B **43**, 1993 (1991).
- [7] G. Bachelet, D.R. Hamann and M. Schlüter Phys. Rev. B **26**, 4199 (1982).
- [8] D. R. Hamann, Phys. Rev. B **40**, 2980 (1989).
- [9] X. Gonze, P. Käckell, M. Scheffler, Phys. Rev. B **41**, 12264 (1990).
- [10] I. Kleinman and D. M. Bylander, Phys. Rev. Lett. **48**, 1425 (1982).
- [11] M. Meyer, G. Onida, M. Palummo and L. Reining, Phys. Rev. B. **64**, 045119 (2001).
- [12] S. G. Louie, S. Froyen and M. L. Cohen, Phys. Rev. B **26**, 1738 (1982).
- [13] M. Bockstedte, A. Kley, J. Neugebauer, M. Scheffler, Comput. Phys. Comm. **107**, 187 (1997).
- [14] M. Weinert and J. W. Davenport, Phys. Rev. B **45**, 13709 (1992).
- [15] R. Car and M. Parrinello, Phys. Rev. Lett. **55**, 2471 (1985).
- [16] D.M. Ceperley and B.I. Alder, Phys. Rev. Lett. **45**, 566 (1980).

- [17] J. P. Perdew and A. Zunger, Phys. Rev. B **23**, 5048 (1981).
- [18] L. Hedin and B. I. Lundqvist, J. Phys. C. **4**, 2064 (1971).
- [19] H. J. Monkhorst and J. D. Pack, Phys. Rev. B **13**, 5188 (1976).
- [20] R.W.G. Wyckoff, *Crystal Structure*, 2nd ed., Interscience, New York (1976).
- [21] However, as long as we are interested in bare LDA result, the overall effect on the 3d - 4s bandstructure and on the absorption spectrum is small and, *a posteriori*, we can simply use our “3d” PP.
- [22] R. O. Jones and O. Gunnarsson, Rev. Mod. Phys. **61**, 689 (1989).
- [23] S. Albrecht, L. Reining, G. Onida, V. Olevano and R. Del Sole, Phys. Rev. Lett. **83**, 3971 (1999).
- [24] E.D. Palik, *Handbook of Optical Constants of Solids* (Academic Press, New York, 1985).
- [25] R. Del Sole and R. Girlanda, Phys. Rev. B **48**, 11789 (1993).
- [26] M. S. Hybertsen and S. G. Louie, Phys. Rev. B **35**, 5585 (1987).
- [27] J. Read and R.J. Needs, Phys. Rev. B **44**, 13071 (1991).
- [28] H. Ehrenreich and H.R. Philipp, Phys. Rev. **128**, 1622 (1962).
- [29] R. D. Mattuck, *A guide to Feynman diagrams in the Many-Body problem*, McGraw-Hill, New York (1976) p. 196-200.

## Chapter 3

# Quasiparticle band structure of Copper in the $GW$ approximation

Experimental techniques for the determination of the electronic bandstructure of solids have made considerable progress in recent years [1]. From the theoretical point of view, state-of-the-art calculations within many-body perturbation theory, described in Section 1.3.1, allow to obtain band energies in a rigorous way, i.e. as the poles of the one-particle Green's function  $G$ . We have seen that, to obtain  $G$ , one needs the electron self-energy  $\Sigma$ , that here is evaluated according to the  $GW$  approximation, as derived by Hedin in 1965 [2], and introduced in Section 1.3.4. However, due to the high complexity and large computational requirements of ab-initio calculations of  $\Sigma$ , the experimental bandstructures are often compared with the results of (simpler) calculations performed within DFT-LDA. The consequences of this approach (which can be set on a firm ground by considering the exchange-correlation potential of the LDA or GGA as an approximation to the self-energy operator) must however be considered with great care, particularly when the system under study differs from those – semiconductors and insulators – for which the approximation is usually made. In the last chapter we have found large deviations between DFT-LDA and experimental bandstructure. This has been confirmed recently in Ref. [1], where the measured Cu bandstructure is compared with state-of-the-art DFT-GGA results: discrepancies between these data are found to be both large and dependent on the considered band and k-point. As a consequence of this result, the authors of Ref. [1] state that it is intriguing to find such pronounced “deviations from the band theory”, copper being much less correlated than metals with an open 3d shell (e.g., Ni).

In the present chapter, I demonstrate that copper does *not* deviate from quasi-

particle band theory. It only deviates from the simple “rigid shift” behavior of the self-energy commonly found in the case of semiconductors and insulators.

The chapter is organized as follows: after a short introduction in Section 3.1 three main sections will provide the necessary theoretical tools (Section 3.2), the numerical details (Section 3.3) and the results (Section 3.4).

## 3.1 Copper: a case study for noble metals

For semiconductors and insulators, the application of the  $GW$  method to computing self-energy corrections on top of ab-initio DFT results has become a quite well-established technique, giving energy levels generally in good agreement with experiments, even for complicated systems like reconstructed surfaces and clusters [3, 4]. The gaps between empty and filled states generally increase by a substantial amount with respect to those obtained in the Kohn-Sham (KS) formulation of DFT, reaching agreement with experimental results. The KS-DFT underestimation of the experimental gap is generally found to be weakly dependent on the particular band or k-point, although some semiconductor surface gaps show a stronger QP corrections than the bulk ones [5]. This is the basis for the introduction of the so-called “scissors operator”, often invoked in order to correct the discrepancies by rigidly shifting upwards the DFT empty bands, hence avoiding explicit self-energy calculations. *A priori*, there is no reason why the “scissors” approach should also work for metals, where no gap exists between filled and empty states.

Unlike semiconductors, the case of metals has received limited attention so far. The band width (i.e., the energy range of filled states) of simple metals has often been compared with that calculated for the homogeneous electron gas (jellium), finding discrepancies of a few tenths of eV [6]. On the other hand, the band structure of transition and noble metals cannot be approximated by that of jellium: valence electrons of d character play an important role both in the electronic structure and in the optical properties of these metals. Previous estimates of many-body corrections to the 3d Cu bandstructure, based on the self-energy of the homogeneous electron gas, yielded only partial agreement with the experimental data, suggesting that in the case of non-free electron metals screening effects (accounted for by the dielectric function) should be included in a more realistic way [7].

Among transition metals, full quasiparticle calculations have been carried out so far only for Ni [8], where  $GW$  yields a good description of photoemission data, except for the 6 eV satellite, which is due to strong short-range correlations within



the partially-filled d-shell. From the computational point of view, the very presence of strongly localized d-bands makes the ab-initio calculations based on plane waves (PW) and norm-conserving pseudopotentials (NCP) for noble metals much heavier than those for semiconductors.

Let us first recall the relations between Kohn-Sham eigenvalues, the poles of the one-particle Green's function  $G$ , and experimental band energies as measured in photoemission (PE) or inverse photoemission (IPE) (described in Chapter 1). In DFT, KS eigenvalues appear as Lagrange multipliers to ensure wavefunction orthonormality in the minimization of the energy functional. In contrast to the Hartree-Fock case, their values cannot be identified with electron addition or removal energies, since there is no equivalent of Koopman's theorem in DFT. Instead, the experimental bandstructure should be compared with the poles of the Green's Function  $G(\mathbf{r}, \mathbf{r}'; \omega)$ . Within many-body theory, the KS energies and wavefunctions  $\psi_{n\mathbf{k}}(\mathbf{r})$  are substituted with the quasiparticle one  $\epsilon_{n\mathbf{k}}^{QP}$  and  $\psi_{n\mathbf{k}}^{QP}(\mathbf{r})$  solution of

$$\left[ -\frac{\Delta_{\mathbf{r}}}{2} + V_{ext}(\mathbf{r}) + V_H(\mathbf{r}) \right] \psi_{n\mathbf{k}}^{QP}(\mathbf{r}, \omega) + \int d\mathbf{r}' \Sigma(\mathbf{r}, \mathbf{r}'; \omega) \psi_{n\mathbf{k}}^{QP}(\mathbf{r}', \omega) = E_{n\mathbf{k}}(\omega) \psi_{n\mathbf{k}}^{QP}(\mathbf{r}, \omega), \quad (3.1)$$

with  $E_{n\mathbf{k}}(\epsilon_{n\mathbf{k}}^{QP}) = \epsilon_{n\mathbf{k}}^{QP}$ . Eq. (3.1) contains the non-local, non-hermitian and frequency dependent self-energy operator  $\Sigma$

$$\Sigma(\mathbf{r}, \mathbf{r}', t) = \Sigma_x(\mathbf{r}, \mathbf{r}') + M(\mathbf{r}, \mathbf{r}', t), \quad (3.2)$$

$$\Sigma_x(\mathbf{r}, \mathbf{r}') = i\nu(\mathbf{r}, \mathbf{r}') G_0(\mathbf{r}, \mathbf{r}', t = 0^-), \quad (3.3)$$

$$M(\mathbf{r}, \mathbf{r}', t) = i\tilde{W}(\mathbf{r}, \mathbf{r}', t) G_0(\mathbf{r}, \mathbf{r}', t) = i \left[ \int d\mathbf{r}'' \nu(\mathbf{r}, \mathbf{r}'') \bar{\epsilon}^{-1}(\mathbf{r}', \mathbf{r}'', t) \right] G_0(\mathbf{r}, \mathbf{r}', t); \quad (3.4)$$

where  $\tilde{W}$  is not the full screening function but only its frequency dependent part

$$\tilde{W}(\mathbf{r}, \mathbf{r}', t) = \int d\mathbf{r}'' \nu(\mathbf{r}, \mathbf{r}'') \bar{\epsilon}^{-1}(\mathbf{r}', \mathbf{r}'', t). \quad (3.5)$$

Similarly for  $\bar{\epsilon}$

$$\bar{\epsilon}^{-1}(\mathbf{r}, \mathbf{r}', t) = \int d\mathbf{r}'' \nu(\mathbf{r}, \mathbf{r}'') \chi(\mathbf{r}'', \mathbf{r}', t). \quad (3.6)$$

with  $\chi(\mathbf{r}, \mathbf{r}', t)$  given in Eq. (2.5).

Eq. (3.1) is formally similar to the Kohn-Sham equations which are solved in the determination of the ground-state properties, but where the local and energy independent exchange-correlation potential  $V_{xc}(\mathbf{r})$  has been substituted by  $\Sigma$ . Hence,

KS eigenvalues can be considered as a zeroth-order approximation to the true QP energies, if the exchange-correlation (xc) potential of the DFT is seen as an approximation to the true self-energy operator  $\Sigma$ .

## 3.2 Theoretical framework

### 3.2.1 Exchange self energy

In order to solve Eq. (3.1) we need the matrix elements of the Mass operator and the exchange self-energy. If we expand the KS field operator in terms of Bloch functions  $\{\phi_{n\mathbf{k}}(\mathbf{r})\}$  (with  $\mathbf{k}$  restricted to the Brillouin zone (BZ) ) the Fourier transform of the Green's function  $G_0(\mathbf{r}_1, \mathbf{r}_2, t)$  is

$$G_0(\mathbf{r}_1, \mathbf{r}_2; \omega) = 2 \sum_n \sum_{\mathbf{k} \in BZ} \phi_{n\mathbf{k}}(\mathbf{r}_1) \phi_{n\mathbf{k}}^*(\mathbf{r}_2) \left[ \frac{f_{n\mathbf{k}}}{\omega - \epsilon_{n\mathbf{k}} - i\delta} + \frac{1 - f_{n\mathbf{k}}}{\omega - \epsilon_{n\mathbf{k}} + i\delta} \right] \quad (3.7)$$

where  $|f_{n\mathbf{k}}| \leq 1$  denoting the electronic occupation and  $\delta = 0^+$ . From Eq. (3.3),

$$\Sigma_x(\mathbf{r}_1, \mathbf{r}_2) = -\frac{1}{|\mathbf{r}_1 - \mathbf{r}_2|} \sum_{n_1} \sum_{\mathbf{k}_1 \in BZ} [\phi_{n_1\mathbf{k}_1}(\mathbf{r}_1) \phi_{n_1\mathbf{k}_1}^*(\mathbf{r}_2) f_{n_1\mathbf{k}_1}]. \quad (3.8)$$

Using the Fourier expansion of Coulomb potential

$$\frac{1}{|\mathbf{r}_1 - \mathbf{r}_2|} = \int_{BZ} \frac{d\mathbf{q}}{(2\pi)^3} \sum_{\mathbf{G}} e^{i(\mathbf{q}+\mathbf{G})\cdot(\mathbf{r}_1-\mathbf{r}_2)} \frac{4\pi}{|\mathbf{q} + \mathbf{G}|^2}, \quad (3.9)$$

(where  $\mathbf{G}$  represents a Reciprocal Lattice (RL) vector) we get

$$\begin{aligned} \langle n\mathbf{k} | \Sigma_x(\mathbf{r}_1, \mathbf{r}_2) | n'\mathbf{k}' \rangle &= \int d\mathbf{r}_1 d\mathbf{r}_2 \phi_{n\mathbf{k}}^*(\mathbf{r}_1) \Sigma_x(\mathbf{r}_1, \mathbf{r}_2) \phi_{n'\mathbf{k}'}(\mathbf{r}_2) \\ &= - \sum_{n_1} \sum_{\mathbf{k}_1 \in BZ} \int_{BZ} \frac{d\mathbf{q}}{(2\pi)^3} \sum_{\mathbf{G}} \frac{4\pi}{|\mathbf{q} + \mathbf{G}|^2} \\ &\quad \langle n\mathbf{k} | e^{i(\mathbf{q}+\mathbf{G})\cdot\mathbf{r}_1} | n_1\mathbf{k}_1 \rangle \langle n_1\mathbf{k}_1 | e^{-i(\mathbf{q}+\mathbf{G})\cdot\mathbf{r}_2} | n'\mathbf{k}' \rangle f_{n_1\mathbf{k}_1}; \end{aligned} \quad (3.10)$$

with

$$\langle n\mathbf{k} | e^{i(\mathbf{q}+\mathbf{G})\cdot\mathbf{r}_1} | n_1\mathbf{k}_1 \rangle = \int d\mathbf{r}_1 u_{n\mathbf{k}}^*(\mathbf{r}_1) u_{n_1\mathbf{k}_1}(\mathbf{r}_1) e^{i(\mathbf{k}_1 - \mathbf{k} + \mathbf{q} + \mathbf{G})\cdot\mathbf{r}_1}, \quad (3.11)$$

$$\langle n_1\mathbf{k}_1 | e^{-i(\mathbf{q}+\mathbf{G})\cdot\mathbf{r}_2} | n'\mathbf{k}' \rangle = \int d\mathbf{r}_2 u_{n_1\mathbf{k}_1}^*(\mathbf{r}_2) u_{n'\mathbf{k}'}(\mathbf{r}_2) e^{-i(\mathbf{k}_1 - \mathbf{k}' + \mathbf{q} + \mathbf{G})\cdot\mathbf{r}_2}. \quad (3.12)$$

where  $u_{n\mathbf{k}}(\mathbf{r})$  is the periodic part of the Bloch function. On changing the integration variable in Eq. (3.11) from  $\mathbf{r}$  to  $\mathbf{r} + \mathbf{R}$ ,  $\mathbf{R}$  being a vector of the direct lattice (DL), we get the conditions

$$\mathbf{k}_1 - \mathbf{k} + \mathbf{q} = \mathbf{G} \quad (3.13)$$

$$\mathbf{k}_1 - \mathbf{k}' + \mathbf{q} = \mathbf{G}' \quad (3.14)$$

from these two conditions it follows that

$$\mathbf{k} = \mathbf{k}' + \mathbf{G} - \mathbf{G}', \quad (3.15)$$

but if  $\mathbf{k}$  and  $\mathbf{k}'$  are inside the BZ we get

$$\mathbf{G} = \mathbf{G}' = \mathbf{G}_{kq} \equiv (\overline{\mathbf{k} - \mathbf{q}}) - (\mathbf{k} - \mathbf{q}). \quad (3.16)$$

where  $(\overline{\mathbf{k} - \mathbf{q}})$  is the vector  $(\mathbf{k} - \mathbf{q})$  translated into the BZ. Finally we obtain

$$\begin{aligned} & \langle n\mathbf{k} | \Sigma_x(\mathbf{r}_1, \mathbf{r}_2) | n'\mathbf{k} \rangle \\ &= - \sum_{n_1} \int_{BZ} \frac{d\mathbf{q}}{(2\pi)^3} \sum_{\mathbf{G}} \frac{4\pi}{|\mathbf{q} + \mathbf{G}|^2} \tilde{\rho}_{nn_1}(\mathbf{k}, \mathbf{q}, \mathbf{G}) [\tilde{\rho}_{n'n_1}(\mathbf{k}, \mathbf{q}, \mathbf{G})]^* f_{n_1(\mathbf{k}-\mathbf{q})}, \end{aligned} \quad (3.17)$$

with

$$\tilde{\rho}_{nn_1}(\mathbf{k}, \mathbf{q}, \mathbf{G}) = \int d\mathbf{r} u_{n\mathbf{k}}^*(\mathbf{r}) u_{n_1(\overline{\mathbf{k}-\mathbf{q}})}(\mathbf{r}) e^{i(\mathbf{G} + \mathbf{G}_{kq}) \cdot \mathbf{r}}. \quad (3.18)$$

### 3.2.2 The screening function

To obtain the matrix elements of the mass operator define in Eq. (3.4) we need the function  $\bar{\epsilon}^{-1}(1, 2)$  and the response function  $\chi(1, 2)$  that we expand in plane waves

$$\bar{\epsilon}^{-1}(\mathbf{r}_1, \mathbf{r}_2; t) = \int_{BZ} \frac{d\mathbf{q}}{(2\pi)^3} \sum_{\mathbf{G}, \mathbf{G}'} e^{i(\mathbf{q} + \mathbf{G}) \cdot \mathbf{r}_1} \bar{\epsilon}_{\mathbf{G}, \mathbf{G}'}^{-1}(\mathbf{q}, t) e^{-i(\mathbf{q} + \mathbf{G}') \cdot \mathbf{r}_2}, \quad (3.19)$$

$$\chi(\mathbf{r}_1, \mathbf{r}_2; t) = \int_{BZ} \frac{d\mathbf{q}}{(2\pi)^3} \sum_{\mathbf{G}, \mathbf{G}'} e^{i(\mathbf{q} + \mathbf{G}) \cdot \mathbf{r}_1} \chi_{\mathbf{G}, \mathbf{G}'}(\mathbf{q}, t) e^{-i(\mathbf{q} + \mathbf{G}') \cdot \mathbf{r}_2}. \quad (3.20)$$

The plane wave components of  $\chi(\mathbf{r}_1, \mathbf{r}_2; t)$  can be calculated with Eq. (1.151) that now has the form

$$\chi_{\mathbf{G}, \mathbf{G}'}(\mathbf{q}, \omega) = \chi_{\mathbf{G}, \mathbf{G}'}^0(\mathbf{q}, \omega) + \sum_{\mathbf{G}''} \chi_{\mathbf{G}, \mathbf{G}''}^0(\mathbf{q}, \omega) \frac{4\pi}{|\mathbf{q} + \mathbf{G}''|^2} \chi_{\mathbf{G}'', \mathbf{G}'}(\mathbf{q}, \omega), \quad (3.21)$$

where  $\chi_{\mathbf{G}, \mathbf{G}'}^0(\mathbf{q}, \omega)$  is

$$\begin{aligned} \chi_{\mathbf{G}, \mathbf{G}'}^0(\mathbf{q}, \omega) &= -i \int d\mathbf{r}_1 d\mathbf{r}_2 e^{i(\mathbf{q} + \mathbf{G}) \cdot \mathbf{r}_1} e^{-i(\mathbf{q} + \mathbf{G}') \cdot \mathbf{r}_2} \\ & \quad \left[ \int \frac{d\omega'}{2\pi} G_0(\mathbf{r}_1, \mathbf{r}_2; \omega') G_0(\mathbf{r}_2, \mathbf{r}_1; \omega' - \omega) \right] \\ &= 2 \sum_{nn'} \sum_{\mathbf{k} \in BZ} [\tilde{\rho}_{nn'}(\mathbf{k}, \mathbf{q}, \mathbf{G})]^* \tilde{\rho}_{nn'}(\mathbf{k}, \mathbf{q}, \mathbf{G}') \\ & \quad [f_{n'(\mathbf{k}-\mathbf{q})} (1 - f_{n\mathbf{k}})] \left[ \frac{1}{\omega - \epsilon_{n\mathbf{k}} + \epsilon_{n'(\mathbf{k}-\mathbf{q})} + i\delta} - \frac{1}{\omega - \epsilon_{n'(\mathbf{k}-\mathbf{q})} + \epsilon_{n\mathbf{k}} - i\delta} \right]. \end{aligned} \quad (3.22)$$

Note that  $\chi_{\mathbf{G},\mathbf{G}'}^0(\mathbf{q},\omega)$  is an odd function in  $\omega$  as a consequence of time-reversal symmetry and in the  $\mathbf{q} \rightarrow \mathbf{0}$  limit both intraband and interband transitions are included following the method discussed in Section 2.4.1. Inverting Eq. (3.21),  $\chi_{\mathbf{G},\mathbf{G}'}(\mathbf{q},\omega)$  is used to construct  $\bar{\epsilon}_{\mathbf{G},\mathbf{G}'}^{-1}(\mathbf{q},\omega)$

$$\bar{\epsilon}_{\mathbf{G},\mathbf{G}'}^{-1}(\mathbf{q},\omega) = \frac{4\pi}{|\mathbf{q} + \mathbf{G}|^2} \chi_{\mathbf{G},\mathbf{G}'}(\mathbf{q},\omega), \quad (3.23)$$

but we introduce a more symmetric definition

$$\tilde{\epsilon}_{\mathbf{G},\mathbf{G}'}^{-1}(\mathbf{q},\omega) = \frac{4\pi}{|\mathbf{q} + \mathbf{G}||\mathbf{q} + \mathbf{G}'|} \chi_{\mathbf{G},\mathbf{G}'}(\mathbf{q},\omega) = \frac{|\mathbf{q} + \mathbf{G}|}{|\mathbf{q} + \mathbf{G}'|} \bar{\epsilon}_{\mathbf{G},\mathbf{G}'}^{-1}(\mathbf{q},\omega), \quad (3.24)$$

so that the square bracketed term in Eq. (3.4) is

$$\begin{aligned} & \left[ \int d3\nu(1,3) \tilde{\epsilon}^{-1}(2,3) \right] \\ &= \int_{BZ} \frac{d\mathbf{q}}{(2\pi)^3} \sum_{\mathbf{G},\mathbf{G}'} e^{i(\mathbf{q}+\mathbf{G})\cdot\mathbf{r}_1} \tilde{\epsilon}_{\mathbf{G},\mathbf{G}'}^{-1}(\mathbf{q},t_1-t_2) \frac{4\pi}{|\mathbf{q} + \mathbf{G}||\mathbf{q} + \mathbf{G}'|} e^{-i(\mathbf{q}+\mathbf{G}')\cdot\mathbf{r}_2}. \end{aligned} \quad (3.25)$$

The last step is the convolution of Eq. (3.25) with the KS Green's function  $G_0(1,2)$

$$\begin{aligned} & \langle n\mathbf{k} | M(\mathbf{r}_1, \mathbf{r}_2, \omega) | n'\mathbf{k}' \rangle \\ &= i \sum_{n_1} \int_{BZ} \frac{d\mathbf{q}}{(2\pi)^3} \left\{ \sum_{\mathbf{G},\mathbf{G}'} \frac{4\pi}{|\mathbf{q} + \mathbf{G}'|^2} \tilde{\rho}_{nn_1}(\mathbf{k}, \mathbf{q}, \mathbf{G}) [\tilde{\rho}_{n'n_1}(\mathbf{k}, \mathbf{q}, \mathbf{G}')]^* \right. \\ & \left. \int \frac{d\omega'}{2\pi} \tilde{\epsilon}_{\mathbf{G},\mathbf{G}'}^{-1}(\mathbf{q}, \omega') \left[ \frac{f_{n_1(\mathbf{k}-\mathbf{q})}}{\omega - \omega' - \epsilon_{n_1(\mathbf{k}-\mathbf{q})} - i\delta} + \frac{1 - f_{n_1(\mathbf{k}-\mathbf{q})}}{\omega - \omega' - \epsilon_{n_1(\mathbf{k}-\mathbf{q})} + i\delta} \right] \right\}. \end{aligned} \quad (3.26)$$

To evaluate the frequency integral we must investigate deeper the analytic properties of the Lehman representation of  $\tilde{\epsilon}_{\mathbf{G},\mathbf{G}'}^{-1}(\mathbf{q},\omega)$ ,

$$\tilde{\epsilon}_{\mathbf{G},\mathbf{G}'}^{-1}(\mathbf{q},\omega) = \sum_I \left[ \frac{R_I^{(+)}(\mathbf{q}, \mathbf{G}, \mathbf{G}')}{\omega - E_I^N + i\delta} - \frac{R_I^{(-)}(\mathbf{q}, \mathbf{G}, \mathbf{G}')}{\omega + E_I^N - i\delta} \right], \quad (3.27)$$

with

$$R_I^{(+)}(\mathbf{q}, \mathbf{G}, \mathbf{G}') = \int d\mathbf{r} d\mathbf{r}' e^{i(\mathbf{q}+\mathbf{G})\cdot\mathbf{r}} i \langle \Psi_N | \hat{\rho}(\mathbf{r}) | \Psi_N^I \rangle \langle \Psi_N^I | \hat{\rho}(\mathbf{r}') | \Psi_N \rangle e^{-i(\mathbf{q}+\mathbf{G}')\cdot\mathbf{r}'}, \quad (3.28)$$

$$R_I^{(-)}(\mathbf{q}, \mathbf{G}, \mathbf{G}') = \int d\mathbf{r} d\mathbf{r}' e^{i(\mathbf{q}+\mathbf{G})\cdot\mathbf{r}} i \langle \Psi_N | \hat{\rho}(\mathbf{r}') | \Psi_N^I \rangle \langle \Psi_N^I | \hat{\rho}(\mathbf{r}) | \Psi_N \rangle e^{-i(\mathbf{q}+\mathbf{G}')\cdot\mathbf{r}'}. \quad (3.29)$$

where  $|\Psi_N^I\rangle$  is the N-electrons interacting excited states with energy  $E_I^N$ . Now  $\chi_{\mathbf{G},\mathbf{G}'}^0(\mathbf{q},\omega)$  is an odd function of  $\omega$ , and from Eq. (3.21) it follows that  $\chi_{\mathbf{G},\mathbf{G}'}(\mathbf{q},\omega)$  (and hence  $\tilde{\epsilon}_{\mathbf{G},\mathbf{G}'}^{-1}(\mathbf{q},\omega)$ ) has the same property; so we get

$$R_I^{(+)}(\mathbf{q}, \mathbf{G}, \mathbf{G}') = R_I^{(-)}(\mathbf{q}, \mathbf{G}, \mathbf{G}') \equiv R_I(\mathbf{q}, \mathbf{G}, \mathbf{G}'). \quad (3.30)$$

Moreover, as consequence of the spatial inversion symmetry it follows

$$R_I(\mathbf{q}, \mathbf{G}, \mathbf{G}') = [R_I(\mathbf{q}, \mathbf{G}, \mathbf{G}')]^*. \quad (3.31)$$

The residues of Eq. (3.27) of  $\tilde{\epsilon}_{\mathbf{G}, \mathbf{G}'}^{-1}(\mathbf{q}, \omega)$  are real, thus

$$\tilde{\epsilon}_{\mathbf{G}, \mathbf{G}'}^{-1}(\mathbf{q}, \omega) = -\frac{1}{\pi} \int_0^\infty d\omega' \left[ \frac{\Im[\tilde{\epsilon}_{\mathbf{G}, \mathbf{G}'}^{-1}(\mathbf{q}, \omega)]}{\omega - \omega' + i\delta} - \frac{\Im[\tilde{\epsilon}_{\mathbf{G}, \mathbf{G}'}^{-1}(\mathbf{q}, \omega)]}{\omega + \omega' - i\delta} \right]. \quad (3.32)$$

Eq.(3.32) states that for systems with time and spatial inversion symmetry the “ $\delta$ -like” part of  $\tilde{\epsilon}$  coincides with its imaginary part. Finally from Eq.(3.32) and Eq. (3.26) we obtain

$$\begin{aligned} \langle n\mathbf{k} | M(\mathbf{r}_1, \mathbf{r}_2, \omega) | n'\mathbf{k}' \rangle = & - \sum_{n_1} \int_{BZ} \frac{d\mathbf{q}}{(2\pi)^3} \left[ \int_{-\infty}^\infty d\omega' \frac{\Gamma_h(nn_1n', \mathbf{k} - \mathbf{q}, \omega')}{\omega - \omega' - \epsilon_{n_1(\mathbf{k}-\mathbf{q})} + i\delta} \right. \\ & \left. + \int_{-\infty}^\infty d\omega' \frac{\Gamma_e(nn_1n', \mathbf{k} - \mathbf{q}, \omega')}{\omega - \omega' - \epsilon_{n_1(\mathbf{k}-\mathbf{q})} - i\delta} \right]; \end{aligned} \quad (3.33)$$

with

$$\begin{aligned} \Gamma_h(nn_1n', \mathbf{k} - \mathbf{q}, \omega') = & 2 \sum_{\mathbf{G}, \mathbf{G}'} \tilde{\rho}_{nn_1}(\mathbf{k}, \mathbf{q}, \mathbf{G}) [\tilde{\rho}_{n'n_1}(\mathbf{k}, \mathbf{q}, \mathbf{G}')]^* \\ & \frac{2f_{n_1(\mathbf{k}-\mathbf{q})}}{|\mathbf{q} + \mathbf{G}| |\mathbf{q} + \mathbf{G}'|} \Im[\tilde{\epsilon}_{\mathbf{G}, \mathbf{G}'}^{-1}(\mathbf{q}, \omega)] \theta(\omega), \end{aligned} \quad (3.34)$$

$$\begin{aligned} \Gamma_e(nn_1n', \mathbf{k} - \mathbf{q}, \omega') = & 2 \sum_{\mathbf{G}, \mathbf{G}'} \tilde{\rho}_{nn_1}(\mathbf{k}, \mathbf{q}, \mathbf{G}) [\tilde{\rho}_{n'n_1}(\mathbf{k}, \mathbf{q}, \mathbf{G}')]^* \\ & \frac{2(1 - f_{n_1(\mathbf{k}-\mathbf{q})})}{|\mathbf{q} + \mathbf{G}| |\mathbf{q} + \mathbf{G}'|} \Im[\tilde{\epsilon}_{\mathbf{G}, \mathbf{G}'}^{-1}(\mathbf{q}, \omega)] \theta(-\omega). \end{aligned} \quad (3.35)$$

$\Gamma_{e/h}(\omega)$  are functions with a well defined energy range  $\{-\Omega_{max}, \Omega_{max}\}$ :

$$\Omega_{max} \equiv Max\{\epsilon_{n\mathbf{k}} - \epsilon_{n_1(\mathbf{k}-\mathbf{q})}\} \quad \forall n, n', \mathbf{k}, \mathbf{q} \quad \text{with } f_{n\mathbf{k}}(1 - f_{n_1(\mathbf{k}-\mathbf{q})}) \neq 0. \quad (3.36)$$

However, for systems without spatial inversion symmetry  $\Gamma_{e/h}(\omega)$  could have high energy tails, requiring a more careful integration of Eq. (3.32).

### 3.3 Numerical details

Our bandstructure calculation starts with a DFT-LDA calculation of the ground-state properties, performed using norm-conserving pseudopotentials (PPs) and a plane waves basis. As shown in Chapter 2, the use of soft (Martins-Troullier [9])

PPs allows us to work at full convergence with a reasonable kinetic energy cutoff, i.e., 60 Rydbergs if the 3s and 3p atomic states are frozen into the core, 160 Rydbergs when they are explicitly included into the valence.

Most *GW* calculations on semiconductor systems use a Plasmon-Pole Approximation (PPA) for  $W(\omega)$  [10], based on the observation that the Fourier components  $\epsilon_{\mathbf{G},\mathbf{G}'}^{-1}(\mathbf{q};\omega)$  of the inverse dielectric function are generally peaked functions of  $\omega$ , and can be approximated by a single pole. Since the evaluation of  $\Sigma_c$  involves an integration over the energy, the fine details of the  $\omega$ -dependence are not critical, and the PPA turns out to work reasonably well for most applications. However, in the case of Cu the use of a PPA becomes more critical. The presence of flat d-bands 2 eV below the Fermi level implies the presence of strong transitions in  $\epsilon_{\mathbf{G},\mathbf{G}'}^{-1}(\mathbf{q};\omega)$  spread over a large energy range. For small values of  $\mathbf{G}$  and  $\mathbf{G}'$ , the behavior of  $\epsilon_{\mathbf{G},\mathbf{G}'}^{-1}(\mathbf{q};\omega)$  is often very different from that of a single-pole function, leading to instabilities when determining the Plasmon-Pole parameters. More precisely the PPA, for any  $(\mathbf{G}, \mathbf{G}', \mathbf{q})$  component of  $\bar{\epsilon}^{-1}$ , reproduces the real part of the matrix at two frequencies. The higher frequency is chosen in order to reproduce correctly the energy tail of  $\epsilon^{-1}(\omega)$ , and consequently of  $W(\omega)$ . The other frequency, however, is chosen at the origin whereby the presence of flat d-bands a few eV below the Fermi level induces large values in  $\epsilon_{\mathbf{G},\mathbf{G}'}^{-1}(\mathbf{q};0)$ . As a consequence, the plasma resonance obtained within the PPA can be found below the total band width energy ( $\sim 10$  eV). In these cases the self-energy is no longer well defined for all the energies because some of its (isolated) poles fall within the band width.

Hence, I have found it more convenient to avoid the PPA. Instead,  $\epsilon_{\mathbf{G},\mathbf{G}'}^{-1}(\mathbf{q};\omega)$  is explicitly computed over a grid of about 200 frequencies from zero to  $\sim 130$  eV and the energy integral is numerically performed. Another characteristic of metallic systems which leads to additional difficulties in practical *GW* calculations is the discontinuity of the band occupation crossing the Fermi surface. This problem already shows up in the evaluation of the bare exchange matrix elements that we will face in the next section.

Performing a full screening calculation also the imaginary part of  $\Sigma$  will be accessible. Further evidence of the limitations imposed by the PPA in the case of Cu will be the role played by the imaginary part of the renormalization factors in the quasiparticle energies.

### 3.3.1 Exchange self-energy: Fermi surface effects

Among all the numerical parameters one of the most important is the  $\mathbf{k}$ -point and the corresponding  $\mathbf{q}$ -point grid; we have left the  $\mathbf{q}$ -space integral in Eq. (3.17)

$$\begin{aligned} \langle n\mathbf{k} | \Sigma_x(\mathbf{r}_1, \mathbf{r}_2) | n'\mathbf{k} \rangle = \\ - \sum_{n_1} \int_{BZ} \frac{d\mathbf{q}}{(2\pi)^3} \sum_{\mathbf{G}} \frac{4\pi}{|\mathbf{q} + \mathbf{G}|^2} \tilde{\rho}_{nn_1}(\mathbf{k}, \mathbf{q}, \mathbf{G}) [\tilde{\rho}_{n'n_1}(\mathbf{k}, \mathbf{q}, \mathbf{G})]^* f_{n_1(\mathbf{k}-\mathbf{q})}, \end{aligned} \quad (3.37)$$

because the approximation of the integral with a  $\mathbf{q}$ -point grid is based on the fundamental “ansatz” that the integrated function is constant in a region of the BZ centered around each  $\mathbf{q}$ -point (that we indicate as  $\{\mathbf{q}_i\}$  for  $i = 1 \dots N_q$ ) of volume  $(2\pi)^3 / (N_q \Omega)$

$$\begin{aligned} \langle n\mathbf{k} | \Sigma_x(\mathbf{r}_1, \mathbf{r}_2) | n'\mathbf{k} \rangle \\ \approx - \sum_{n_1} \frac{(2\pi)^3}{N_q \Omega} \sum_{\mathbf{q}_i} \sum_{\mathbf{G}} \frac{4\pi}{|\mathbf{q}_i + \mathbf{G}|^2} \tilde{\rho}_{nn_1}(\mathbf{k}, \mathbf{q}_i, \mathbf{G}) [\tilde{\rho}_{n'n_1}(\mathbf{k}, \mathbf{q}_i, \mathbf{G})]^* f_{n_1(\mathbf{k}-\mathbf{q}_i)}. \end{aligned} \quad (3.38)$$

Unfortunately, in metallic systems like Cu, this ansatz is not correct for the discontinuity of  $f_{n_1(\mathbf{k}-\mathbf{q}_i)}$  induced by the Fermi surface. This “Fermi Surface effect” can be understood with a simple two-dimensional example: in Fig. 3.1 the upper-right quadrant of a square BZ is shown together with two different uniform sets of  $\mathbf{k}$ -points (indicated by full and empty circles). The uniformity of the two grids allows us to divide the BZ in regions, called  $R_{\mathbf{k}_i}$ , centered around each  $\mathbf{k}$ -point, that cover the whole BZ without overlapping; the thick (thin) lines enclose the regions related to empty (full) circles grid. A spherical Fermi line is introduced and the dark gray region is the approximated Fermi Surface defined by

$$f_{n\mathbf{k}} = f_{n\mathbf{k}_i} \neq 0 \quad \text{for } \mathbf{k} \in R_{\mathbf{k}_i} \quad (3.39)$$

for the larger  $\mathbf{k}$ -points set while the light gray region joined with the dark one is relative to the smaller set. We see immediately that a large difference in the definition of the Fermi Surface (the Fermi volume in the three-dimensional case) is introduced and, as we will see, this corresponds to a large numerical error in the matrix elements of the exchange self-energy near the Fermi level.

To avoid this numerical error we rewrite Eq. (3.38) as

$$\begin{aligned} \langle n\mathbf{k} | \Sigma_x(\mathbf{r}_1, \mathbf{r}_2) | n'\mathbf{k} \rangle \approx - \sum_{n_1} \sum_{\mathbf{q}_i} \sum_{\mathbf{G}} \left\{ \tilde{\rho}_{nn_1}(\mathbf{k}, \mathbf{q}_i, \mathbf{G}) [\tilde{\rho}_{n'n_1}(\mathbf{k}, \mathbf{q}_i, \mathbf{G})]^* \right. \\ \left. \left[ \int_{BZ'(\mathbf{q}_i)} \frac{d\mathbf{q}}{(2\pi)^3} f_{n_1(\mathbf{k}-\mathbf{q})} \frac{4\pi}{|\mathbf{q} + \mathbf{G}|^2} \right] \right\}. \end{aligned} \quad (3.40)$$

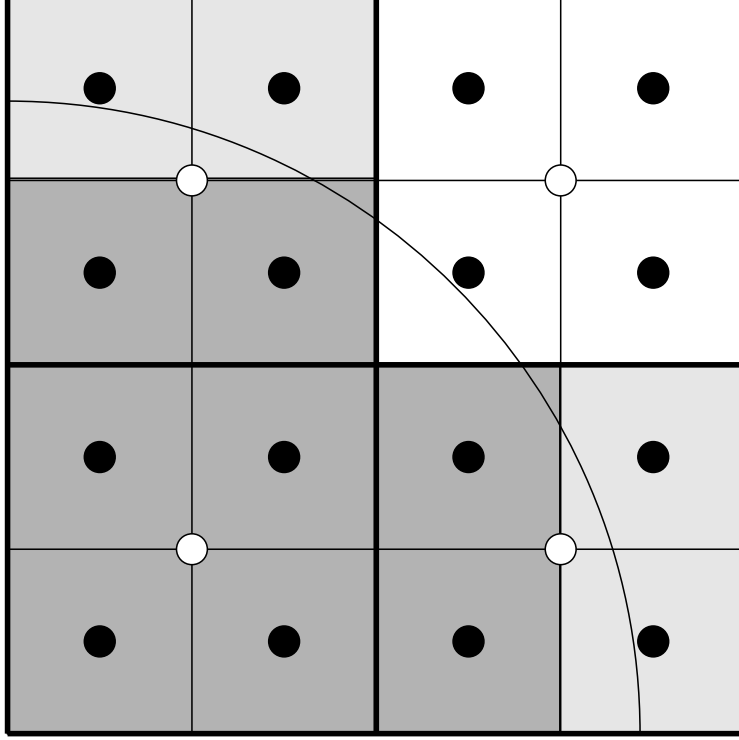


Figure 3.1: Fermi Surface effects due to the discretization of the RL space integration, as explained in the text.

The ansatz about the continuity of the integrated function of Eq. (3.37) is restricted here only to the  $\tilde{\rho}_{nn'}$  factors, while for the occupation numbers and for the Fourier components of the Coulomb interaction, the integration over the  $\mathbf{q}$ -space is divided into  $N_q$  integrations in the regions named  $BZ'(\mathbf{q}_i)$ . These regions must be carefully defined so to cover the BZ without overlapping; a simple procedure can be carried out in the case of a uniform  $\mathbf{q}$ -grid where the grid is itself a Bravais lattice and the  $BZ'(\mathbf{q}_i)$  are the Brillouin Zones of this *small* lattice.

Numerically we define the integrals

$$\begin{aligned}
 B_e(n_1, \mathbf{k}, \mathbf{q}_i, \mathbf{G}, \mathbf{G}') &= \int_{BZ'(\mathbf{q}_i)} \frac{d\mathbf{q}}{(2\pi)^3} f_{n_1(\mathbf{k}-\mathbf{q})} \frac{1}{|\mathbf{q}_i + \mathbf{G}| |\mathbf{q}_i + \mathbf{G}'|} \\
 &= \int_{BZ'(\Gamma)} \frac{d\mathbf{q}}{(2\pi)^3} f_{n_1(\mathbf{k}-\mathbf{q}-\mathbf{q}_i)} \frac{1}{|\mathbf{q} + \mathbf{q}_i + \mathbf{G}| |\mathbf{q} + \mathbf{q}_i + \mathbf{G}'|}, \quad (3.41)
 \end{aligned}$$

which we calculate by generating  $N_r$  random  $\mathbf{q}$ -points  $\{\mathbf{Q}_j\}$  inside the *small* Brillouin Zone  $BZ'(\Gamma)$  centered around  $\mathbf{q} = \mathbf{0}$

$$B_e(n_1, \mathbf{k}, \mathbf{q}_i, \mathbf{G}, \mathbf{G}') \approx \frac{(2\pi)^3}{N_q \Omega N_r} \sum_{j=1 \dots N_r} f_{n_1(\mathbf{k}-\mathbf{Q}_j-\mathbf{q}_i)} \frac{1}{|\mathbf{Q}_j + \mathbf{q}_i + \mathbf{G}| |\mathbf{Q}_j + \mathbf{q}_i + \mathbf{G}'|}. \quad (3.42)$$



The  $f_{n_1(\mathbf{k}-\mathbf{Q}_j-\mathbf{q}_i)}$  are fitted with the occupation numbers of a set of 13,050 random  $\mathbf{k}$ -points chosen near the Fermi surface whose energies were calculated within DFT-LDA.

We have found that convergence in the matrix elements of  $\hat{\Sigma}_x$  is reached using  $10^6$  random  $\mathbf{q}$ -points in Eq. (3.42) and a numerical lighter version of Eq. (3.40),

$$\begin{aligned} & \langle n\mathbf{k} | \Sigma_x(\mathbf{r}_1, \mathbf{r}_2) | n'\mathbf{k} \rangle \\ & \approx - (2\pi) \sum_{n_1} \sum_{\mathbf{q}_i} \tilde{\rho}_{nn_1}(\mathbf{k}, \mathbf{q}_i, \mathbf{G}) [\tilde{\rho}_{n'n_1}(\mathbf{k}, \mathbf{q}_i, \mathbf{G})]^* B_e(n_1, \mathbf{k}, \mathbf{q}_i, \mathbf{0}, \mathbf{0}) \\ & + \sum_{n_1} \frac{(2\pi)^3}{N_q \Omega} \sum_{\mathbf{q}_i} \sum_{\mathbf{G} \neq \mathbf{0}} \tilde{\rho}_{nn_1}(\mathbf{k}, \mathbf{q}_i, \mathbf{G}) [\tilde{\rho}_{n'n_1}(\mathbf{k}, \mathbf{q}_i, \mathbf{G})]^* \frac{4\pi N_e(n_1, \mathbf{k}, \mathbf{q}_i)}{|\mathbf{q} + \mathbf{G}|^2}, \end{aligned} \quad (3.43)$$

where the time-consuming calculation of Eq. (3.42) is restricted to  $\mathbf{G} = \mathbf{G}' = \mathbf{0}$  and a new function  $N_e(n_1, \mathbf{k}, \mathbf{q}_i)$  is introduced,

$$N_e(n_1, \mathbf{k}, \mathbf{q}_i) = \frac{(2\pi)^3}{N_q \Omega N_r} \sum_{j=1 \dots N_r} f_{n_1(\mathbf{k}-\mathbf{Q}_j-\mathbf{q}_i)}. \quad (3.44)$$

In the following we will refer to Eq. (3.43) as the ‘‘Random Integration Method’’ (RIM).

	without RIM		with RIM	
Point	19 $\{\mathbf{q}_i\}$	44 $\{\mathbf{q}_i\}$	19 $\{\mathbf{q}_i\}$	44 $\{\mathbf{q}_i\}$
$X_1$	-23.17	-23.27	-25.26	-25.34
$X_3$	-25.10	-25.26	-26.63	-26.69
$X_2$	-25.13	-25.05	-28.07	-28.15
$X_5$	-25.44	-25.50	-27.37	-27.39
$X_4$	-8.31	-8.58	-9.59	-9.65

Table 3.1: Comparison of diagonal matrix elements of  $\hat{\Sigma}_x$  at the X point for the first 5 bands (the fifth is a metallic band). The first two columns use Eq. (3.38) with 19 and 44  $\mathbf{q}$ -points respectively, while the last two columns use Eq. (3.43). In the case of Eq. (3.38) a spherical region around  $\mathbf{q} = \mathbf{0}$  is used to avoid the singularity of the Coulomb potential.

To test this procedure we have used two sets of Monkhorst-Pack [11]  $\mathbf{k}$ -points : 10 and 28 points in the irreducible wedge of Brillouin zone (IBZ). Each set corresponds to a  $\mathbf{q}$ -point grid constructed by all the possible differences of  $\mathbf{k}$ -points, namely 19 points for the first set and 44 for the second set. Both  $\mathbf{q}$ -point grids are of BCC Bravais lattice type so the regions  $BZ'(\mathbf{q}_i)$  differ only in volume. The number of  $\mathbf{G}$  vectors included are 1395 while the wave functions of Cu contain a maximum of

600 plane-waves. In Table 3.1 the values of  $\langle n\mathbf{k}|\hat{\Sigma}_x(\mathbf{r}_1, \mathbf{r}_2)|n\mathbf{k}\rangle$  at the X  $\mathbf{k}$ -point for the first five bands are reported both with and without the RIM. From the comparison of the two methods two conclusions can be drawn:(a) using the RIM the discrepancy between the matrix element of  $\hat{\Sigma}_x$  for the sixth band  $X_4$  calculated with the two sets of  $\mathbf{q}$ -points decreases considerably, (b) the overall intensity of the matrix elements decreases. While the first point occurs as a direct consequence of the correct inclusion of the Fermi surface discontinuity the latter depends on the integration of the Coulomb potential inside the regions  $BZ'(\mathbf{q}_i)$ . Finally, we can affirm that with the random integration method the matrix elements of  $\hat{\Sigma}_x$  are well converged with 19  $\mathbf{q}$ -points in the IBZ.

The same method used for  $\hat{\Sigma}_x$  must be extended to the matrix elements of the mass operator; Eqs. (3.33), (3.34) and (3.35) are replaced with

$$\langle n\mathbf{k}|M(\mathbf{r}_1, \mathbf{r}_2, \omega)|n'\mathbf{k}\rangle = -\sum_{n_1} \sum_{\mathbf{q}_i} \left[ \int_{-\infty}^{\infty} d\omega' \frac{\Gamma_h(nn_1n', \mathbf{k} - \mathbf{q}_i, \omega')}{\omega - \omega' - \epsilon_{n_1(\mathbf{k}-\mathbf{q}_i)} + i\delta} + \int_{-\infty}^{\infty} d\omega' \frac{\Gamma_e(nn_1n', \mathbf{k} - \mathbf{q}_i, \omega')}{\omega - \omega' - \epsilon_{n_1(\mathbf{k}-\mathbf{q}_i)} - i\delta} \right], \quad (3.45)$$

with

$$\begin{aligned} & \Gamma_h(nn_1n', \mathbf{k} - \mathbf{q}_i, \omega') \\ &= 2\tilde{\rho}_{nn_1}(\mathbf{k}, \mathbf{q}, \mathbf{0}) [\tilde{\rho}_{n'n_1}(\mathbf{k}, \mathbf{q}, \mathbf{0})]^* B_h(n_1, \mathbf{k}, \mathbf{q}_i, \mathbf{0}, \mathbf{0}) \Im [\tilde{\epsilon}_{\mathbf{G}, \mathbf{G}'}^{-1}(\mathbf{q}, \omega)] \theta(\omega) \\ +2 & \sum_{\mathbf{G} \neq \mathbf{0}, \mathbf{G}' \neq \mathbf{0}} \tilde{\rho}_{nn_1}(\mathbf{k}, \mathbf{q}, \mathbf{G}) [\tilde{\rho}_{n'n_1}(\mathbf{k}, \mathbf{q}, \mathbf{G}')]^* \frac{4\pi N_h(n_1, \mathbf{k}, \mathbf{q}_i)}{|\mathbf{q} + \mathbf{G}|^2} \Im [\tilde{\epsilon}_{\mathbf{G}, \mathbf{G}'}^{-1}(\mathbf{q}, \omega)] \theta(\omega), \end{aligned} \quad (3.46)$$

$$\begin{aligned} & \Gamma_e(nn_1n', \mathbf{k} - \mathbf{q}_i, \omega') \\ &= 2\tilde{\rho}_{nn_1}(\mathbf{k}, \mathbf{q}, \mathbf{0}) [\tilde{\rho}_{n'n_1}(\mathbf{k}, \mathbf{q}, \mathbf{0})]^* B_e(n_1, \mathbf{k}, \mathbf{q}_i, \mathbf{0}, \mathbf{0}) \Im [\tilde{\epsilon}_{\mathbf{G}, \mathbf{G}'}^{-1}(\mathbf{q}, \omega)] \theta(-\omega) \\ +2 & \sum_{\mathbf{G} \neq \mathbf{0}, \mathbf{G}' \neq \mathbf{0}} \tilde{\rho}_{nn_1}(\mathbf{k}, \mathbf{q}, \mathbf{G}) [\tilde{\rho}_{n'n_1}(\mathbf{k}, \mathbf{q}, \mathbf{G}')]^* \frac{4\pi N_e(n_1, \mathbf{k}, \mathbf{q}_i)}{|\mathbf{q} + \mathbf{G}|^2} \Im [\tilde{\epsilon}_{\mathbf{G}, \mathbf{G}'}^{-1}(\mathbf{q}, \omega)] \theta(-\omega). \end{aligned} \quad (3.47)$$

Two new quantities were introduced

$$B_h(n_1, \mathbf{k}, \mathbf{q}_i, \mathbf{G}, \mathbf{G}') \approx \frac{(2\pi)^3}{N_q \Omega N_r} \sum_{j=1 \dots N_r} \left( 1 - f_{n_1(\mathbf{k}-\mathbf{q}_j-\mathbf{q}_i)} \right) \frac{4\pi}{|\mathbf{Q}_j + \mathbf{q}_i + \mathbf{G}| |\mathbf{Q}_j + \mathbf{q}_i + \mathbf{G}'|}, \quad (3.48)$$

$$N_h(n_1, \mathbf{k}, \mathbf{q}_i) = \frac{(2\pi)^3}{N_q \Omega N_r} \sum_{j=1 \dots N_r} \left(1 - f_{n_1}(\mathbf{k} - \mathbf{Q}_j - \mathbf{q}_i)\right). \quad (3.49)$$

An approach similar to the RIM introduced so far has been used by Pulci [5] to improve the  $\mathbf{q}$ -grid convergence of  $\langle \Sigma_x \rangle$  for *GW* calculations of surface bands corrections. The present treatment, however, also solves the discontinuity induced by the metallic Fermi surface.

### 3.3.2 Matrix elements of the mass operator

#### Convergence tests

Using the  $\mathbf{q}$ -grid chosen for the  $\hat{\Sigma}_x$  matrix elements in Section 3.3.1, other numerical parameters must be set for the matrix elements of mass operator defined in Eq. (3.45).

- **Plane Waves:** While the matrix elements of  $\hat{\Sigma}_x$  converge with a number of plane waves higher than that used for wave functions we have converged Eq. (3.45) to within 10 meV using only 307 plane waves (the same number of plane-waves are used to invert Eq. (3.23)). However we found crucial to use a direct space grid during Fast Fourier Transformation (FFT) that was large enough to preserve wave function orthonormalization.
- **Bands:** Band summation enters at two different points of our calculation: the first is in the definition of  $\chi_{\mathbf{G}, \mathbf{G}'}^0(\mathbf{q}, \omega)$ , Eq. (3.21), where it is found that higher the number of bands used the higher the energy cut-off on the possible hole-electron excitations accessible to the system. The numerical weight of the whole *GW* calculation increases rapidly with the number of bands included in the calculation of  $\chi_{\mathbf{G}, \mathbf{G}'}^0(\mathbf{q}, \omega)$ . We have chosen 40 bands (corresponding to a cutoff of about 130 eV on the electron-hole excitation energies) looking at the Electron Energy Loss Spectrum (EELS) whereby the main structures are localized at about 30 eV, a region that, on comparing with experiment, is well described by theoretical calculations as shown in Section 2.4.2.

Eq. (3.45) displays a second band summation (over  $n_1$ ): these bands determine the energy cut-off on the intermediate states involved in the screened exchange and should be high enough to correctly describe the long range behavior of the real part of the self-energy. We have found that 100 bands (corresponding to an energy cut-off of about 300 eV) are enough to obtain matrix elements of the mass operator converged to within 10 meV.

- **k-grid:** For the construction of  $\chi_{\mathbf{G},\mathbf{G}'}^0(\mathbf{q},\omega)$  we need to define a **k**-grid that can, in principle, be different from that used to integrate the self-energy. We have used a **k**-points grid obtained joining a MP grid of 10 **k**-points in the IBZ and its copy expanded in the BZ and then shifted in the origin, that, reduced in the IBZ, gives other 19 **k**-points.
- **Frequency grid:** the main difference between a Plasmon-Pole and our full screening calculation is the possibility that the former may reduce to an analytic form for the correlation part of the Self-energy. On the other hand, in Eq. (3.45) we must evaluate a frequency integral on a discrete frequency grid. The screening function of Cu is characterized by the absence of any well defined sharp plasmon peak, and so a relatively small number of frequency points is sufficient to obtain a full converged frequency integral. We have divided the energy range of hole-electron excitation energies (130 eV) into 100 steps, together with a lorentzian broadening of 0.1 eV in  $\chi_{\mathbf{G},\mathbf{G}'}^0(\mathbf{q},\omega)$  with  $\delta$  in Eq. (3.45) set to 0.01 eV. We have tested different grid constructions and the Lorentzian broadening of either the screening function and the KS Green's function, and obtained well converged final results for the quasiparticle energies.

The convergence tests done for  $\hat{\Sigma}_x$  matrix elements in Section 3.3.1 have showed that with a grid of 19 **q**-points in the IBZ, convergence is reached to within 0.1 eV; this numerical error is conserved in

$$\langle n\mathbf{k}|\Sigma_x(\mathbf{r}_1,\mathbf{r}_2) + M(\mathbf{r}_1,\mathbf{r}_2,\omega)|n'\mathbf{k}\rangle \quad (3.50)$$

due to the rather small errors found in the matrix elements of the mass operator.

### Off-diagonal matrix elements

So far we have used a matrix notation for the mass and bare-exchange operator. However, off-diagonal matrix elements of  $\hat{\Sigma}_x$  are found to be negligible with respect to the diagonal one.

If we consider the first four occupied bands at the X point, the  $M(\mathbf{r}_1,\mathbf{r}_2;\omega)$

matrix elements calculated at the quasiparticle energies  $\epsilon_{nX}^{QP}$  are

$$\langle nX_1 | M(\mathbf{r}_1, \mathbf{r}_2; -4.91 \text{ eV}) | n'X_1 \rangle = \begin{pmatrix} -0.8747 & 0.0002 & 0.0022 & -0.0018 \\ 0.0002 & 0.5864 & 0.0006 & -0.0064 \\ 0.0017 & 0.0004 & 5.3815 & 0.0012 \\ -0.0016 & -0.0064 & 0.0016 & 5.7892 \end{pmatrix} \text{ eV} \quad (3.51)$$

$$\langle nX_3 | M(\mathbf{r}_1, \mathbf{r}_2; -4.51 \text{ eV}) | n'X_3 \rangle = \begin{pmatrix} -1.1661 & 0.0002 & 0.0020 & -0.0017 \\ 0.0002 & 0.2510 & 0.0006 & -0.0062 \\ 0.0018 & 0.0004 & 5.2115 & 0.0012 \\ -0.0016 & -0.0062 & 0.0015 & 5.5833 \end{pmatrix} \text{ eV} \quad (3.52)$$

$$\langle nX_2 | M(\mathbf{r}_1, \mathbf{r}_2; -2.28 \text{ eV}) | n'X_2 \rangle = \begin{pmatrix} -2.6320 & 0.0001 & 0.0016 & -0.0014 \\ 0.0001 & -1.3222 & 0.0004 & -0.0052 \\ 0.0016 & 0.0004 & 3.2510 & 0.0012 \\ -0.0014 & -0.0052 & 0.0012 & 3.7660 \end{pmatrix} \text{ eV} \quad (3.53)$$

$$\langle nX_4 | M(\mathbf{r}_1, \mathbf{r}_2; -2.03 \text{ eV}) | n'X_4 \rangle = \begin{pmatrix} -2.7546 & 0.0002 & 0.0016 & -0.0014 \\ 0.0001 & -1.4540 & 0.0004 & -0.0051 \\ 0.0016 & 0.0004 & 3.0853 & 0.0011 \\ -0.0014 & -0.0051 & 0.0011 & 3.5975 \end{pmatrix} \text{ eV} \quad (3.54)$$

From these matrices we see that the off-diagonal elements of mass-operator are also rather small. However, when compared with those of  $\hat{\Sigma}_x$ , the ratio with the diagonal elements is higher; not enough, of course, to induce any effect on the DFT-LDA wave-functions.

This can be considered as the proof, in the case of copper, of the identity between DFT-LDA and quasiparticle wavefunctions. Consequently, the quasiparticle energies are solution of the scalar motion equation

$$\left[ -\frac{\Delta_{\mathbf{r}}}{2} + V_{ext}(\mathbf{r}) + V_H(\mathbf{r}) \right] \psi_{n\mathbf{k}}(\mathbf{r}, \omega) + \int d\mathbf{r}' \Sigma(\mathbf{r}, \mathbf{r}'; \omega) \psi_{n\mathbf{k}}(\mathbf{r}', \omega) = E_{n\mathbf{k}}(\omega) \psi_{n\mathbf{k}}(\mathbf{r}, \omega), \quad (3.55)$$

Point	$\epsilon_{n\mathbf{k}}$	$\Sigma_x^{n\mathbf{k}} - V_{xc}^{n\mathbf{k}}$	$M_{n\mathbf{k}}(\epsilon_{n\mathbf{k}})$	$\epsilon_{n\mathbf{k}}^{QP} - \epsilon_{n\mathbf{k}}$
$X_1$	-5.10	-4.27	8.50	4.23
$X_3$	-4.63	-3.89	8.90	5.01
$X_2$	-1.59	-2.29	7.79	5.50
$X_5$	-1.40	-1.49	7.11	5.62
$X_4$	1.44	2.41	-2.70	-0.30

Table 3.2: Approximated quasiparticle corrections at the point X (following Eq. (3.60) shown together with separate matrix elements of bare exchange minus exchange-correlation potential and mass operator.

that when averaged, reduces to the simple form

$$\epsilon_{n\mathbf{k}}^{QP} - \epsilon_{n\mathbf{k}} = \Sigma_x^{n\mathbf{k}} + M_{n\mathbf{k}}(\epsilon_{n\mathbf{k}}^{QP}) - V_{xc}^{n\mathbf{k}}, \quad (3.56)$$

where

$$\Sigma_x^{n\mathbf{k}} \equiv \langle n\mathbf{k} | \Sigma_x(\mathbf{r}_1, \mathbf{r}_2) | n\mathbf{k} \rangle, \quad (3.57)$$

$$M_{n\mathbf{k}}(\omega) \equiv \langle n\mathbf{k} | M(\mathbf{r}_1, \mathbf{r}_2, \omega) | n\mathbf{k} \rangle, \quad (3.58)$$

$$V_{xc}^{n\mathbf{k}} \equiv \langle n\mathbf{k} | V_{xc}(\mathbf{r}) | n\mathbf{k} \rangle. \quad (3.59)$$

### Role of 3s/3p core levels

Normally (e.g., in *GW* calculations for semiconductors), the calculation of  $G$  and  $W$  to correct the DFT valence bandstructure can be performed by including only valence states, and fully neglecting the core states which have been frozen in the pseudopotential approach. In copper, however, when  $\Sigma$  is computed neglecting the 3s and 3p atomic core states (which in the solid create two flat bands, at about 112 and 70 eV, respectively, below the Fermi level), the resulting QP corrections on the d-bands are clearly nonphysical. This is evident looking at the approximate solution of Eq. (3.56)

$$\epsilon_{n\mathbf{k}}^{QP} - \epsilon_{n\mathbf{k}} \approx \Sigma_x^{n\mathbf{k}} + M_{n\mathbf{k}}(\epsilon_{n\mathbf{k}}) - V_{xc}^{n\mathbf{k}}. \quad (3.60)$$

In Table 3.2 these quasiparticle corrections are shown for the first five non degenerate bands at point X. Quasiparticle corrections are too large; a conclusion that remains after any more accurate solution of Dyson Equation. The reason for these results must be found in the comparison of  $M_{n\mathbf{k}}(\epsilon_{n\mathbf{k}})$  and  $(\Sigma_x^{n\mathbf{k}} - V_{xc}^{n\mathbf{k}})$  at  $X_4$  with the same quantities evaluated for example, at  $X_1$ : we see that while for  $X_4$  (a *s/p*-like state)

the correlation part is of the same order of the static one at  $X_1$  (a  $d$ -like state), the mass operator is much larger than  $(\Sigma_x^{nk} - V_{xc}^{nk})$ . From one point of view that is the first evidence of the strong correlation felt by the  $d$ -like states, but on the other hand something prevents the static part of self-energy to balance the strong correlation contribution.

Further evidence of the anomalous behavior of static part of self-energy is the similarity between  $(\Sigma_x^{nk} - V_{xc}^{nk})$  for Cu and Si [12] as shown in Fig. 3.2: the comparison shows that in the case of Cu there's no evidence of the localization of the  $d$  orbitals of Cu that, however, is fully present in the matrix elements of mass operator.

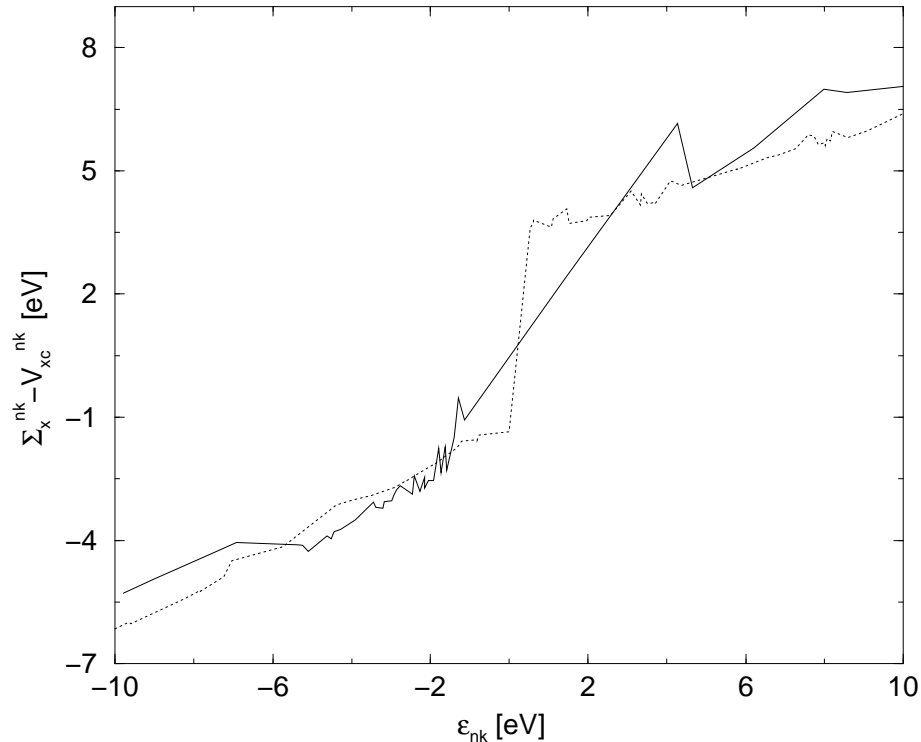


Figure 3.2: Left Frame:  $(\Sigma_x^{nk} - V_{xc}^{nk})$  values plotted as function of the non-interacting energies  $\epsilon_{nk}$  for Copper (—) and for Silicon (···) without core bare-exchange contributions.

The solution of this puzzling situation is provided by the role of the above-mentioned 3s and 3p states, which, despite being well separated *in energy* from the 3d ones, have a large *spatial* overlap with the latter. As a consequence, non-negligible contributions to the self-energy are expected to arise from the *exchange* contributions between 3d and 3s/3p states. These contributions can be included in our calculation in a straightforward way by starting with a pseudopotential which puts the whole  $3^{\text{rd}}$  atomic shell into the valence (see Chapter 2). Letting  $G_0^{\text{core}}$  represents the non-interacting Green's function also containing the 3s/3p levels, the self-energy computed as  $G_0^{\text{core}}W$  will yield the desired dynamical exchange between

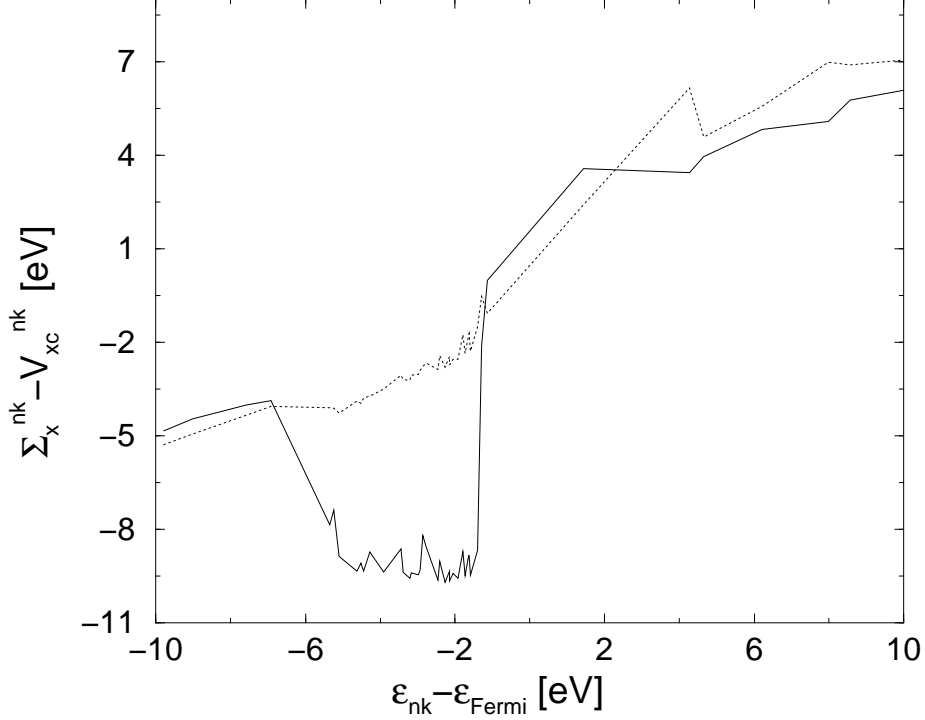


Figure 3.3: As in Fig. 3.2 but *including* core bare-exchange contributions.

3d bands and core bands composed of a bare exchange (static) contribution, plus a correlation part. Naturally, a larger plane-wave cutoff (160 Ry) is needed for convergence. As a result, we find large bare-exchange contributions from core levels, leading to very different values of  $\langle \Sigma_x^{nk} - V_{xc}^{nk} \rangle$  for s/p and d states, as illustrated in Fig. 3.3. The role of core levels in the calculation of the bare exchange contributions (whose importance was already addressed for transition metals by Aryasetiawan and Gunnarsson [3], but estimated to be of the order of 1 eV) is hence crucial in the case of copper [13].

The inclusion of core levels into the exchange self-energy decreases the  $(\Sigma_x^{nk} - V_{xc}^{nk})$  values for d-bands of  $\sim 8$  eV.

Point	$\epsilon_{nk}$	$\Sigma_x^{nk} - V_{xc}^{nk}$	$M_{nk}(\epsilon_{nk})$	$\epsilon_{nk}^{QP} - \epsilon_{nk}$
$X_1$	-5.10	-8.87	8.50	-0.37
$X_3$	-4.63	-9.33	8.90	-0.44
$X_2$	-1.59	-9.47	7.79	-1.68
$X_5$	-1.40	-8.66	7.11	-1.56
$X_4$	1.44	3.56	-2.70	0.86

Table 3.3: As in Table 3.2 but including bare core exchange.

This large bare-exchange is able, as shown in Table 3.3 for X point, to balance



the strong correlation energy of  $d$ -like states, giving a reasonable quasiparticle corrections with Eq. (3.60). The presence of such a large bare exchange between core and valence states can, in principle, involve some similar effects in the mass operator. Physically this corresponds to allowing both screened exchange and polarization effects between core and valence/conduction states: if we call  $\tilde{W}_{core}(1, 2)$  the dynamic part of the screening function containing core-conduction hole-electron excitations and  $G_{core}^0(1, 2)$  the KS Green's function relative to the  $3s$  and  $\{3p\}$  states we get

$$M(1, 2) = i \left[ \tilde{W}(1, 2) G^0(1, 2) + \tilde{W}(1, 2) G_{core}^0(1, 2) + \tilde{W}_{core}(1, 2) G^0(1, 2) + \tilde{W}_{core}(1, 2) G_{core}^0(1, 2) \right]. \quad (3.61)$$

However, Fig. 3.3 shows that core levels have a strong interaction only with  $d$  orbitals, completely full in copper. This means that  $\tilde{W}$  could involve only excitation from core levels to  $s/p$  conduction bands, leading to very small contributions to  $M$  that we neglect. The final diagrammatic form of the Self-energy operator used here is shown in Fig. 3.4.

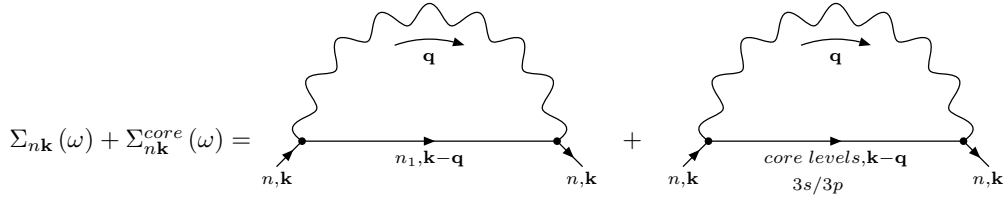


Figure 3.4: Diagrammatic form of the  $GW$  self-energy including the core levels contribution

If  $M_{n\mathbf{k}}^{core}(\omega)$  is the contribution to  $M_{n\mathbf{k}}(\omega)$  due to *only* the  $3s/3p$  levels (rhs of Fig. 3.4)

$$M_{n\mathbf{k}}^{core}(\omega) = i \int dt e^{i\omega t} \langle n\mathbf{k} | \tilde{W}(\mathbf{r}_1, \mathbf{r}_2, t) \left[ G_{3s}^0(\mathbf{r}_1, \mathbf{r}_2, t) + \sum_{i=1,3} G_{3p_i}^0(\mathbf{r}_1, \mathbf{r}_2, t) \right] | n'\mathbf{k} \rangle, \quad (3.62)$$

the high binding energies of the core levels push the poles of  $M_{n\mathbf{k}}^{core}(\omega)$  far from the Fermi Level; thus in the region of the valence states energies the only contribution of  $M_{n\mathbf{k}}^{core}(\omega)$  comes from the real part. Moreover, being far from the poles of the self-energy, the real part is dominated by the asymptotic behavior of the Hilbert transformation that is well approximated (to within 1 meV) by a constant

$$\Re[M_{n\mathbf{k}}^{core}(\omega)] \approx M_{n\mathbf{k}}^{core} \quad \text{for} \quad |\omega - \epsilon_{n\mathbf{k}}| \leq 2 \text{ eV}. \quad (3.63)$$

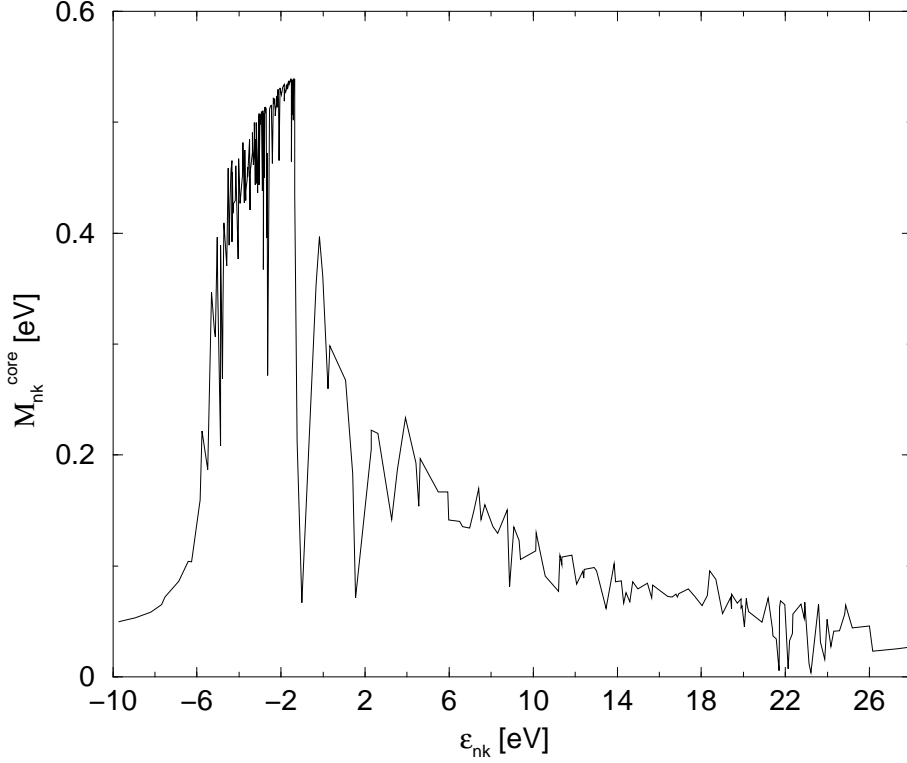


Figure 3.5:  $M_{n\mathbf{k}}^{core}$  as function of  $\epsilon_{n\mathbf{k}}$

In Fig. 3.5  $M_{n\mathbf{k}}^{core}$  is shown as a function of  $\epsilon_{n\mathbf{k}}$  and we see a strong peak in the  $d$ -like states region. Despite of the small values of  $M_{n\mathbf{k}}^{core}$ , we will see their important role in the comparison with experiment.

### 3.3.3 Iterative solution of quasiparticle equation

In the preceding section we have studied the role of core levels on the quasiparticle energies starting from Eq. (3.60). In this section we will study in more detail the determination of quasi particle energies far from Fermi level, where the non negligible imaginary part of the self-energy requires a more appropriate solution of the QP equation.

We have found that the QP wave-functions are identical to the DFT-LDA ones by observing that the off-diagonal elements of either mass-operator and exchange self-energy are negligible. Therefore, by neglecting band mixing we can calculate directly the interacting Green's function in the Bloch representation using the Dyson Eq. (3.1) and adding the core contribution  $M_{n\mathbf{k}}^{core}$

$$G_{n\mathbf{k}}(\omega) = \frac{G_{n\mathbf{k}}^0(\omega)}{1 - G_{n\mathbf{k}}^0(\omega) [\Sigma_x^{n\mathbf{k}} + M_{n\mathbf{k}}(\omega) + M_{n\mathbf{k}}^{core} - V_{xc}^{n\mathbf{k}}]}, \quad (3.64)$$

with  $G_{n\mathbf{k}}(\omega)$  defined as

$$G_{n\mathbf{k}}(\omega) = \int d\mathbf{r}_1 d\mathbf{r}_2 \phi_{n\mathbf{k}}^*(\mathbf{r}_1) G(\mathbf{r}_1, \mathbf{r}_2, \omega) \phi_{n\mathbf{k}}(\mathbf{r}_2). \quad (3.65)$$

From the expression for  $G_{n\mathbf{k}}^0(\omega)$  we get

$$G_{n\mathbf{k}}(\omega) = \frac{1}{\omega - \epsilon_{n\mathbf{k}} - [\Sigma_x^{n\mathbf{k}} + M_{n\mathbf{k}}(\omega) + M_{n\mathbf{k}}^{core} - V_{xc}^{n\mathbf{k}}]}, \quad (3.66)$$

and the quasi-particle Eq. (1.168) reduces to

$$\left[ G_{n\mathbf{k}}(\epsilon_{n\mathbf{k}}^{QP}) \right]^{-1} = \epsilon_{n\mathbf{k}}^{QP} - \epsilon_{n\mathbf{k}} - \left[ \Sigma_x^{n\mathbf{k}} + M_{n\mathbf{k}}(\epsilon_{n\mathbf{k}}^{QP}) + M_{n\mathbf{k}}^{core} - V_{xc} \right] = 0. \quad (3.67)$$

To find  $\epsilon_{n\mathbf{k}}^{QP}$  we proceed in two steps: first we look for an approximated real QP energy  $\epsilon_{n\mathbf{k}}^{QP,0}$  defined by

$$\epsilon_{n\mathbf{k}}^{QP,0} = \epsilon_{n\mathbf{k}} - \left[ \Sigma_x^{n\mathbf{k}} + \Re \left[ M_{n\mathbf{k}}(\epsilon_{n\mathbf{k}}^{QP,0}) \right] + M_{n\mathbf{k}}^{core}, -V_{xc} \right] \quad (3.68)$$

following an iterative procedure based on the *secant* method [14]; this method is particularly fast and doesn't need the first derivative like in the commonly used perturbative Newton method [10]. The second step starts by defining the analytic continuation of  $M_{n\mathbf{k}}(\omega)$  near  $\epsilon_{n\mathbf{k}}^{QP,0}$  as

$$M_{n\mathbf{k}}(z) \approx M_{n\mathbf{k}}(\epsilon_{n\mathbf{k}}^{QP,0}) + M'_{n\mathbf{k}}(\epsilon_{n\mathbf{k}}^{QP,0}) (z - \epsilon_{n\mathbf{k}}^{QP,0}), \quad (3.69)$$

with  $z$  complex. From Eq. (3.68-3.69) it follows immediately that the analytic continuation of  $G_{n\mathbf{k}}(\omega)$  is

$$G_{n\mathbf{k}}(z) \approx \frac{1}{z - \epsilon_{n\mathbf{k}}^{QP,0} - i\Im \left[ M_{n\mathbf{k}}(\epsilon_{n\mathbf{k}}^{QP,0}) \right] - M'_{n\mathbf{k}}(\epsilon_{n\mathbf{k}}^{QP,0}) (z - \epsilon_{n\mathbf{k}}^{QP,0})} = \frac{Z_{n\mathbf{k}}}{z - \epsilon_{n\mathbf{k}}^{QP,0} - iZ_{n\mathbf{k}}\Im \left[ M_{n\mathbf{k}}(\epsilon_{n\mathbf{k}}^{QP,0}) \right]}, \quad (3.70)$$

with

$$Z_{n\mathbf{k}} = \left[ 1 - M'_{n\mathbf{k}}(\epsilon_{n\mathbf{k}}^{QP,0}) \right]^{-1}. \quad (3.71)$$

Using Eq. (3.70) the QP complex energy solution of Eq. (3.67) is

$$\Re \left[ \epsilon_{n\mathbf{k}}^{QP} \right] = \epsilon_{n\mathbf{k}}^{QP,0} - \frac{\Im \left[ M'_{n\mathbf{k}}(\epsilon_{n\mathbf{k}}^{QP,0}) \right] \Im \left[ M_{n\mathbf{k}}(\epsilon_{n\mathbf{k}}^{QP,0}) \right]}{\left( 1 - \Re \left[ M'_{n\mathbf{k}}(\epsilon_{n\mathbf{k}}^{QP,0}) \right] \right)^2 + \left( \Im \left[ M'_{n\mathbf{k}}(\epsilon_{n\mathbf{k}}^{QP,0}) \right] \right)^2}, \quad (3.72)$$

$$\Im \left[ \epsilon_{n\mathbf{k}}^{QP} \right] = \frac{\left( 1 - \Re \left[ M'_{n\mathbf{k}}(\epsilon_{n\mathbf{k}}^{QP,0}) \right] \right) \Im \left[ M_{n\mathbf{k}}(\epsilon_{n\mathbf{k}}^{QP,0}) \right]}{\left( 1 - \Re \left[ M'_{n\mathbf{k}}(\epsilon_{n\mathbf{k}}^{QP,0}) \right] \right)^2 + \left( \Im \left[ M'_{n\mathbf{k}}(\epsilon_{n\mathbf{k}}^{QP,0}) \right] \right)^2}. \quad (3.72')$$

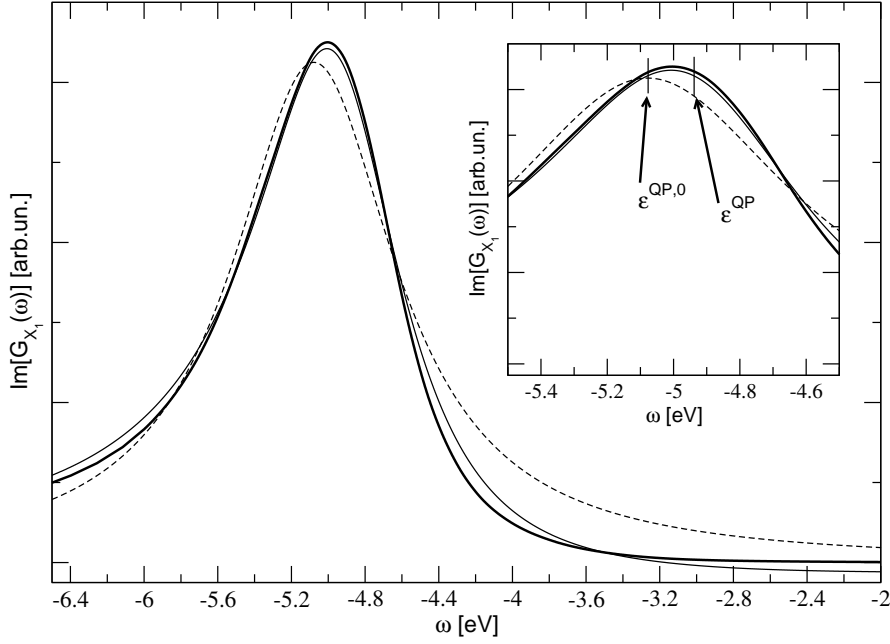


Figure 3.6: Quasiparticle approximations to the imaginary part of  $GW$  Green's function at  $X_1$  point. Tick full line: Green's function from Eq. (3.66). Thin full line: QP approximation solved on the complex plane. Dashed line: QP approximation solved on the real plane.

From Eqs. (3.72) we see that  $\epsilon_{n\mathbf{k}}^{QP}$  reduces to  $\epsilon_{n\mathbf{k}}^{QP,0}$  when  $\Im \left[ M'_{n\mathbf{k}} \left( \epsilon_{n\mathbf{k}}^{QP,0} \right) \right] = 0$ . As the imaginary part of  $M$  is, generally, much smaller than the real part the approximate solution  $\epsilon_{n\mathbf{k}}^{QP,0}$  could appear reasonably. The corresponding imaginary part is

$$\Im \left[ \epsilon_{n\mathbf{k}}^{QP,0} \right] = \left( 1 - \Re \left[ M'_{n\mathbf{k}} \left( \epsilon_{n\mathbf{k}}^{QP,0} \right) \right] \right)^{-1} \Im \left[ M_{n\mathbf{k}} \left( \epsilon_{n\mathbf{k}}^{QP,0} \right) \right]. \quad (3.73)$$

Indeed this is the case for the low (binding) energy conduction (valence) states. However for deeper valence states (and for high conduction levels) differences of  $\sim 0.1$  eV can be found between  $\epsilon_{n\mathbf{k}}^{QP,0}$  and  $\epsilon_{n\mathbf{k}}^{QP}$ . This is shown in detail for the state  $X_1$  in Fig. 3.6. A successful QP energy and renormalization factor  $Z_{n\mathbf{k}}$  should be able to correctly reproduce the Green's function  $G_{n\mathbf{k}}(\omega)$  around the main peak. Following the definition of  $\epsilon_{n\mathbf{k}}^{QP}$  and  $\epsilon_{n\mathbf{k}}^{QP,0}$  we have

$$G_{n\mathbf{k}}^{QP,0}(\omega) = \frac{Z_{n\mathbf{k}}^0}{\omega - \epsilon_{n\mathbf{k}}^{QP,0}} \quad \text{with} \quad Z_{n\mathbf{k}}^0 \equiv \left( 1 - \Re \left[ M'_{n\mathbf{k}} \left( \epsilon_{n\mathbf{k}}^{QP,0} \right) \right] \right)^{-1} \in \mathcal{R} \quad (3.74)$$

and

$$G_{n\mathbf{k}}^{QP}(\omega) = \frac{Z_{n\mathbf{k}}}{\omega - \epsilon_{n\mathbf{k}}^{QP}} \quad \text{with} \quad Z_{n\mathbf{k}} \equiv \left( 1 - M'_{n\mathbf{k}} \left( \epsilon_{n\mathbf{k}}^{QP,0} \right) \right)^{-1} \in \mathcal{C} \quad (3.75)$$

In Fig. 3.6 the imaginary part of  $G_{n\mathbf{k}}(\omega)$  (full thick line),  $G_{n\mathbf{k}}^{QP}(\omega)$  (full thin line) and  $G_{n\mathbf{k}}^{QP,0}(\omega)$  (dashed line) are compared. From the comparison two conclusions can be drawn:

- (i) The lorentzian shape of  $\Im \left[ G_{n\mathbf{k}}^{QP,0}(\omega) \right]$  badly reproduces the exact  $\Im \left[ G_{n\mathbf{k}}(\omega) \right]$ . This is a consequence of the large, not negligible,  $\Im \left[ M'_{n\mathbf{k}} \left( \epsilon_{n\mathbf{k}}^{QP,0} \right) \right] \sim -0.18$  at the  $X_1$  point that gives a clear Fano-like low-energy asymmetry.
- (ii)  $\epsilon_{n\mathbf{k}}^{QP,0}(\omega)$  underestimates the peak position, correctly reproduced by  $\epsilon_{n\mathbf{k}}^{QP}$ .

The particular case of Fig. 3.6 is readily extrapolated to the general case. The imaginary part of  $Z_{n\mathbf{k}}$  increases the QP energies of full states where  $\Im \left[ M'_{n\mathbf{k}} \left( \epsilon_{n\mathbf{k}}^{QP,0} \right) \right] < 0$  and  $\Im \left[ M_{n\mathbf{k}} \left( \epsilon_{n\mathbf{k}}^{QP,0} \right) \right] > 0$  while decreases the empty bands energies where  $\Im \left[ M_{n\mathbf{k}} \left( \epsilon_{n\mathbf{k}}^{QP,0} \right) \right]$  changes sign.

### 3.4 Band Structure Results

		LDA-DFT	$GW_{(1)}$	$GW_{(2)}$	$GW_{(3)}$	Experiment
Positions	$\Gamma_{12}$	-2.27	-3.10	-2.82	-2.81	-2.78
of	$X_5$	-1.40	-2.35	-2.04	-2.04	-2.01
d-bands	$L_3$	-1.63	-2.55	-2.24	-2.24	-2.25
	$\Gamma_{12} - \Gamma_{25'}$	0.91	0.64	0.63	0.60	0.81
Widths	$X_5 - X_3$	3.22	2.55	2.58	2.49	2.79
of	$X_5 - X_1$	3.69	2.99	3.04	2.90	3.17
d-bands	$L_3 - L_3$	1.58	1.25	1.28	1.26	1.37
	$L_3 - L_1$	3.72	2.82	2.91	2.83	2.91
Positions	$\Gamma_1$	-9.79	-9.40	-9.37	-9.24	-8.60
of sp-bands	$L_{2'}$	-1.14	-0.62	-0.57	-0.57	-0.85
L-gap	$L_1 - L_{2'}$	5.41	4.64	4.58	4.76	4.95

Table 3.4: Comparison of band widths and energy position with experimental values [15] at high-symmetry points. All energies in eV.  $GW_{(1)}$ :  $GW$  calculation along real axes without screened core exchange.  $GW_{(2)}$ :  $GW$  calculation along real axes with screened core exchange.  $GW_{(3)}$ :  $GW$  calculation on complex plane with screened core exchange.

In Table 3.4 is shown the comparison between  $GW$  results, DFT-LDA and experimental data. The first column ( $GW_{(1)}$ ) contains  $\Re \left[ \epsilon_{n\mathbf{k}}^{QP,0} \right]$  with  $M_{n\mathbf{k}}^{core} = 0$  while in

the second column ( $GW_{(2)}$ )  $\epsilon_{nk}^{QP,0}$  is calculated with  $M_{nk}^{core} \neq 0$ . The third column ( $GW_{(3)}$ ) includes  $M_{nk}^{core}$  and the Fano effect discussed in the last section.

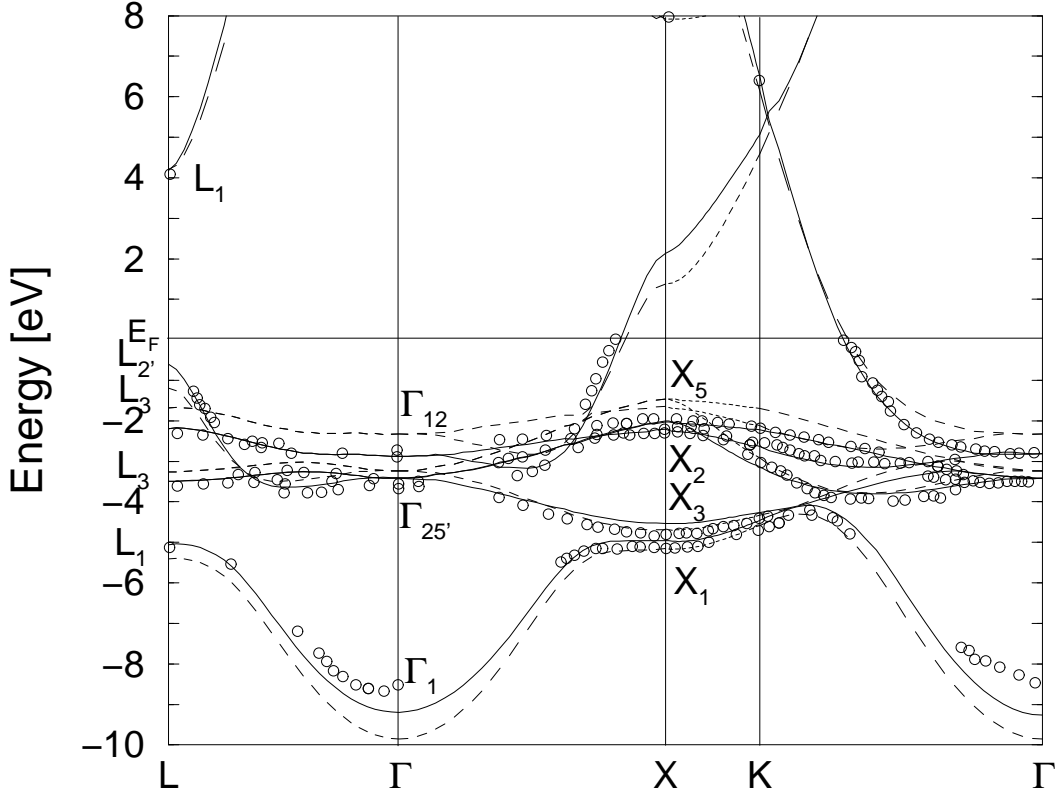


Figure 3.7: Comparison of experimental band structure ( $\circ \circ \circ$ ) with DFT-LDA ( $- - -$ ) and  $GW$  results ( $-$ )

In Fig. 3.7 the full theoretical band structure is compared with experimental data: the agreement is remarkably good and the fact that the  $GW$  corrections cannot be reproduced by any rigid shift of the LDA bands clearly appears. For instance, at the  $L$  point the shifts change sign for different valence bands, with QP corrections ranging from  $-0.29$  eV to  $-0.61$  eV, to  $0.57$  eV for the three d-bands. As a consequence, the  $L_1 - L_{2'}$  gap *decreases* after inclusion of self-energy corrections (see also Table 3.4, last line), in contrast with the usual behavior occurring in semiconductors and insulators. The other gaps at  $L$  and  $X$ , however, increase. All gaps come to good agreement with experimental data. Unoccupied (conduction) bands at points  $L$ ,  $X$  and  $K$  are also obtained in very good agreement with the experimental data. These findings demonstrate that the strong deviations from the single quasiparticle band theory in copper, as suggested in Ref. [1], do not occur. QP band-theory in the  $GW$  approximation, instead, remarkably deviates from the DFT-LDA + scissors-operator approach, due to the interplay of the different localization

and correlation properties of d and s/p states.

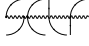
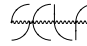
On solving the Dyson equation on the complex plane and on including  $M_{nk}^{core}$  terms the lower points ( $X_1, X_3, \Gamma_1$  and  $L_1$ ) are raised, as expected from the discussion of Section 3.3.2; this worsens the comparison with experimental *d*-like states but is in accordance with the physical fact that in the *GW* approximation hole-hole scattering diagrams are absent, which are contained in the “T-Matrix” approximation.

In conclusion the single-quasiparticle bandstructure computed within Hedin’s *GW* approximation for the electron self-energy turns out to be in very good agreement with experiments. The *GW* method, originally devised to describe the *long-range* charge oscillations [16], is hence shown to yield a good description also of copper, a system characterized by localized orbitals and short-range correlation effects. The corrections to the LDA Kohn–Sham eigenvalues for the d-bands are highly non-trivial, since even their *sign* turns out to be k-point and band-dependent, ruling out the validity of any “scissors operator” approximation. Furthermore, exchange effects between d-electrons and 3s, 3p core states play a key role and cannot be neglected in the calculation of QP corrections.





# Bibliography

- [1] See, for example, V.N. Strocov, R. Claessen, G. Nicolay, S. Hüfner, A. Kimura, A. Harasawa, S. Shin, A. Kakizaki, P.O. Nilsson, H.I. Starnberg, and P. Blaha, Phys. Rev. Lett. **81**, 4943 (1998).
- [2] L. Hedin, Phys. Rev. **139**, A796 (1965).
- [3] F. Aryasetiawan and O. Gunnarsson, Rep. Prog. Phys. **61**, 237-312 (1998).
- [4] See e.g.: W.G. Aulbur, L. Jönsson and J.W. Wilkins, Solid State Physics **54**, 1 (1999).
- [5] O. Pulci, G. Onida, R. Del Sole and L. Reining, Phys. Rev. Lett. **81**, 5374 (1998).
- [6] G.D. Mahan and B.E. Sernelius, Phys. Rev. Lett. **62**, 2718 (1989) and references therein.
- [7] P.O. Nilsson and C.G. Larsson, Phys. Rev. **B 27**, 6143 (1983).
- [8] F. Aryasetiawan, Phys. Rev. B **46**, 13051 (1992).
- [9] N. Troullier and J.L. Martins, Phys. Rev. B **43**, 1993 (1991).
- [10] M. S. Hybertsen and S. G. Louie, Phys. Rev. B **34**, 5390 (1986); R.W. Godby and R.J. Needs, Phys. Rev. Lett. **62**, 1169 (1989).
- [11] H. J. Monkhorst and J. D. Pack, Phys. Rev. B **13**, 5188 (1976).
- [12] The values of  $\Sigma_x^{n\mathbf{k}}$  for silicon were obtained using , the same code used for copper. For details about  see the Appendix.
- [13] A similar conclusion was obtained by M. Rohlfing, P. Krüger and J. Pollmann, Phys. Rev. Lett. **75**, 3489 (1995) for CdS, where the inclusion of core levels in the *GW* calculation lowers the *d*-bands position of about 3 eV.

- [14] W. H. Press, B. P. Flannery, S. A. Teukolosky and W. T. Vetterling, *Numerical Recipes (FORTRAN Version)*, Cambridge University Press 1986, pp 248-251
- [15] R. Courths and S. Hufner, Phys. Rep. **112**, 53 (1984).
- [16] L. Hedin, J. Phys.: Condens. Matter **11**, R489 (1999).

# Chapter 4

## Lifetimes of d–holes in Copper

Electron and hole dynamics in the bulk as well as at various surfaces of a solid play a key role in a great number of physical and chemical phenomena. The link between electron/hole dynamical and transport properties (already discussed in Chapter 1) has numerous practical applications for various electronic and optical devices. As modern electronic devices are scaled down at very small dimensions and their operating speed becomes faster, the temporal fast scale of electronic many–body effects ( $\sim$  fs) become relevant.

However our quantitative understanding of the excitation mechanisms and their relaxation channels is far from being complete. Two experimental techniques are used to investigate the relaxation times of holes and electrons in solids:

- (i) For filled states Angle Resolved Photoemission Spectra (ARPES) measures the angle projected density of states along high symmetry lines. The peak positions are a measure of the quasiparticle energies while the quasiparticle width  $\Gamma_{n\mathbf{k}}$  is linked to the quasiparticle lifetime by  $\tau_{n\mathbf{k}} \sim 1/\Gamma_{n\mathbf{k}}$ .
- (ii) For unoccupied states ARPES can not be used, because these states are not directly ionizable. In these cases Time Resolved two Photon Photoemission (TR2PPE) is used. This technique uses a first laser pulse to “pump” an electron from valence states into low–lying conduction states (these electrons are called “hot–electrons”). Then, with a fixed time delay, a second laser ionizes (probes) the pumped electron. The intensity of the photoelectron beam is measured as function of the laser delay. This is linked to the population dynamics of the excited states and its tail at long times is dominated by the electronic lifetime.

Although *GW* has also become the state–of–the–art method for computing lifetimes [1], the results, compared to those for quasiparticle band structure, are far

from being definitive.

There is a wide experimental evidence that at copper surfaces the hot–electron lifetimes (probed with TR2PPE) do not follow an inverse quadratic dependence  $\theta \propto (E - E_f)^2$ , as found in *GW* calculations and expected from simple phase space arguments. In this case, however, a possible explanation could be found in the TR2PPE technique itself. During the hot–electron relaxation the system is ionized, and the relaxation occurs in presence of the hole, created with the primary laser. Therefore, beyond the simple optical recombination, short time excitonic effects could appear, while they are not allowed within *GW*.

However also for the (simpler) ARPES experiments recent *GW* calculations of the d–band lifetimes in copper [2] found only a qualitative agreement with experimental results with a surprising overestimation of the d–hole lifetimes. In this chapter I will show that this overestimation does not occur *if* the full, non trivial, quasiparticle band structure calculated in the last chapter is included.

In Section 4.1 the theoretical framework of *GW* will be revisited in order to clarify the physics and the numerical implementation. This will be described in Section 4.2. In Section 4.3 the results will be discussed together with the effect of self–consistency and their connection with vertex corrections beyond *GW*.

## 4.1 The *GW* equations revisited

Quasiparticle energies and widths are, of course, strictly linked. In the last chapter I have written all the equations necessary to calculate the QP energies and, consequently, the QP widths

$$\Im \left[ \epsilon_{n\mathbf{k}}^{QP} \right] \equiv \Gamma_{n\mathbf{k}} = \text{Re} [Z_{n\mathbf{k}}] \text{Im} \left[ M_{n\mathbf{k}} \left( \epsilon_{n\mathbf{k}}^{QP,0} \right) \right], \quad (4.1)$$

with

$$Z_{n\mathbf{k}} = \left( 1 - M'_{n\mathbf{k}} \left( \epsilon_{n\mathbf{k}}^{QP,0} \right) \right)^{-1}, \quad (4.2)$$

and  $\epsilon_{n\mathbf{k}}^{QP,0}$  solution of Dyson equation on the real axes (See Section 3.3.3)

$$\epsilon_{n\mathbf{k}}^{QP,0} = \epsilon_{n\mathbf{k}} - \left[ \Sigma_x^{n\mathbf{k}} + \Re \left[ M_{n\mathbf{k}} \left( \epsilon_{n\mathbf{k}}^{QP,0} \right) \right] + M_{n\mathbf{k}}^{core} - V_{xc}^{n\mathbf{k}} \right] \quad (4.3)$$

We have, also, obtained in Section 3.2.2 a closed form for the mass operator  $M_{n\mathbf{k}}(\omega)$

$$M_{n\mathbf{k}}(\omega) = - \sum_{n_1} \int_{BZ} \frac{d\mathbf{q}}{(2\pi)^3} \left[ \int_{-\infty}^{\infty} d\omega' \frac{\Gamma_h(nn_1n, \mathbf{k} - \mathbf{q}, \omega')}{\omega - \omega' - \epsilon_{n_1(\mathbf{k}-\mathbf{q})} + i\delta} + \int_{-\infty}^{\infty} d\omega' \frac{\Gamma_e(nn_1n, \mathbf{k} - \mathbf{q}, \omega')}{\omega - \omega' - \epsilon_{n_1(\mathbf{k}-\mathbf{q})} - i\delta} \right], \quad (4.4)$$

with

$$\Gamma_h(nn_1n, \mathbf{k} - \mathbf{q}, \omega') = 2 \sum_{\mathbf{G}, \mathbf{G}'} \tilde{\rho}_{nn_1}(\mathbf{k}, \mathbf{q}, \mathbf{G}) [\tilde{\rho}_{nn_1}(\mathbf{k}, \mathbf{q}, \mathbf{G}')]^* \frac{2f_{n_1(\mathbf{k}-\mathbf{q})}}{|\mathbf{q} + \mathbf{G}||\mathbf{q} + \mathbf{G}'|} \Im [\tilde{\epsilon}_{\mathbf{G}, \mathbf{G}'}^{-1}(\mathbf{q}, \omega)] \theta(\omega), \quad (4.5)$$

$$\Gamma_e(nn_1n, \mathbf{k} - \mathbf{q}, \omega') = 2 \sum_{\mathbf{G}, \mathbf{G}'} \tilde{\rho}_{nn_1}(\mathbf{k}, \mathbf{q}, \mathbf{G}) [\tilde{\rho}_{nn_1}(\mathbf{k}, \mathbf{q}, \mathbf{G}')]^* \frac{2(1 - f_{n_1(\mathbf{k}-\mathbf{q})})}{|\mathbf{q} + \mathbf{G}||\mathbf{q} + \mathbf{G}'|} \Im [\tilde{\epsilon}_{\mathbf{G}, \mathbf{G}'}^{-1}(\mathbf{q}, \omega)] \theta(-\omega). \quad (4.5')$$

Thus we might be able to calculate the QP widths following the same procedure used in Chapter 3. However, lifetimes calculation requires a approach different from that used for the QP energies. This point will be demonstrated in the next section where we will focus the two parameters in the  $GW$  approach, that, in contrast with the calculation of the QP energies are crucial in the present context

- (i) *Energy range step.* To calculate the *real* part of the mass operator the dielectric matrix must be calculated over a large energy range. Although numerically heavy, the summation over all the components of the matrix allows to use a, relatively large energy step of  $\sim 1$  eV. However, we are going to calculate QP widths of the order of meV, three orders of magnitude smaller than the correlation energy, and too small compared with the energy step.
- (ii) *The  $W$  broadening.* The screening function has been calculated with a broadening of 0.1 eV. This is, again, too much large compared with the resolution required for the lifetime calculations.

In order, therefore, to introduce the correct numerical procedure to follow and, also, to understand better the physics underlying the  $GW$  approach to the lifetimes problem we may rewrite the  $GW$  equations as follows. Using the relation

$$\frac{1}{\omega - \omega' - \epsilon_{n_1(\mathbf{k}-\mathbf{q})} \pm i\delta} = \mp i\pi\delta(\omega - \omega' - \epsilon_{n_1(\mathbf{k}-\mathbf{q})}) + \mathcal{P} \frac{1}{\omega - \omega' - \epsilon_{n_1(\mathbf{k}-\mathbf{q})}}, \quad (4.6)$$

we can simplify Eq. (4.4) using the fact that  $\Gamma_{h/e}$  functions are real

$$\begin{aligned} \text{Im}[M_{n\mathbf{k}}(\omega)] = & 2\pi \sum_{n_1} \sum_{\mathbf{q}} \sum_{\mathbf{G}, \mathbf{G}'} \left\{ \tilde{\rho}_{nn_1}(\mathbf{k}, \mathbf{q}, \mathbf{G}) [\tilde{\rho}_{nn_1}(\mathbf{k}, \mathbf{q}, \mathbf{G}')]^* \right. \\ & \left( \int_{BZ'(\mathbf{q})} \frac{d\mathbf{q}'}{(2\pi)^3} \frac{1}{|\mathbf{q} + \mathbf{G}||\mathbf{q} + \mathbf{G}'|} \right) \text{Im} [\tilde{\epsilon}_{\mathbf{G}, \mathbf{G}'}^{-1}(\mathbf{q}, \omega - \epsilon_{n_1(\mathbf{k}-\mathbf{q})})] \\ & \left. \left[ \underbrace{(2 - f_{n_1(\mathbf{k}-\mathbf{q})}) \theta(\omega - \epsilon_{n_1(\mathbf{k}-\mathbf{q})})}_{\mathbf{A}} - \underbrace{f_{n_1(\mathbf{k}-\mathbf{q})} \theta(\epsilon_{n_1(\mathbf{k}-\mathbf{q})} - \omega)}_{\mathbf{B}} \right] \right\}. \quad (4.7) \end{aligned}$$

In Eq. (4.7) the “Random Integration Method” introduced in Section 3.3.1 has been applied only to the Coulomb Fourier components, while the occupation factors are left outside the  $\mathbf{q}'$  integral. With this approximation we neglect the “Fermi Surface” effects observed in the bare-exchange matrix elements in Section 3.3.1. In this case, however, this neglect is reasonable because, at difference with  $\Sigma_x$ , the contribution to the QP width coming from states near the Fermi level is small due to the simple phase space effects which yield the well known behavior  $\theta \propto (E - E_f)^2$ . Regarding the two parameters discussed above, Eq. (4.7) does not require, anymore, an energy step to calculate the  $\tilde{\epsilon}_{\mathbf{G},\mathbf{G}'}^{-1}(\mathbf{q},\omega)$  function, as this is calculated at exactly each allowed energy transition  $\epsilon_{n\mathbf{k}}^{QP,0} - \epsilon_{n_1(\mathbf{k}-\mathbf{q})}$ .

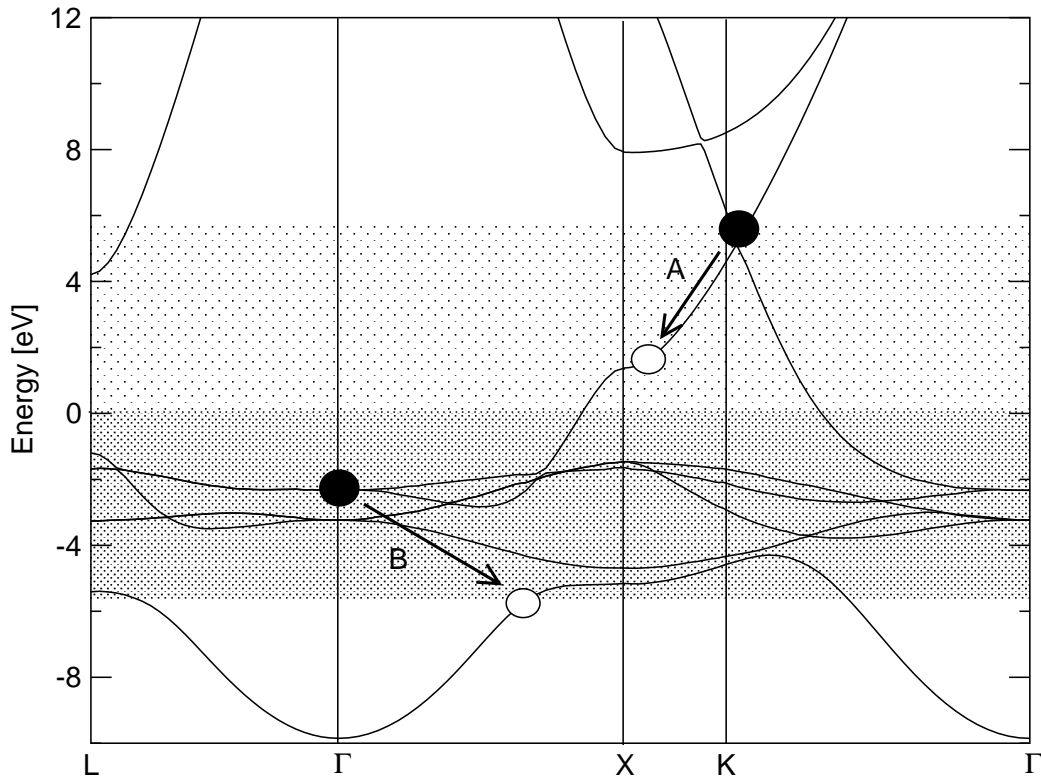


Figure 4.1: Schematical representation of the two relaxation channels (A) and (B) of Eq. (4.7). Filled circles are electrons while empty ones are holes. The two different patterns delimit the energy regions corresponding to condition (A) and (B).

The two terms, labeled with A and B, in the last line of Eq. (4.7) correspond to two distinct process involving the conduction/valence states.

If  $\Gamma_{n\mathbf{k}} = \text{Re}[Z_{n\mathbf{k}}] \text{Im}\left[M_{n\mathbf{k}}\left(\epsilon_{n\mathbf{k}}^{QP,0}\right)\right]$  we have two possible cases:

$$(2 - f_{n_1(\mathbf{k}-\mathbf{q})}) \neq 0 \quad \omega > \epsilon_{n_1(\mathbf{k}-\mathbf{q})}, \quad (A)$$

$$f_{n_1(\mathbf{k}-\mathbf{q})} \neq 0 \quad \omega < \epsilon_{n_1(\mathbf{k}-\mathbf{q})}. \quad (B)$$

The contribution from  $\omega = \epsilon_{n_1(\mathbf{k}-\mathbf{q})}$  has been omitted because the corresponding transferred energy would be vanishingly small, and  $Im[\tilde{\epsilon}_{\mathbf{G},\mathbf{G}'}^{-1}(\mathbf{q}, 0)] = 0$ . The two terms (A) and (B) are shown, schematically, in Fig. 4.1

(A): An electron can decay into any empty state (i.e., with energy above the Fermi level) with lower energy.

(B): A hole can decay into any filled state (i.e., with energy below the Fermi level) with higher energy.

Both relaxation processes are directed towards virtual final states  $|n1, \mathbf{k} - \mathbf{q}\rangle$  that, in the present non selfconsistent *GW*, conserves the energy lost in the decay. This energy is dissipated in hole–electron excitations contained in the screening function.

The two processes (A) and (B) are energetically distinct, except in the presence of a fictitious electronic temperature introduced in order to smooth the occupation of states near the Fermi surface, or to achieve the correct number of electrons using small  $\mathbf{k}$ -point grids. In these cases, a level very near the Fermi energy can be partially occupied, and, as a consequence, both decay channels (A) and (B) would be allowed. However these (few) cases are not physical, having derived from a fictitious electronic temperature, and thus are omitted in the present calculations.

## 4.2 The numerical approach

Eq. (4.7) can be calculated straightforwardly to check the convergence of the QP widths with respect to the various parameters that characterize the calculation:

1. Number of Fourier components in  $\tilde{\epsilon}_{\mathbf{G},\mathbf{G}'}^{-1}(\mathbf{q}, \omega)$ : Eq. (4.7).
2. Number of  $\mathbf{q}$  ( $\mathbf{k}$ ) points:  $\sum_{\mathbf{q}}$  in Eq. (4.7).
3. Number of bands in the RPA polarization function, Eq. (3.22) that, through Eqs. (3.21), (3.23) and (3.24) define the symmetric dielectric function.
4. The broadening  $\eta$  in the RPA polarization function, Eq. (3.22).

All the convergence tests will be done at the first four bands at X point, using the approximate equation

$$\Gamma_{n\mathbf{k}} \sim Im [M_{n\mathbf{k}} (\epsilon_{n\mathbf{k}}^{DFT-LDA})] . \quad (4.8)$$

The number of bands in the intermediate states ( $\sum_{n_1}$  in Eq. (4.7)) is not a free parameter, because only a limited number is reached due to the energy constraints imposed by conditions (A) and (B) of Eq. (4.7).

A first calculation is shown in Fig. 4.2 at fixed number of 89  $\mathbf{G}$ 's, 20 bands in the RPA polarization and two different sets of  $\mathbf{q}$ -points: 19 (circles and full line) coming from the 10  $\mathbf{k}$ -points Monkhorst–Pack [3] grid and 44 (squares and dashed line), corresponding to the 28  $\mathbf{k}$ -points MP grid. Changing the broadening  $\eta$  we see great oscillations in both the curves, with very different values at low broadening.

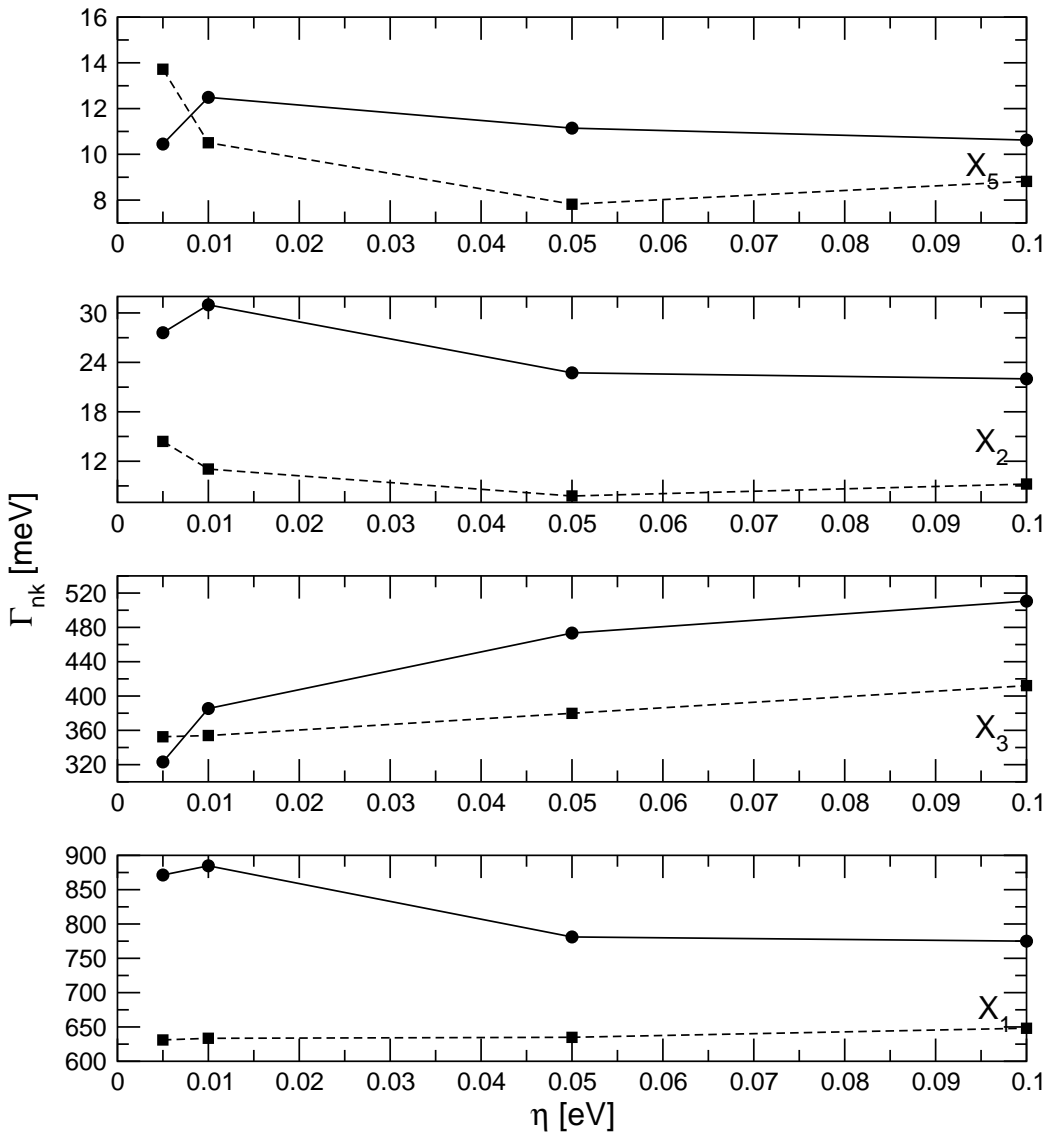


Figure 4.2: Quasiparticle widths (Eq. (4.8)) at of 89  $\mathbf{G}$ 's vectors, 20 bands in the RPA polarization and for  $\eta = 5, 10, 50, 100$  meV. Two different sets of  $\mathbf{q}$ -points are used: 19 (circles and full line) and 44 (squares and dashed line).



This result is rather unsatisfactory, because, theoretically, we should retain only the width obtained in the  $\eta \rightarrow 0$  limit. In the presence of results not depending on the  $\eta$  value (like in the QP energies case) this parameter is not critical but in the present case its effect on the QP widths is enormous. Clearly we have an indication of the poor  $\mathbf{k}$  sampling of the BZ, that gives large numerical noise in the screening function.

A first solution could be to increase the number of  $\mathbf{k}$ -points (and the corresponding  $\mathbf{q}$  grid) in the RPA polarization function construction leading to an increasing numerical weight. Although this is the general procedure used in the literature, an alternative approach can be introduced, following the ‘‘Random Integration Method’’ discussed in Section 3.3.1. From Eqs. (3.21) (3.23) and (3.24) the RPA polarization function  $\chi_{\mathbf{G},\mathbf{G}'}^0(\mathbf{q},\omega)$  defines the symmetric dielectric function  $\tilde{\epsilon}_{\mathbf{G},\mathbf{G}'}^{-1}(\mathbf{q},\omega)$ , whose poor sampling is the origin of the results of Fig. 4.2. Therefore, we adopt the following ansatz

$$\begin{aligned} \chi_{\mathbf{G},\mathbf{G}'}^0(\mathbf{q},\omega) &= 2 \sum_{n n'} \int_{BZ} \frac{d\mathbf{k}}{(2\pi)^3} [\tilde{\rho}_{nn'}(\mathbf{k},\mathbf{q},\mathbf{G})]^* \tilde{\rho}_{nn'}(\mathbf{k},\mathbf{q},\mathbf{G}') \\ & [f_{n'(\mathbf{k}-\mathbf{q})}(1-f_{n\mathbf{k}})] \left[ \frac{1}{\omega - \epsilon_{n\mathbf{k}} + \epsilon_{n'(\mathbf{k}-\mathbf{q})} + i\delta} - \frac{1}{\omega - \epsilon_{n'(\mathbf{k}-\mathbf{q})} + \epsilon_{n\mathbf{k}} - i\delta} \right] \\ & \approx 2 \sum_{n n'} \sum_{\mathbf{k}_i} [\tilde{\rho}_{nn'}(\mathbf{k}_i,\mathbf{q},\mathbf{G})]^* \tilde{\rho}_{nn'}(\mathbf{k}_i,\mathbf{q},\mathbf{G}') \\ & \int_{BZ'(\mathbf{k}_i)} \frac{d\mathbf{k}}{(2\pi)^3} \left\{ [f_{n'(\mathbf{k}-\mathbf{q})}(1-f_{n\mathbf{k}})] \left[ \frac{1}{\omega - \epsilon_{n\mathbf{k}} + \epsilon_{n'(\mathbf{k}-\mathbf{q})} + i\delta} - \right. \right. \\ & \left. \left. \frac{1}{\omega - \epsilon_{n'(\mathbf{k}-\mathbf{q})} + \epsilon_{n\mathbf{k}} - i\delta} \right] \right\}. \quad (4.9) \end{aligned}$$

Like in the case of the bare exchange self-energy in Eq. (4.9) the oscillator strengths are supposed to remain constant in each ‘‘small BZ’’  $BZ'(\mathbf{k}_i)$ . These regions are defined in Section 3.3.1 starting from a  $\mathbf{q}$ -grid. In this case the same procedure is used for a  $\mathbf{k}$ -grid. The only requirement is that the base set of  $\mathbf{k}$ -points must itself be a Bravais Lattice. The last two lines of Eq. (4.9) can be considered as a random integration of the *Green’s function part* of the RPA polarization and we expect that using a large set of  $\mathbf{k}$ -points (and energies  $\epsilon_{n'(\mathbf{k}-\mathbf{q})}$  and  $\epsilon_{n\mathbf{k}}$ ) to integrate its energy dependence the corresponding polarization functions will be much smoother.

An illustration of Eq. (4.9) is showed in Fig. 4.3, where the absorption spectrum of copper is shown using Eq. (3.22) (naively discretized) and Eq. (4.9). Compared with a fully converged  $\epsilon_2$ , the method introduced above improves considerably the lineshape of the two spectra calculated with only 29 and 72 MP  $\mathbf{k}$ -points in the IBZ. The  $BZ'(\mathbf{k}_i)$  integrals are performed with a set of 5,000 random points divided in

each small BZ.

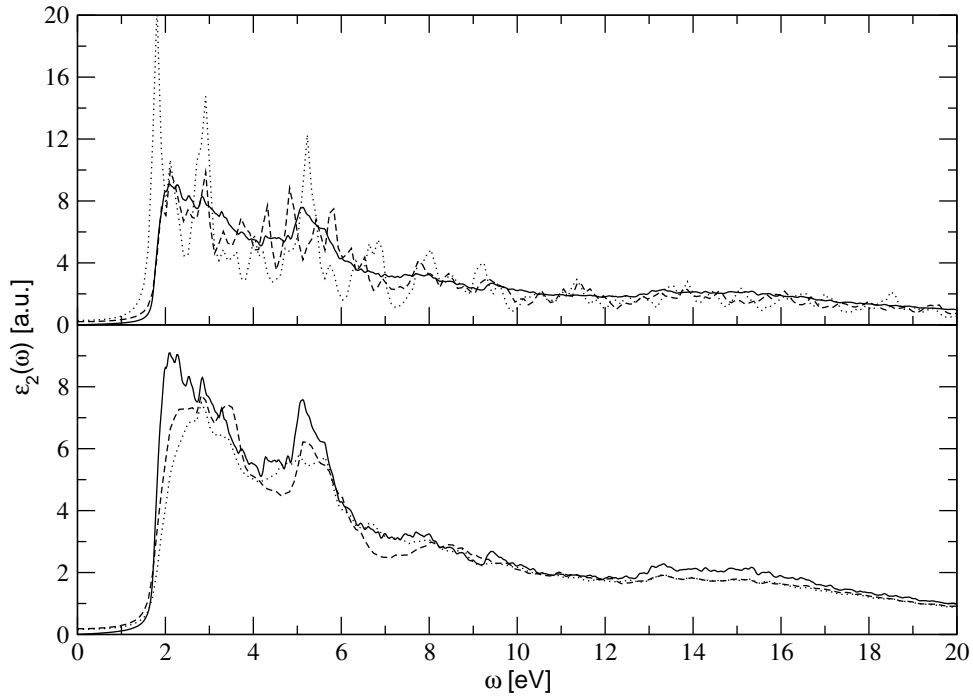


Figure 4.3: Dielectric function calculated with and without the “random integration method” of Eq. (4.9). In both frames: 29  $\mathbf{k}$ -points grid (dotted line), 72  $\mathbf{k}$ -points grid (dashed line) and 11,000 random  $\mathbf{k}$ -points in all the BZ (full line). In the upper frame the RPA polarization is calculated naively, while in the lower frame the “random integration method” is used with 5,000  $\mathbf{k}$ -points in all the BZ used to integrate the small  $BZ'(\mathbf{k}_i)$ .

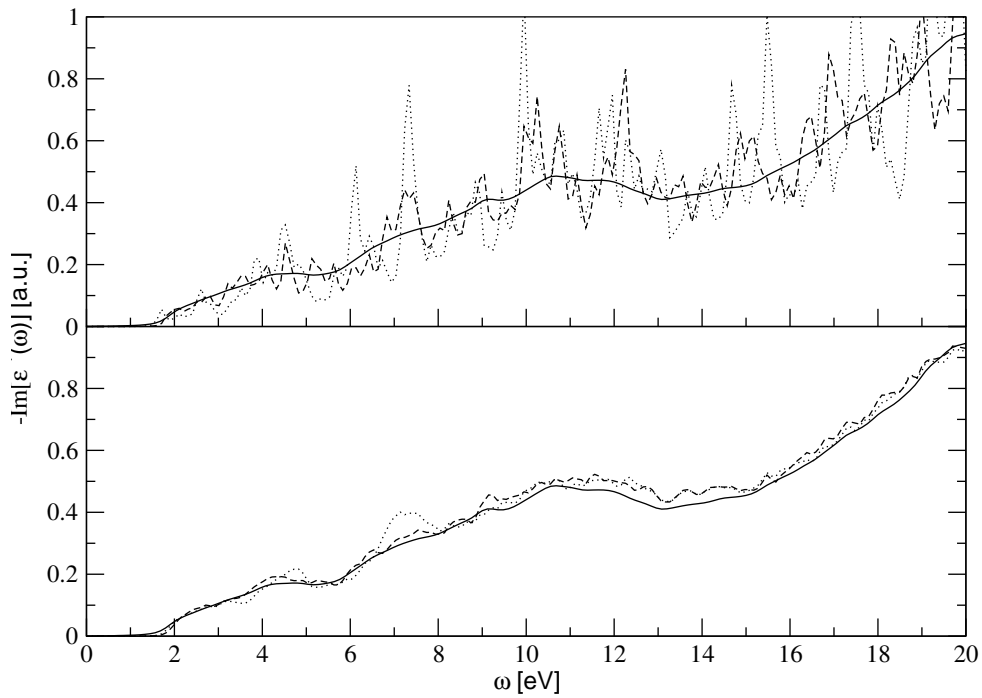


Figure 4.4: As in Fig. 4.3 for the EEL spectra.

For the calculation of the QP widths the inverse dielectric function must be calculated. In Fig. 4.4 the same comparison is made for the EEL spectra. In the upper frame the oscillations responsible of the bad behavior of  $\Gamma_{n\mathbf{k}}$  shown in Fig. 4.2 are evident. In the lower frame these oscillations are much smaller and, as showed in Fig. 4.5 the effect on  $\Gamma_{n\mathbf{k}}$  is crucial. On lowering the broadening  $\eta$  for all the bands at the X point, a 5% relative discrepancy between the widths calculated with 19 and 44  $\mathbf{q}$  points is found and, most importantly, this result is achieved with a low computational load. Hence all the calculations from now on will be performed at  $\eta = 5$  meV, which can be considered to be the required  $\eta \rightarrow 0$  limit of the QP widths.

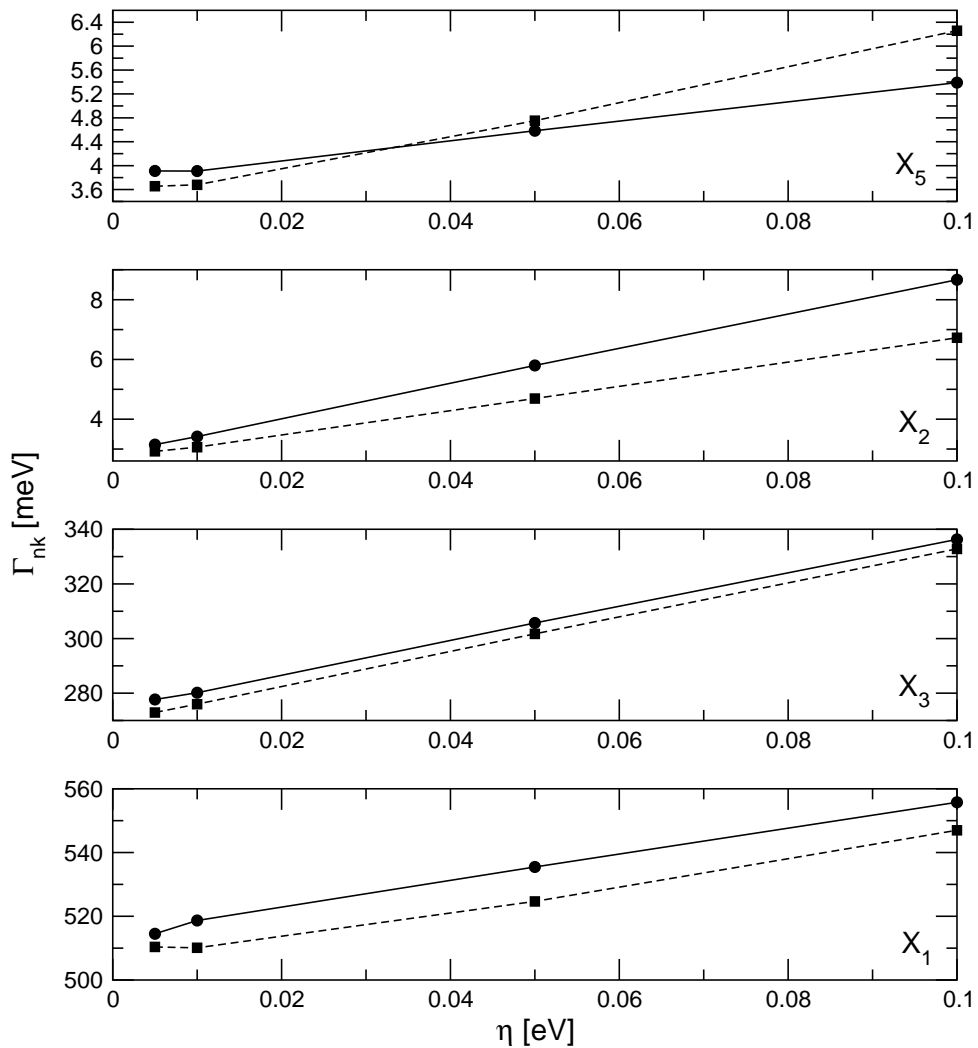


Figure 4.5: As in Fig. 4.2 but using the “random integration method” of Eq. (4.9). 1,000 random  $\mathbf{k}$ -points in all the BZ are used to integrate the small  $BZ'(\mathbf{k}_i)$ .

Although the calculation time is now largely reduced, a last test should be made on the number of  $\mathbf{k}$ -points required to converge Eq. (4.9). In Fig. 4.5 a random

set of  $\mathbf{k}$ -points was used. However, using random points Eq. (4.9) cannot be used as it is, because the transitions  $n\mathbf{k} \rightarrow n'(\mathbf{k} - \mathbf{q})$  always conserves the transferred momenta  $\mathbf{q}$ . A random grid corresponds to a random  $\mathbf{q}$  grid, whereas we want to use a MP  $\mathbf{q}$ -grid. To overcome this point the transitions  $n\mathbf{k} \rightarrow n'(\mathbf{k} - \mathbf{q})$  are defined allowing transitions from any  $\mathbf{k}$ -point contained in the  $BZ'(\mathbf{k})$  to any  $\mathbf{k}$ -point in  $BZ'(\mathbf{k} - \mathbf{q})$ . This corresponds a numerical uncertainty on the transferred momenta  $\mathbf{q}$  that, however, is consistent with the numerical integration defined with Eq. (4.7).

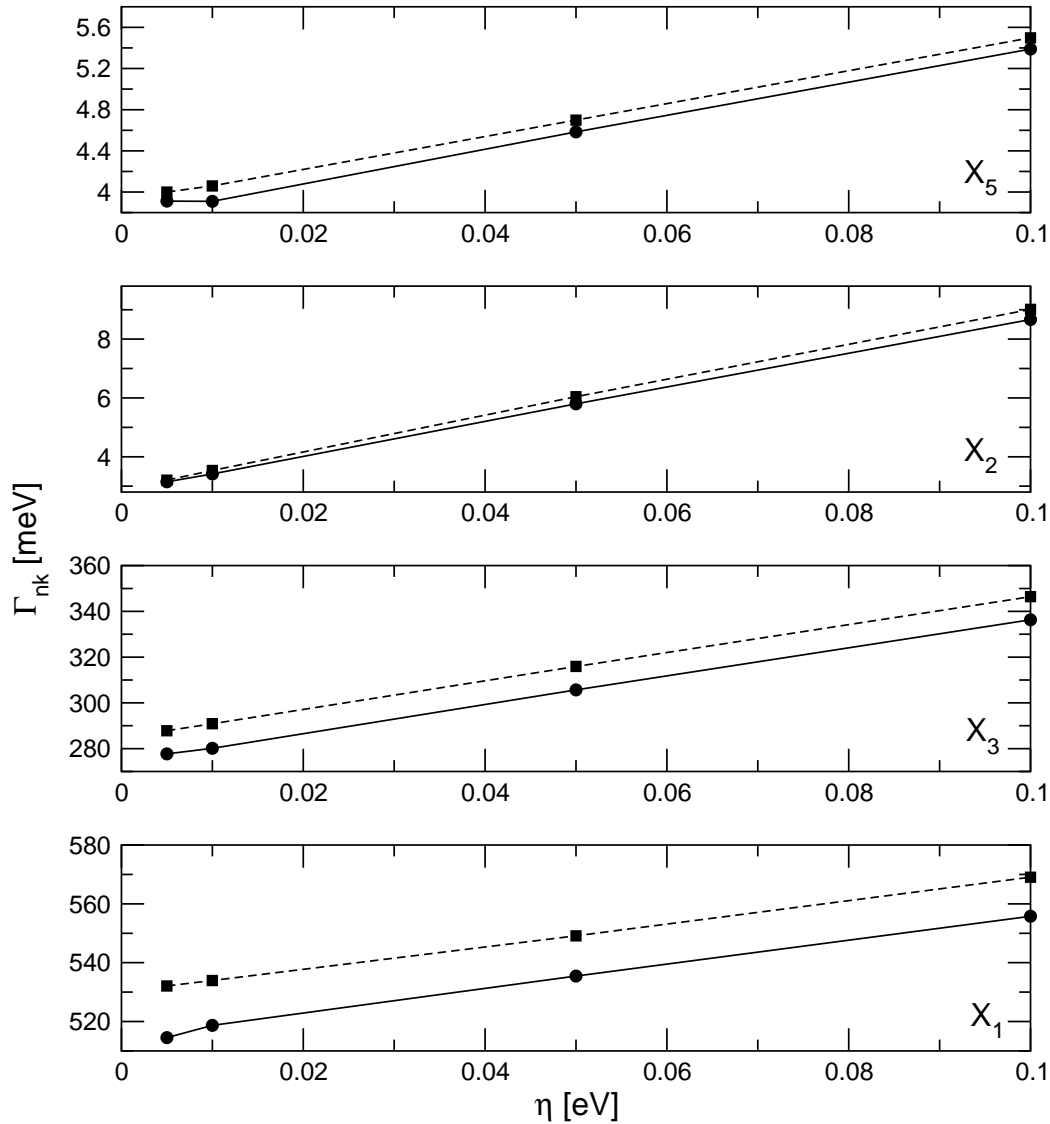


Figure 4.6: Quasiparticle widths (Eq. (4.8)) at 89  $\mathbf{G}$ 's vectors, 20 bands in the RPA polarization and for 19  $\mathbf{q}$ 's in the IBZ. Two different sets of  $\mathbf{k}$ -points in the integration of Eq. (4.9) are used: 1,000 (circles and full line) and 5,000 (squares and dashed line).

Using this “trick” we can minimize, also, the number of random  $\mathbf{k}$ -points, as shown in Fig. 4.6, where calculations at 19  $\mathbf{q}$ 's and 89  $\mathbf{G}$ 's are done with 1,000 and

5,000  $\mathbf{k}$ -points in the electron/hole Green's function integration. We find that fully converged results are obtained using 1,000  $\mathbf{k}$ -points.

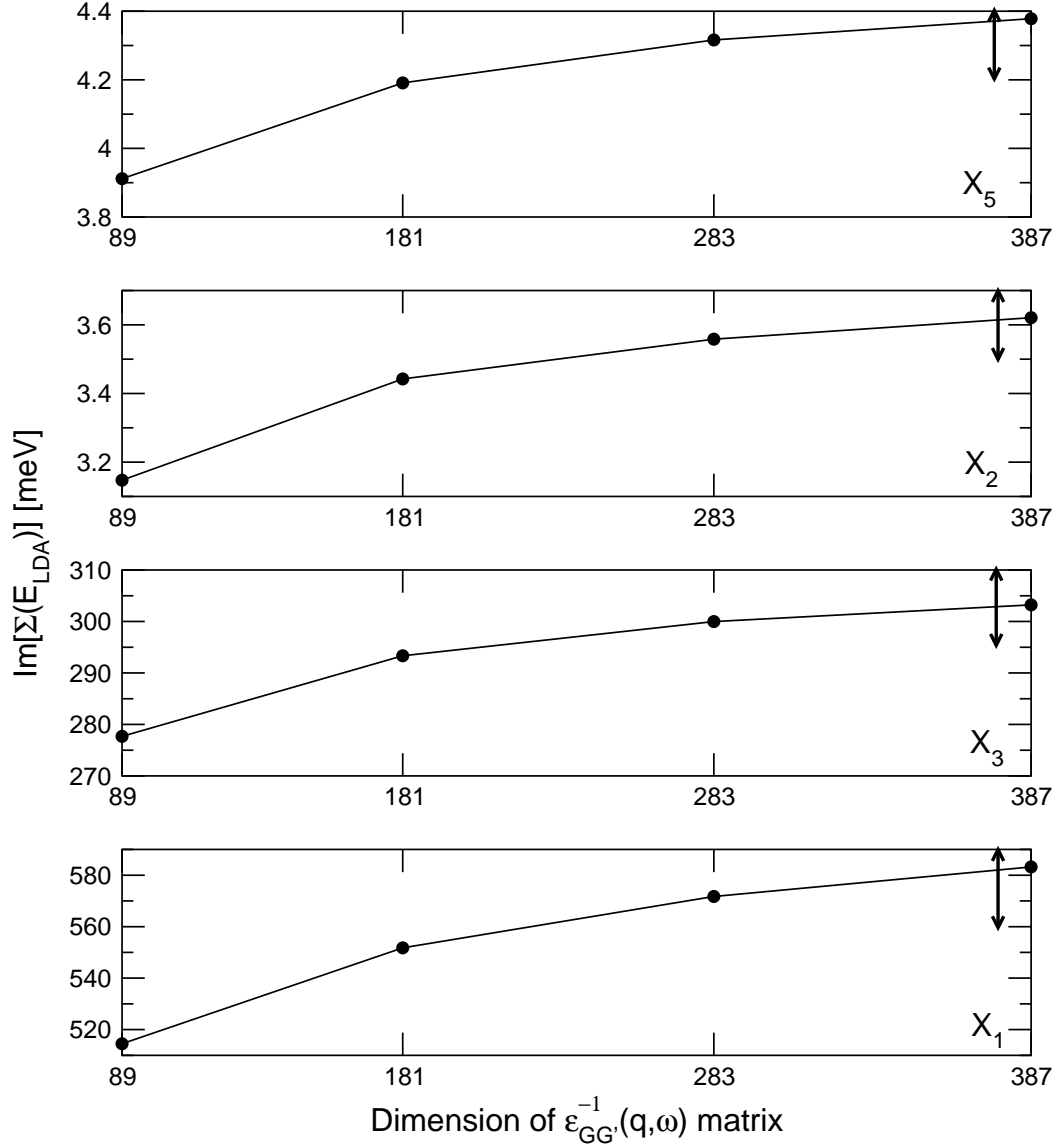


Figure 4.7: Quasiparticle widths (Eq. (4.8)) as function of the number of  $\mathbf{G}$ 's in the inverse dielectric function. 20 bands in the RPA polarization are used, 19  $\mathbf{q}$ 's in the IBZ,  $\eta = 5$  meV and 1,000  $\mathbf{k}$ -points in the integration of Eq. (4.9). Vertical arrows indicates the 5% of the converged value chosen as maximum numerical margin.

The last parameters to fix are the number of  $\mathbf{G}$  components of the inverse dielectric matrix and the number of bands in the RPA polarization function. In Fig. 4.7 the bands in  $\chi^0$  are fixed at 20 and the  $\mathbf{G}$  components are increased until convergence is reached. We note that QP widths requires a (slight) lower number of  $\mathbf{G}$  with respect to the real part, 283 compared to 307.

Band	20 bands in $\chi^0$	40 bands in $\chi^0$	Relative error
$X_1$	3.91	4.27	8%
$X_3$	3.15	3.09	2%
$X_2$	277.70	288.28	4%
$X_5$	514.52	523.79	2%

Table 4.1: Comparison of the QP widths at the X point obtained using 20 and 40 bands in the RPA polarization. 89  $\mathbf{G}$ 's are used.

The effect of the number of bands used to construct  $\chi^0$  is shown in Table 4.1 where the result of the calculations with 20 and 40 bands are compared. 89  $\mathbf{G}$ 's are used. All the relative errors agree within 10%, and only the value at  $X_1$  is above the 5% margin.

### 4.3 Results and discussion

In all the preceding chapters we have used the notation  $GW$  to indicate the non-selfconsistent solution of the Dyson equation. Since, in the following sections, we will study the effect of self-consistency, I will refer to the QP energies found in Chapter 3 as  $G_0W_0$  results.

Eq. (4.8) fully neglects the QP correction  $Re \left[ \sum_{n\mathbf{k}} \left( \epsilon_{n\mathbf{k}}^{QP,0} \right) \right]$  assuming  $\epsilon_{n\mathbf{k}}^{QP,0} = \epsilon_{n\mathbf{k}}^{DFT-LDA}$  and consequently  $Z_{n\mathbf{k}} = 1$ . We will refer to them as “on shell”  $G_0W_0$  because the input energies of the QP equation are supposed to remain constant and used to calculate the QP lifetimes.

In Fig. 4.8 we compare the “on shell”  $G_0W_0$  calculation with  $G_0W_0$ , the full solution of Eqs. (4.1–4.3) and the experimental results [2] for the states  $X_3, \Gamma_{25'}, \Gamma_{12}, X_2$  and  $X_5$ . The “on shell”  $G_0W_0$  yields lifetimes underestimated by a factor of 4 at the top of the  $d$ -bands and overestimated by a factor of 3 at the  $d$ -bands bottom while the  $G_0W_0$  results are in good agreement with experiment. Also, the energy position of the quasiparticle peaks are well reproduced in  $G_0W_0$ , while in the “on shell” calculation the QP energies are spread over a larger range of energies reflecting the well-known discrepancies between DFT–LDA and experimental band structure. The origin for the large lifetime differences between the two calculations are the QP corrections for the  $d$ -bands of copper which are completely neglected in the “on shell” calculations.

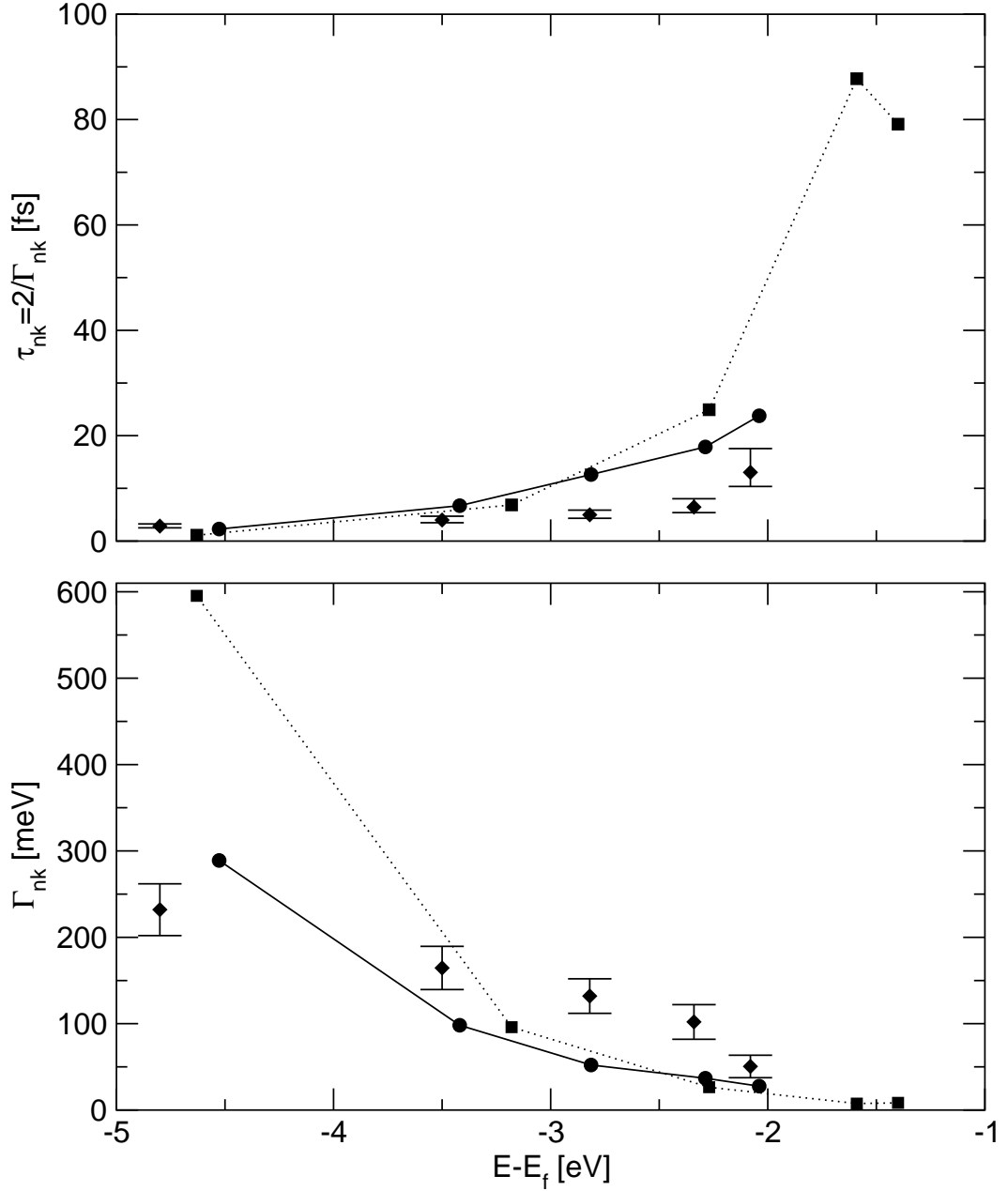


Figure 4.8: Quasiparticle lifetimes (upper frame) and widths (lower frame) calculated within “on shell”  $G_0W_0$  (dotted line and squares) and  $G_0W_0$  (full line and circles) compared with experiment [2] (diamonds). QP energies are relative to the Fermi level.

Because of the inclusion of these non trivial corrections,  $d$  levels acquire important decay channels that are completely neglected in the “on shell” approach. These can be understood by rewriting the hole contribution to Eq. (4.7) as follows:

$$\Gamma_{nk}^{hole} \propto \sum_{n'} \sum_{\mathbf{q}} \text{Im} \left[ W_{n\mathbf{k} \rightarrow n'(\mathbf{k}-\mathbf{q})} \left( \epsilon_{n'(\mathbf{k}-\mathbf{q})}^{DFT-LDA} - \epsilon_{n\mathbf{k}}^{QP,0} \right) \right] \theta \left( \epsilon_{n'(\mathbf{k}-\mathbf{q})}^{DFT-LDA} - \epsilon_{n\mathbf{k}}^{QP,0} \right) f_{n'(\mathbf{k}-\mathbf{q})}, \quad (4.10)$$

where  $W(\omega)$  is the dynamically screened potential. For the top of the  $d$  bands  $G_0W_0$  yields negative QP corrections, as shown in Fig. 3.7 and Table 3.4 of Chapter 3. This means that Eq. (4.10) also contains contributions coming from the decay of the QP  $d$  band to *exactly the same* DFT–LDA band. We will refer to these transitions as “intraband decay channels”. These contributions are important because the  $d$ -bands of copper are flat and the corresponding density of states is large. In the “on shell” calculation the intermediate states ( $n'(\mathbf{k} - \mathbf{q})$  in Eq. (4.8)) have the same energies of the quasiparticle; this means that the “intraband decay channels” are not allowed, as explained at the end of Section 4.1. This leads to the usual interpretation of the large lifetimes calculated at the top of the  $d$  bands as being due to the fact that these  $d$  states can decay only in  $s/p$  states that contribute less than bands with the same character.

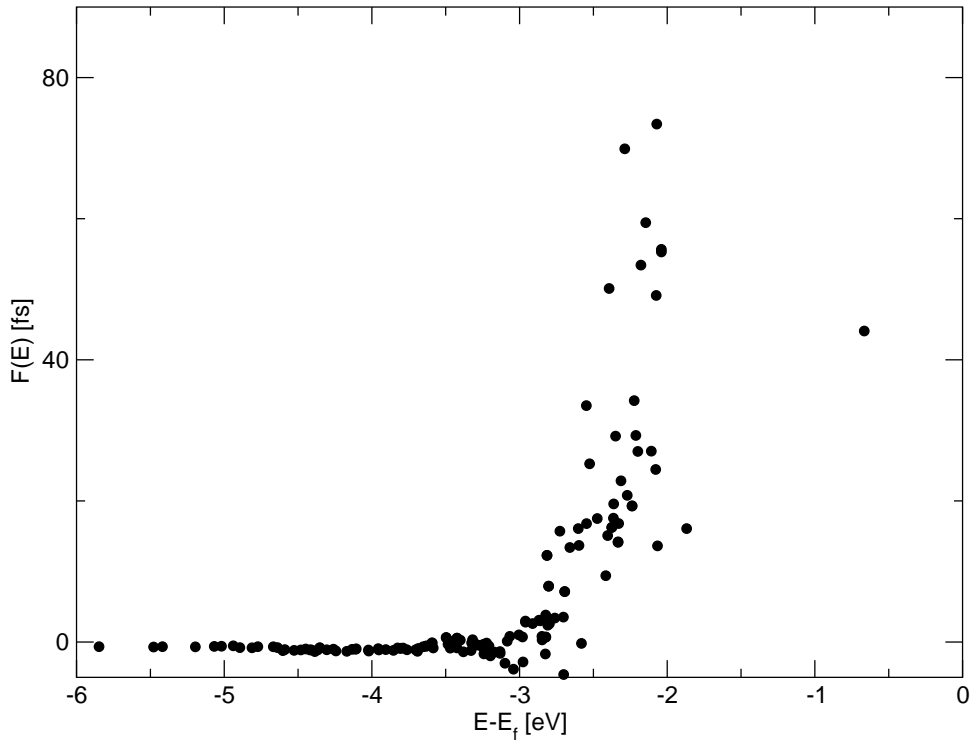


Figure 4.9: Difference of the quasiparticle lifetimes calculated within “on shell”  $G_0W_0$  and full  $G_0W_0$  for a large set of  $\mathbf{k}$ -points and bands.

The great importance of these “intraband decay channels” in  $G_0W_0$  is shown also in Fig. 4.9 where we plot the function

$$F\left(\epsilon_{n\mathbf{k}}^{QP,0}\right) \equiv 2 \left( \frac{1}{\text{Im} \left[ M_{n\mathbf{k}} \left( \epsilon_{n\mathbf{k}}^{DFT-LDA} \right) \right]} - \frac{1}{\text{Re} \left[ Z_{n\mathbf{k}} \right] \text{Im} \left[ M_{n\mathbf{k}} \left( \epsilon_{n\mathbf{k}}^{QP,0} \right) \right]} \right), \quad (4.11)$$



which contains contribution mainly from these channels. We see that in the region of the d-bands the difference is as large as 80 fs, and it constitutes the main contribution to the hole lifetime. This confirms that, in order to reproduce correctly the experimental data, these "intraband decay channels" must be included. Moreover their presence is a direct consequence of the strong QP corrections found in the last chapter.

## 4.4 A model self-consistent calculation

Even if the results of  $G_0W_0$  are in good agreement with experiment a natural question is the physical meaning of the "intraband decay channels" described above. Not being at self-consistency, the solid is described within  $G_0W_0$  as composed of quasiparticle states and virtual states (those involved in the hole decay) with different energies. The "on shell" approximation removes this difference describing both sets of states within DFT-LDA.

Mathematically the virtual states are, in Eq. (4.10), those called  $|n'(\mathbf{k} - \mathbf{q})\rangle$ . Although Eq. (4.10) contains a delta function that conserves the energy in the transition  $|n\mathbf{k}\rangle \rightarrow |n'(\mathbf{k} - \mathbf{q})\rangle$  mediated by the screening function these virtual state are *not* stable, physical, states. The delta function is a consequence of the approximated non selfconsistent approach we are using. By physical states I mean observable states. The physical quantity is the imaginary part of the interacting Green's function  $G_{n\mathbf{k}}(\omega)$  that, near the quasiparticle peak, is characterized by an energy indetermination allowed by uncertainty principle. So there is no way to select any of these intermediate states.

But, in any case, the description given by  $G_0W_0$  is, in some way, surprising. A satisfactory approximation for the self-energy operator, as we already know from Chapter 1, should preserve some conserved quantities, and this is achieved only at self-consistency. So, physically, within the quasiparticle approximation I should expect a description of the interacting system all in term of quasiparticle and not of different types of particles.

However if the  $G_0W_0$  approach to lifetimes seems to contain some physical contradictions the mathematical framework puts the results on a firm ground. The "intraband decay channels" derive from the fact that we are *not* at self-consistency; they must be included because of their relation to the same method that yields quasiparticle energies in such good agreement with experiment.

At this point a natural question is: "*can selfconsistency solve this apparent con-*

tradiction confirming the results of  $G_0W_0$  found in this and in the last chapter?".

So far a full selfconsistent  $GW$  calculation has been carried out only for the homogeneous electron gas [4] and simple semiconductors and metals [5] yielding results generally worse than the non selfconsistent  $G_0W_0$ . If the construction of the selfconsistent  $GW$  self-energy is a formidable task even for the simple systems mentioned above, in copper the update of the screening function is numerically rather demanding for the presence of localized  $d$  orbitals. To test the effect of selfconsistency on QP energies and lifetimes we use a simplified  $GW_0$  method where the self-energy operator is defined as

$$\Sigma^i(\mathbf{r}, \mathbf{r}'; \omega) \equiv \int_{\mathcal{C}} d\omega' G_{i-1}(\mathbf{r}, \mathbf{r}'; \omega') W_0(\mathbf{r}, \mathbf{r}'; \omega - \omega'), \quad (4.12)$$

where  $i$  is the iteration number (for  $i = 0$  we have DFT-LDA).  $\mathcal{C}$  is the contour in the complex frequency plane defined as a straight line from  $-\infty$  to  $0$  just above the real axes and from  $0$  to  $\infty$  below.  $G_{(i-1)}$  involves the QP energies obtained from  $\Sigma_{(i-1)}$  without considering renormalization factors, lifetimes and energy structures beyond QP peaks

$$G_i(\mathbf{r}, \mathbf{r}'; \omega) = 2 \sum_n \sum_{\mathbf{k} \in BZ} \phi_{n\mathbf{k}}(\mathbf{r}) \phi_{n\mathbf{k}}^*(\mathbf{r}) \left[ \frac{f_{n\mathbf{k}}}{\omega - \text{Re}(\epsilon_{n\mathbf{k}}^{QP,i}) - i\delta} + \frac{1 - f_{n\mathbf{k}}}{\omega - \text{Re}(\epsilon_{n\mathbf{k}}^{QP,i}) + i\delta} \right]. \quad (4.13)$$

I have supposed that the occupation numbers remain mainly unchanged. Analogously to Eq.(4.1-4.3) we define

$$\Gamma_{n\mathbf{k}}^i = \text{Re} [Z_{n\mathbf{k}}^i] \text{Im} \left[ M_{n\mathbf{k}}^i \left( \epsilon_{n\mathbf{k}}^{QP,i} \right) \right], \quad (4.14)$$

with

$$Z_{n\mathbf{k}}^i = \left( 1 - \left| \frac{dM_{n\mathbf{k}}^i(\omega)}{d\omega} \right|_{\omega=\epsilon_{n\mathbf{k}}^{QP,i}} \right)^{-1}, \quad (4.15)$$

and  $\epsilon_{n\mathbf{k}}^{QP,i}$  the solution of Dyson equation

$$\epsilon_{n\mathbf{k}}^{QP,i} = \epsilon_{n\mathbf{k}}^{QP,i-1} - \left[ \Sigma_x^{n\mathbf{k}} + \Re \left[ M_{n\mathbf{k}}^i \left( \epsilon_{n\mathbf{k}}^{QP,i} \right) \right] + M_{n\mathbf{k}}^{core} - V_{xc}^{n\mathbf{k}} \right]. \quad (4.16)$$

Clearly for  $i = 0$  we have that  $\epsilon_{n\mathbf{k}}^{QP,i} = \epsilon_{n\mathbf{k}}^{DFT-LDA}$ . As the QP bandstructure resulting from the first iteration is in excellent agreement with experiment, our first step is an “on shell”  $G_1W_0$  calculation. This means that the quasiparticle energies are fixed at the  $G_0W_0$  level and the lifetimes are calculated as

$$\Gamma_{n\mathbf{k}}^{i=2, on-shell} = \text{Re} [Z_{n\mathbf{k}}^{i=1}] \text{Im} \left[ M_{n\mathbf{k}}^{i=2} \left( \epsilon_{n\mathbf{k}}^{QP,i=1} \right) \right]. \quad (4.17)$$

The resulting lifetimes are compared with experiment in Fig. 4.10. We see that forcing the QP energies to be equal to those of the intermediate virtual states lifetime results are similar to those of the “on shell”  $G_0W_0$  method. The same overestimation of the top of the  $d$  bands lifetime is found. This confirms that the key to understand the qualitative agreement of  $G_0W_0$  is the inclusion of the “intraband decay channels” described by Eq. (4.8).

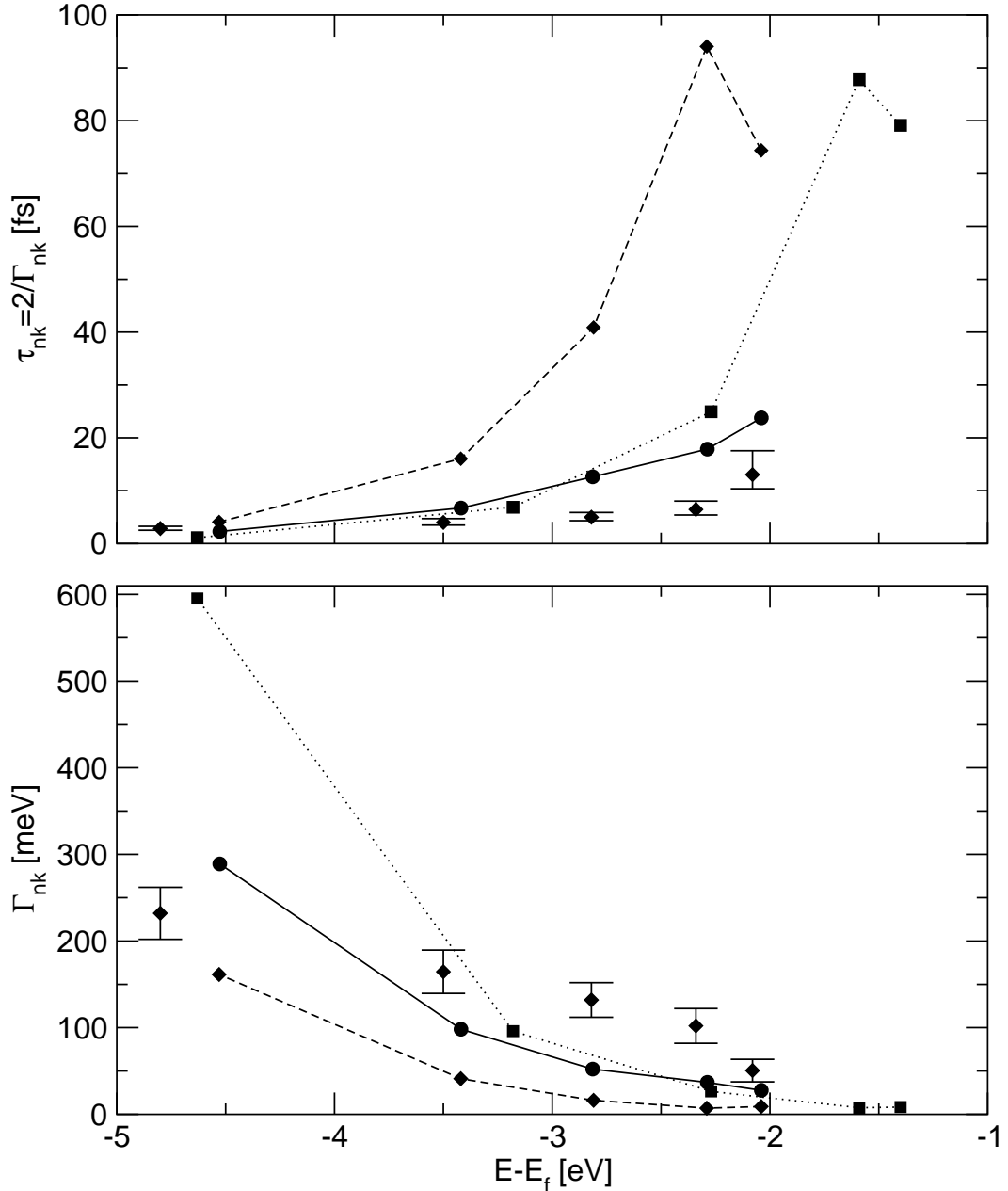


Figure 4.10: Quasiparticle lifetimes (upper frame) and widths (lower frame) calculated within “on shell”  $G_0W_0$  (dotted line and squares),  $G_0W_0$  (full line and circles) and “on shell”  $G_1W_0$  (dashed line and diamonds) compared with experiment [2] (diamonds). QP energies are relative to the Fermi level.

A further question could be whether selfconsistency leaves unchanged the good quasiparticle energies obtained within  $G_0W_0$  while improving the lifetimes. However at higher iteration orders of the  $GW_0$  QP equation the resulting energies worsen, as shown in Table 4.2. The  $d$ -bands width decreases and the agreement with experiment worsens, with discrepancies well above the DFT–LDA values.

		DFT–LDA	$G_0W_0$	$G_1W_0$	$G_2W_0$	Experiment
	$\Gamma_{12} - \Gamma_{25'}$	0.91	0.60	0.38	0.23	0.81
Widths of	$X_5 - X_3$	3.23	2.49	1.99	1.65	2.79
	$X_5 - X_1$	3.70	2.90	2.31	1.92	3.17
$d$ -bands	$L_3 - L_3$	1.58	1.26	1.03	0.90	1.37
	$L_3 - L_1$	3.72	2.83	2.13	1.65	2.91
L-gap	$L_1 - L_{2'}$	5.40	4.76	4.78	3.77	4.95

Table 4.2: Comparison of experimental bands widths of copper with first five  $GW_0$  iterations.

The increasing disagreement of the QP band structure at increasing iterations of the Dyson equation does not allow any further study of the lifetimes. This is because energies and width are strictly linked, as discussed before, and we expect that an increasing disagreement in QP band structure leads to similar result for the lifetimes.

The results presented so far suggest further research in the field of vertex corrections beyond  $GW$ . As the “intraband decay channels” found are characteristic of a non selfconsistent treatment of  $GW$ . At self-consistency these channels disappear and, from what I have found, lifetimes are expected to show the general behavior of the “on-shell” calculations discussed above.

Although the  $GW_0$  treatment used in this chapter approximates the analytic form of the Green’s function  $G$  with those described in Eq. (4.13) the results obtained seem rather general. To clarify better this point, and in order to generalize the conclusions of this section, a further application of the present  $GW_0$  approach to silicon is presented.

#### 4.4.1 The case study of silicon

The application of the same approach described with Eq. (4.12–4.16) for silicon reveals a simple interpretation for the reason of the “bad-performance” of the approximated  $GW_0$  approach proposed in the last section.

	DFT-LDA	$G_0W_0$		$G_1W_0$	Experiment	
		Present work	HL	GSS		
$\Gamma$ gap	2.56	2.93	3.35	3.30	3.27	3.40
$X$ gap	3.50	3.90	4.43	3.39	4.27	4.2 $4.6 \pm 0.2$
$L$ gap	2.76	3.21	3.54		3.62	3.45
$X_5 - \Gamma_4$	0.60	0.87	1.29	1.24	1.12	1.17

Table 4.3: Comparison of experimental silicon gaps with  $G_{i=0,1}GW_0$ , DFT-LDA and various calculations found in literature. HL: Hybertsen and Louie [7], using Plasmon-Pole approximation. GSS: Godby, Schlüter and Sham [8], without Plasmon-Pole approximation, using imaginary frequency integration.

As expected, the same approach used for copper yields, for the direct gaps at  $\Gamma, X, L$  and for the indirect gap, the results shown in Fig. (4.11) (presented in detail in Table 4.3). All the gaps increases monotonically and, rather interesting, an excellent agreement with the experimental values is obtained at the  $G_1W_0$  level [6].

This is not in agreement with previous results obtained using the Plasmon-Pole approximation [7] or a full screening calculation with the frequency integral of Eq. (4.12) made on the imaginary axes [8] with a small number of frequencies. The discrepancies may be linked to the approximations involved in these calculations and the present result can be assumed to be more accurate.

A simple interpretation of the results obtained so far can be made using a simple, and reasonable assumption on the frequency dependence of the  $G_iW_0$  self-energy operator. We assume that the quasiparticle states follows a simple scissor-operator behavior

$$\epsilon_{n\mathbf{k}}^{QP,i} \sim \epsilon_{n\mathbf{k}}^{QP,i-1} + \begin{cases} \Delta_c^i < 0 & n \text{ conduction} \\ \Delta_v^i > 0 & n \text{ valence} \end{cases}, \quad (4.18)$$

Considering only the hole contribution ( $\Gamma_h$  function, first line of Eq. (4.4)) to the valence self-energy, and only the electron contribution ( $\Gamma_e$  function, second line of Eq. (4.4)) to the conduction self-energy we would obtain

$$\Sigma_{n\mathbf{k}}^i(\omega) = \Sigma_x^{n\mathbf{k}} + M_{n\mathbf{k}}^i(\omega) - V_{xc}^{n\mathbf{k}} \sim \Sigma_{n\mathbf{k}}^{i-1}(\omega - \Delta_{c/v}^{i-1}). \quad (4.19)$$

However, in order to account for the presence of the hole/electron contribution to the electron/hole part of the self-energy we use a modified version of this equation

$$\Sigma_{n\mathbf{k}}^i(\omega) \sim \Sigma_{n\mathbf{k}}^{i-1}(\omega - \alpha \Delta_{c/v}^{i-1}), \quad (4.20)$$

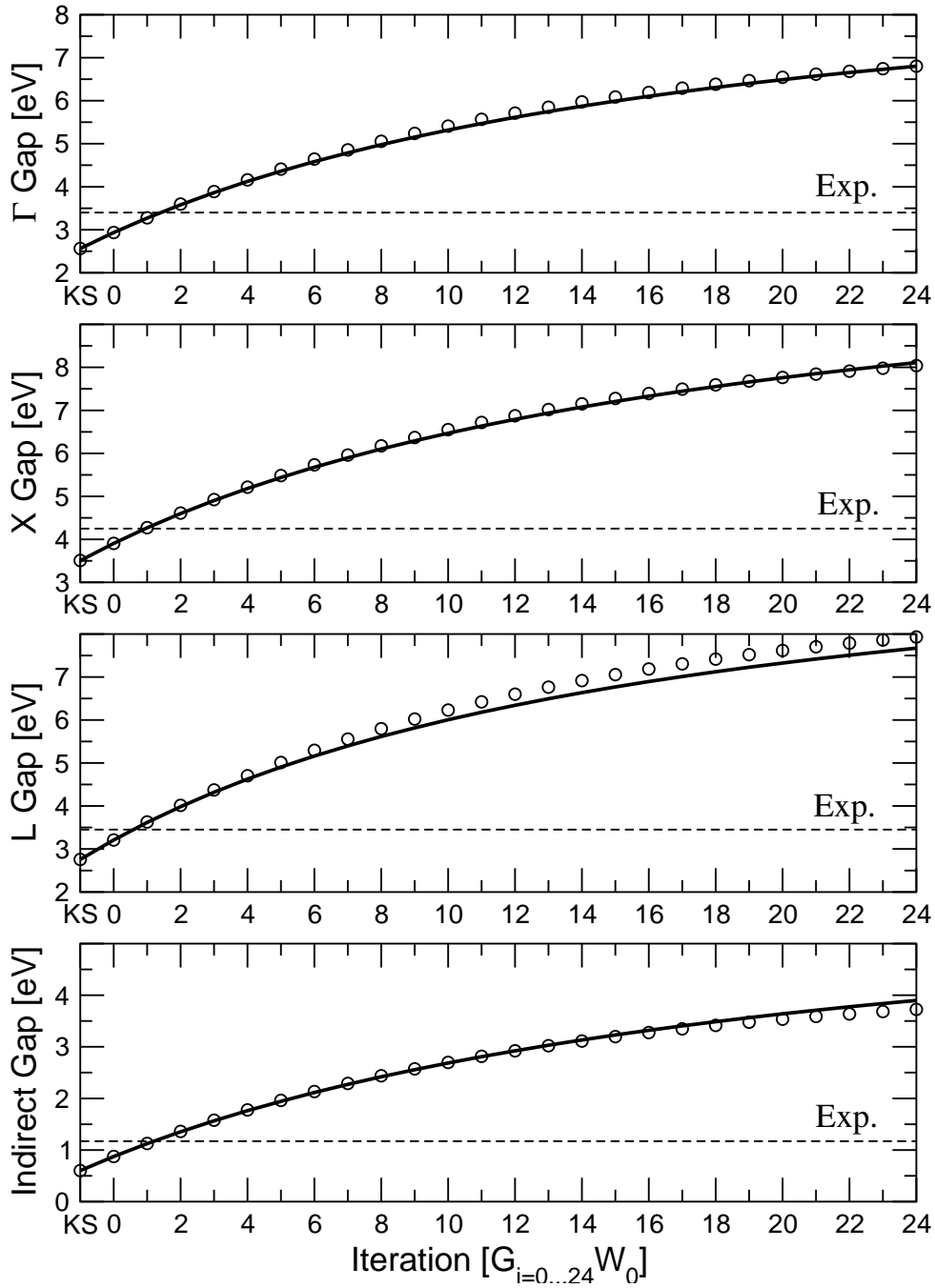


Figure 4.11: Quasiparticle gaps for silicon for several iterations of  $G_iGW_0$ . The dashed lines represent the experimental value (Tab. VII of Ref. [7]). Circles are the theoretical model to reproduce the self-consistency effects on the silicon gap (see text).

with  $\alpha$  to be considered as a parameter to be fixed later. Using this equation and assuming that

$$\left. \frac{d\Sigma_{n\mathbf{k}}^i(\omega)}{d\omega} \right|_{\omega=\epsilon_{n\mathbf{k}}^{QP,i}} = \beta \quad \forall i, \quad (4.21)$$

a closed solution of QP equation is obtained in a recursive form:

$$\Delta_{c/v}^i = \Delta_{c/v}^{i-1} \frac{(1 - \alpha\beta)}{(1 - \beta)}. \quad (4.22)$$

Fitting  $\alpha = 0.73196$  using the  $\Gamma$  gap behavior of Fig. 4.11 we obtain the data denoted by circles. The agreement is surprisingly good, illustrating that the assumption used is rough but reasonable. A further proof of the effect of the gaps opening on the  $G_iW_0$  iterative procedure is shown in Fig. 4.12. The real part of the  $\Gamma_{25'}$  self-energy moves toward higher binding energy as the iterations of the Dyson equation increases, as assumed above.

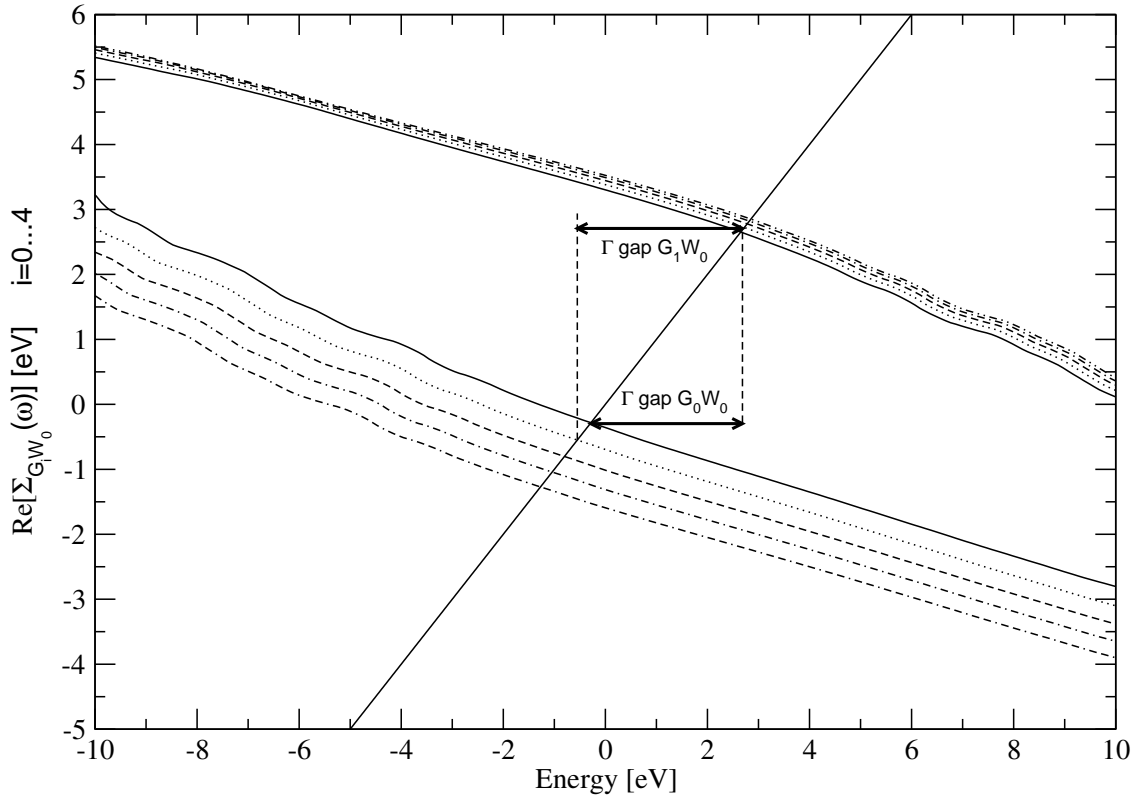


Figure 4.12: Real part of self-energy of silicon for  $\Gamma_{25'}$  (lower curves) and  $\Gamma_{15}$  (upper curves) for several iterations of  $G_iGW_0$  procedure. The function  $f(\omega) = \omega$  is also plotted; its intersection with the self-energy curve represents the quasiparticle energy. The increasing of  $\Gamma$  direct gap is shown schematically.

This study of Si has shown that the characteristics of the QP corrections found at the  $G_0W_0$  level (like the d-bands width increase, or the gap opening) are enhanced at higher orders of the simplified  $GW_0$  method used in this chapter. Moreover recently Olevano and Reining [9] showed, by using the self-energy to include quasiparticle corrections to the DFT-LDA energy bands without excitonic effects in the standard

RPA, that the shape of the plasmon peak worsens. The electron–hole interaction cancels the quasiparticle corrections improving the result. This means that a correct screening function with excitonic effects and QP corrections is similar to the RPA one used in the  $GW_0$  method. So the result presented here are indicative of what could happen if excitonic effects, or QP corrections are included in the screening function *without vertex corrections*.



# Bibliography

- [1] For a review see P.M. Echenique, J.M. Pitarke, E.V. Chulkov and A. Rubio, *Chemical Physics* **251**, 1 (2000).
- [2] A. Gerlach, K. Berge, A. Goldmann, I. Campillo, A. Rubio, J.M. Pitarke and P.M. Echenique *Phys. Rev. B* **64**, 085423.
- [3] H. J. Monkhorst and J. D. Pack, *Phys. Rev. B* **13**, 5188 (1976).
- [4] U.V. Barth and B. Holm, *Phys. Rev.* **B 54**,8411 (1996).
- [5] W.D. Schöne and A.G. Eguiluz, *Phys. Rev. Lett.* **81**, 1662 (1998).
- [6] X. Zhu and S. G. Louie, *Phys. Rev. B* **43**, 14142 (1991).
- [7] M. S. Hybertsen and S. G. Louie, *Phys. Rev. B* **34**, 5390 (1986).
- [8] R. W. Godby, M. Schlüter and L. J. Sham, *Phys. Rev. B* **37**, 10159 (1988).
- [9] V. Olevano and L. Reining, *Phys. Rev. Lett.* **86**, 5962 (2001).



# Chapter 5

## The plasmon resonance and the reflectance spectrum of Silver in the $GW$ approximation

Although the coexistence of quasiparticles and density-fluctuation excitations in a fully interacting system is a well known property, our knowledge of their properties and mutual interaction in real materials is far from being complete.

In the last two chapters I have showed that  $GW$  successfully describes the quasiparticle excitations of Cu. Starting from a non-interacting representation of the system, electrons and holes are screened by the surrounding electronic cloud created through the Coulomb interaction. The interaction of the undressed particle with the screening cloud is responsible, also, for the electron/hole damping, correctly reproduced within  $GW$  as shown in the last chapter. In contrast to the quasiparticle picture, describing the fully interacting system as a gas of non interacting renormalized particles, plasmons are due to collective modes. The plasmon frequency  $\omega_p$  is defined by the condition (see Eq. (1.44) in Section 1.1.1)

$$\epsilon''(\omega_p) = 0, \tag{5.1}$$

$$\epsilon'(\omega_p) = 0. \tag{5.1'}$$

Strictly speaking, Eqs. (5.1) have no real-valued solution. The plasmon can decay in electron/hole pairs acquiring a finite lifetime. This yields a formal analogy between plasmons and quasiparticles. Condition given in Eq. (5.1) also defines the relation between the plasmon frequency and the many body effects required to calculate the

dielectric function. This is defined (see Section 1.3.3) through the equation

$$\epsilon(\mathbf{r}, \mathbf{r}'; \omega) = \delta(\mathbf{r} - \mathbf{r}') - \int d\mathbf{r}'' \frac{1}{|\mathbf{r} - \mathbf{r}''|} \tilde{\chi}(\mathbf{r}'', \mathbf{r}'; \omega), \quad (5.2)$$

where  $\tilde{\chi}$  is the irreducible polarization. Thus to calculate  $\epsilon$  we must propose an approximation for  $\tilde{\chi}$ . As discussed in Section 1.3.3, equations defining  $\tilde{\chi}$  can be solved in a closed form only by approximating the interaction Kernel  $\tilde{\Xi}$ . The most intuitive physical process that should be included in the polarization function  $\tilde{\chi}$  are excitonic effects. However in the Baym–Kadanoff approach of Section 1.3.1 we have seen that a norm–conserving approximation for  $\tilde{\chi}$  is obtained by calculating  $\tilde{\Xi}$  from the same self–energy used to calculate the underlying band structure. If we want to correctly describe excitonic effects beyond the static approximation for the hole–electron interaction, we lose the simplicity of Hartree–Fock equation for  $\tilde{\chi}$  (See Eq. (1.131) and Fig. 1.3). Hedin’s equations, on the other hand, consider screened excitonic effects but the corresponding (norm–conserving) equation for  $\tilde{\chi}$  contains complicated vertex corrections.

What is done in practice is to use an approximation for the Bethe–Salpeter equation where the frequency dependence of the screening function is neglected. A three–points functions  $\tilde{L}(\mathbf{r}\mathbf{r}', \mathbf{r}''; \omega)$  is defined

$$\tilde{\chi}(\mathbf{r}, \mathbf{r}'; \omega) \equiv \lim_{\mathbf{r}'' \rightarrow \mathbf{r}'} \tilde{L}(\mathbf{r}\mathbf{r}', \mathbf{r}''; \omega), \quad (5.3)$$

solution of

$$\begin{aligned} \tilde{L}(\mathbf{r}\mathbf{r}', \mathbf{r}''; \omega) = & -i \left[ G_0(\mathbf{r}, \mathbf{r}''; \omega) \times G_0(\mathbf{r}'', \mathbf{r}'; \omega) \right] + \\ & \int d\tilde{\mathbf{r}} \tilde{\mathbf{r}} \left[ G_0(\mathbf{r}, \tilde{\mathbf{r}}; \omega) \times G_0(\tilde{\mathbf{r}}, \mathbf{r}'; \omega) \right] W(\tilde{\mathbf{r}}, \tilde{\mathbf{r}}; \omega = 0) \tilde{L}(\tilde{\mathbf{r}}\tilde{\mathbf{r}}, \mathbf{r}''; \omega), \end{aligned} \quad (5.4)$$

with  $\times$  indicating the convolution operator

$$f(\omega) \times g(\omega) \equiv \int d\omega' f(\omega') g(\omega - \omega'). \quad (5.5)$$

Although Eq. (5.4) has been used in many cases to calculate the absorption spectrum, its application to the EEL spectra has been faced only recently. In the case of silicon, Olevano and Reining [1] showed that using the *GW* self–energy to include quasiparticle (QP) corrections to the DFT–LDA energy bands, without including excitonic effects, worsens the shape of the plasmon peak with respect to experiment. Inclusion of both effects yields spectra very similar to DFT–LDA ones and to experiment. For simple metals, Ku and Eguiluz [2] obtained a correct positive dispersion

of the plasmon width in K simply using RPA. They showed that many-body effects (quasiparticle corrections and/or excitonic effects) are not required to get a good description of experimental data. These results agree with the general feeling that excitonic effects partially cancel self-energy corrections. A similar result has been found in Chapter 2 for Cu: the RPA response function without many-body corrections yields good agreement with experimental EEL spectra.

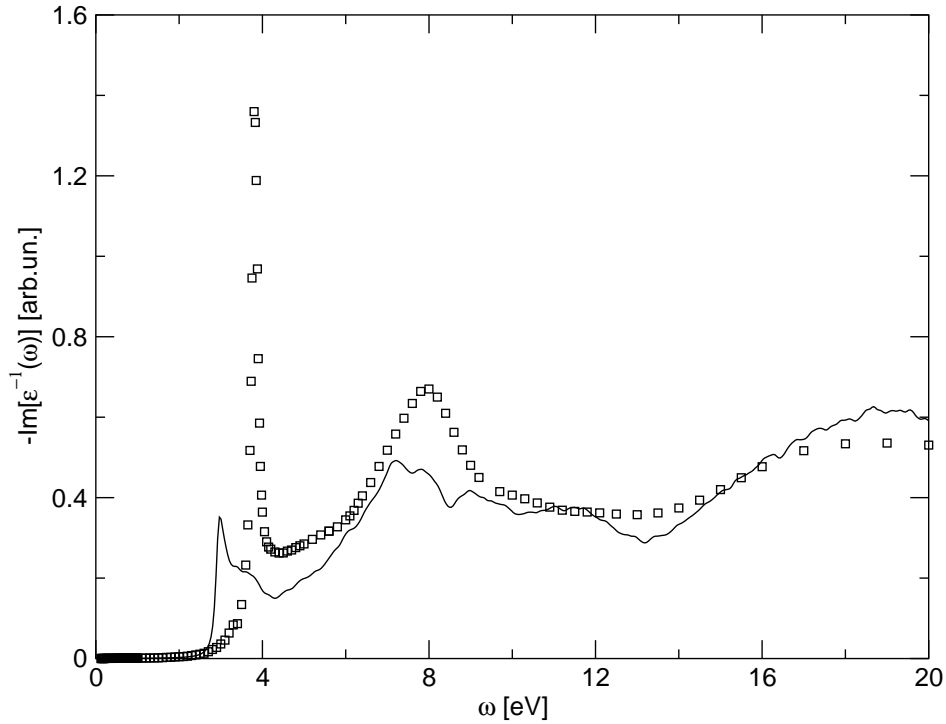


Figure 5.1: Electron energy loss function of Silver. Solid line: DFT-LDA. Boxes: experiment [5].

In this framework the case of Silver is rather surprising: the experimental EELS is dominated by a sharp plasmon peak at 3.83 eV, whose position and width are badly reproduced in DFT-LDA RPA (see Fig. 5.1). In particular, a width of about 0.5 eV is obtained within this approach, to be contrasted with a much narrower experimental width ( $\sim 100$  meV). A similar discrepancy occurs in the reflectance spectrum, where a very narrow dip at 3.92 eV is hardly reproduced by DFT-LDA calculations. Some papers have recently appeared [3, 4] which correct DFT-LDA results by empirical scissors-operators shifts (or similar), meant to better account for the band structure. Improved dielectric functions are obtained in this way, but no solution of the puzzle mentioned above has been given. In this chapter I show that

the non trivial quasiparticle correction on the  $d$ -bands renormalize the plasmon position and width, leading them close to the experimental values. This result is interpreted as due to  $d$ -orbitals polarization effects, which make the difference with respects to the cases of simple metals and Silicon described above. Also the reflectance dip at 3.92 eV is very well described.

## 5.1 DFT–LDA and $GW$ band structure

Following the same procedure described in Chapter 2 a theoretical calculation of the band structure of silver starts with the diagonalization of the Kohn–Sham (KS) Hamiltonian. Like in copper, norm-conserving soft Martins-Troullier [6] pseudopotentials have been used so to work at full convergence with a reasonable kinetic energy cutoff (50 Ry.). The charge has been converged using the same set of 28 irreducible Monkhorst–Pack  $\mathbf{k}$ -points used for Cu. The  $GW$  implementation has also followed the same procedure extensively described in Chapter 3. The deep  $4s/4p$  levels have been included in the screened exchange. The larger Ag unit cell volume has required 229  $\mathbf{G}$ 's vectors to achieve full converged quasiparticle energies, in contrast with the 307 used for copper.

		DFT–LDA	$GW$	Experiment
Positions of $d$ -bands	$\Gamma_{12}$	−3.57	−4.81	−4.95
	$X_5$	−2.49	−3.72	−3.97
	$L_3(2)$	−2.71	−3.94	−4.15
Widths of $d$ -bands	$\Gamma_{12} - \Gamma_{25'}$	1.09	0.94	1.11
	$X_5 - X_3$	3.74	3.39	3.35
	$X_5 - X_1$	3.89	3.51	3.40
	$L_3(2) - L_3(1)$	1.98	1.85	1.99
	$L_3 - L_1$	3.64	3.17	2.94
	$X_5 - X_2$	0.27	0.29	0.38

Table 5.1: Theoretical band widths and band energies for silver, at high-symmetry points.  $GW$  energies are relative to the new QP Fermi Level. The values in the last column are from ref.[7] where spin–orbit splittings have been removed when relevant.

The resulting quasiparticle band structure of Ag is compared with DFT–LDA in Fig. 5.2 and also with experiment in Table 5.1. We see that the  $d$  band widths decrease improving the agreement with experimental results. While the deep energy

levels remain mostly unchanged, a downward shift of about 1.3 eV of the top  $d$  bands leads to excellent agreement with experiment. Like in copper,  $GW$  corrections *do not* act as a rigid shift of the whole occupied band structure with respect to the unoccupied part, as in semiconductors. QP corrections are highly non trivial since even their sign turns out to be band/ $\mathbf{k}$ -point dependent.

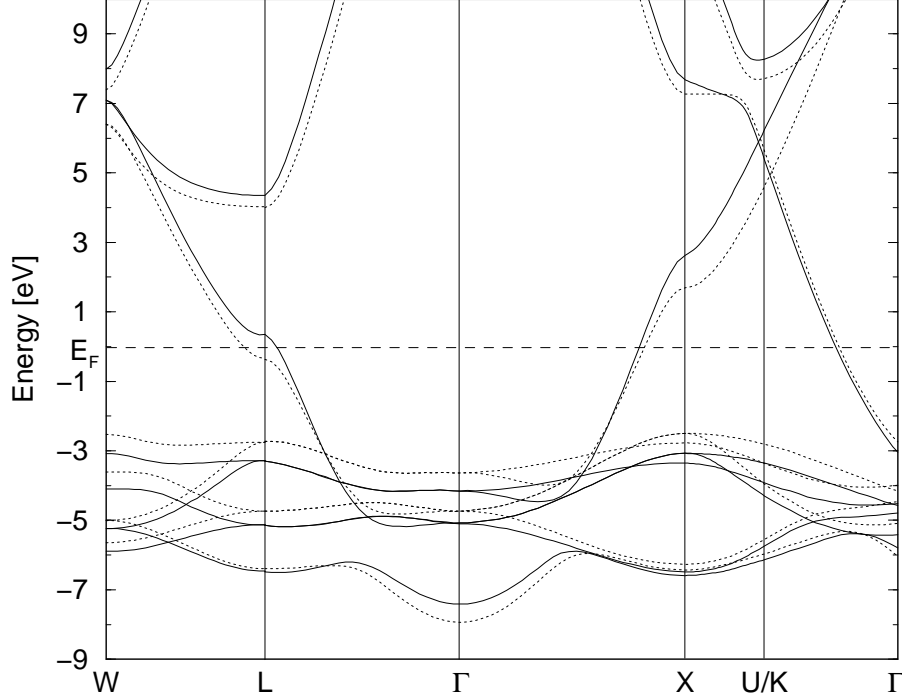


Figure 5.2: Comparison of DFT-LDA (---) band structure and  $GW$  results (—)

## 5.2 Electron energy loss and reflectance spectrum

To calculate the EELS spectra we use the QP band structure obtained so far to evaluate the inverse dielectric function  $\epsilon^{-1}(\omega)$ :

$$\epsilon^{-1}(\omega) = \left[ \epsilon_{ib}(\omega) - \frac{\omega_D^2}{\omega(\omega + i\eta)} \right]^{-1}, \quad (5.6)$$

where  $\omega_D = 9.48$  eV is the Drude plasma frequency calculated *ab-Initio* by means of the longitudinal  $f$ -sum rule described in Section 2.4.1, and  $\epsilon_{ib}(\omega)$  is the intra-band RPA absorption spectrum, given by

$$\epsilon_{ib}(\omega) = 1 - 4\pi \lim_{\mathbf{q} \rightarrow 0} \int_{BZ} \frac{d^3\mathbf{k}}{(2\pi)^3} \sum_{n \neq n'} \Omega_{nn'}(\mathbf{k}, \mathbf{q}) \frac{f_{n', \mathbf{k}-\mathbf{q}} - f_{n, \mathbf{k}}}{\omega + E_{n, \mathbf{k}-\mathbf{q}} - E_{n', \mathbf{k}} + i\eta}, \quad (5.7)$$

with

$$\Omega_{nn'}(\mathbf{k}, \mathbf{q}) = \frac{|\langle n' \mathbf{k} - \mathbf{q} | e^{-i\mathbf{q} \cdot \mathbf{r}} | n \mathbf{k} \rangle|^2}{|\mathbf{q}|^2}, \quad (5.8)$$

where  $0 \leq f_n(\mathbf{k}) \leq 2$  represents the occupation number summed over spin components.

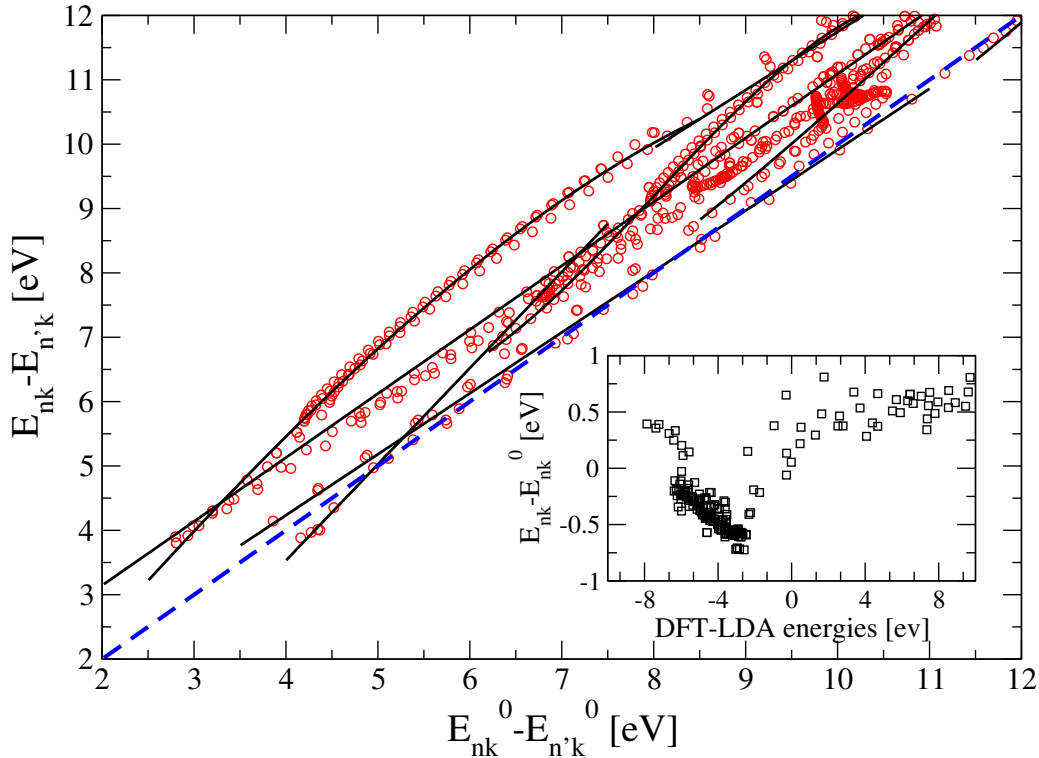


Figure 5.3: *GW* optical transition energies (circles) plotted as function of the DFT–LDA ones for a grid of 29  $\mathbf{k}$ –points in the irreducible Brillouin zone. The dashed line corresponds to a vanishing *GW* corrections while full lines are our fitted curves. In the inset the *GW* corrections on the corresponding DFT–LDA energies are shown.

*GW* optical transition energies ( $E_{n,\mathbf{k}} - E_{n',\mathbf{k}}$ ) are obtained by fitting the QP corrections calculated on 29  $\mathbf{k}$ –points in the irreducible Brillouin zone (BZ). Separate fitting procedures have been used for selected band pairs ( $n, n'$ ) in order to correctly reproduce the energy dependence of the quasiparticle corrections. These fitted curves are plotted in Fig. 5.3 together with the behavior of  $(E_{n,\mathbf{k}} - E_{n',\mathbf{k}})$  plotted as function of the DFT–LDA energy transitions ( $E_{n,\mathbf{k}}^0 - E_{n',\mathbf{k}}^0$ ). From Fig. 5.3 is evident that *GW* corrections are highly non–trivial (ranging from  $-1$  to  $1$  eV, as shown in the inset). *GW* optical transitions energies occurs systematically above the dashed–line (representing the condition of vanishing *GW* corrections), corresponding to a shift of the hole–electron energies to higher energy. However between 4 and 5 eV the hole–electron energies shift is negative. These correspond to transitions at the L point from the Fermi level to the 6th metallic band.



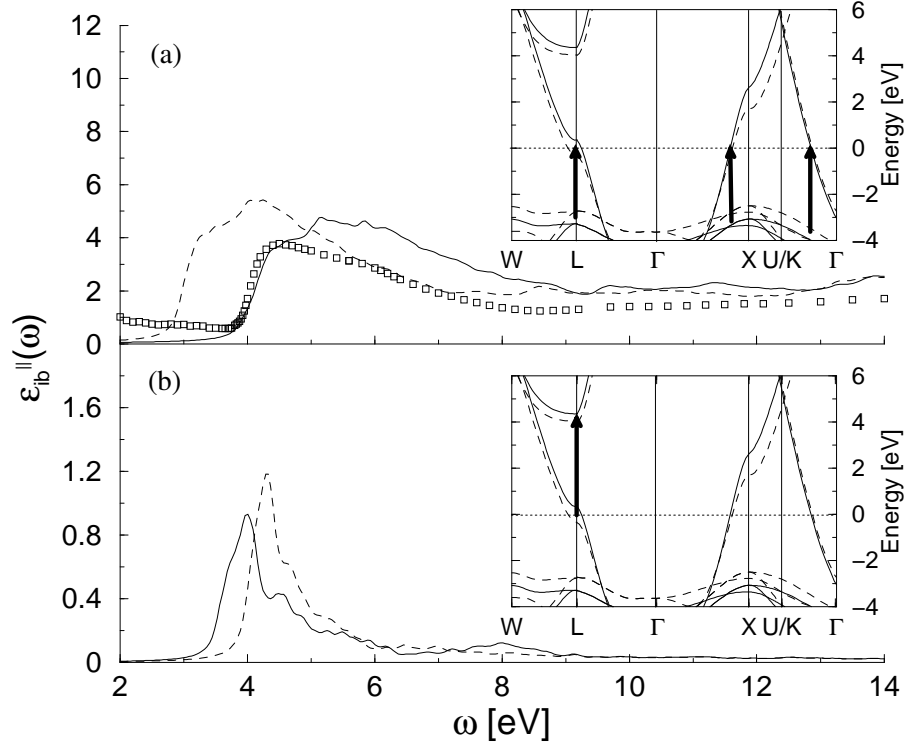


Figure 5.4: Interband absorption spectrum  $\epsilon''_{ib}(\omega)$  of Ag calculated using the quasiparticle  $GW$  band structure. Theoretical spectra do not contain intraband contributions. In both frames and insets: solid line,  $GW$ ; dashed line, DFT-LDA. Only in frame (a): boxes, full experimental  $\epsilon''(\omega)$  [5]. In the insets the DFT-LDA band structure is compared with the  $GW$  result, the arrows indicate the most important bands' transitions involved in  $\epsilon''_{ib}(\omega)$  shown in the corresponding frame.

In Fig. 5.4 the  $GW$  interband contribution  $\epsilon''_{ib}(\omega)$  is compared with the DFT-LDA result. In the upper frame the transitions involving the top  $d$ -bands as initial levels are selected:  $GW$  corrections shift the whole spectra to *higher* energies, with the threshold energy at  $\sim 4$  eV, in agreement with experiment. In panel (b) the energy transitions from the Fermi level to the conduction bands near the L point are considered: at difference with panel (a),  $GW$  shifts the DFT-LDA spectra towards *lower* energies, with a large contribution below the interband threshold. The two different effects of  $GW$  corrections on  $\epsilon''_{ib}(\omega)$  shown in Fig. 5.4 are crucial in determining the plasmon resonance properties. The relation between the dielectric function  $\epsilon(\omega)$  and the plasmon frequency  $\omega_p$  is similar to that between the self-energy operator and the quasiparticle energy [8]: the plasmon energy is defined through the relation

$$\epsilon_{ib}(\omega_p) - \frac{\omega_D^2}{\omega_p^2} = 0. \quad (5.9)$$

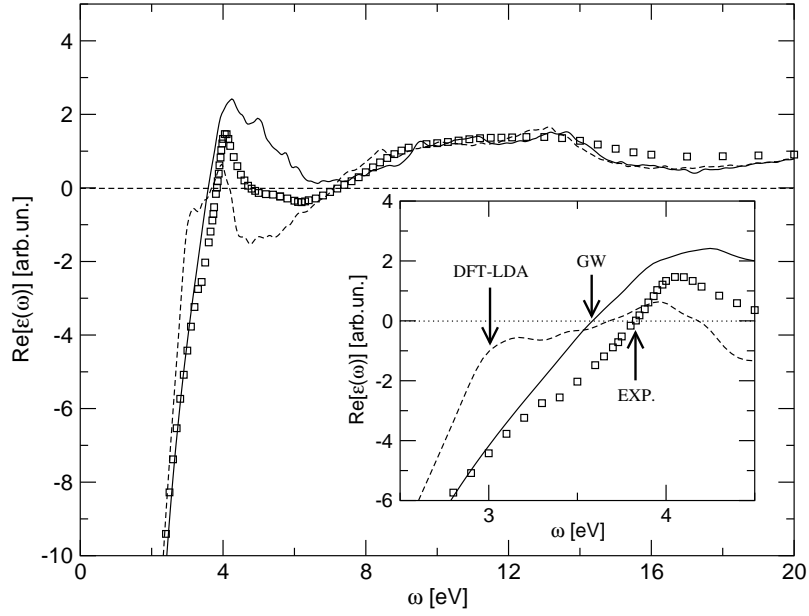


Figure 5.5: Real part of the dielectric function  $\epsilon(\omega)$  of Silver. Solid line: *GW*. Dashed line: DFT-LDA. Boxes: experiment [5]. In the inset the same comparison is made in a small energy range around the plasmon resonance; arrows indicates the frequencies corresponding to the solution of real part of Eq. (5.9).

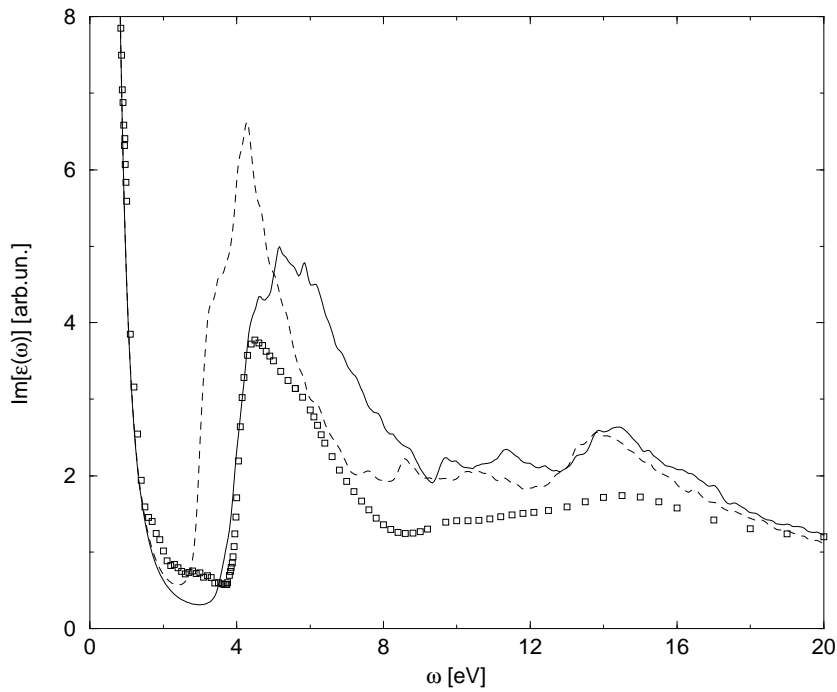


Figure 5.6: Imaginary part of the dielectric function  $\epsilon(\omega)$  of Silver. Solid line: *GW*. Dashed line: DFT-LDA. Boxes: experiment [5].

$\omega_p$  is, in general, complex since decay into electron–hole pairs gives to the plasmon a width proportional to  $\epsilon''_{ib}(\omega_p)$ . Now, the sharp onset of  $\epsilon''_{ib}(\omega)$  at  $\sim 4$  eV (frame (a), Fig. 5.4) is responsible for a dampless solution of Eq. (5.9) just below the interband threshold, as shown for a model hamiltonian in Ref. [9]. In Figs. 5.5 and 5.6 the total  $GW$   $\epsilon(\omega)$  is compared with experimental data and DFT–LDA results. For both real and imaginary part the shape of the spectra improves considerably with respect to DFT–LDA. To define a sharp plasmon resonance, as observed experimentally, Eq. (5.9) requires a zero of  $\epsilon'(\omega)$  and  $\epsilon''(\omega)$ . From Fig. 5.6 the second condition is satisfied only below the absorption threshold,  $\sim 3$  eV for DFT–LDA and  $\sim 4$  eV for  $GW$ . As shown in Fig. 5.5 DFT–LDA has no zero in  $\epsilon'(\omega)$  below the threshold. On the other hand,  $GW$  has a distinct zero in  $\epsilon'(\omega)$  at  $\omega_p = 3.58$  eV. Although below the 4 eV of the threshold from Fig. 5.4, frame (b), we see that there are a few transitions from the Fermi surface to the first conduction band at the L point, contributing to the plasmon width  $\epsilon''_{ib}(\omega_p)$  in agreement with the experimental results that, using temperature and alloying techniques, have selected the optical transitions responsible for the plasmon damping [10].

$GW$  corrected EELS is compared with DFT–LDA and experimental results in Fig. 5.7: the plasmon peak underestimated in intensity and position in DFT–LDA is enhanced and shifted towards higher energies by  $GW$  corrections in excellent agreement with experiment. The  $GW$  plasmon frequency, at 3.58 eV, is 0.25 eV lower than the experimental value, due to the theoretical overestimation of  $\epsilon''_{ib}(\omega)$  already found in copper. A possible explanation of this overestimation is the effect of hole–electron interaction.

Thus the highly non–trivial QP corrections turn out to be crucial in reproducing the experimental EELS. Despite the overestimation of the absorption spectrum, reflected in a small underestimation of the plasmon frequency, a full *ab–initio* RPA  $GW$  calculation of the polarization function of silver is able to reproduce correctly the plasmon resonance. Our theoretical calculations do not contradict previous results for semiconductors and simple metals (where many–body effects are not important) if the role played by  $d$  orbitals is correctly interpreted. The situation can be summarized as follows: Drude oscillations in the partially filled band underlay plasma resonances in simple metal like K; collective oscillations of bound electrons are responsible for plasmon resonances in semiconductors, like Si. In both cases interband transitions occur at energies far from that of the plasma resonance, hence they do not play an important role on the EELS spectra. A strong cancellation of self energy and electron–hole interaction effects occurs, so that a good description is

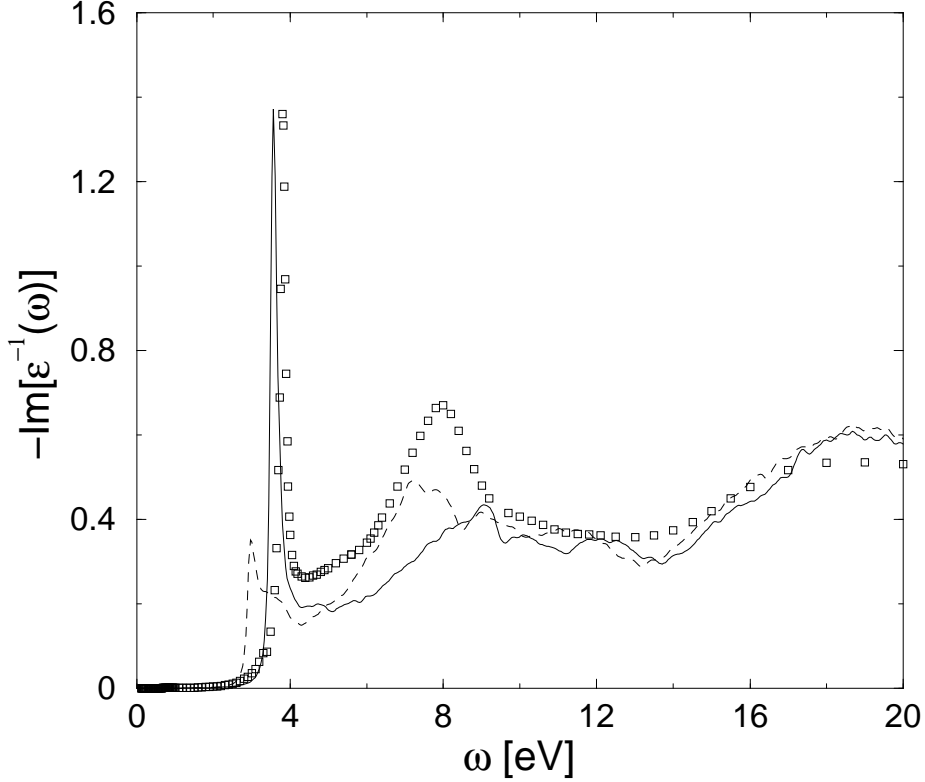


Figure 5.7: Electron Energy Loss Spectra (EELS) of Silver. Solid line: *GW*. Dashed line: DFT-LDA. Boxes: experiment [5]. The non trivial quasiparticle *GW* corrections improve considerably the DFT-LDA plasmon peak, yielding a striking agreement with the experiment.

obtained using the single particle (DFT-LDA) approach. In the case of Cu and Ag, instead, interband transitions involving *d*-bands are close in energy to the Drude plasma frequency; virtual interband transitions screen the electron-electron interaction in the half-filled bands, leading to a renormalization of the plasma frequency. More importantly, real interband transitions completely damp plasma oscillations in Cu, but not in Ag, since in the latter case their onset occurs slightly above the renormalized plasma frequency. As a result the plasma resonance is completely damped in Cu, but narrow and strong in Ag. This shows that, despite the free electron like interpretation often associated to the plasmon peak of silver, *d* bands play a key role.

An important quantity strictly linked to the correct description of the plasmon frequency is the reflectivity  $R(\omega)$

$$R(\omega) = \frac{(n(\omega) - 1)^2 + k^2(\omega)}{(n(\omega) + 1)^2 + k^2(\omega)} \quad (5.10)$$

where  $\epsilon''(\omega) = 2n(\omega)k(\omega)$  and  $\epsilon'(\omega) = (n^2(\omega) - k^2(\omega))$ . In Fig. 5.8 the DFT-LDA  $R(\omega)$  is compared with the *GW* calculation and the experimental result [5]. The

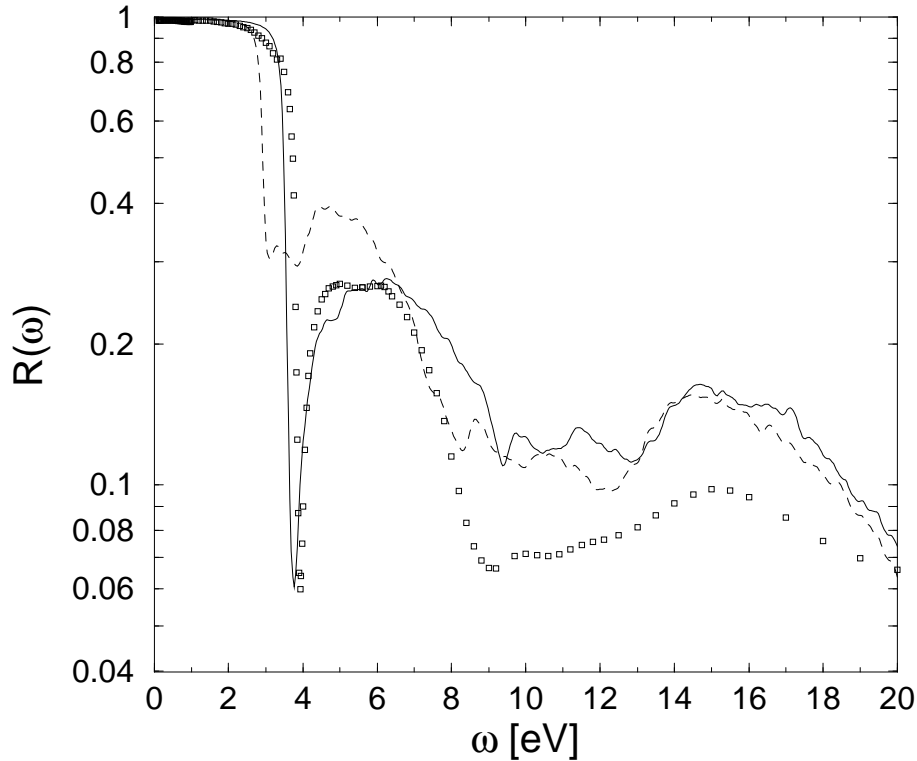


Figure 5.8: Reflectivity spectra of Silver. Solid line: *GW*. Dashed line: DFT-LDA. Boxes: experiment [5]. The sharp dip at the bulk resonance energy is correctly reproduced, with a substantial improvement of DFT-LDA spectra. As consequence of this result an improvement of Ag surface electronic properties is expected, as discussed in the text.

experimental reflectance shows a very narrow dip at 3.92 eV, close to the plasmon frequency, arising from the zero-reflectance point  $\omega_0$ , defined as  $\epsilon(\omega_0) = 1$ . Again, the width and depth of this reflectance dip are related to the imaginary part of  $\epsilon(\omega)$ . *GW* corrections make  $\omega_0$  to occur below the main onset of interband transitions, and hence produce a very narrow and deep reflectance minimum. Here the agreement between *GW* results and experiments for the intensity and width of the dip at 3.92 eV is even more striking than in the EELS.

This result is of great importance for the optical and EELS properties of the Ag(110) *surface*. Very recent calculations of Reflectance Anisotropy Spectra (RAS) within DFT-LDA [12] were not able to reproduce quantitatively a sharp dip observed experimentally. This peak, at energy  $\omega_p^s = 3.8$  eV, has been assigned to a bulk resonance, defined as  $\epsilon'(\omega_p^s) = 1$ . Hence, it is the same occurring in the reflectance spectrum of Fig. 5.8. Its width and shape are strongly related to the reflectance dip of Fig. 5.8 and therefore need *GW* corrections to be well reproduced.



# Bibliography

- [1] V. Olevano and L. Reining, Phys. Rev. Lett. **86**, 5962 (2001).
- [2] W. Ku and A. G. Eguiluz, Phys. Rev. Lett. **82**, 2350 (1999).
- [3] K. Stahrenberg et al., Phys. Rev. B **64**, 115111 (2001).
- [4] V. P. Zhukov et al., Phys. Rev. B **64**, 195122 (2001).
- [5] E.D. Palik, *Handbook of Optical Constants of Solids* (Academic Press, New York, 1985).
- [6] N. Troullier and J.L. Martins, Phys. Rev. B **43**, 1993 (1991).
- [7] G. Fuster, J.M. Tyler, N.E. Brener, J. Callaway and D. Bagayoko, Phys. Rev. B **42**, 7322 (1990).
- [8] For a formal analogy between plasmon resonances and quasiparticles see B. Farid, G. E. Engel, R. Daling and W. van Haeringen, Phys. Rev. B **44**, 13349 (1991).
- [9] M. A. Cazalilla, J. S. Doldao, A. Rubio and P.M. Echenique, Phys. Rev. B **61**, 8033 (2000).
- [10] F. Wooten, *Optical properties of solids* (Academic Press, New York, 1972), pp. 126.
- [11] S. Albrecht, L. Reining and R. Del Sole, Phys. Rev. Lett. **80**, 4510 (1998).
- [12] P. Monachesi, M. Palumbo, R. Del Sole, R. Ahuja and O. Eriksson, Phys. Rev. B **64**, 115421 (2001).





# Conclusions

Several conclusions can be drawn from the results presented in this thesis. We have shown that fully converged Density-Functional-Theory (DFT) in the Local-Density Approximation (LDA) calculations for bulk copper and silver using plane waves can be performed without requiring an exceedingly large basis set, by using soft norm-conserving pseudopotentials including the 3d electrons in the valence.

The strong non-locality implied by such pseudopotentials manifests itself in a very large contribution of the commutator between the PP and the position operator in the calculation of the matrix elements entering the dielectric function.

Similar calculations including also the 3s and 3p shells in the valence are also feasible using plane waves, but show very little difference on the bandstructure and on the optical matrix elements not directly involving those shells.

At difference with the case of simple semiconductors, the disagreement between the LDA theoretical bandstructure and the experimental one cannot be corrected by a rigid shift of the Kohn-Sham eigenvalues. By contrast, the computed optical mass, which involves only intraband transitions at the Fermi energy, is in very good agreement with the experimental data. Also the theoretical absorption spectrum, where only LDA eigenvalues within a few eV around the Fermi energy are important, displays a quite satisfactory agreement with the experimental one. The overall overestimation of about 20 percent in the amplitude of the main peaks cannot be attributed to the effect of wavefunction pseudization *inside* the core region, and should be ascribed to the neglect of self-energy (and excitonic) effects. Local field effects on the macroscopic dielectric function turn out to be negligible, with or without the inclusion of the Drude term.

The discrepancies showed by DFT-LDA bandstructure are, then, corrected using the quasiparticle theory in the Hedin's *GW* approximation for the electron self-energy. The resulting single-quasiparticle bandstructure turns out to be in very good agreement with experiments, with highly non trivial corrections being distinctly band- and  $\mathbf{k}$ -dependent.

This represents the first ab-initio quasi-particle calculation for a noble metal whose implementation has required the solution of several problems, namely: the large number of plane waves needed to describe  $d$  orbitals; the calculation of  $k$ -space sums close to the Fermi surface; and the inclusion of the exchange interaction between valence and core levels. The results presented here show that there are two different contributions, of different sign, to the quasiparticle corrections: the bare exchange of  $d$ -levels with core levels and the  $d$ - $d$  correlation energy. Although the resulting quasiparticle corrections are of the order of  $1\text{ eV}$ , the large correlation energy indicates that copper is not “a prototype weakly correlated system”.

A full screening calculation has been performed, skipping the plasmon pole approximation. The resulting self-energy imaginary part has been used to calculate the quasiparticle lifetimes. In contrast with recent findings I have showed that the quasiparticle corrections are crucial in describing the experimental lifetimes. At the  $d$ -bands top, I found lifetimes four times smaller than those calculated without quasiparticle corrections on the underlying band-structure. Studying in detail the  $GW$  approximation, such large difference is showed to be consequence of the non selfconsistent approach to the Dyson equation. The interacting system turns out to be described in terms of quasiparticles that can decay to lower energy *non* interacting (DFT-LDA) states.

In Chapter 5 I have performed a calculation of the electron energy loss and reflectivity spectra of silver within the RPA approach, using the quasiparticle band structure of silver calculated within GW method. I have shown that the peculiar, well known plasmon peak observed experimentally in electron energy loss spectra and the deep reflectivity minimum are correctly reproduced for the first time, without using adjustable parameters. The theoretical calculations are shown to not contradict previous results for semiconductors and simple metals (where many-body effects are not important) if the role played by  $d$  orbitals is correctly interpreted. In simple metals Drude oscillations in the partially filled band underlay plasma resonances, while collective oscillations of bound electrons are responsible for plasmon resonances in semiconductors, like Si. In both cases interband transitions occur at energies far from that of the plasma resonance, hence they do not play an important role. A strong cancellation of self energy and electron-hole interaction effects occurs, so that a good description is obtained using the single particle (DFT-LDA) approach. In the case of Cu and Ag, instead, interband transitions involving  $d$ -bands are close in energy to the Drude plasma frequency and therefore virtual interband transitions screen the electron-electron interaction in the half-filled bands, leading

to a renormalization of the plasma frequency. More importantly, real interband transitions completely damp plasma oscillations in Cu, but not in Ag, since in the latter case their onset occurs slightly above the renormalized plasma frequency.

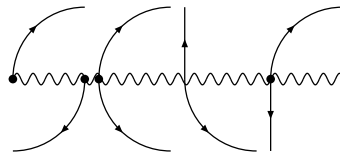
In the four Chapters 2– 5, that describe the original results of this thesis, the  $d$ -orbitals have strongly characterized the underlying physics. Their role has been shown to be crucial in solving puzzling results, apparently completely non physical: the low-energy part of the absorption spectrum of copper, completely underestimated if the matrix elements between  $d$  and  $s/p$ -orbitals are not correctly evaluated. The quasiparticle corrections to the  $d$ -bands as large as  $10\text{ eV}$  if the bare-exchange with core levels are not included. The lifetimes at the top of the  $d$ -bands, overestimated by a factor of 4, if the  $GW$  quasiparticle corrections are not included.

The results presented here also are a starting point for future applications. The methods developed, the code written (see below) can be extrapolated to the study of other  $d$ -metals leading *ab-initio* based Many-Body calculations a standard approach to study their electronic and optical properties.

Finally, it is important to mention the numerical code used to calculate the  $GW$  band structure and lifetimes, as well as the local field effects in the absorption spectrum that fully include the Drude contribution. The code is extensively described in the Appendix and its development composes an important part of this thesis. It has been applied to semiconductors bulk and surfaces and I hope it will have several future applications.



# Appendix



## The Self-Energy/Local Field code

```
K xterm@alessia

      ### S.E.L.F. ###
      or
### Semi-universal solution of dyson equation ###
      or
      ### Self-Energy / Local-Field code ###

      ### MAIN MENU ###

1. Show data.* parameters
2. General Preparation run [data.gops/.q0limit/.qpt/.qptindex]
3. Local-Field effects
4. SELF preparation run (1): integrals of 1/(|q+G||q+G'|) [data.qpgint]
5. V_xc/Sigma_x [data.vxcsigma_x]
6. GW preparation run (1): Plasmon-Pole parameters [data.plas.pole]
7. GW preparation run (2): Full Screen [data.W]
8. GW real QP
9. GW lifetimes
10. View self.in
11. Exit from main menu

Choose: █
```

The user prompt of 

To perform all the calculations contained in this thesis two codes have been used. The first is an, already existing, Car-Parrinello code to calculate the DFT-LDA band eigenstates and eigenvalues in a Plane Wave basis. This code has been modified to handle metallic systems, both in the electronic charge construction and in the optical matrix elements calculation. Moreover it has been added the calculation of Drude frequency as described in Chapter 1.

Using as input the DFT–LDA eigenstates and eigenvalues I have written a new code,  $\text{\textcircled{SELF}}$  (S.E.L.F.), or **S**elf **E**nergy and **L**ocal **F**ield code, to perform the following calculations

1. Local Field effects in copper, including the intraband contribution (See Section 2.4.1).
2. Non self–consistent  $GW$  band structure of copper and silver including bare– and screened– exchange contributions with core levels (Section 3.3.2).
3. Lifetimes of  $d$ –holes in copper.
4. Self–consistent  $GW_0$  lifetimes and band structure of Copper and Silicon (See Chapter 4).

The code is, actually, a package of applications that help the user to handle the Brillouin zone sampling (`kptool.x`), to define (numerically) the shape of the Fermi surface for metallic systems (`fermisurface.x`) and to write the main input configuration file (`prompt.x`).

The code is extensively described in the following sections that want to be a useful manual for any future user (I hope) will use  $\text{\textcircled{SELF}}$ .

## A.3 The Input/Output

$\text{\textcircled{SELF}}$  uses six types of files to communicate with the user, to read the Kohn–Sham states and report the calculated quantities and/or status of the calculation. These files are characterized by a common prefix that indicates their function in the code. In this section I will introduce the general properties of these files. A deeper description will be done in each specific section.

In Table 2 the first group of files:

**SELF:** (INPUT) There are two classes of these files. *self.gen*, *self.vkb* and *self.wfc* are unformatted files containing the Kohn–Sham eigenstates and eigenvalues together with general informations about the system symmetries and lattice constants, the Plane Wave cutoff, the  $\mathbf{G}$  components (all these general informations are in *self.gen*). They are generated by our Car–Parrinello code.

*self.in* is the main input control file and will be described below.

The others **SELF** files are all unformatted files user–defined. They tune the behavior of the code and are either results of precedent  $\text{\textcircled{SELF}}$  runs or outputs of the utilities (`kptool.x` and `fermisurface.x`) contained in the  $\text{\textcircled{SELF}}$  package.

FLAG: (INPUT) These are *empty* files that, if found, switches on/off some flags in the code. To create them in the directory where  $\text{\textcircled{S}}\text{\textcircled{C}}\text{\textcircled{F}}$  is running use the `touch` Unix command as in the following example

```
> touch [ flag name ]
```

LIMIT: (INPUT) These files contains limits to some important variables in the code that, usually, are defined on the basis of the DFT–LDA input parameters.

DATA: (OUTPUT/INPUT/INTERNAL) These file are created by the code and read again at each next run. They avoid the code to calculate basic quantities (as the  $\mathbf{q}$ –points grid, the bare–exchange self–energy) at each run. They must not be moved from the working directory.

Input Files			Code Files
<i>self.in</i>	<i>flag.causal</i>	<i>limits.sigx</i>	<i>data.gops</i>
<i>self.gen</i>	<i>flag.fullrange</i>	<i>limits.W</i>	<i>data.q0limit</i>
<i>self.wfc</i>	<i>flag.noqpgint</i>	<i>limits.comp</i>	<i>data.qpt</i>
<i>self.vkb</i>	<i>flag.noq0limit</i>	<i>limits.BZgrid</i>	<i>data.qptindex</i>
<i>self.qpt</i>			<i>data.BZgrid</i>
<i>self.qp</i>			<i>data.qpgint</i>
<i>self.Ghe</i>			<i>data.vxcsigmax</i>
<i>self.qpLife</i>			<i>data.plas.pole</i>
			<i>data.W</i>
			<i>data.epsm1</i>

Table 2: Input and internal files

Together with the input files described above  $\text{\textcircled{S}}\text{\textcircled{C}}\text{\textcircled{F}}$  uses the output files listed in Table 3

REPORT: (OUTPUT) In these file  $\text{\textcircled{S}}\text{\textcircled{C}}\text{\textcircled{F}}$  reports details about the run or about some specific parts of the calculation (like the FFT grid). *report.self* is the main file with details about each calculation done (Fermi level,  $\mathbf{k}$  and  $\mathbf{q}$  points and so on). Note that also the standard output reports detail of the calculation but with a different format, adequate for an “on–flight” control of the run.

OUT: (OUTPUT) These are the output files that can be plotted after the  $\text{\textcircled{S}}\text{\textcircled{C}}\text{\textcircled{F}}$  run. They contain quantities as the dielectric function, EEL spectra, *GW* self–energy and Green’s functions, etc.

Output Files	
<i>report.self</i>	<i>out.BZgrid</i>
<i>report.fft</i>	<i>out.eel</i>
<i>report.lifestates</i>	<i>out.epsm1</i>
	<i>out.eps</i>
	<i>out.qp</i>
	<i>out.sigc*</i>
	<i>out.G*</i>
	<i>out.fermitest</i>
	<i>out.lifetimes</i>
	<i>out.decay_channels</i>

Table 3: Output files

## A.4 The user prompt and the main input file

*self.in* is the file that controls the main action(s) of  $\text{SELF}$ . It can be written manually but the `prompt.x` utility offers an easy way to go through all the parameters needed for the specified calculation.

To use `prompt.x` one has simply to run it in the directory where *self.gen*, *self.wfc* and *self.vkb* files have been stored. The following prompt will be offered to the user

```

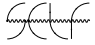
### S.E.L.F. ###
      or
### Semi-universaL solution of dyson equation ###
      or
### Self-Energy / Local-Field code ###

### MAIN MENU ###

1. Show data.* parameters
2. General Preparation run [data.gops/.q0limit/.qpt/.qptindex/.BZgrid]
3. Local-Field effects
4. SELF preparation run (1): integrals of 1/(|q+G||q+G'|) [data.qpgint]
5. V_xc/Sigma_x [data.vxcsigmax]
6. GW preparation run (1): Plasmon-Pole parameters [data.plas.pole]
7. GW preparation run (2): Full Screen [data.W]
8. GW real QP
9. GW lifetimes [data.epsm1]
10. View self.in
11. Exit from main menu

```



From this point on `prompt.x` helps to choose the parameters needed on the basis of the  runlevel (2-9) chosen.

For each runlevel `prompt.x` will ask to the user several parameters. These are written on the `self.in` file that has the following form (parameters names are those used in the code source)

```

### [A] Main actions ###
LOCALF : Local Field effects
GWSIG  : GW self-energy
GWPP   : Plasmon-Pole approximation ?
LLIFE  : GW lifetimes calculation

### [B] General ###
ZERO           : Definition of "0^+" [ev]
Q0(1) Q0(2) Q0(3) : Cartesian q -> 0 direction
NGFFT         : Number of PWs in FFT
NBN           : Max number of bands used

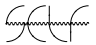
### [C] Pre-Self-Energy setup ###
PREQPGINT : Integration of 1/(|q+G||q+G'|) ?
NPT       : Random q-points in integration of 1/(|q+G||q+G'|)
NGQPGINT  : Plane-Waves in the 1/(|q+G||q+G'|) integration
PRESIGX   : Pre-Self-Energy run of Sigmax ?
PRESIG    : Pre-Self-Energy run of Plasmon-Pole or W
EPSM1WR   : Writing of the eps^{-1} matrix [W and/or lifetimes run]

### [D] Drude ###
DRUDEL           : Drude contribution ?
WDRUDER WDRUDEI : Drude plasma frequency [ev]

### [E] Response function and W ###
NGBLK NGDIAG : Block and max diagonal dimension
WMIN WMAX   : wmin, wmax [ev]
NW          : Energy steps [ev]
NBNCHI     : Number of bands used for Chi0

### [F] GW ###
SIGPERT     : Perturbative solution of Dyson equation
NGWSIGX    : Number of PWs in exchange SE
NBNMIX     : Width of the off-diagonal terms in GW matrix
KSIG1 KSIG2 : First and last kpt for the GW-Corrections
NSIG1 BSIG2 : First and last band for the GW-Corrections

```

To describe the use of each parameters in the following sections I will show what happens in each possible runlevel of the user-prompt of . I will discuss the

parameters needed and the link with the theory described in the chapters of this thesis.

In Fig. 9 the flowchart of  $\mathcal{S}$  in RUNLEVEL 2/4 is showed. I will refer to the group of actions showed as **Initialization** of the code. Indeed each time  $\mathcal{S}$  is run it executes all the **Initialization** actions skipping the sections where the corresponding DATA file is found.

## A.5 Runlevel 2: general preparation run N<sup>0</sup> 1

---

<b>Purpose:</b>	<b>G</b> - and <b>k</b> -space operations. Calculation of $\mathbf{q} \rightarrow 0$ oscillators' strengths. Setup of files for hole-electron Green's function energy random integration.
<b>Input files used:</b>	<i>self.in</i> , <i>self.qpt</i> (optional)
<b>Output files:</b>	<i>data.qpt</i> , <i>data.qptindex</i> , <i>data.q0limit</i> , <i>data.BZgrid</i>
<b>Parameters used:</b>	Q0(1),Q0(2),Q0(3) (REAL) WDRUDER (REAL) NBNCHI (INTEGER) NGWSIGX (INTEGER)
<b>Flags .true. in self.in:</b>	None

---

In this runlevel  $\mathcal{S}$  constructs the map corresponding to the symmetries actions on the **G**- (*data.gops*) and **k**-points (*data.qpt* and *data.qptindex*).

NGWSIGX represents the maximum number of **G**-vectors that are supposed to be used in all the following calculations. The maximum value allowed is that corresponding to the number of plane waves in the Kohn-Sham charge (read from *self.gen*).

*data.gops* is needed to construct the closed shells in **G**-space so that  $\mathcal{S}$  stops after its constructions asking to be run again without any modifications. In this way the **G**-vectors settings in the "main dimensions settings" showed in Fig. 9 will be correctly closed to the nearest **G**-space shell (read now in *data.gops*).

*data.q0limit* contains the matrix elements

$$\lim_{\mathbf{q} \rightarrow 0} \langle n' \mathbf{k} - \mathbf{q} | e^{-i\mathbf{q} \cdot \mathbf{r}} | n \mathbf{k} \rangle = -i\mathbf{q} \cdot \frac{\langle \phi_{n' \mathbf{k} - \mathbf{q}} | [\mathbf{r}, H] | \phi_{n \mathbf{k}} \rangle}{\epsilon_{n'}(\mathbf{k}) - \epsilon_n(\mathbf{k})} + O(q^2), \quad (\text{A.11})$$

and Q0(1),Q0(2),Q0(3) is  $\mathbf{q}$  in Cartesian coordinates, units of  $2\pi/a_{lat}$  (a.u.). NBNCHI is the maximum band index used in the above equation.

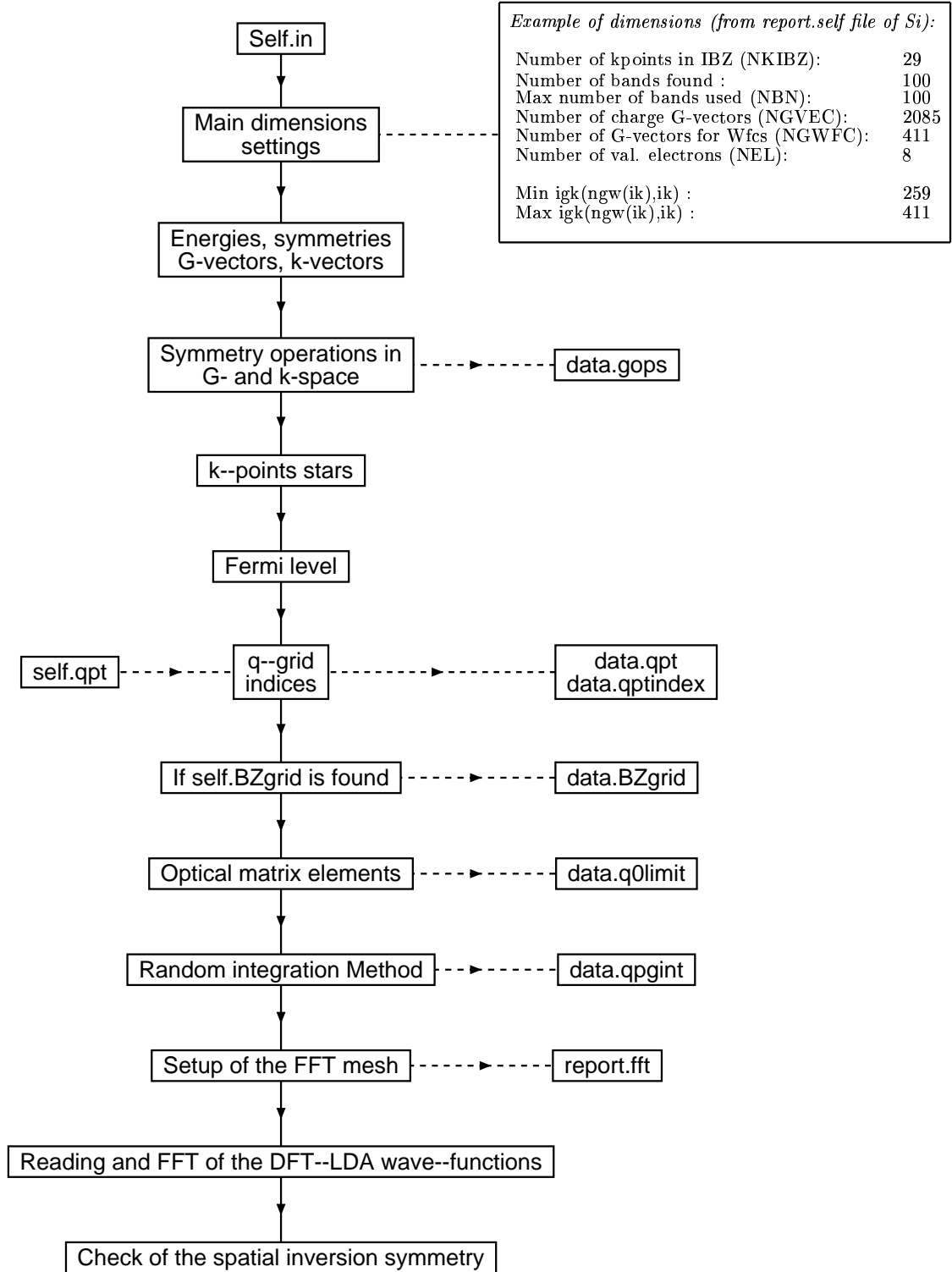


Figure 9: Flowchart of the code in the RUNLEVELS2/4. The central row represents the main code actions. On the left the user-defined input files (SELF), on the right the code output file. In the first run the code executes all the action of this flowchart while, in the next run those corresponding to an output DATA are skipped.

WDRUDER ( $\omega_D$ ) is the Drude plasma frequency of the systems. It must be calcu-

lated using the intraband longitudinal f–sum rule described in Section 2.4.1. In this runlevel  $\text{\textcircled{L}}\text{\textcircled{F}}$  reports an important quantity linked to the Drude contribution: “the maximum intraband transition energy”. According to the homogeneous electron gas this energy is given by  $k_F|\mathbf{q}|$  with  $k_F$  Fermi momentum given by  $k_F = (3\pi\omega_D^2/4)^{1/3}$  (for detail see below). As the  $\mathbf{q}$  vector of this runlevel will be used in all the following calculations, the maximum intraband transition energy should be as small as possible. Too large values can appear as a nonphysical discontinuity of the absorption spectrum at low energies.

*self.qpt* is the only user–defined file that can be used in this runlevel. It is generated by the *kptool.x* utility. It forces  $\text{\textcircled{L}}\text{\textcircled{F}}$  to search only some  $\mathbf{q}$ –vectors obtained as corresponding grid of a smaller set of the given  $\mathbf{k}$ –points differences. For details see the separate *kptool.x* README file contained in the  $\text{\textcircled{L}}\text{\textcircled{F}}$  package.

## A.6 Runlevel 3: Local Field effects

---

<b>Purpose:</b>	Inclusion of Local Field effects in the absorption spectrum and energy loss spectra including the Drude contributions.
<b>Input files used:</b>	DATA files of runlevel 1, <i>self.in</i> , <i>flag.causal</i> (optional)
<b>Output files:</b>	<i>out.eel</i> , <i>out.eps</i> , <i>out.epsm1</i>
<b>Parameters used:</b>	DRUDEL (LOGICAL) WDRUDER, WDRUDEI (REAL) ZERO (REAL) WMIN (REAL) WMAX (REAL) NW (INTEGER) NBNCHI (INTEGER) NGBLK (INTEGER) NGDIAG (INTEGER)
<b>Flags .true. in self.in:</b>	LOCALF

---

According to Equations of Section 2.4 the macroscopic dielectric function  $\epsilon_M(\omega)$  is given by:

$$\epsilon_M(\omega) = \langle\langle\epsilon_L^{-1}(\mathbf{r}\mathbf{r}', \omega)\rangle\rangle_0^{-1}, \quad (\text{A.12})$$

with

$$\langle\langle \epsilon_L^{-1}(\mathbf{r}\mathbf{r}', \omega) \rangle\rangle_0 = 1 + \lim_{\mathbf{q} \rightarrow 0} \frac{4\pi}{|\mathbf{q}|^2} \chi_{\mathbf{G}=0 \mathbf{G}'=0}(\mathbf{q}, \omega), \quad (\text{A.13})$$

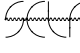
and

$$\chi_{\mathbf{G} \mathbf{G}'}(\mathbf{q}, \omega) = \chi_{\mathbf{G} \mathbf{G}'}^0(\mathbf{q}, \omega) + \sum_{\mathbf{G}''} \chi_{\mathbf{G} \mathbf{G}''}^0(\mathbf{q}, \omega) \frac{4\pi}{|\mathbf{q} + \mathbf{G}''|^2} \chi_{\mathbf{G}'' \mathbf{G}'}(\mathbf{q}, \omega). \quad (\text{A.14})$$

In  the  $\chi$  matrix has two dimensions (NGBLK and NGDIAG):

$$\chi_{\mathbf{G} \mathbf{G}'}(\mathbf{q}, \omega) = \begin{pmatrix} \dots & \dots & \uparrow & 0 & \uparrow \\ \dots & \dots & \text{NGBLK} & 0 & \vdots \\ \dots & \dots & \downarrow & 0 & \text{NGDIAG} \\ 0 & 0 & 0 & \dots & \downarrow \\ 0 & 0 & 0 & 0 & \dots \end{pmatrix} \quad (\text{A.15})$$

while NBNCHI represents the number of bands in Eq. (A.14) (that can be lower than those contained in the *self.q0limit* file). ZERO is the lorentzian broadening of  $\chi$ . The energy variable  $\omega$  range in  $\chi$  is [WMIN, WMAX] divided into NW steps. The energies are given in eV.

 usually performs T-ordered calculations, but with *flag.causal* it can be forced to calculate a causal dielectric function.

### A.6.1 The Jellium polarization function

If the system under study is a metal DRUDEL must be set `.true.` in order to include intraband transitions. In Section 2.4.2 I have shown how the Drude contribution is introduced in all the  $\mathbf{G}$  components of the  $\chi$  function. In this section I want to explain in detail the analytic and numerical properties  $\pi_0(\mathbf{q}, \omega)$ , the non-interacting polarization calculated for a jellium model [1] with a density  $n_{el}$  of electrons yielding a classic plasma frequency  $\omega_D$

$$\pi_0(\mathbf{q}, \omega) = -\frac{1}{2\pi^2|\mathbf{q}|} \int_0^{k_F|\mathbf{q}|} x dx \left( \frac{1}{\omega - k_F|\mathbf{q}| + i\eta} - \frac{1}{\omega - k_F|\mathbf{q}| - i\eta} \right), \quad (\text{A.16})$$

where

$$x = \frac{\omega}{k_F|\mathbf{q}|}, \quad (\text{A.17})$$

and

$$k_F = (3\pi\omega_D^2/4)^{1/3}. \quad (\text{A.18})$$

It turns out that

$$\pi_0(\mathbf{q}, \omega) = \frac{1}{2\pi^2|\mathbf{q}|} \left[ 2k_F|\mathbf{q}| + (\omega + i\delta) \log \frac{\omega + i\delta - k_f|\mathbf{q}|}{\omega + i\delta} - (\omega - i\delta) \log \frac{\omega - i\delta + k_f|\mathbf{q}|}{\omega - i\delta} \right] \quad (\text{A.19})$$

Unfortunately this equation is hard to calculate numerically because the logarithmic functions becomes unstable when  $\omega \gg k_f|\mathbf{q}|$ . To solve this problem ~~we~~ uses Eq. (A.19) for  $\omega < 10 k_f|\mathbf{q}|$  and the perturbative expansion

$$\log(1 - x) \sim -x - x^2/2 - x^3/3 + \dots \quad \omega > 10 k_f|\mathbf{q}|, \quad (\text{A.20})$$

matching the two behaviors at  $\omega = 10 k_f|\mathbf{q}|$ .

The two parameters WDRUDER, WDRUDEI are, respectively,  $\omega_D$  and  $\delta$  in Eq. (A.19).

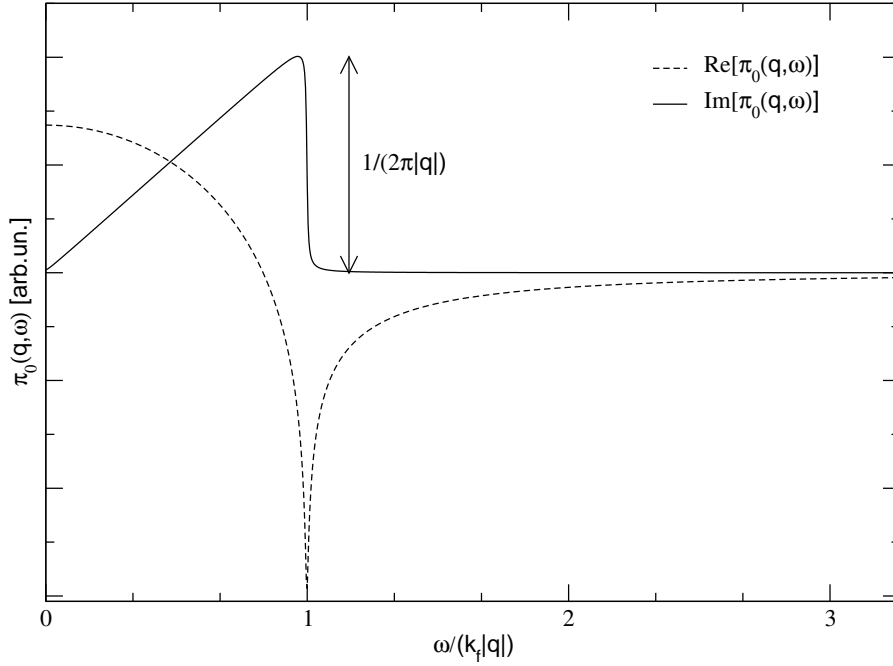


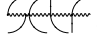
Figure 10: The Jellium polarization function,  $\pi_0(\mathbf{q}, \omega)$ .

## A.7 Runlevel 4: general preparation run N<sup>0</sup> 2

---

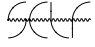
<b>Purpose:</b>	<i>Random integration of <math>f_{n\mathbf{k}}/ ( \mathbf{q} + \mathbf{G}   \mathbf{q} + \mathbf{G}' )</math>.</i>
<b>Input files used:</b>	DATA files of runlevel 1, <i>self.in</i> , <i>data.fermisurf</i> (Metallic systems)
<b>Output files:</b>	<i>data.qpgint</i>

**Parameters used:** NGWSIGX (INTEGER)  
NPT (INTEGER)  
**Flags .true. in self.in:** PREQPGINT

In Section 3.3.1 I have introduced the *Random Integration Method*. This is the purpose of this runlevel. The method is used to reduce the ansatz about the continuity of the integrated function of Eq. (3.37) only to the oscillators' strengths  $\tilde{\rho}_{nn'}$ . For the occupation numbers and for the Fourier components of Coulomb interaction the integration over the  $\mathbf{q}$ -space is divided into  $N_q$  integrations in the regions  $BZ'(\mathbf{q}_i)$ .  defines these regions so to cover the BZ without overlapping; a simple procedure can be carried out in the case of a uniform  $\mathbf{q}$ -grid where the grid is itself a Bravais Lattice and the  $BZ'(\mathbf{q}_i)$  are the Brillouin Zones of this *small* lattice. The integrals

$$\int_{BZ'(\Gamma)} \frac{d\mathbf{q}}{(2\pi)^3} f_{n_1(\mathbf{k}-\mathbf{q}-\mathbf{q}_i)} \frac{1}{|\mathbf{q} + \mathbf{q}_i + \mathbf{G}| |\mathbf{q} + \mathbf{q}_i + \mathbf{G}'|} \\ \approx \frac{(2\pi)^3}{N_q \Omega N_r} \sum_{j=1 \dots N_r} f_{n_1(\mathbf{k}-\mathbf{Q}_j-\mathbf{q}_i)} \frac{1}{|\mathbf{Q}_j + \mathbf{q}_i + \mathbf{G}| |\mathbf{Q}_j + \mathbf{q}_i + \mathbf{G}'|}, \quad (\text{A.21})$$

are calculated generating NPT ( $N_r$ ) random  $\mathbf{q}$ -points  $\{\mathbf{Q}_i\}$  inside the *small* Brillouin Zone  $BZ'(\Gamma)$  centered around  $\mathbf{q} = \mathbf{0}$ . Eq. (A.21) is calculated for (NGWSIGX)  $\mathbf{G}$ -vectors.

For metallic systems the occupations  $f_{n_1(\mathbf{k}-\mathbf{Q}_j-\mathbf{q}_i)}$  are fitted using the Fermi surface parametrized in the file `data.fermisurface` generated with the application `fermisurface.x` contained in the  package.

## A.8 Runlevel 5: exchange–correlation and bare–exchange matrix elements

**Purpose:** Matrix elements of bare–exchange and exchange–correlation potential

**Input files used:** DATA files of runlevel 1 and 4, *self.in*

**Output files:** *data.vxcsigmax*

**Parameters used:** NGWSIGX (INTEGER)  
NBNMIX (INTEGER)  
KSIG1, KSIG2 (INTEGER)  
BSIG1, BSIG2 (INTEGER)

Flags `.true. in self.in:`    PRESIGX

---

In this section `SCF` calculates the matrix-elements of bare-exchange and Ceperley-Alder [3] exchange-correlation potential, parametrized by Perdew and Zunger [4]. for  $\mathbf{k}$ -points from KSIG1 to KSIG2 and for bands from BSIG1 to BSIG2.

To calculate the bare-exchange the summation over the  $\mathbf{G}$ -vectors is done using NGWSIGX plane waves. NBNMIX represents the band-mixing for the off-diagonal matrix elements. This means that, for example

$$\langle n\mathbf{k}|\Sigma_x(\mathbf{r}_1, \mathbf{r}_2)|n'\mathbf{k}\rangle \neq 0 \quad \text{if} \quad |n - n'| \leq \text{NBNMIX} \quad (\text{A.22})$$

## A.9 Runlevel 6: Plasmon-Pole parameters

---

<b>Purpose:</b>	Plasmon-Pole parameters for $\tilde{\epsilon}_{\mathbf{G},\mathbf{G}'}^{-1}$ matrix
<b>Input files used:</b>	DATA files of runlevel 1, <i>self.in</i>
<b>Output files:</b>	<i>data.plas.pole</i>
<b>Parameters used:</b>	NGBLK (INTEGER) NGDIAG (INTEGER) ZERO (REAL)
<b>Flags <code>.true. in self.in:</code></b>	PRESIG GWPP

---

The plasmon-pole [5] parameters for the screening function are calculated in this runlevel. For each  $\mathbf{q}$  vector `SCF` calculates the  $\tilde{\epsilon}_{\mathbf{G},\mathbf{G}'}^{-1}(\mathbf{q}, \omega)$  matrix (See Section 3.2.2, Eq. (3.24)) for two frequencies:  $0 + i0$  and  $0 + i$  (ZERO). The  $\tilde{\epsilon}^{-1}$  matrix has dimensions NGBLK and NGDIAG as discussed above for the Local Field section.

Note that in this case `SCF` uses automatically the *flag.serial* option calculating a causal dielectric matrix.


## A.10 Runlevel 7: the full screening function

---

<b>Purpose:</b>	Full screening function for <i>GW</i> calculations
<b>Input files used:</b>	DATA files of runlevel 1 and 4, <i>self.in</i>
<b>Output files:</b>	<i>data.W</i> , <i>data.epsm1</i> (if EPSM1WR=.true.)



<b>Parameters used:</b>	DRUDEL (LOGICAL)
	DRUDER (REAL)
	DRUDEI (REAL)
	NBN (INTEGER)
	NBNCHI (INTEGER)
	NGBLK (INTEGER)
	NGDIAG (INTEGER)
	ZERO (REAL)
	WMAX (REAL)
	NW (INTEGER)
	NBNMIX (INTEGER)
	KSIG1, KSIG2 (INTEGER)
	BSIG1, BSIG2 (INTEGER)
<b>Flags .true. in self.in:</b>	PRESIG
	EPSM1WR (optional)

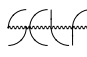
In this section  calculates the main quantity in the full screening  $GW$ , the screening function  $\Gamma_{h/e}(nn_1n', \mathbf{k} - \mathbf{q}, \omega)$ . The definition used in the code is the same introduced in Chapter 3, Eq. (3.33–3.35)

$$\langle n\mathbf{k}|M(\mathbf{r}_1, \mathbf{r}_2, \omega)|n'\mathbf{k}'\rangle = -\sum_{n_1} \int_{BZ} \frac{d\mathbf{q}}{(2\pi)^3} \left[ \int_{-\infty}^{\infty} d\omega' \frac{\Gamma_h(nn_1n', \mathbf{k} - \mathbf{q}, \omega')}{\omega - \omega' - \epsilon_{n_1(\mathbf{k}-\mathbf{q})} + i\delta} + \int_{-\infty}^{\infty} d\omega' \frac{\Gamma_e(nn_1n', \mathbf{k} - \mathbf{q}, \omega')}{\omega - \omega' - \epsilon_{n_1(\mathbf{k}-\mathbf{q})} - i\delta} \right], \quad (\text{A.23})$$

with

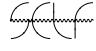

$$\Gamma_h(nn_1n', \mathbf{k} - \mathbf{q}, \omega') = 2 \sum_{\mathbf{G}, \mathbf{G}'} \tilde{\rho}_{nn_1}(\mathbf{k}, \mathbf{q}, \mathbf{G}) [\tilde{\rho}_{n'n_1}(\mathbf{k}, \mathbf{q}, \mathbf{G}')]^* \frac{2f_{n_1(\mathbf{k}-\mathbf{q})}}{|\mathbf{q} + \mathbf{G}||\mathbf{q} + \mathbf{G}'|} \Im [\tilde{\epsilon}_{\mathbf{G}, \mathbf{G}'}^{-1}(\mathbf{q}, \omega)] \theta(\omega), \quad (\text{A.24})$$

$$\Gamma_e(nn_1n', \mathbf{k} - \mathbf{q}, \omega') = 2 \sum_{\mathbf{G}, \mathbf{G}'} \tilde{\rho}_{nn_1}(\mathbf{k}, \mathbf{q}, \mathbf{G}) [\tilde{\rho}_{n'n_1}(\mathbf{k}, \mathbf{q}, \mathbf{G}')]^* \frac{2(1 - f_{n_1(\mathbf{k}-\mathbf{q})})}{|\mathbf{q} + \mathbf{G}||\mathbf{q} + \mathbf{G}'|} \Im [\tilde{\epsilon}_{\mathbf{G}, \mathbf{G}'}^{-1}(\mathbf{q}, \omega)] \theta(-\omega). \quad (\text{A.25})$$

DRUDEL, DRUDER, DRUDEI, NBNCHI, NGBLK, NGDIAG, WMAX, NW and ZERO defines the matrix  $\tilde{\epsilon}_{\mathbf{G}, \mathbf{G}'}^{-1}(\mathbf{q}, \omega)$  as already described in the Local Field section. Note the WMIN is not required because  put  $WMIN = 0$  in order to expand the screening function in the range  $[-WMAX, WMAX]$ .

NBN is, generally, higher than NBNCHI and represents the number of bands contained in the single particle Green's function  $G$  of the  $GW$  approximation. The corresponding index in Eq. (A.23) is  $n_1$ .

As in the bare-exchange matrix elements KSIG1, KSIG2, BSIG1, BSIG2 and NBNMIX parameters decide the dimension of the mass-operator matrix (band index  $n$  and  $n'$  in Eq. (A.23)).

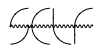
In this runlevel the EPSM1WR flag is particularly useful. Setting EPSM1WR=.true.  writes in the *data.epsm1* file the frequency and  $\mathbf{q}$  components of the  $\tilde{\epsilon}_{\mathbf{G},\mathbf{G}'}^{-1}(\mathbf{q}, \omega)$  matrix. Calculating other *data.W* relative to other KSIG1, KSIG2, BSIG1, BSIG2 parameters if  finds the *data.epsm1* a large part of the calculation is skipped. Clearly the *data.epsm1* file can be very large, but, on the other hand, it can reduce sensibly the computational time.

## A.11 Runlevel 8: $GW$ quasiparticle energies

---

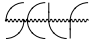

<b>Purpose:</b>	Full screening/plasmon-pole $GW$ energies
<b>Input files used:</b>	DATA files of runlevel 1, <i>data.W</i> corresponding to the KSIG1, KSIG2, BSIG1, BSIG2 chosen, <i>flag.fullrange</i> (optional), <i>self.in</i>
<b>Output files:</b>	<i>out.qp</i> , <i>out.G*</i> and <i>out.sigc*</i> if <i>flag.fullrange</i> is found
<b>Parameters used:</b>	SIGPERT (LOGICAL) NBN (INTEGER) ZERO (REAL) WMIN (REAL) (optional) WMAX (REAL) (optional) NW (INTEGER) (optional) NBNMIX (INTEGER) (optional) KSIG1, KSIG2 (INTEGER) (optional) BSIG1, BSIG2 (INTEGER) (optional)
<b>Flags .true. in self.in:</b>	PRESIG


---

In this runlevel  performs the energy integral of Eq. (A.23). The number of bands NBN, the parameters NBNMIX, KSIG1, KSIG2 and BSIG1, BSIG2 of the screening function can also be changed in the range of the values used for the *data.W* file.

SIGPERT controls the method used to solve the Dyson Equation (See Section 3.3.3)

$$\left[ G_{n\mathbf{k}} \left( \epsilon_{n\mathbf{k}}^{QP} \right) \right]^{-1} = \epsilon_{n\mathbf{k}}^{QP} - \epsilon_{n\mathbf{k}} - \left[ \Sigma_x^{n\mathbf{k}} + M_{n\mathbf{k}} \left( \epsilon_{n\mathbf{k}}^{QP} \right) + M_{n\mathbf{k}}^{core} - V_{xc}^{n\mathbf{k}} \right] = 0 \quad (\text{A.26})$$


- a. If SIGPERT=.true.  uses the iterative procedure described in Section 3.3.3 based on the secant method [2].
- a. If SIGPERT=.false.  us the Newton method at the first iteration, introducing the mass-operator derivative.

If  finds the *flag.fullrange* file the Self-energy and *GW* Greens' functions energy dependence for the  $\mathbf{k}$ -points and bands selected are reported in the files *out.G\** and *out.sigc\**. The extension of these files indicates the  $\mathbf{k}$ -point/band

```
out.G.kpt1.ib.1.ibp.1      out.G.kpt18.ib.3.ibp.3
out.G.kpt1.ib.10.ibp.10   out.G.kpt18.ib.4.ibp.4
out.G.kpt1.ib.2.ibp.2     out.G.kpt18.ib.5.ibp.5
out.G.kpt1.ib.3.ibp.3     out.G.kpt18.ib.6.ibp.6
out.G.kpt1.ib.4.ibp.4     out.G.kpt18.ib.7.ibp.7
```

and

```
out.sigc.kpt1.ib.5.ibp.5   out.sigc.kpt19.ib.1.ibp.1
out.sigc.kpt1.ib.6.ibp.6   out.sigc.kpt19.ib.10.ibp.10
out.sigc.kpt1.ib.7.ibp.7   out.sigc.kpt19.ib.2.ibp.2
out.sigc.kpt1.ib.8.ibp.8   out.sigc.kpt19.ib.3.ibp.3
```

In this case  asks also for the energy range of these files, [WMIN,WMAX] and for the number of steps NW.

## A.12 Runlevel 9: *GW* quasiparticle lifetimes

---

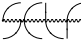
<b>Purpose:</b>	Full screening calculation of the <i>GW</i> quasiparticle lifetimes
<b>Input files used:</b>	DATA files of runlevel 1, <i>self.qp</i> (optional), <i>data.epsm1</i> (if found), <i>self.in</i>
<b>Output files:</b>	<i>report.lifestates</i> , <i>out.lifetimes</i> <i>data.epsm1</i> (if EPSM1WR=.true.)

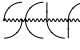
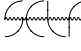

<b>Parameters used:</b>	DRUDEL (LOGICAL)	
	DRUDER (REAL)	
	DRUDEI (REAL)	
	NBNCHI (INTEGER)	
	NGBLK (INTEGER)	
	NGDIAG (INTEGER)	
	WMAX (REAL) (if EPSM1WR=.true.)	
	NW (INTEGER) (if EPSM1WR=.true.)	
	ZERO (REAL)	
	KSIG1, KSIG2 (INTEGER)	
	BSIG1, BSIG2 (INTEGER)	
	<b>Flags .true. in self.in:</b>	LLIFE
		EPSM1WR (optional)

---

In this section the  $GW$  quasiparticle lifetimes are calculated. As in the sections above DRUDEL ,DRUDER ,DRUDEI ,NBNCHI ,NGBLK ,NGDIAG and ZERO defines the matrix  $\tilde{\epsilon}_{\mathbf{G},\mathbf{G}'}^{-1}(\mathbf{q},\omega)$ . For the details of the theory see Chapter 4. KSIG1, KSIG2 and BSIG1, BSIG2 define the quantum numbers of the quasiparticle. From the particular case of the hole lifetimes Eq. (4.10) says that, at the non self-consistent  $GW$  level

$$\Gamma_{n\mathbf{k}}^{hole} \propto \sum_{n'} \sum_{\mathbf{q}} \text{Im} \left[ W_{n\mathbf{k} \rightarrow n'(\mathbf{k}-\mathbf{q})} \left( \epsilon_{n'(\mathbf{k}-\mathbf{q})}^{DFT-LDA} - \epsilon_{n\mathbf{k}}^{QP,0} \right) \right] \theta \left( \epsilon_{n'(\mathbf{k}-\mathbf{q})}^{DFT-LDA} - \epsilon_{n\mathbf{k}}^{QP,0} \right) f_{n'(\mathbf{k}-\mathbf{q})} \quad (\text{A.27})$$

The files *data.epsm1* and *self.qp* are needed by  to solve two problems related to Eq. (A.27)

1. If we are interested in a large number of states, the number of energies  $\epsilon_{n'(\mathbf{k}-\mathbf{q})}^{DFT-LDA} - \epsilon_{n\mathbf{k}}^{QP,0}$  where the inverse dielectric matrix has to be calculated can be very large, increasing the memory needed and the time of the calculation. At the very first run of the lifetime calculation  reports at the end of the file *report.lifestates* the maximum energy transition  $\epsilon_{n'(\mathbf{k}-\mathbf{q})}^{DFT-LDA} - \epsilon_{n\mathbf{k}}^{QP,0}$ . Using this value a first calculation of the  $\tilde{\epsilon}^{-1}$  matrix can be done specifying the parameters WMAX and NW and setting EPSM1WR=.true.. In this case at all the next runs  will use an interpolation method to calculate Eq. (A.27) with an important decrease of the computing time.
2. To perform  $GW_0$  calculations like those described in Chapter 4  used th

external file *self.qp* (a slightly modified *out.qp* file obtained as output of runlevel 8) to overwrite the energies read from *self.gen*. Also the renormalization factors are read.



# Bibliography

- [1] R. D. Mattuck, *A guide to Feynman diagrams in the Many-Body problem*, McGraw-Hill, New York (1976) p. 196-200.
- [2] W. H. Press, B. P. Flannery, S. A. Teukolosky and W. T. Vetterling, *Numerical Recipes (FORTRAN Version)*, Cambridge University Press 1986, pp 248-251.
- [3] D.M. Ceperley and B.I. Alder, Phys. Rev. Lett. **45**, 566 (1980).
- [4] J. P. Perdew and A. Zunger, Phys. Rev. B **23**, 5048 (1981).
- [5] M. S. Hybertsen and S. G. Louie, Phys. Rev. B **34**, 5390 (1986).





# Publications

## **Plane-wave DFT-LDA calculation of the electronic structure and absorption spectrum of copper**

A. Marini, G. Onida, and R. Del Sole, Phys. Rev. B **64**, 195125 (2001).

## **All-electron versus Pseudopotential Calculation of Optical Properties: The Case of GaAs**

P. Monachesi, A. Marini, G. Onida, M. Palummo, and R. Del Sole, Phys. Stat. Sol. (a) **184**, No. 1, 101-104 (2001).

## **Theory for Modeling the Optical Properties of Surfaces**

G. Onida, W. G. Schmidt, O. Pulci, M. Palummo, A. Marini, C. Hogan, and R. Del Sole, In press on Phys. Stat. Sol. (a).

## **Quasiparticle electronic structure of Copper in the $GW$ approximation**

A. Marini, G. Onida, and R. Del Sole, Phys. Rev. Lett. **88**, 016403 (2002).

## **The plasmon resonance and the reflectance spectrum of Silver in the $GW$ approximation**

A. Marini, R. Del Sole, and G. Onida, in preparation.

## **Quasiparticle band structure effects on the lifetimes of $d$ holes in copper within the $GW$ approximation**

A. Marini, R. Del Sole, A. Rubio, and G. Onida, in preparation.

